Nanostructured lithium metal orthosilicates for Li-ion battery cathode application: Two-step hydrothermal-annealing synthesis and structural changes during electrochemical cycling

Huijing Wei

Department of Mining and Materials Engineering

McGill University, Montreal, Canada

March 2021

A thesis submitted to the Faculty of Graduate and Postdoctoral Studies of McGill University in partial fulfilment of the degree of Doctor of Philosophy

Abstract

Lithium metal silicates, Li_2MSiO_4 (*M*=Fe, Mn, Co) have been proposed as potential candidates for lithium-ion battery (LIB) cathode applications during the past decade. In this thesis, mesoporous nanostructured lithium iron silicate (Li_2FeSiO_4) and mixed iron-manganese silicate and ($Li_2Fe_{1-x}Mn_xSiO_4$) materials were successfully synthesized via a novel two-step synthesis method using organic-assisted hydrothermal precipitation and reductive annealing and afterwards were electrochemically evaluated. In a departure from previous LFS synthesis works, ferric iron salt is used in place of ferrous salt as an iron precursor source in the present work to provide unexplored crystallization pathways to sustainable cathode material production. The first hydrothermal step involves the formation of a poorly-crystalline reaction intermediate of ferric silicate starting from the concentrated ferric precursor solution (1 M). In the second reductive annealing step (5% vol. H_2), the reaction intermediate transforms into crystalline LFS yielding two different nanostructured products at 400°C and 700°C (LFS400 and LFS700) retained for electrochemical evaluation. Both ethylene glycol and ethylenediamine are used as crystallization controlling agents. It is demonstrated that the formation of LFS from Fe(III) precursor is made possible by the action of ethylenediamine. Obtained LFS particles are found to be predominantly monoclinic and bear an *in situ* formed via organic decomposition N-doped carbon coating layer. The reductive annealing-induced phase transformation sequence leading to LFS crystallization is characterized and the enabling role of ethylenediamine is discussed.

Initial galvanostatic cycling indicates that the annealing temperature of LFS formation influences the Li-ion storage profile as it shifts from two-phase reaction in ball-milled LFS700 sample to solid solution reaction type in nanograined LFS400 sample. Stable charging and discharging capacity equivalent to one Li ion intercalation were reached for the first three cycles at various cycling rates. To study the long-term electrochemical response and structural evolution, the ball-milled LFS700 material was subjected to extended period of galvanostatic cycling tests at different cycling rates at 45°C and the structure of the cycled LFS was analyzed using high-energy synchrotron X-ray diffraction analysis. It is demonstrated that the LFS material undergoes a partial oxidation reaction induced by the electrolyte that leads to an irreversible formation of partially delithiated monoclinic LFS phase containing a fraction of ferric species. With the progression of cycling a complex structural evolution was observed to occur manifested as a combination of

irreversible crystal transformation of monoclinic $Li_2Fe^{II}SiO_4$ to monoclinic $LiFe^{III}SiO_4$ (inert to further intercalation) and simultaneous introduction of crystal disordering. The kinetics of these structural transformations are dependent on the applied cycling rates, with slower rates promoting the irreversible formation of the monoclinic $LiFe^{III}SiO_4$ phase. By contrast the induced crystal disordering is believed to have a beneficial effect to overall capacity retention of the LFS700 cathode as no significant capacity fading was observed after 30 days (25 cycles at C/20, 75 cycles at C/10, 240 cycles at C/5 or 800 cycles at C/2).

Mixed lithium iron manganese silicates ($Li_2Fe_{1-x}Mn_xSiO_4$) were also prepared using the same synthesis method but replacing part of ferric salt precursor with manganese salt in various ratios in a preliminary effort to evaluate the effect of Mn on capacity attainment and charge compensation. One of the mixed metal silicates, the equimolar $Li_2Fe_{0.5}Mn_{0.5}SiO_4$ (LFMS) obtained at 700°C was subjected to 1.5 galvanostatic cycles (charge-discharge-charge) using post-mortem and *in situ* synchrotron X-ray analyses to probe the type of structural and redox state changes occurring during the formation cycle. The LFMS material registered 1.5 Li exchange (250 mAh/g charging capacity) during the first charge which however was found to be followed by severe irreversible loss during discharge accompanied by significant degree of structure disordering. While charge compensation via metal redox activity involving Fe^{2+}/Fe^{3+} and Mn^{2+}/Mn^{3+} accounting for 1 Li exchange was confirmed, questions remain if the Mn^{3+}/Mn^{4+} couple in LFMS could indeed enable attainment of reversible capacity beyond 1 Li.

This work provides new methods and insight into the synthesis of LFS and LFMS, the structural evolution of LFS during long term cycling, and the Mn influence on the first cycle redox chemistry of $Li_2Fe_{0.5}Mn_{0.5}SiO_4$. As such it contributes to the continuing efforts of further understanding and development of the orthosilicates as cathode materials.

Résumé

Au cours de la dernière décennie, plusieurs matériaux alternatifs pour les cathodes des batteries lithium-ion (LIB) ont été développés, parmi lesquels on retrouve le Li_2MSiO_4 (*M*=Fe, Mn, Co). Cette thèse démontre une nouvelle approche pour synthétiser des particules nanostructurées mésoporeuses de Li_2FeSiO_4 et $Li_2Fe_{1-x}Mn_xSiO_4$. Celle-ci se déroule en deux étapes comprenant une précipitation hydrothermale et un recuit en atmosphère réductrice à 400°C ou 700°C (LFS400 et LFS700). S'inscrivant en continuité avec des études antérieures, les présents travaux de recherche utilisent un sel ferrique en remplacement du sel ferreux comme source de fer ce qui permet d'explorer une méthode de cristallisation innovatrice et durable. En premier lieu, des cristaux de silicates ferriques peu structurés sont formés à partir d'une solution concentrée de ce précurseur. Ensuite, lors d'une étape de recuit en atmosphère réductrice (5% H_2), les produits de la première étape se transforment en deux nanostructures cristallines de LFS différentes selon les températures de recuit retenues pour les caractérisations électrochimiques soient, à 400°C et à 700°C (LFS400 et LFS700). Lors de ce traitement thermique, l'éthylène glycol et l'éthylènediamine sont utilisés comme agents de contrôle de la cristallisation. Il a été démontré que la formation de LFS depuis un précurseur de Fe(III) est possible seulement par l'action de l'éthylènediamine. Les particules de LFS ainsi obtenues sont principalement monocliniques et sont recouverts d'une couche de carbone formée in-situ via une déposition organique. La séquence de transformation de phase menant aux cristaux de LFS a été étudiée en se basant sur les résultats de caractérisation et le rôle de l'éthylènediamine est discuté.

Les résultats préliminaires de cyclages galvanostatiques ont dévoilés que la température de recuit du LFS influence les propriétés d'emmagasinage du lithium, passant d'une réaction de type bi-phasée pour l'échantillon broyé recuit à 700°C (LFS700) à une réaction de type solution solide pour l'échantillon nanométrique LFS400. Des capacités stables de charge et de décharge pour le premier atome de lithium ont été obtenues à différentes densités de courant. Afin30 d'étudier la réponse électrochimique et les changements structuraux à long terme, l'échantillon LFS700 a été soumis à un cyclage galvanostatique de longue durée à différentes densités de courant et à 45°C puis analysé à l'aide de la diffraction à rayon X de haute énergie à synchrotron couplée à une analyse quantitative de la structure. Il a été démontré que le matériau LFS a subi une oxydation partielle induite par l'électrolyte ce qui mène à la formation irréversible d'une phase LFS

monoclinique en partie délithiée. Cette phase est composée de parties d'espèces ferriques et montre un certain taux de désordre cristallin. Dès la naissance des cristaux, il a été observé que la phase LFS monoclinique délithiée croit et le désordre cristallin prend de l'ampleur, plus spécialement à faible densité de courant. Il est supposé que ce désordre procure un effet bénéfique sur la rétention des capacités galvaniques, puisqu'aucune baisse de capacité significative n'a été observée jusqu'à 30 jours après le début du cyclage (25 cycles à C/20, 75 cycles à C/10, 240 cycles à C/5 ou 800 cycles à C/2). Cependant, le cyclage à une densité de courant plus faible (C/50) et/ou une augmentation de la température de cyclage à 55°C a mené à l'épuisement de la batterie. Ces travaux procurent une nouvelle compréhension des mécanismes de synthèse et de l'évolution structurale du LFS lors du cyclage à long terme.

Des particules nanostructurées $Li_2Fe_{1-x}Mn_xSiO_4$ sont synthétiséés en utilisent la même approche. Un sel manganèse remplace le sel ferreux dans différents rapports pour évaluer l'effet du manganèse sur la rétention des capacités. $Li_2Fe_{0.5}Mn_{0.5}SiO_4$ (LFMS), un échantillon recuit à 700°C, a été soumis à un cyclage galvanostatique de 1.5 cycle puis analysé à la diffraction à rayon X de haute énergie à synchrotron pour étudier les changements structuraux et oxydation/réduction pendant le premier cycle. L'échantillon LFMS a démontré 250 mAh/g de capacité de charge (1.5 Li délithiée) pendant le première charge. Mais après, une baisse de capacité significative et irréversible a été observée pendant le première décharge avec du désordre cristallin. Il a été démontré que les oxydations de Fe^{2+}/Fe^{3+} et Mn^{2+}/Mn^{3+} pour le premier lithium est confirmé, mais c'est encore discutable si l'oxydation de Mn^{3+}/Mn^{4+} contribue à la rétention des capacités.

Les présents travaux de recherche fournissent de nouvelles méthodes et perspectives pour synthétiser LFS et LFMS, les changements structuraux à long terme, et l'effet du manganèse au premier cycle galvanostatique de $Li_2Fe_{0.5}Mn_{0.5}SiO_4$. Ces travaux contribuent à la compréhension et au développement des Li_2MSiO_4 matériaux pour les cathodes des batteries lithium-ion.

Acknowledgement

This work was generously funded by Hydro-Quebec and NSERC (Natural Sciences and Engineering Research Council of Canada) through a CRD grant. In addition, I would like to acknowledge some people who have supported me during my study at McGill University. Firstly, I would like to thank my supervisor, Prof. George P. Demopoulos for his guidance over the past six year. He is a very kind and intelligent person and he is very caring and patient to his students. He has spent a lot of time with me going over my experimental details and results, and gave me a lot of support and courage during my thesis writing and revision, which I truly appreciate.

I would also like to thank my fellow colleagues in the HydroMET group for their help and support. I thank those with whom we have spent years of joyful time working and hanging out together. I would especially like to thank Marianna Uceda, my precious friend who dragged me out of darkness. I also truly appreciate the help from François Larouche for the French translation of the thesis abstract.

I would also like to thank Canadian Light Source for the synchrotron facility and Dr. Joel Reid for his help with the XRD data acquisitions. Prof. De-tong Jiang and his students Zach Arthur, Vincent Emond, as well as Dr. Ning Chen at HXMA beamline have offered me valuable help and days (and nights) of hands-on experience with the synchrotron X-ray beamline. I also thank Prof. Gauvin and Nicholas Brodusch for the help of SEM characterizations, Dr. Xuedong Liu and Dr. Bin Wei for TEM characterization assistance.

In the end, I would like to thank my family and friends for their support and understanding throughout my study. I appreciate that my parents visit me every year from China when I am too busy to go back. I thank my husband, Dr. Kaiwen Hu for the valuable discussions on research. I also appreciate the accompany of our furry buddies at home for always comforting me and cheering me up. I also thank my piano teacher, Beguentch Gueldyev, for helping me grow into a true classical pianist over the past five years. I also thank my psychiatrist, my therapists who helped me through my depression and mental illness, and help me become a better self.

Table of Contents

List of symbols

A surface area (m^2)

a, b, c unit cell length in three axes in lattice parameter (Å)

B isotropic atomic displacement factors

C specific charge capacity (mAh/g)

C/x C-rate, where x is the numbers of hours to reach the full capacity

D diffusivity (m^2/s)

d interplanar spacing (Å)

g atomic site occupancy

E energy (J)

E^0 equilibrium potential (V)

e electron charge (C)

F Faraday's constant (C/mol)

G Gibbs free energy (J)

I current (A)

M molecular mass (g/mol)

n number of mols

Q charge (C)

R resistance (Ω)

R_{wp} weighted profile R factor

T temperature (°C)

V_{oc} open circuit voltage (V)

V volume (m^3)

x composition fraction of solid solution

x_i, x_j solubility limits (mol/L)

x, y, z atomic positions

Z atomic number

z valence state

β angle between a and c axis in the lattice parameter (°)

μ	chemical potential (J/mol)
θ	diffraction angle (°)
λ	wavelength (nm)

List of abbreviations and subscripts

A	anode
BET	Brunauer–Emmett–Teller
C	cathode
CV	cyclic voltammetry
DFT	Density function theory
DMC	Dimethyl carbonate
EC	Ethylene carbonate
FTIR	Fourier-transform infrared spectroscopy
HOMO	highest occupied molecular orbital
LCO	lithium cobalt oxide
LFMS	lithium iron-manganese silicate
LFP	lithium iron phosphate
LFS	lithium iron silicate
LIB	lithium-ion batteries
LMS	lithium manganese silicate
LUMO	lowest unoccupied molecular orbital
NMP	N-methyl pyrrolidinone
PVDF	polyvinylidene fluoride
R	reaction or number of hours
SAED	selected area electron diffraction
SEI	solid-electrolyte interface
SEM	Scanning electron microscopy
SOC	state of charge
TEM	Transmission electron microscopy
TGA	Thermo gravimetric analysis
XANES	X-ray absorption near-edge spectroscopy
XRD	X-ray diffraction

List of Figures

List of Tables

Chapter 1 Introduction

1.1 Energy demand and sustainability

As the world population expands and economy grows, worldwide energy supply and demand also increases. The Statistical Review of World Energy in 2018 states that the world primary energy consumption reached 13,511 million tons of oil equivalent in 2017 with an average annual growth rate of energy consumption of 1.5%; similarly, the world electricity generation has reached over 25,500 terawatt-hours in 2017, with an average growth rate of 2.5% over the past ten years.[1] Among the different sources of energy production, oil, natural gas and coal still serve as the three major sources of energy. However, the renewable energy generated from wind and solar sources have increased over the past decade and it is predicted that renewable energy will gradually replace the traditional sources of energy to help make economy growth more sustainable. Since renewable energy is intermittent in nature, it needs to be stored as standby power for future use; batteries provide the ideal mechanism to generate electric power from electrochemical reactions.

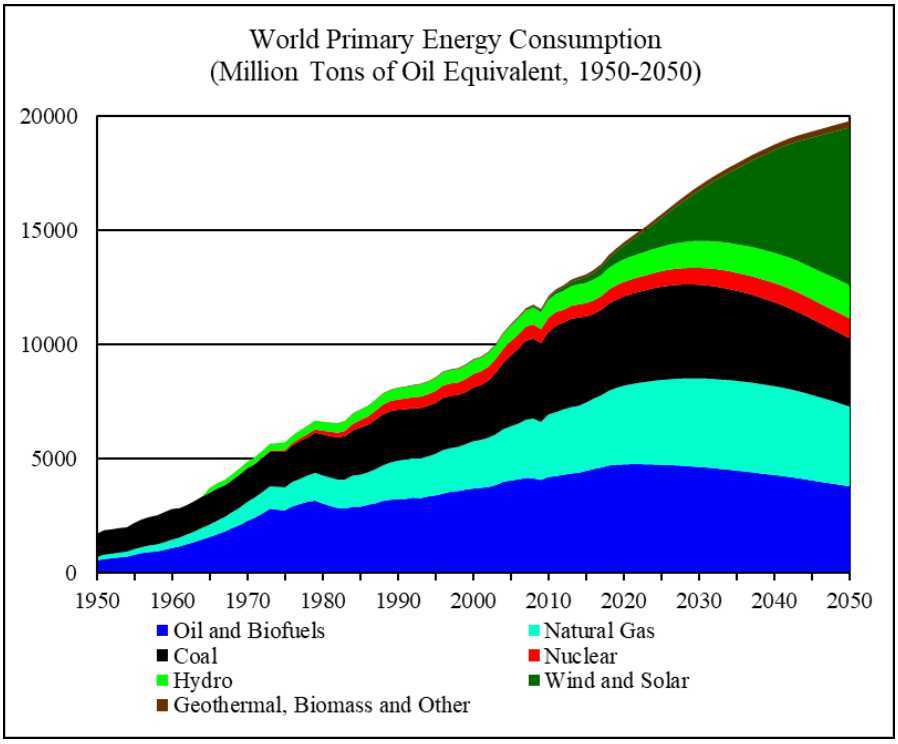

Figure 1.1. The total world primary energy consumption divided by sources, 1950-2050.[1]

1.2 Different types of batteries

Batteries are electrochemical cells that store electrical energy. A battery consists of a pair of electrodes, the anode and the cathode, and the electrolyte. There are different types of batteries of different sizes and uses, from disposable single-use alkaline batteries, to rechargeable room-sized battery banks used as emergency power supply for telecommunication centers and data centers or to store intermittently generated renewable energy from photovoltaic or wind harvesting. Batteries are omnipresent in consumer electronics, including laptops and smartphones, hearing aids and other devices. They are also used to power new forms of electric transportation as evidenced by the introduction of several types of electric vehicles in both the consumer and commercial markets.[2] By far, lithium-ion batteries (LIB) drive the "revolution" in new energy storage applications as consumer and industry standards increasingly call for higher energy and power density, long cycle life, low cost and sustainable materials.[3]

1.3 Li-ion batteries

An electrochemical cell involves electrochemical reactions at the two electrodes (anode and cathode) and transportation of electrons (through an external circuit) and ions (through the electrolyte) between the two electrodes.[4] The potential difference between the two electrodes, defined as the cell potential and expressed in the unit of V (Volt, where 1 V = 1 J/C, Joule/Coulomb), when the circuit is open (V_{OC}), i.e. at equilibrium, is described in the equation below.[5]

$$V_{oc} = \frac{\mu_A - \mu_C}{e} \qquad (1.1)$$

Where μ_A and μ_C are the chemical potentials of the anode and cathode and e the charge of one mole of electrons. The open-circuit voltage (V_{OC}) is the theoretical potential determined by the thermodynamics of the internal electrochemical cell reaction, also represented with E in the well-known equation:

$$-\Delta G = nFE \qquad (1.2)$$

Where ΔG is the Gibbs free energy of the electrochemical reaction, n is the number of exchanged electrons per formula unit, and F is the Faraday constant (96,485.3 C/mol of electrons).[4]

The overall chemical reaction of an electrochemical cell can be split into two half-reactions which describe the electrode reactions at each electrode/electrolyte interface. When the circuit is closed and current flows due to internal spontaneous reaction the magnitude of cell voltage will decrease from its theoretical value due to kinetic resistances at each electrode and the electrolyte identified as overpotentials or polarization.

One example of the earliest developed rechargeable batteries that is still in wide use is the lead-acid battery, which operates based on the following reaction with theoretical cell voltage of 2.05V [6]:

$$Pb(s) + PbO_2(s) + 2H_2SO_4\,(aq) \rightarrow 2PbSO_4\,(s) + 2H_2O\,(l) \qquad (1.3)$$

The reaction (during discharge) at the anode is the oxidation of metallic lead to lead sulfate and the reaction at the cathode the reduction of Pb^{IV} (PbO_2) to Pb^{II} ($PbSO_4$). During charging the reverse reactions occur.

Later, rechargeable batteries based on the phenomenon of ion intercalation reaction were developed or proposed, such as the Li-, Na-, Mg-, Al- ion batteries [7-11]. In this case a shuttling ion moving from the anode to the cathode during discharging enters the structure of the cathode material (intercalation or insertion) and moves out during charging (de-intercalation or de-insertion) returning to the anode. More specifically lithium ion batteries (LIBs) are devices that convert chemical energy to electrical energy based on the reversible intercalation of lithium ions into the two electrodes through reduction-oxidation reactions. Thanks to the commercialization of the Li-ion battery more than 25 years featuring graphite as anode and $LiCoO_2$ as cathode the wide proliferation of all sorts of mobile electronics became possible[7] .

A key performance metric of a LIB is its energy density. Energy density may be defined based on mass or volume. The former more specifically termed as *specific energy* is given in *Wh/kg* units while the latter termed *energy density* is given in *Wh/L* units[8] . In this thesis the term “energy density” is used to denote the gravimetric energy density, i.e. Wh/kg.

The Energy density is the product of the voltage and the amount of charge stored otherwise known as specific capacity (mAh/g). The more lithium ions the cathode can store, the higher the specific capacity, as described by the following equation,[4]

$$C = \frac{nF}{3.6M} \qquad (1.4)$$

where *n* is the number of exchanged electrons per formula unit, M is the molecular mass of the cathode compound. At the same time, for a given anode, say graphite, the higher the intercalation potential of the cathode, the higher energy density of the device.

Another important metric is the C rate, defined as C/x where x is the number of hours required to fully discharge its maximum (theoretical) specific capacity[8] . For example, for $LiCoO_2$ the theoretical specific capacity calculated with the aid of equation (1.4) is 274 mAh/g, meaning that at 1C rate 274 mAh/g will be discharged in one hour; and if the rate is C/10 the same amount of charge will be discharged in 10 hours.

However, the actual voltage of an operating cell as well as its accessible charge storage capacity depend on the current (C-rate) and the properties of the intercalation electrodes hence the practical energy density may be significantly lower than the theoretically calculated value[8-9]. Thus, the useful charge capacity, hence the gravimetric energy density, decreases with increasing rate, i.e. increasing current and similarly the cell voltage output decreases due to progressive development of overpotential-derived resistances at the two electrode/electrolyte interfaces. A good example again is the benchmark cathode made of $LiCoO_2$ that has a practical specific capacity of 140mAh/g[9] vs. the theoretical 274 mAh/g value mentioned above with corresponding practical energy density been only 250 Ah/kg while the theoretical value is 1000 Ah/kg [10].

As LIBs are called now to power the electrification of transportation there is a need for the development of higher energy density LIBs[3]. In this regard, intensive research is underway to develop new cathode materials with high specific capacity, i.e. high energy density [11]. But a next-generation rechargeable lithium ion battery other than having high energy density must meet additional criteria including long cycle life, good rate capability, structural/thermal stability, as well as made of abundant elements via low cost and scalable processes. In this context, lithium transition metal orthosilicates (Li_2MSiO_4, where M=Fe, Mn) have been proposed[12] as high-energy density cathode materials because they carry two Li ions per formula unit (translating to 330 mAh/g theoretical capacity) within a stable poly-oxyanion framework while made of abundant elements (Fe, Mn, Si) hence offering a potentially highly sustainable solution. Progress with the development of

these cathode materials however has been hampered because of complex crystal structure chemistry that complicates synthesis and electrochemical response.[35,94]

In the research described in this thesis, various aspects of lithium iron silicate (LFS; Li_2FeSiO_4) and mixed iron/manganese lithium metal silicate (LFMS; $Li_2Fe_{1-x}Mn_xSiO_4$) are studied in terms of synthesis, nanostructuring, and short- as well as long-term electrochemical behavior combined with post-mortem analysis. The overall goal of the research is to provide new insight into the crystallization chemistry and electrochemistry of LFS and LFMS and thereby contribute to their further development as high capacity cathodes for Li-ion rechargeable batteries.

1.4 Objectives of this research

The specific objectives of the research are: firstly to study the formation of different nanostructured LFS materials via a novel synthesis method that combines organic-assisted hydrothermal precipitation and subsequent annealing in a reducing atmosphere over the temperature range 400-700 °C. Secondly, to correlate synthesis conditions and structural characteristics of the different LFS cathode materials (LFS400 vs. LFS700) to their Li-ion storage properties via short-term electrochemical cycling studies. Thirdly, to probe the structural evolution of the LFS@700 upon long-term cycling at different rates via post-mortem analysis. And finally, to apply the novel synthesis method to the preparation of mixed lithium iron/manganese silicates and assess their short-term electrochemically induced intercalation/de-intercalation response via *in situ* synchrotron XRD and XANES monitoring.

1.5 Thesis structure

This thesis is in a traditional chapter-based format. After this introductory chapter (Chapter 1), chapter 2 reviews the literature of lithium iron (manganese mixed) silicates as compared to conventional cathode materials, various synthesis methods and challenges previously faced, as well as certain contradictory findings in terms of phase identifications and structural transformations upon electrochemical cycling. In chapter 3, the experimental methods and characterization techniques used in the project are given. The results along their discussion are presented in chapters 4 to 7. Chapter 4 presents the crystallization and characterization of the LFS materials obtained using the new dual step hydrothermal and annealing synthesis method. Chapter 5 presents the electrochemical response of the initial cycles of two LFS materials obtained at different annealing conditions,

LFS400 and LFS700, and correlates to their nanostructural characteristics. Chapter 6 further continues the work of chapter 5 and discusses the structural evolution of LFS700 after long-term cycling at various rates. Chapter 7 presents a preliminary study of lithium iron/manganese silicates (LFMS) in terms of synthesis and structural/chemical changes as a function of state of charge during the first cycle via *in situ* XRD and XANES analysis. Finally, the conclusion chapter (chapter 8) summarizes the major findings of this research project, identifies the original contributions to knowledge, and proposes some ideas for future research.

Part of the thesis (chapters 4 and 5) is based on a previously published paper:

Wei, H., Lu, X., Chiu, H.C., Wei, B., Gauvin, R., Arthur, Z., Emond, V., Jiang, D.T., Zaghib, K. and Demopoulos, G.P., 2018. Ethylenediamine-enabled sustainable synthesis of mesoporous nanostructured $Li_2FeIISiO_4$ particles from Fe (III) aqueous solution for Li-ion battery application, *ACS Sustainable Chemistry & Engineering*, 6(6), pp.7458-7467.

The author of this thesis carried out the materials synthesis, characterization, electrochemical measurements, structural analysis and data interpretation in each chapter. In some microscopic characterization she was assisted by N. Brodusch and Dr. B. Wei from Prof. Gauvin's group and Dr. D. Liu from Facility for Electron Microscopy Research, McGill University. In synchrotron X-ray data acquisition, she was assisted by Z. Arthur, V. Emond, and Prof. Jiang from University of Guelph. Additional post-mortem synchrotron X-ray diffraction data was acquired with the help of Dr. Joel Reid at Canadian Light Source. Useful comments were also received from Dr. X. Lu, Dr. H-C. Chiu, and Dr. K. Zaghib.

Chapter 2. Literature Review

2.1 The Lithium-ion batteries: general

2.1.1 Components and operation

A typical lithium-ion battery comprises of three components: a positive electrode (cathode), a negative electrode (anode) and electrolyte. The pair of electrodes serve as the source and sink for lithium ions, while the electrolyte is intrinsically an ionic conductor, facilitating Li-ion transport across the two electrodes. As lithium ions flow through the electrolyte, electrons generated from the redox reactions flow through the external circuit. A schematic picture showing the transport of lithium ions and electrons during charging and discharging of a lithium-ion battery is presented in Figure 2.1.[13] The operation is based on the reversible intercalation of lithium ion into graphite (anode) and lithium-metal oxide (cathode).

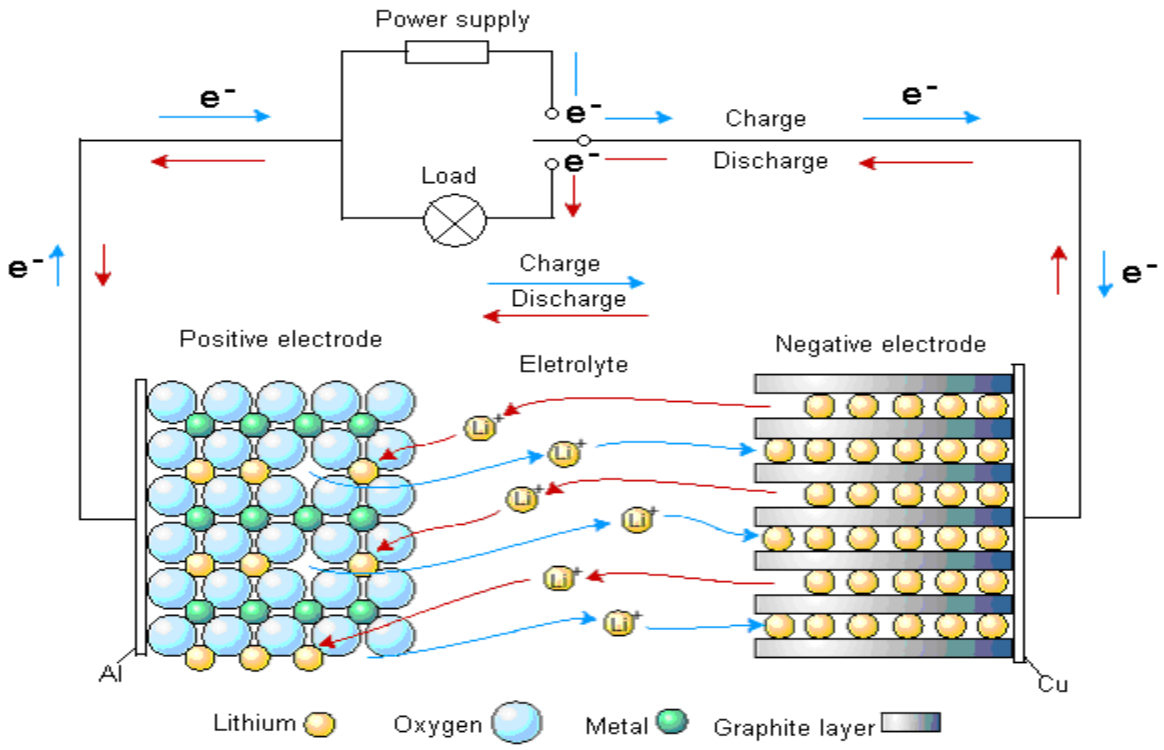

Figure 2.1. Schematic representation of the charging and discharging principles of rechargeable LIBs. [13]

2.1.2 Commercialized cathode materials

There are several key characteristics for a material to be an ideal cathode in rechargeable LIBs. In principle, the cathode material contains an element in an oxidized state that is reducible allowing the reversible insertion of lithium ions. From a thermodynamic aspect, this determines the capacity, voltage, and the overall energy storage (density) of the cathode. From a kinetic aspect, fast ion insertion and extraction lead to high rate performance and power density, while reversibility governs the cyclability, capacity retention, and, is associated with the structural stability upon lithiation and delithiation. Furthermore, an ideal cathode material should also be a good electronic conductor to allow easy electron transport.[14] Based on these criteria, there are different families of cathode materials that have been invented as discussed below.

2.1.2.1 Lithium Cobalt Oxide, $LiCoO_2$

$LiCoO_2$ is a cubic closed packed material that also has layered structure for intercalation based on the following reaction, $LiCoO_2 + C_6 \rightarrow Li_xC_6 + Li_{1-x}CoO_2$. In 1980, J.B. Goodenough discovered that lithium ions could be electrochemically inserted and removed from the parent $LiCoO_2$ ordered rock-salt structure (Fig. 2.2a) at a high voltage (4.0 V) with good reversibility at current densities up to 4 mA/cm^2. [15] In 1990s, SONY commercialized $LiCoO_2$/C batteries, however, the practical capacity of $LiCoO_2$ cell is relatively low, at around 140 mAh/g[9]. This is because only 0.5 Li can be reversibly (de)lithiated per unit of $LiCoO_2$ to maintain the structural stability while avoiding capacity loss and structure collapse when lithium concentration is low.[16] A concern lies in the safety of $LiCoO_2$ due to its poor thermal stability. At elevated operating temperatures above 130 °C or, in the case of overcharging, $LiCoO_2$ decomposes and generates oxygen gas, which readily reacts with the organic solvent in the electrolyte exothermically and causes combustion.[17] Research has focused on improving the thermal stability of $LiCoO_2$ by coating a metal oxide or phosphate layer on the surface of $LiCoO_2$ particles.[18] In such research, the capacity of $LiCoO_2$ was increased to 170 mAh/g without fading upon 70 cycles between 2.75V and 4.4V. In addition, better capacity retention is found by switching the electrolyte from $LiPF_6$ to lithium bis(oxalato)borate (LiBOB), (up to 180 mAh/g at a cut off voltage of 4.5 V in lab testing environment).[19] In addition to the limited capacity and poor thermal stability, the availability and cost of Co is another drawback of $LiCoO_2$ cathode hence its application is limited in mobile electronics such as cellphones, cameras and laptops.

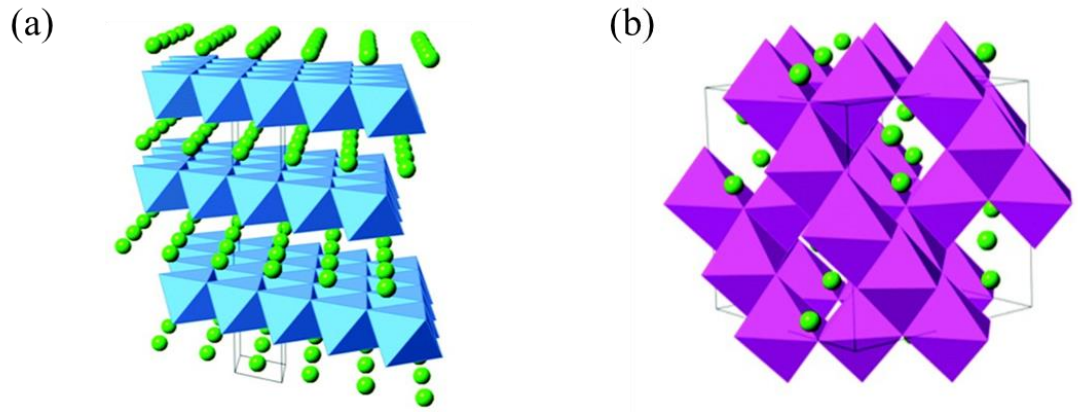

Figure 2.2. (a) Layered structure of α-$LiCoO_2$ with lithium ions (green) residing between the closed packed octahedral cobalt oxide slabs (blue); and (b) cubic structure $LiMn_2O_4$ spinel. [20]

2.1.2.2 Spinel, $LiMn_2O_4$

The spinel family has been widely studied as an alternative candidate to replace the costly lithium cobalt oxide cathode. Discovered by M. Thackeray et al. in 1983, lithium spinel compounds $Li[B_2]X_4$ (B= transition metal cation) can provide a host structure to accommodate lithium through a three-dimensional interstitial framework.[21] The crystal structure of $LiMnO_2$ is shown in Figure 2.2b.

By varying the metal cation type, the working voltage can be tuned over a wide range, a realization that also led to the development of $Li_4Ti_5O_{12}$ anode.[22] Among the spinel cathodes, Li-Mn-O is the most extensively studied system. There are many possible stoichiometric compositions in the Li-Mn-O phase diagram, which can be represented by the general formula $Li_{1+x}Mn_{2-x}O_4$.[23] The lithium insertion reaction of $LiMn_2O_4$ occurs through the following reaction at 2.96V.

$$Li + Li[Mn^{III\text{-}IV}{}_2]O_4 \rightarrow Li_2[Mn^{III}{}_2]O_4 \qquad (2.1)$$

In this reaction, the cubic spinel $LiMn_2O_4$ phase is transformed into the tetragonal rock-salt phase $Li_2Mn_2O_4$, and the phase change causes a lattice distortion with 16% increase in c/a ratio. This severe anisotropic structure distortion causes rapid capacity loss upon cycling at 3 V.[21]

Capacity fade in $LiMn_2O_4$ spinel cathode depends on temperature. At room temperature capacity fading is slow but when the operating temperature exceeds 40-50°C, the capacity loss becomes accentuated. This behavior is due to three reasons: first, disproportionation of Mn^{3+} occurs at the electrode surface through the following reaction: $2Mn^{3+}$ (solid) → Mn^{4+} (solid) + Mn^{2+} (solution);[24] second, the structural instability of highly delithiated $Li_{1-x}Mn_2O_4$ arising from oxygen atom loss and reduction of Mn^{4+} to Mn^{3+};[23] third, the Jahn-Teller distortion above 3 V where tetragonal $Li_2Mn_2O_4$ phase forms at the surface of the spinel phase.[25] These challenges have driven the research towards other cathode materials.

2.1.2.3 Olivine, $LiFePO_4$

The iron-based olivine cathode material ($LiFePO_4$) was first discovered in 1997 by A. K. Padhi and J. B. Goodenough.[26] The discharge potential of $LiFePO_4$ is around 3.4 V and its capacity approaches 170 mAh/g with no obvious capacity fade and structural degradation after many cycles. Nishijima et al. reported 70% capacity retention after 10,000 cycles for doped LFP cells.[27] The material can be synthesized through various methods such as hydrothermal, sol-gel and solid-state reactions under controlled reducing synthesis conditions [28] to obtain the crystalline structure with good intercalation properties. The crystal structure of olivine $LiFePO_4$ is shown in Fig. 2.3.[29]

Due to the low electronic conductivity of pristine $LiFePO_4$ (10^{-9} S/cm), and the slow diffusion of lithium, the theoretical capacity can only be reached at very low current density or elevated temperature.[30] Research has been done to improve the electrochemical performance of $LiFePO_4$ by reducing the particle size to nanometer scale and applying a carbon-coating layer which can increase the conductivity to about 10^{-5}-10^{-6} S/cm.[31] Other methods, such as doping have also been reported to result in increased conductivity by a factor of ~10^8.[32]

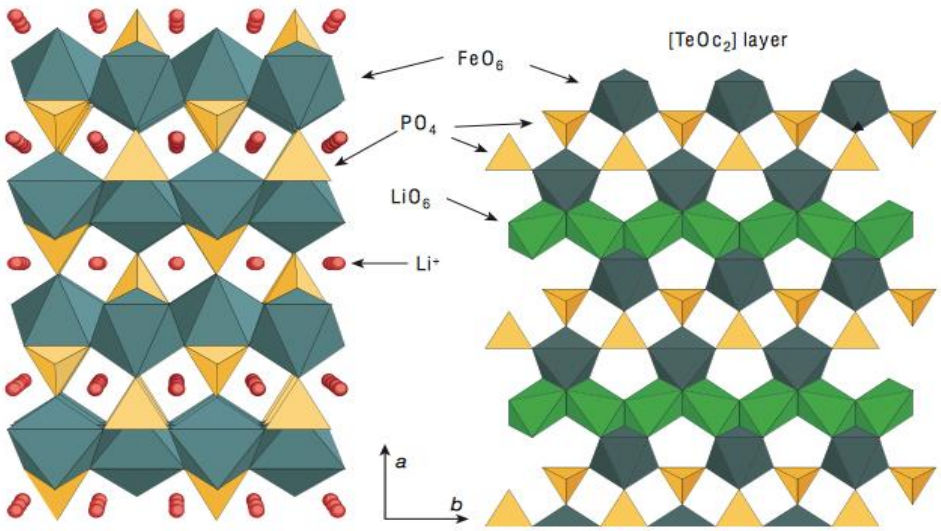

Figure. 2.3. Olivine $LiFePO_4$ structure in projection along [001]. The left image shows the framework of FeO_6 octahedra linked through corner sharing and PO_4 tetrahedra with lithium ions inside the tunnels. The right image shows Li, Fe, P distribution between two distorted HCP oxygen-dense layers, with edge sharing LiO_6 octahedra. Li ions may diffuse along [010] and [001] directions. [29]

Although many different types of cathode materials for rechargeable lithium ion batteries have been investigated, all (including lithium iron phosphate) are characterized by only modest charge storage capacity. In 2000, M. Armand and co-workers proposed that one possible way to achieve higher capacities is to design a material that can reversibly extract two lithium ions, and the metal's redox oxidation state can change by two accordingly.[12] One possible group of materials that theoretically meets this criterion is lithium metal orthosilicates, which, if successfully developed to realize their full storage capacity, could offer solutions for new applications such as hybrid electric vehicles and grid scale stationary energy storage.

2.2 Lithium metal silicates

2.2.1 Introduction

As alternative cathode materials, polyoxyanion lithium metal orthosilicates, proposed by M. Armand and co-workers [12] have attracted growing research interest. Due to the strong binding of oxygen and silicon within SiO_4, Li_2MSiO_4 (M=Fe^{2+}, Mn^{2+}, Co^{2+}, Ni^{2+}) has enhanced structural stability and thus inherent safety when compared to the oxide layered or spinel compounds. Moreover, because of the two lithium ions per formula unit that can be potentially extracted through

redox processes M^{2+}/M^{3+} and M^{3+}/M^{4+}, it has twice the theoretical capacity (above 300 mAh/g) compared to previously developed cathode materials. Among Li_2MSiO_4, the Li_2FeSiO_4 is attracting most research interest due to its better cyclability potential. Besides lithium iron silicate, the lithium metal orthosilicate family includes members with other transition metal cations such as Li_2MnSiO_4 (LMS); or mixed metal silicates through cationic substitution such as the lithium iron manganese silicate ($Li_2Fe_{1-x}Mn_xSiO_4$). The extraction of the second Li from Li_2MSiO_4 requires oxidation of the transition metal to the tetravalent (IV) state. In this context it has been thought Li_2MnSiO_4 to be particularly attractive as Mn^{IV} state is accessible at lower voltage than the corresponding Fe^{IV} state.[35,33]However, earlier electrochemical studies revealed the LMS to suffer from severe capacity fate and structure deterioration due to the Jahn-Teller distortion phenomenon[94]. This prompted research into mixed Fe-Mn orthosilicates aiming at synergistic benefits with Fe playing a structure stabilizing role and Mn allowing for accessing higher Li-ion storage via the Mn^{3+}/Mn^{4+} redox couple.[35,33]

2.2.2 Polymorphs

Li_2MSiO_4 compounds can exist in a range of polymorphs and metastable phases depending on what tetrahedral sites cations reside within the tetragonally packed oxyanion scaffold and further, as a result of various structural distortions.[34] The structures of the Li_2FeSiO_4 polymorphs and their relationship with space group symmetry are shown in Fig. 2.4.[35] The polymorphism of these compounds relates to the tetrahedral structures that are divided into β and γ families as in Li_3PO_4. In β structure, all tetrahedra are corner sharing, pointing in the same direction perpendicular to the close packed planes. In γ structure, the edge-sharing tetrahedra are arranged in groups of three with central tetrahedron pointing in the opposite direction to the outer two. The β phase can transform to the γ phase, when inversion occurs at half of the tetrahedral sites; the γ phase is generally stable at higher temperature. Depending on the long-range ordering and lattice distortion, both β and γ structures can be sub-divided into and designated as β_I, β_{II}, γ_0, γ_{II} and γ_s. For simplicity, the β and the γ notations are often omitted and only the space group symbols (i.e. *p21n, pmn21*, and *pmnb*) are used to describe the crystal system (i.e. monoclinic vs. orthorhombic), where the letters and numeric notations follow the Hermann-Mauguin notation, indicating the lattice type (i.e. *p* for primitive), symmetry with respect to axis direction (number 1 or 2), glide plane or mirror plane perpendicular to a certain axis (*m, n*), and symmetry related to diagonals. Because of the high temperature synthesis and annealing

conditions used to produce these polymorphs the γ_s (*p21n*) is also known as the high temperature monoclinic phase and the γ_{II} (*pmnb*) as the high temperature orthorhombic phase. The β_{II}/*pmn21* is known as the low temperature orthorhombic phase and the inverse β_{II}/*pmn21* is known as the inverse orthorhombic phase.[33] The temperature-dependent phase formation will be discussed in detail in the following sections.

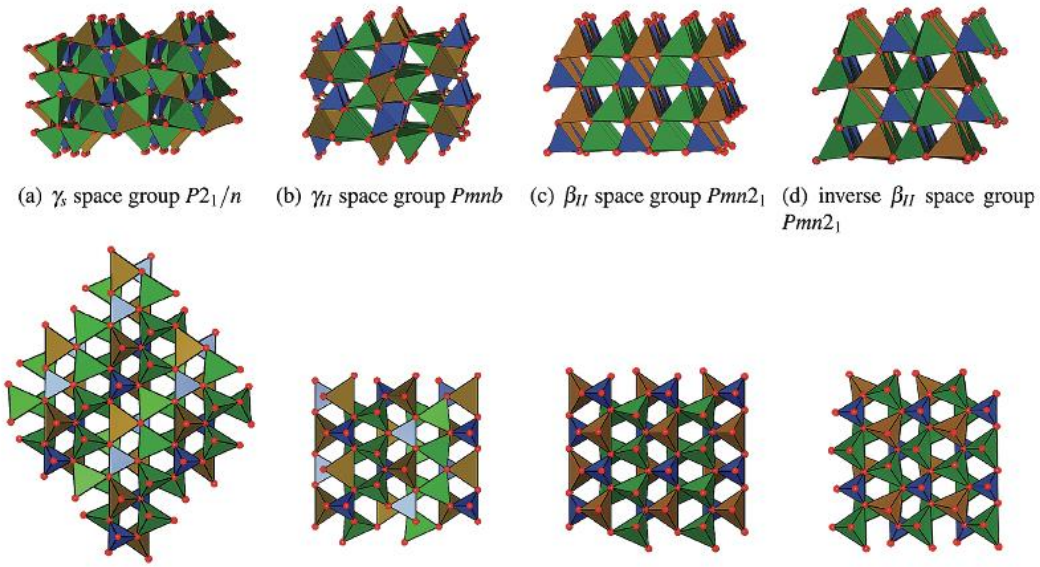

Figure. 2.4. Li_2FeSiO_4 polymorphs, viewed each one from two orthogonal directions. [35]

Equivalent to LFS polymorphs are also exhibited by mixed metal silicates.[34]. The structure and different polymorphs of the $Li_2Fe_{1-x}Mn_xSiO_4$ solid-solution series have been characterized and studied using various techniques such as X-ray powder diffraction [36-37], neutron diffraction [36], ^{6}Li and ^{7}Li MAS NMR spectroscopy [38], XANES and XAFS spectroscopy [39-40] and DFT-based computational techniques [20] for detailed understandings of the local bonding nature of the metal oxide tetrahedron and the orthosilicate polyoxyanion framework. The overall structure of $Li_2Fe_{1-x}Mn_xSiO_4$ at different Fe to Mn ratios are in general quite similar for all the three polymorphs, with slight difference in the cation tetrahedra arrangements, anisotropy shifts, and variable transitional energy towards specific polymorph, changes that may have a complex impact on structural stability and phase transformation during cycling (lithiation/delithiation) and thus the overall electrochemical behavior.

2.3 Synthesis of $Li_2(Fe,Mn)SiO_4$ and $Li_2Fe_{1-x}Mn_xSiO_4$

2.3.1 Temperature-dependent phase formation

2.3.1.1 Li_2FeSiO_4

Depending on the synthesis conditions, particularly the annealing temperature, different Li_2FeSiO_4 (LFS) polymorphs have been reported to form. In the pioneering work published by Nyten *et al.*,[41] the solid-state reaction method was used involving heat-treating a precursor mixture at 750 ℃ under reducing gas flow. It was claimed that phase-pure β_{II} *pmn21* (low temperature orthorhombic) was obtained with the presence of unidentified peaks (shown in Figure 2.5 a). However, it was later revealed by Nishimura *et al.*[42] that those peaks are in fact signature peaks of the LFS *p21n* phase and heat treatment at such (around 700°C) temperature is now accepted to yield the monoclinic *p21n* phase. In Armstrong *et al.*,[43] similar XRD pattern was observed for LFS sample synthesized through a hydrothermal and annealing method (600°C) (shown in Figure 2.5 b). It was noticed that the peak labelled with asterisk at 31° in Nyten's work is also present in the XRD pattern reported by Armstrong, however, the corresponding peak at 40° in their case was due to a different wavelength of their XRD sources. Although similar XRD patterns were observed, the space group symmetry of the structure was indexed differently by different groups.

The confusion and ambiguity in phase identification are seen not only in early works but also in recent works. For example, in the recent study published by Qu *et al.* in 2018, similar monoclinic XRD pattern was observed for LFS obtained at 600°C and it was claimed by the author to be phase-pure orthorhombic *pmn21*.[44], whereas it is widely agreed that the LFS phase obtained at such heat treatment condition is in fact monoclinic instead.

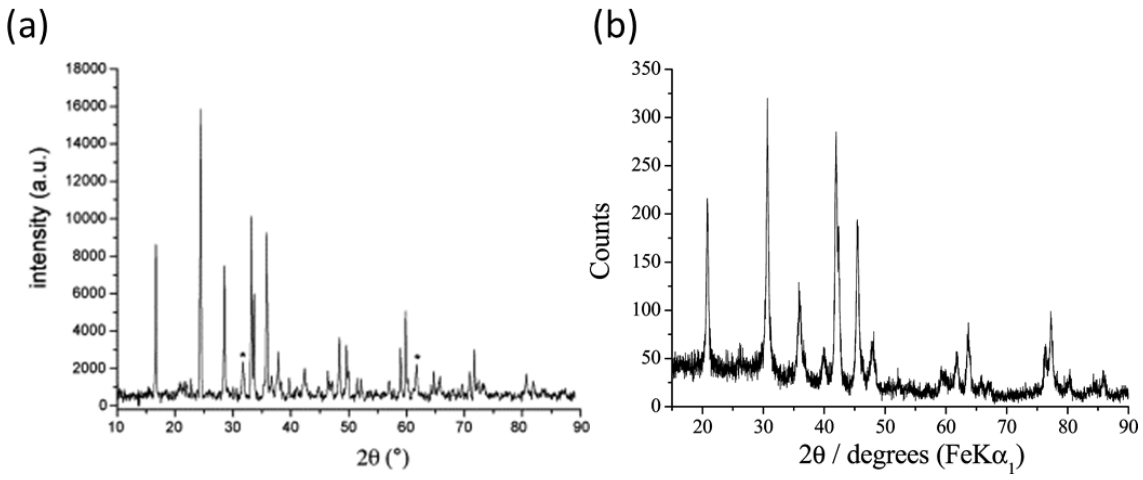

Figure 2.5. (a) Pristine Li_2FeSiO_4 prepared through solid-state reaction method at 750°C by Nyten *et al.* The structure was fit as *pmn21* orthorhombic and the identified peaks were labelled with asterisks (*)[41] and (b) LFS sample synthesized through a hydrothermal and annealing method (600°C) by Armstrong *et al.*, the sample was indexed as *p21n* monoclinic.[43]

Later, other researchers proposed a hydrothermal method [45] at relatively low temperature (200°C) indexed to the *pmn21* and labeled low temperature orthorhombic phase. The same group of researchers have reported on the synthesis and structure of the monoclinic γ_s (*p21n)* phase synthesized at 700°C and the γ_I *pmnb* (high temperature orthorhombic phase) synthesized at 900°C.[46] The three temperature-dependent structures obtained via a combination of hydrothermal and annealing methods are illustrated in Figure 2.6.[45]

It should be mentioned here that the formation energies of these polymorphs are very close, making their isolation and characterization difficult.[34, 47] As a result, although in literature, many groups have claimed they have synthesized phase pure materials, the reported phase compositions remain to be verified. High energy XRD with better resolution is needed to obtain high quality XRD spectra to resolve all peak features for phase identification.

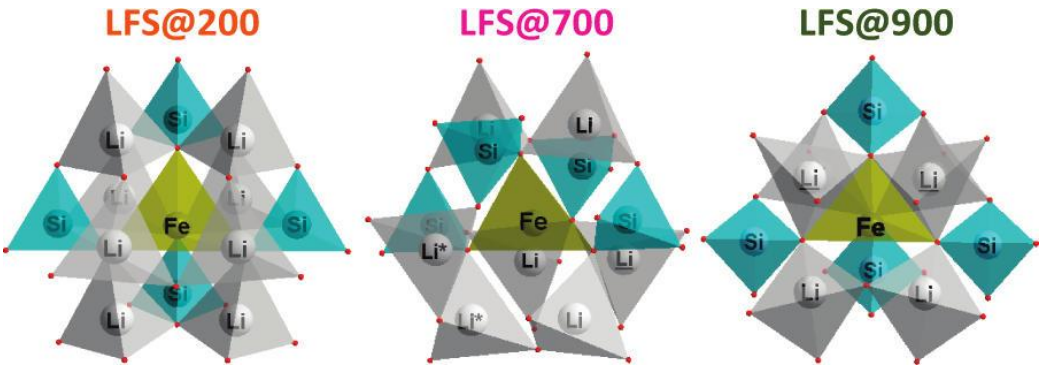

Figure 2.6. The three LFS polymorphs obtained at 200°C, 700°C and 900°C. The LFS200 is indexed as *pmn21* (low temperature orthorhombic) with only corner sharing between FeO_4 and LiO_4. The LFS700 is indexed as *p21n* (monoclinic) with only one edge being shared between FeO_4 and LiO_4. The LFS900 is indexed as *pmnb* (high temperature orthorhombic) with a given FeO_4 tetrahedron shares two edges with LiO_4 tetrahedra [45]

2.3.1.2 Li_2MnSiO_4 and $Li_2Fe_{1-x}Mn_xSiO_4$

Similar to Li_2FeSiO_4, Li_2MnSiO_4 also exists in different polymorphs and exhibits a temperature dependent phase transition from low temperature orthorhombic phase to monoclinic phase, and to high temperature orthorhombic phase as the annealing temperature increases. [45, 6] However, the phase transition of Li_2MnSiO_4 has been observed to occur at a higher temperature range (around 150ºC) as compared to Li_2FeSiO_4, and the mixed $Li_2Fe_xMn_{1-x}SiO_4$ is expected to behave similarly while with a phase transition temperature somewhat in between.[34] For example, Bini *et al.* reported that for lithium metal silicates obtained with sol-gel method followed by calcination/annealing at 650ºC, the LFS material was reported as *p21n* (monoclinic) while the LMS material was found to be *pmn21* (low temperature orthorhombic). However at 900ºC, the LFS was found to be *pmnb* (high temperature orthorhombic) but the LMS a mixture of *pmnb* and *p21n*.[38] A nice graphical summary of the temperature-dependent polymorphism of $Li_2Fe_{1-x}Mn_xSiO_4$, and the two end-members, LFS and LMS, is presented in Figure 2.7.[44]

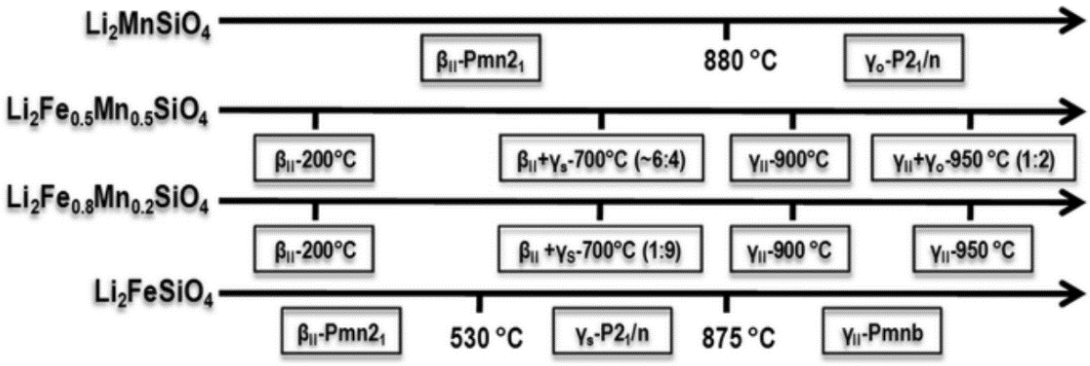

Figure 2.7. Temperature-dependent formation of $Li_2Fe_{1-x}Mn_xSiO_4$ (x=1, 0.2, 0.5 and 0) polymorphs as reported by Sirisopanaporn *et al*. [36] Note that β_{II} stands for *pmn21*, γ_0 and γ_s stand for *p21n* and γ_{II} stands for *Pmnb*. The difference between γ_s and γ_0 or γ_s structure is that the tetrahedra are not edge-sharing as per conclusions by Nishimura *et al*.[42]

The Mn analogue of LFS was firstly synthesized by Dominko *et al.* using a sol-gel technique. [48] Unlike the pure LFS which was obtained directly via hydrothermal method at 150-200°C, the pure Mn silicate, Li_2MnSiO_4 (LMS) could not be synthesized using the same hydrothermal synthesis route. According to Dominko *et al*., the LMS obtained at 700°C had an "all-up" tetrahedral arrangement (Figure 2.8) with distortion that was indexed with a *pmn21* space group symmetry. This arrangement differs from the LFS crystal structure, which has alternating orientation of the tetrahedral arrangement. It is believed based on DFT calculations this arrangement to cause structural instability and distortion and be responsible for leading to an unstable amorphized delithiated structure upon cycling.[49]

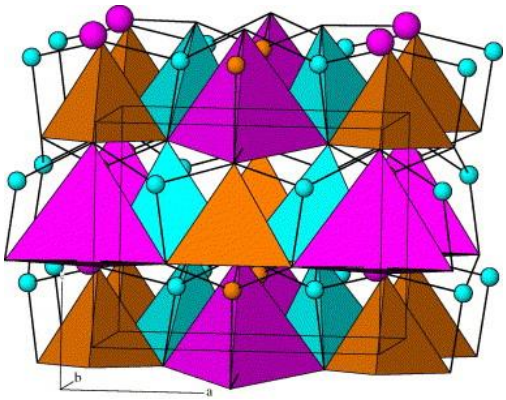

Figure 2.8. The slightly distorted "all-up" tetrahedral arrangement of Li_2MnSiO_4 (*pmn21*) orthorhombic crystal structure obtained at 700 °C. The balls represent alternate Li (turquoise), Mn (purple) , Si (brown) atoms which are tetrahedrally connected to oxygen atoms.[48]

Since the early work of Dominko *et al.*[50] various synthesis methods for LFMS have been reported including sol-gel method[50], polyol method[51], solvothermal method,[52] and supercritical fluid method.[53] In general, the synthesis of $Li_2Fe_{1-x}Mn_xSiO_4$ is analogous to the preparation of Li_2FeSiO_4, with the Mn content stoichiometrically controlled by replacing part of the iron source with manganese source during precursor mixing. As an example, Shao *et al*. reported a synthesis route to prepare $Li_2Fe_xMn_{1-x}SiO_4$ (with x=0.2, 0.5 and 0.8) nanospheres using a complex multi-step method that consists of spray pyrolysis of a precursor solution at 400°C followed by wet ball milling and annealing at 600°C.[54] The spray pyrolysis and annealing step were carried in N_2 atmosphere. The resulting XRD patterns of LFMS nanospheres were indexed as *pmn2₁* space group symmetry with certain amount of SiO_2 and FeO_x impurities.[54] In another work published by Gao *et al*., a simple solid-state synthesis method was applied involving calcination at 700°C of a finely ground dry precursor mixture of lithium, iron, and manganese acetate salts, along nano-silica, and 10 wt.% of glucose as carbon source, which yielded $Li_2Fe_{1-x}Mn_xSiO_4$ (x from 0 to 0.5) aggregates.[55] In both cases, the LFMS at various Fe: Mn ratios were identified as *Pmn2₁*, which is the most studied LFMS phase in the literature due to its relatively low formation temperature. The LFMS products were determined to constitute solid solutions of Mn and Fe as confirmed by the XRD peaks shifts due to the different cationic radius of Fe^{2+} (0.77 Å) and Mn^{2+} (0.82 Å). [54, 56] The relevant XRD patterns with peak shifts of LFMS produced at various Fe-Mn ratios are shown in Figure 2.9. [56]

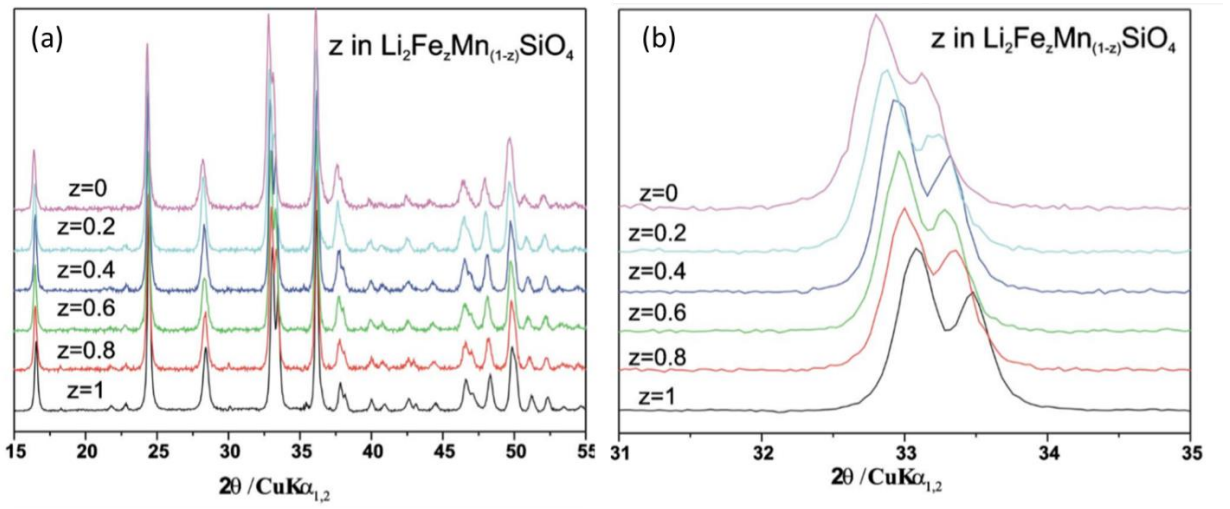

Figure 2.9. (a) The XRD patterns of LFMS produced at various Fe-Mn ratios; (b) zoomed-in view at 31-35° showing the shifts in XRD peak position as the Fe-Mn ratio changes.[56]

2.3.2 Carbon-coating

Due to the low intrinsic conductivity of lithium metal silicate (approximately 6×10^{-14} s/cm), [57] efforts have been made to form carbon coatings both *in situ* and *ex situ* and to reduce the particle size prompting the development of solution-mediated synthesis methods as alternatives to the conventional solid-state synthesis approach. Thus in 2007, Dominko *et al*.[52, 58] successfully prepared LFS using different synthesis techniques including hydrothermal, Pechini, and sol-gel processes. Drawing from the vast number of solution synthesis methods developed for lithium iron phosphate (LFP),[59] researchers have resorted to the use of organic molecules and/or reducing agents for the solution synthesis of Li_2FeSiO_4. This type of synthesis is highly beneficial in terms of nano-sizing, homogeneity of particle size and composition, morphology control and modification. Typically, ferrous salts are used as source of Fe^{2+} while the source of silicate varies from SiO_2 nanoparticles to $Si(CH_3COO)_4$ and tetraethyl orthosilicates (TEOS). In terms of organic additives, citric acid, ethylene glycol, diethylene glycol (DEG) or acetic acid are mentioned. Further reducing agents such as ascorbic acid and oleic acid can still be added, especially when air oxidation is a concern. These organic additives also serve as sources of *in situ* carbon coating.[60]

Alternative to using carbon-containing organic compounds as chelating agents and sources of *in-situ* carbon coating, other carbon coating methods have also been developed. Similar to the previously developed processing techniques for $LiFePO_4$,[61-62] methods to integrate nano-sized carbon with LFS include incorporating carbon nanotubes (CNT), conductive polymer (PEDOT) and reduced graphene-oxide (rGO).[63]

2.3.3 Nanocrystal morphology control of LFS

In addition to the conventional solid-state synthesis and hydrothermal synthesis[45], other solution-based methods, such as sol-gel method[64], template-assisting method[65], and supercritical fluid method[66], can be used to achieve particle size and morphology control for material property optimization. In 2010, Muraliganth *et al.* reported a microwave-solvothermal synthesis method [67] and generated approximately 20 nm diameter nanospheres of Li_2FeSiO_4. In this experiment, 0.3 M LiOH, 0.15 M ferrous acetate and 0.15 M tetraethyl orthosilicates (TEOS) were dissolved in 30 ml of tetraethylene glycol (TEG). The homogeneous mixture was microwave treated at 300°C, 30 bar, for 20 minutes. The mixture was rinsed with acetone and the entire process was carried out in argon atmosphere. The product was determined by XRD refinement as *p21* monoclinic phase and the

nanocrystals were then ball milled with 30 wt.% sucrose and carbonized under constant Ar flow at 650 °C for 6 h. Based on thermogravimetric analysis (TGA), 12 wt.% of carbon content was added in the Li_2FeSiO_4/C composite. The annealed carbon-coated Li_2FeSiO_4 exhibited good thermostability and cyclability. The capacity stabilized at around 150 mAh/g at the rate of C/20, up to 40 cycles, which corresponds to close to one Li ion extraction.

In 2012, D. Rangappa *et al.* reported a successful extraction of two lithium ions from ultrathin 2D Li_2FeSiO_4 nanosheets synthesized using supercritical fluid (SCF) method [68]. In this method, water and ethanol were used as SCF reaction media. $FeCl_2$, tetraethyl orthosilicate (TEOS), LiOH and ascorbic acid were used as precursors. The reaction was carried out in a stainless-steel reactor at 350-420°C at 38 MPa for 4-10 min. The product was washed and centrifuged with ethanol and then dried in vacuum for 12hr at 120°C. The resulting crystalline nanosheets were then ball milled with 10 wt.% PEDOT and 5 wt.% multiwall carbon nanotubes (MWCNT) for 12 h followed by heat treatment in Ar at 300°C for 4 h. The electrochemical testing was done using a three-electrode cell, using 1 M $LiClO_4$ in ethylene carbonate (EC)/diethyl carbonate (DEC) as electrolyte, which can stay stable at a higher potential range comparing to $LiPF_6$ in EC/DMC. At 4.8 V, the second lithium extraction was observed. Those nanosheets of Li_2FeSiO_4 exhibited high capacity 340 mAh/g only for the initial 20 cycles. However, the cell failure started at the 21st cycle with only half of the charging/discharging capacity (150 mAh/g) observed thereafter.

Integrating Li_2FeSiO_4 with other cathode materials such as $LiFePO_4$ was also reported as an effective way to enhance the metal orthosilicate's performance. In this context an LFS-LFP composite was synthesized that yielded a capacity corresponding to more than one lithium ion extraction.[69] The intergrown nanocomposite (1-x)Li_2FeSiO_4.x$LiFePO_4$-C was prepared at different compositions using an *in-situ* sol-gel method featuring tartaric acid as both chelating agent and source of carbon coating. The product was characterized as *p21n* phase and the optimal electrochemical behavior was observed when x=0.04 in (1-x)Li_2FeSiO_4.x$LiFePO_4$-C nanocomposite with capacity remaining slightly over 180 mAh/g after 100 cycles at C/5. The improved performance of the nanocomposite was attributed to fast Li diffusion enabled by the LFP shell in analogy to another study featuring amorphous Li_2SiO_3 shell on Li_2FeSiO_4.[60]

Meanwhile, crystal morphology control in the case of Li_2MnSiO_4 has been achieved by rather special solution methods and template-assisted synthesis methods.[70] For example, the production of

Li_2MnSiO_4 nanosheets[68] and nanocubes[71] has been reported. Recent research on lithium manganese silicate has shifted towards carbon incorporated composite materials. [50, 72,73] All these approaches, however involve complex synthesis protocols raising questions as to their reproducibility and feasibility for larger scale application.

2.4 Electrochemical behavior of Li_2FeSiO_4 and $Li_2Fe_{1-x}Mn_xSiO_4$

2.4.1 The reversibility and accessibility of the two Li ions

The redox potentials of Li_2FeSiO_4 for the two-step lithium ion insertion/extraction based on the redox reactions of Fe^{2+}/Fe^{3+} and Fe^{3+}/Fe^{4+} are 2.8V and 4.8V, respectively.[33] Within the electrolyte stability window (<4.5V), Li_2FeSiO_4 typically delivers a theoretical capacity corresponding to one Li ion exchange endowed by the Fe^{2+}/Fe^{3+} redox couple (166 mAh/g) or practically even less (140 mAh/g) upon cycling, depending on the applied conditions.[41, 74] The Li extraction process, as shown below, takes place around 3.1V in the first charge cycle, but shifts to a lower voltage around 2.8V in the subsequent cycles.[75]

$$Li_2Fe^{(II)}SiO_4 \rightarrow LiFe^{(III)}SiO_4 + Li^+ + e^- \qquad (2.2)$$

In 2006, Nyten *et al.* were the first who investigated the mechanism of this shift in potential plateau using cyclic voltammetry (CV), although in their CV test, a fast scan rate of 72 mV/s was used, which may not be suitable to observe all relevant features.[75] Since then, many researchers have used CV at slower rate to reveal the changes during electrochemical cycling but, this is typically done only for the first few cycles, and the resulting interpretations are generally ambiguous.[76-77]

In the work published by Zhang et al. (Fig 2.10) [78] a slow scan rate of 0.1 mV/s was used for the initial cycles. In the first cycle, two anodic peaks (3.41V and 4.47V) and only one cathodic peak (2.37V) were observed. The two anodic peaks were assigned as Fe^{2+}/Fe^{3+} and Fe^{3+}/Fe^{4+} stepwise oxidations. It was also observed in the following cycles that the peak at 4.47V diminishes while the peak at 3.41V shifts to 3.11V. In their galvanostatic charging and discharging curves, similar potential shifts were also observed. The electrochemical behavior of the first cycle differs significantly from the following cycles, indicating irreversible reactions during the formation cycle. However, the assigned Fe^{3+}/Fe^{4+} anodic peak is questionable because it is not seen in the subsequent cycles, and it is more like a parasitic reaction during the formation cycle. Their structural transition-

related assumptions based solely on CV are not convincing due to the lack of other evidences. Thus, further electrochemical and structural characterization studies are required.

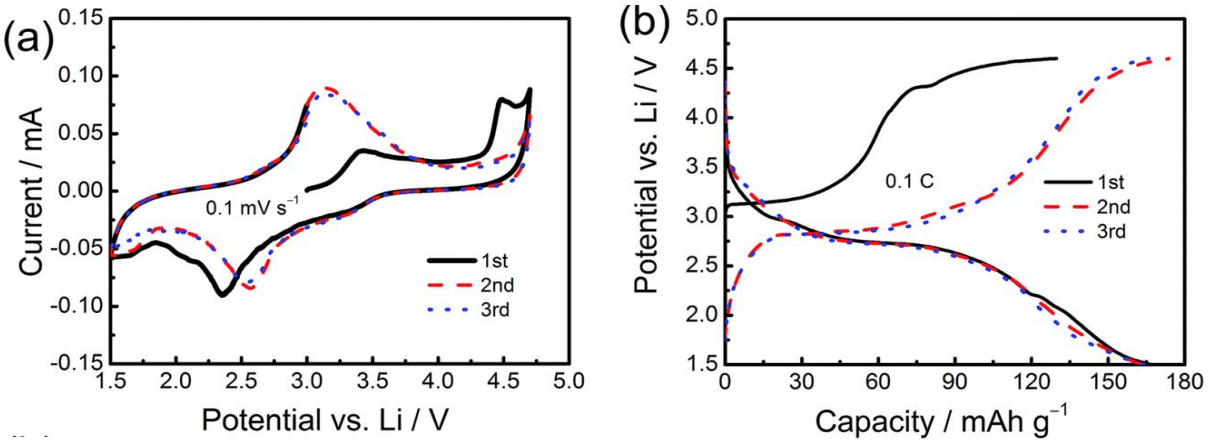

Figure 2.10. (a) Cyclic voltammograms of carbon-coated Li_2FeSiO_4 electrode at a scan rate of 0.1mV/s and (b) galvanostatic charging and discharging profile upon the first 3 cycles at room temperature.[78]

2.4.2 Distinct behavior among polymorphs

The different LFS polymorphs have been discussed in the previous section (section 2.2.2). Among the three LFS polymorphs (low T orthorhombic *pmn21*, monoclinic *p21n*, and high T orthorhombic *pnma*), the monoclinic phase has been studied the most and, is observed to have the best electrochemical property upon cycling comparing to the other two. In one of the earliest reports by Dominko *et al*., the galvanostatic charging/discharging profiles of hydrothermally prepared LFS (labeled "HTS", prepared at 150°C for 72 hrs under hydrothermal condition), and LFS prepared with modified Pechini method (labeled "MPS"): MPS700 (monoclinic) and MPS900 (high T orthorhombic) were compared as shown in Figure 2.11.[58] The fourth sample (labeled "PS") was a carbon-containing sample obtained through a standard Pechini method fired at certain temperatures not disclosed by the authors. The galvanostatic charging/discharging was carried out at 60°C at a rate of C/20 over the voltage range 2.0-3.8V using LiBOB in ethylene carbonate (EC)/ diethyl carbonate (DEC) (1:1) as the electrolyte. All four samples behaved differently upon cycling. The MPS900 sample (high T orthorhombic) was found to have the lowest reversible capacity and the carbon-containing sample (PS) was found to have the best electrochemical behavior. However, the reversible Li content was much less than one Li. For their HTS150 and MPS700 samples, less than 0.15 Li was reversible; while for their MPS900 sample, the reversible Li was even lower, with reversible capacity equivalent to 0.08 Li. The authors attributed the poor reversible Li capacity

performance to the large particle size and lack of carbon content; but even the 0.6 Li reversible amount exhibited by the PS sample that was carbon-coated (5.5% C) is not considered satisfactory.

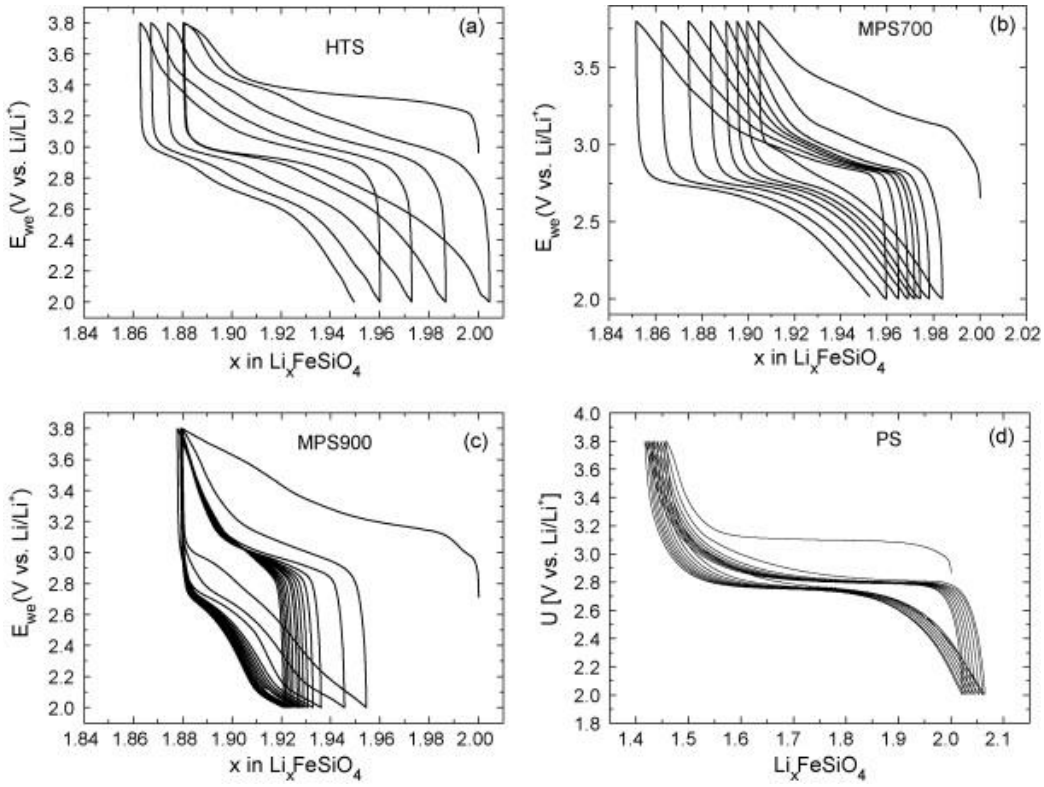

Figure 2.11. Cycle performance of Li_2FeSiO_4 samples at C/20 rate: (a) hydrothermal sample (HTS, obtained at 150°C), (b) modified Pechini synthesis sample fired at 700 °C (MPS700), (c) modified Pechini synthesis sample fired at 900 °C (MPS900) and (d) Pechini synthesis sample (PS-Li_2FeSiO_4). [58]

Since that early study of Dominko *et al.*, several other research groups have studied the electrochemistry of the different LFS polymorphs. For example, Kageyama *et al.*[79] reported the hydrothermal synthesis at 150°C of six-armed starfruit-shaped LFS *pmn21* (low T orthorhombic) crystals with enhanced electrochemical performance attributed to the crystal structure facilitating Li-ion diffusion. The electrochemical performance of three different particle size LFS products is shown in Fig. 2.12. Note that their cell testing was carried out at 60°C, 1.5-4.8V with $LiClO_4$ in in ethylene carbonate (EC)/ diethyl carbonate (DEC) (1:1) as the electrolyte. No carbon coating was applied except the use of the branched poly(ethyleneimine) (BPEI) organic reagent as morphology controlling agent during the hydrothermal reaction. Slightly over one Li ion extraction was achieved at initial cycles followed by severe capacity fading after ten cycles.

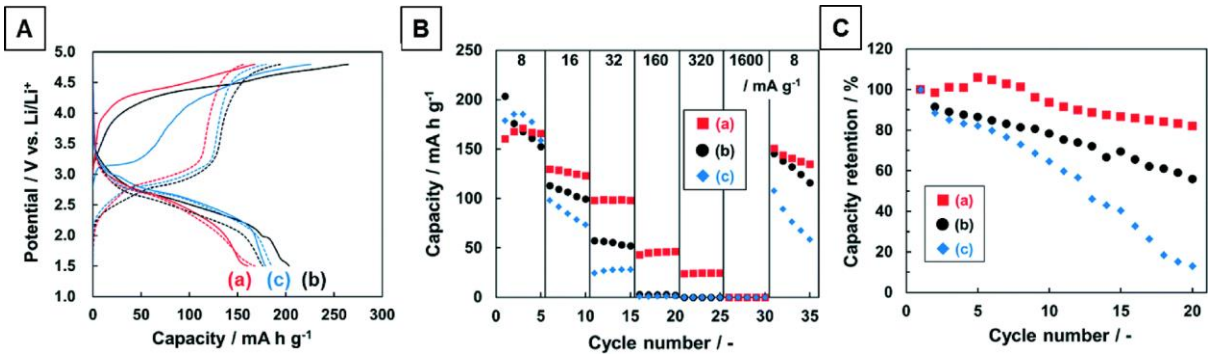

Figure 2.12. Cycle performance of the six-armed Li_2FeSiO_4 (*pmn21*) nanoparticles: (a) charging/discharging profile of the LFS with three different particle sizes, (b) the discharge capacity at variable current densities, (c) capacity retention vs. cycle number at 8mA/g.[79] Sample labels (a), (b), (c) indicate the large six-armed particles, the small six-armed particles, and the nanoparticle aggregates obtained with BPEI respectively.

The low temperature orthorhombic LFS phase (produced hydrothermally at 180°C) was also studied by Yang *et al.*[80] Shuttle-like LFS *pmn21* crystals were obtained and the electrochemical response is shown in Fig. 2.13. Note that $LiPF_6$ in EC: DMC: EMC (1:1:1) was used as the electrolyte, with voltage range from 1.5-4.8V, while the cell testing temperature was not reported. The material again exhibits only one Li ion extraction at C/10 and even less reversible Li content at faster rates.

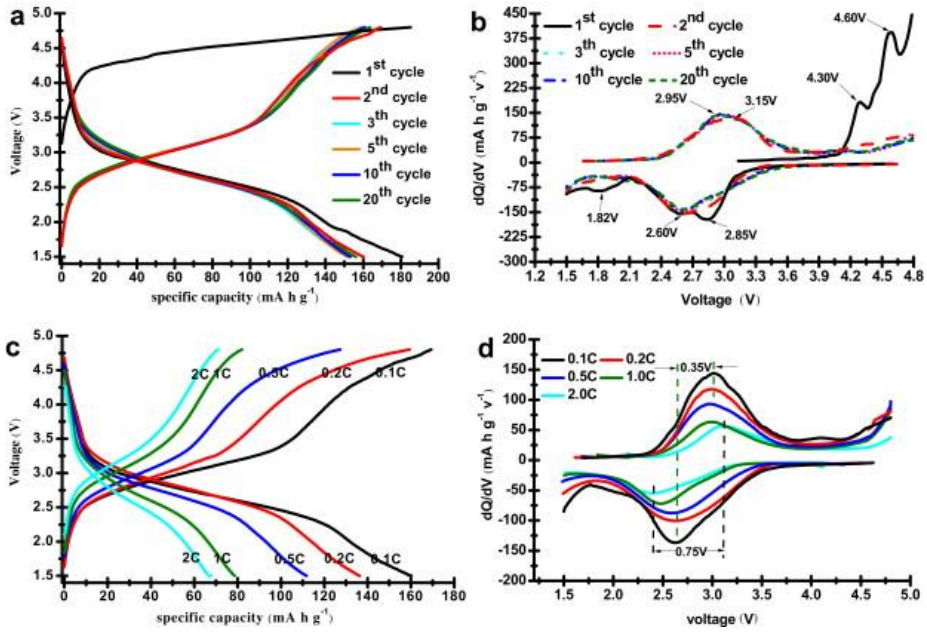

Figure 2.13. Electrochemical performance of the shuttle-like Li_2FeSiO_4 crystals obtained at 180°C. (a) Typical charge–discharge curves and (b) dQ/dV vs. voltage plots of the charge–discharge curves at 0.1 C (1 C = 166 mA g−1), (c) the rate charge–discharge curves and (d) dQ/dV vs. voltage plots of the charge–discharge curves under various current densities. [80]

The LFS monoclinic phase has been studied the most among the three polymorphs. This is attributed to its better electrochemical performance than that of the orthorhombic phases observed in early studies.[48] Thus, as reported by Sirisopanaporn *et al.*,[45] the LFS700 monoclinic phase obtained by annealing at 700°C has reached capacity equivalent to 0.8 Li at the formation cycle (Voltage range: 2-4V) (Fig. 2.14 (a,b)). Armstrong *et al*. reported reversible capacity equivalent to 0.8 Li up to the 10th cycle (Fig. 2.14 (c)),[43] which is consistent with Sirisopanaporn *et al.*'s results[42]. In another study by Yi *et al.* where crystal morphology control was applied via a complex sol-gel method, over one Li-ion extraction was achieved with good cycling stability up to 100 cycles for the monoclinic *p21* LFS product (Fig. 2.15).[57] The authors attributed the good electrochemical behavior to the porous structure and large surface area inherited from the Fe_2O_3 precursor (spherical and cubic); however, their BET results showed a rather low surface area (11-27 m^2/g) without further explanation as to what other factors contributed to such high reversible capacity. In order to achieve better understanding on the behavior of the cathode material, post-mortem analysis is needed to identify the structural changes before and after cycling, as discussed in the following sections.

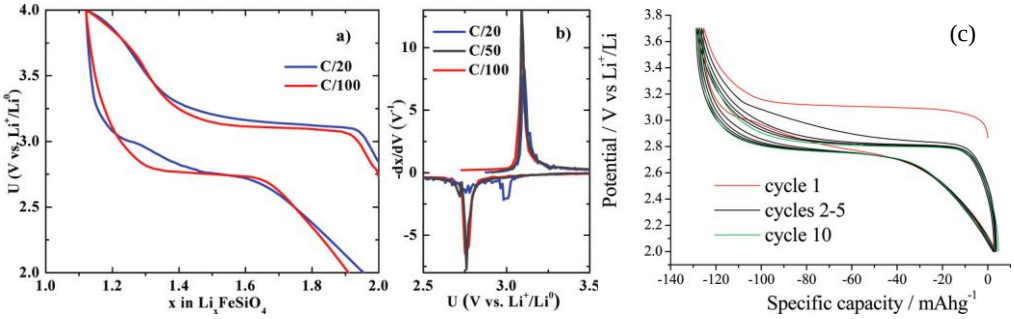

Figure 2.14. (a) First cycle galvanostatic curves and (b) corresponding derivative plots of LFS700 polymorph. [45] (c) Charging/discharging profile of the initial ten cycles of the monoclinic LFS synthesized at 600°C. [43]

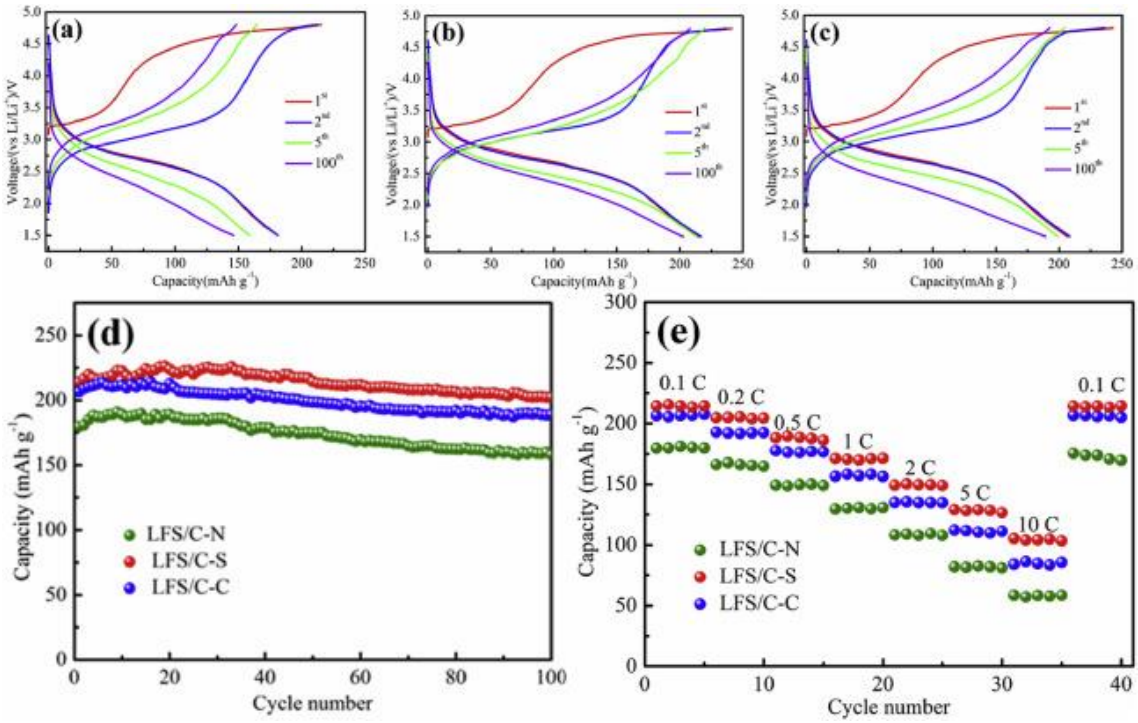

Figure 2.15. (a), (b), (c) Charge/discharge curves; (d) cycling performances; and (e) rate-dependent capacities of the monoclinic Li_2FeSiO_4/C synthesized using a sol-gel method from Fe_2O_3 precursor. [57]

2.4.3 Electrochemistry of $Li_2Fe_{1-x}Mn_xSiO_4$

The electrochemical response of Mn-substituted LFS, $Li_2Fe_{1-x}Mn_xSiO_4$ (LFMS), has been studied and compared to that of Li_2FeSiO_4 and Li_2MnSiO_4, and the effect of different Fe: Mn ratios has been investigated to some extent in a number of studies. These investigations were pursued following the earlier research that determined the pure Mn-analogue, Li_2MnSiO_4 did not have promising electrochemical properties due to serious capacity fade caused by structural instability.[39, 52] In these investigations it was the *pmn2₁* low temperature orthorhombic phase that was mostly studied as it is the one more conveniently produced by calcination at ~ 700 °C as already discussed in a previous section.

Dominko *et al.* studied in 2010 the electrochemistry of $Li_2Fe_{0.8}Mn_{0.2}SiO_4$ obtained through hydrothermal and annealing method (700°C) and the electrochemical response of the first three cycles were recorded, as shown in Figure 2.16. Although a high capacity of up to 250 mAh/g corresponding to 1.4 Li^+ extraction was observed for the initial cycles, severe capacity fading was observed after 15 cycles that ended in total failure. It is also noticed that the initial charging capacity

was greater than the discharging capacity, indicating irreversible chemical reactions during charging. To investigate the underlying chemistry and charge compensation mechanism, the authors used *in situ* Mössbauer spectroscopy and *in situ* XANES spectroscopy to monitor the Fe and Mn cation redox changes during the first charging/discharging cycle. These measurements revealed that only part of the initial capacity was related to Fe and Mn redox reactions pointing to parasitic reactions at the cathode/electrolyte interface involving extensive electrolyte degradation reflecting apparently the rather high temperature (60°C) applied during cycling. [56]

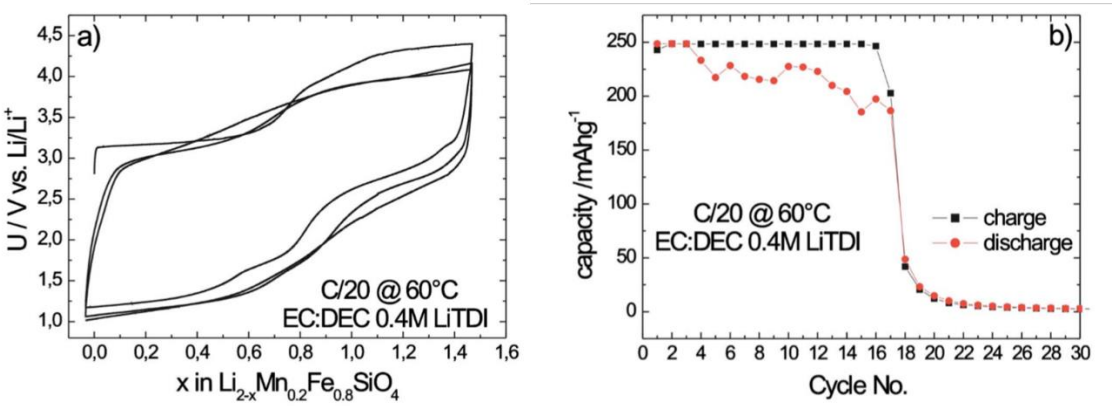

Figure 2.16. (a) The initial three charging/discharging cycles of $Li_2Fe_{0.8}Mn_{0.2}SiO_4$ and (b) its capacity evolution upon cycling at C/20 and 60°C according to Dominko *et al*. [56]

The work of Dominko *et al.* was followed in 2013 by that of R. Chen *et al.* who this time evaluated various mixed Fe/Mn silicate compounds, $Li_2Fe_{1-x}Mn_xSiO_4$ (x = 0, 0.2, 0.5, 1) synthesized via sol-gel and sintering/calcination at 700°C.[33] To avoid electrolyte degradation they chose the roon temperature for their cycling tests but they used a high cut-off voltage (4.8 V) that in general is known to also induce electrolyte reaction. Their study provided some mechanistic insight as to redox changes of iron and manganese during cycling via structural characterizations presenting evidence of amorphization. In terms of electrochemical performance their data showed cyclability to become progreesively worse as the Mn content increase in comparison to LFS as it can be evaluated by examining Figure S4 in their paper that is reproduced here as Figure 2.17.

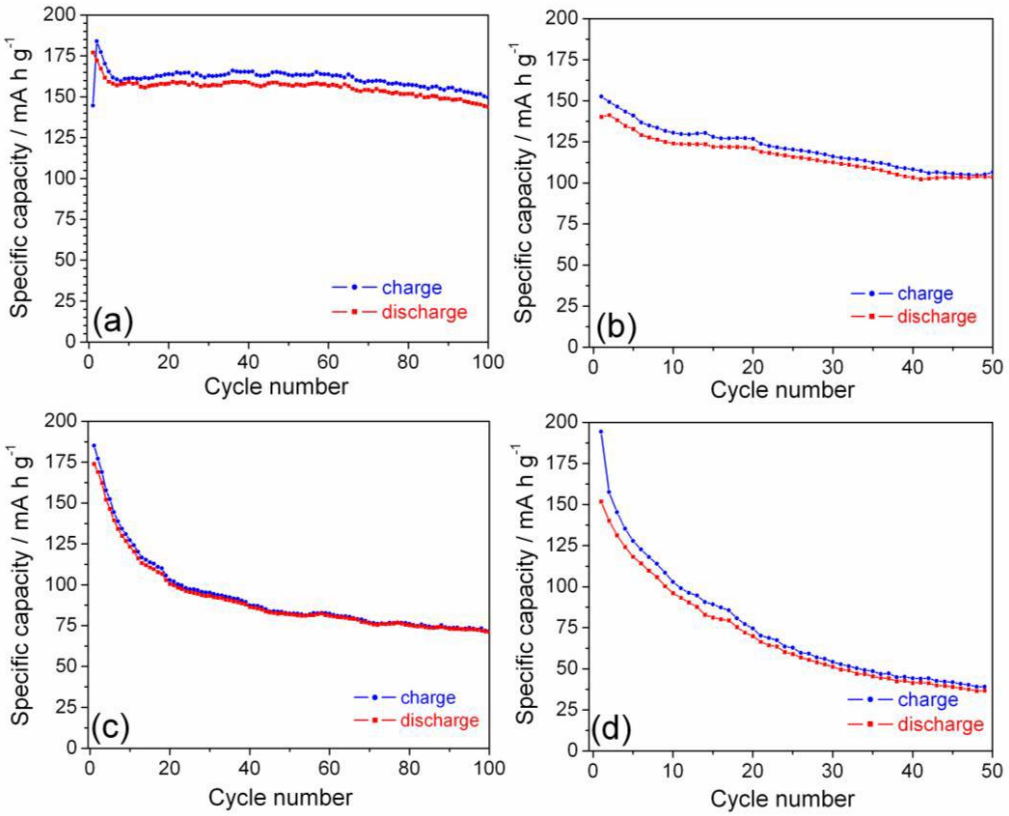

Figure 2.17. Cyclability data of $Li_2Fe_{1-x}Mn_xSiO_4$ at a current density of C/20: (a) x= 0, (b) x= 0.2, (c) x= 0.5, (d) x= 1. (This is reproduction of Figure S4 in the SI of R. Chen *et al.*'s publication[33]).

Based on the data of R. Chen *et al.*'s work reproduced in Figure 2.17 the conclusion may be drawn that mixed Fe/Mn silicates have not promise as cathode materials. This is contradicted however by a more recent work published by Zhang *et al.* in 2018.[82] In this work, $Li_2Fe_xMn_{1-x}SiO_4$ (LFMS) particles of *pmn21* phase with carbon coating were synthesized using a solvolthermal-annealing method. The variable Fe:Mn ratio LFMS compounds from 0:1 (pure LMS/C (corresponding to Fe=0) to 1:3 (LFMS/C-1:3, corresponding to Fe=0.25), 1:2 (LFMS/C-1:2, corresponding to Fe=0.33), 1:1 (LFMS/C-1:1, corresponding to Fe=0.5), and 2:1 (LFMS/C-2:1, corresponding to Fe=0.67) were electrochemically tested and their cycling performance at 0.1C rate is presented in Figure 2.18. According to these results the Fe:Mn =1:2 LFMS (corresponding to $Li_2Fe_{0.33}Mn_{0.67}SiO_4$) is seen to have the best cycling properties in terms of capacity attained and retention over the first 20 cycles. The exhibited electrochemical performance significantly exceeded that of previously reported LFMS results. [54, 68, 81-84] However, the authors provided no explanation

or discussion of the underlying mechanism for their results. Hence further studies are needed to clarify the redox chemistry and performance of the Fe/Mn mixed silicates as cathodes.

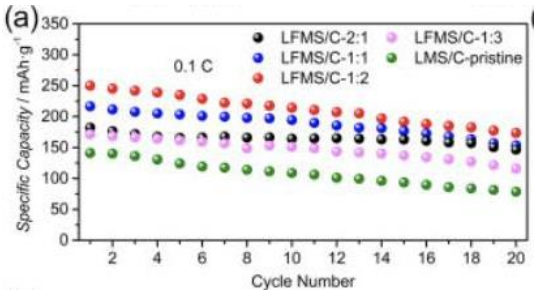

Figure 2.18. Cycle performance of LFMS compounds with variable Fe-Mn ratios (LMS=Li_2MnSiO_4; LFMS-1:3=$Li_2Fe_{0.25}Mn_{0.}75SiO4$; LFMS-1:2=$Li_2Fe_{0.33}Mn_{0.67}SiO_4$; LFMS-1:1=$Li_2Fe_{0.5}Mn_{0.5}SiO_4$; LFMS-2:1=$Li_2Fe_{0.67}Mn_{0.33}SiO_4$).[85]

2.5 Cycling-induced phase transformation of monoclinic LFS

2.5.1 General

As it is deduced from the electrochemical data presented in the previous sections, the formation cycle of Li_2FeSiO_4 is often different than the subsequent cycles both in terms of a noticeable voltage drop and a change in shape of the charging/discharging curves. In addition, the cyclic voltammogram (shown in Fig. 2.10(a)) of the first cycle shows unique peak features that did not present in the subsequent cycles, where changes in the redox potential are evident. Therefore, researchers have proposed that the LFS undergoes a structural transformation during the formation cycle. Because there have been three identified polymorphs (namely, the *pmn21, p21n* and *pmnb*) for as-prepared LFS, one possible hypothesis is that a certain phase of LFS can transform to another during electrochemical cycling due to their highly similar structures and closeness in thermodynamic formation energy [34, 47]. Of the three polymorphs, the LFS monoclinic *p21n* phase has been mostly studied in terms its electrochemistry and associated phase transformations. Most research works have been focused on the formation cycle, and the first 1.5 cycle (namely, the formation cycle and the second charging) and both *in situ* and post-mortem techniques have been used to track the structure changes at different state of charge (SOC), and end of charging/discharging states. XRD and Rietveld refinement have been used as a standard technique to monitor and quantify the different phases. Other techniques such as X-ray absorption near edge structure (XANES), Mossbauer Spectroscopy, Nuclear magnetic resonance (NMR), Scanning transmission X-ray microscopy

(STXM) have also been used to further elucidate the complex structural transformation mechanism. However, different research groups have proposed different end structures at various states, and thus different structural transformation mechanisms, as presented in the following sections. It is also worth noticing that the XRD patterns of many of the reported post-mortem structures are in fact quite similar, but the interpretations are quite different from one study to the other complicating the analysis of the underlying phenomena.

2.5.2 Contradictory phase identifications

In 2011, Armstrong *et al.* proposed that the monoclinic LFS undergoes phase transformation towards an orthorhombic structure.[43] The post-mortem analysis was carried out on pre-cycled electrode material after ten cycles. Using XRD and neutron powder diffraction, the cycled LFS was indexed as orthorhombic with *pmn21* space group at the end of discharging, with 10% of the original *p21n* LFS present as a minor secondary phase. (Fig. 2.19) However due to the fluorescence effect of the Fe Kα XRD source, a broad background is observed especially in the post-cycling XRD pattern. This inevitably causes losses of XRD peak features especially at lower angle region, which can cause inaccurate phase identification and unreliable Rietveld refinement.

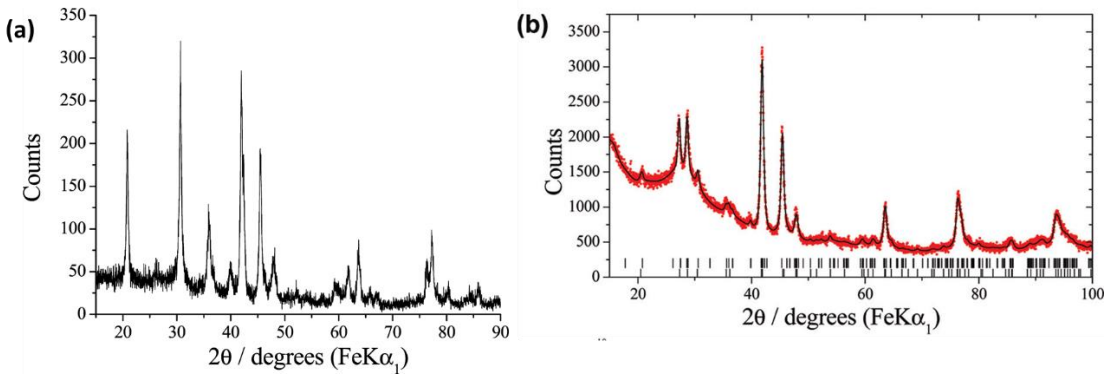

Figure 2.19. XRD patterns of (a) the as-prepare LFS600 (identified as monoclinic *p21n*) and (b) after ten cycles of cycling at the end of discharging (indexed as 90% orthorhombic *pmn21* and 10% original monoclinic *p21n*.). The tick patterns in (b) are the reference patterns of monoclinic LFS (top, as-prepared LFS) and orthorhombic LFS (bottom, cycled LFS).[43] Note that the broad background noise in the cycled XRD pattern is very likely due to the fluorescence of the Fe Kα source. Also note that only a small fraction of the reference peaks is visible in the experimentally obtained XRD pattern.

In contradiction to Armstrong's result, Kojima *et al.* also reported the cycled structure of monoclinic LFS however they suggested the space group symmetry not to have undergone change.[86]

In other words, they proposed the monoclinic structure to remain intact. In their work, the first 1.5 cycle was studied and samples at different states of charge was characterized using high resolution XRD. (Fig. 2.20) The XRD pattern at the end of discharging looks very similar to Armstrong's end of discharging pattern, while the XRD quality is significantly improved comparing to Armstrong's. With more of the detailed diffraction peak features resolved, it is more reliable for subsequent structural identifications and proper indexing of the crystal lattice.

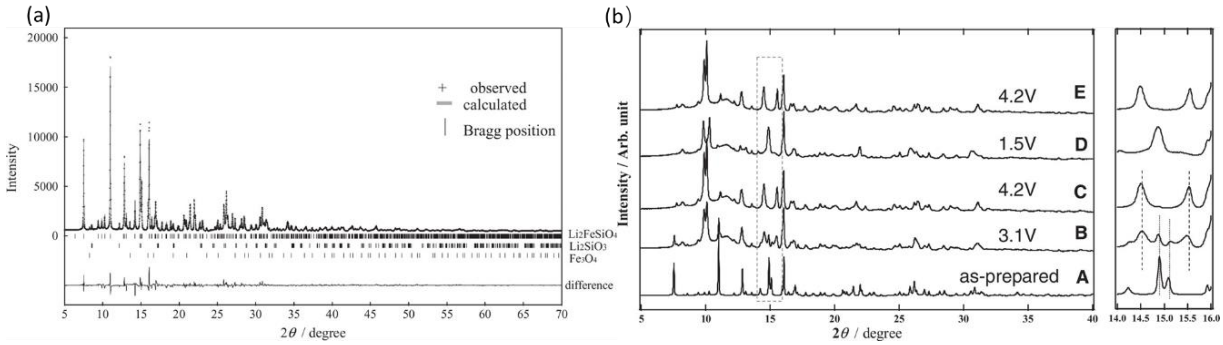

Figure 2.20. XRD patterns of (a) the as-prepare LFS (identified as monoclinic *p21n*) and (b) different stages of the first 1.5 cycle [86]

It is interesting to note that although the two groups have reported different post-cycling structures, their post-mortem XRD patterns are quite similar when comparing the end of discharging state (compare Figure 2.20(b) from Kojima's paper to Figure 2.19 (b) from Armstrong's paper), with both patterns showing the signature new doublet peak at the position of the original triplet peak position in the monoclinic Li_2FeSiO_4; (2θ position ~10° in Kojima's case, ~28-29° in Armstrong's case due to different wavelengths of the source of radiation) and similarly the next two major peaks with slight difference in intensity which overlap with the third and fourth major peak in the monoclinic Li_2FeSiO_4 (2θ position ~15-16° in Kojima's case, ~41-43° in Armstrong's case).

In Lv *et al.*, *in situ* XRD and XANES were used and the authors claimed that for the first time, a new phase associated with Fe^{4+} is observed in the case of over 1 Li ion extraction.[87] The XRD pattern obtained at the end of discharging again looks very similar to Kojima and Armstrong's results, with the presence of the characteristic doublet peak, at about 17-18°, in their case, as shown in Fig. 2.21. The authors only studied the formation cycle and claimed the exceptionally high capacity (close to 300 mAh/g) of the initial charging (Fig. 2.21) to correspond to 1.5 Li-ion extraction per unit, yielding $Li_{0.5}FeSiO_4$ as the charged phase where Fe exists as a mixture of Fe^{3+} and Fe^{4+}.

However, the presence of Fe^{4+} is rather questionable. The authors reported the voltage of the oxidation reaction from $LiFeSiO_4$ to $Li_{0.5}FeSiO_4$ to occur at 4.3V, which was proved by the XANES characterizations reported by Brownrigg *et al.* that at this redox potential there is no evidence for the Fe^{3+}/Fe^{4+} but rather the parasitic reaction of the degradation of electrolyte[40]. Although both works used in situ XANES to monitor the chemical composition changes at certain redox potentials, the interpretation of the XANES results are contradictory to each other. In the work by Lv. *et al.*, *In situ* Fe K-edge XANES spectra during the formation cycle were collected to monitor the Fe oxidation state changes (Fig 2.21f), however the Fe pre-edge feature is not clear and the interpretation is ambiguous: "*Compared to reference compounds, it is found that when Li_2FeSiO_4 is discharged to 2.7 V, the formed Fe^{4+} at the end of charge process is reduced to Fe^{3+} and then further reduced to $Fe^{2+\cdots}$*." The authors did not provide the names of the reference compounds used as reference for Fe^{4+} (in fact, it remains debatable if such Fe^{4+} containing compound exists). From the *in situ* XRD pattern (Fig 2.21 a, c), the authors assigned the charged phase $LiFeSiO_4$ and $Li_{0.5}FeSiO_4$ as β and γ phase respectively, which are new phases for which simulated XRD patterns were provided (Fig. 2.21 (b)) but their space group was not provided. It is also noticed that the first discharging capacity is 33% lower than the first charging capacity, indicating a substantial irreversible reaction during the first charging cycle, either due to part of the Li ions being unable to re-insert in the host LFS structure or, due to side reactions involving the electrolyte. Electrochemical responses of the subsequent cycles would be highly valuable to complete the understanding of the behavior of the battery, but unfortunately, only the first cycle was reported.

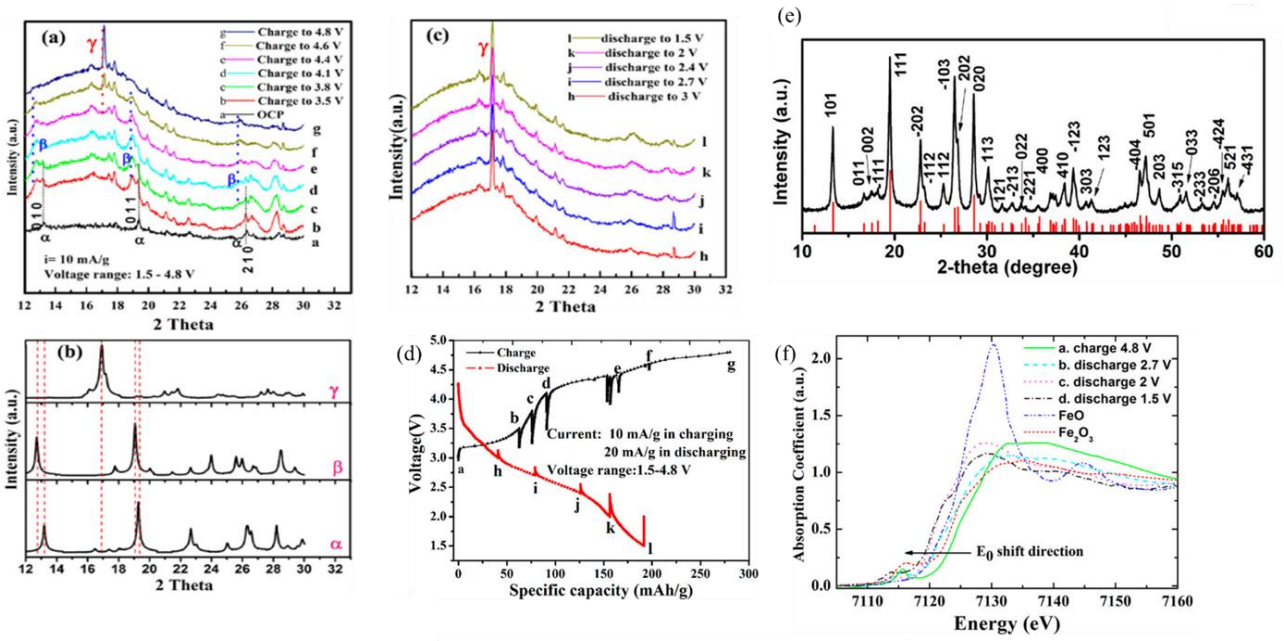

Figure 2.21 (a) *In situ* XRD patterns of Li_2FeSiO_4 electrode at different pre-set voltages during charging process (traces a−g); (b) computational XRD patterns of pristine Li_2FeSiO_4 (α), charged $LiFeSiO_4$ (β), and $Li_{0.5}FeSiO_4$(γ); (c) *in situ* XRD patterns of Li_2FeSiO_4 electrode at different pre-set voltages during discharging process (traces h and i); (d) the first charging and discharging profile during the *in situ* XRD measurement; (e) the XRD pattern of the as-prepared monoclinic *p21n* LFS product using solution-polymerization method followed by annealing at 600°C; (f) the in situ XANES Fe K-edge spectra of various charging/discharging states of the formation cycle. [87]

2.5.3 The rate dependency

In 2014, Masese *et al*. proposed two different phase transformation mechanisms upon different cycling rates.[88] In their work, the first 1.5 cycle of charging/discharging was investigated at two rates: C/10 and C/50. Using post-mortem XRD and Rietveld refinement technique, it was proposed that at C/50, the monoclinic LFS (*p21n*) gradually transforms into the thermodynamically favorable orthorhombic LFS after first charging (*pnma*, notice that it is isostructural to the high temperature orthorhombic *pmnb* phase); while at C/10, the monoclinic structure remains as a metastable phase after first charging. It is also proposed that the metastable monoclinic phase can transform into the orthorhombic phase after post-cycling relaxation for 300 hours. The proposed phase transformation mechanism by Masese *et al*. is presented in Figure 2.22 below.

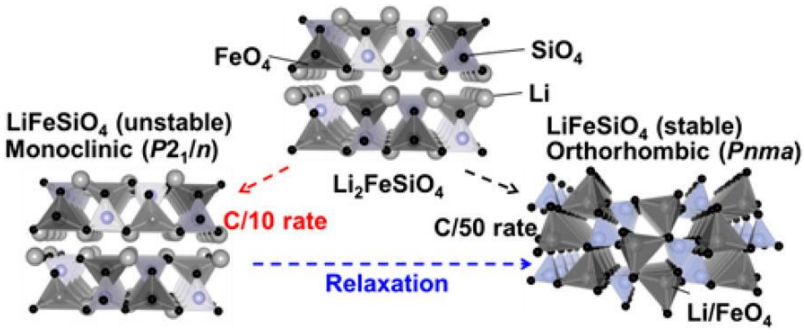

Figure 2.22. The phase transformation of pristine monoclinic LFS upon first charging at different rates and after relaxation. [88]

According to Masese *et al.,* it is worth noticing that at C/50 the cycled structure after the first charging is fitted with the *pnma* high temperature orthorhombic structure, while after the first discharging the author claims that the *pnma* becomes *pmn21*, which is consistent with Armstrong *et al.*'s previously reported result.[43] The authors also mentioned that the *pmn21* phase of the discharged form ($LiFeSiO_4$) is energetically favorable: "*At C/50 rate, the original monoclinic Li_2FeSiO_4 structure transforms to the orthorhombic $LiFeSiO_4$ structure which is thermodynamically stable during initial lithium extraction...*" However, the authors did not provide further proof of their stipulated phase, which contradicts the theoretical calculations as reported by Eames *et al*.[35] According to the latter theoretical study, the calculation of total energy shows that after one Li extraction the inverse orthorhombic phase (*pmn21*) has significantly lower energy (0.18 eV) than the high temperature orthorhombic phase (*pmnb,* equivalent to *pnma*). Therefore, it is unlikely that the monoclinic LFS transforms into high temperature orthorhombic phase after the extraction of one Li ion from the thermodynamic point of view. Secondly, the Rietveld refinement reported by Masese *et al*. excluded many "parasitic" peaks from the original XRD patterns, without any identifications of which phases these peaks belong to. Undoubtedly, such refinement is rather ambiguous and questionable. The Rietveld refinement reported by Masese *et al*. is presented in Fig. 2.23 below. In addition, as noticed in Fig 2.23, a huge background is present at the lower angle region between 5-15°, indicating the presence of significant amount of amorphous/disordered phase, a point not taken into account by the authors in analyzing/discussing their results.

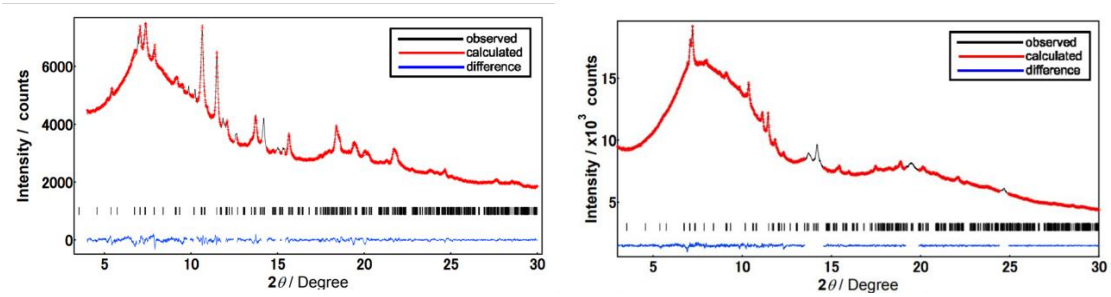

Figure 2.23. The Rietveld refinement of charged LFS (left) and discharged LFS (right) upon the first cycle at C/50.[88] Notice that the calculated curves (red) are discontinuous and many original peaks are excluded from the fittings as the author claims that those are parasitic peaks and cannot be indexed. Also notice that the amorphous background between 5-15°.

Thirdly, it is noticed that the XRD pattern of the charged LFS after relaxation for 300 hours at OCV condition reported by Masese *et al.* (Fig. 2.24) in fact looks very similar to the post-cycling XRD patterns reported by Kojima *et al.* and Armstrong *et al.* (Fig. 2.19 and Fig. 2.20 above). Although different source wavelengths were applied, the new doublet peaks appeared at the position of where it was originally flat triplet peaks in all post-mortem XRD patterns of the three groups, the respective 2θ position been ~10º in Kojima's case, ~28-29º in Armstrong's case, and ~7º in Masese's case. As mentioned above, each of the groups indexed this phase differently and so far, it was indexed as monoclinic *p21n* (Kojima), orthorhombic *pmn21* (Armstrong) and orthorhombic *pnma* (Masese). Therefore, the identification of the cycled phase(s) remains debatable.

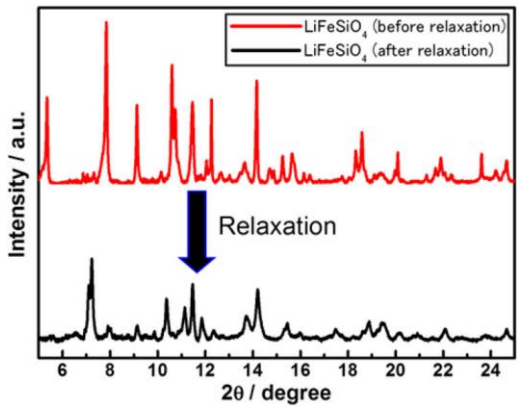

Figure 2.24. The XRD patterns of charged LFS before (top) and after (bottom) relaxation at OCV conditions for 300 hours.[88]

Although Masese *et al*. studied the phase transformation at different C rates (C/10 vs. C/50)[88], only the first 1.5 cycles were reported and from the electrochemical aspect, there is no noticeable

difference from their reported charging/discharging profile. One Li extraction was reached for both rates upon the initial cycle, with slanted charging/discharging curves representing a solid-solution type of reaction. (Fig. 1 in Masese *et al.*'s paper) [88] Another rate-dependent study reported previously by our group [89] shows the distinct rate-dependent electrochemical behavior among LFS synthesized at different temperature (LFS400, LFS700 and LFS900). In this study, 20 cycles were reported. [89] It was found that the monoclinic LFS400 material shows about 160 mAh/g capacity (equivalent to one Li-ion extraction) while the orthorhombic LFS900 material shows only 30 mAh/g capacity. The LFS700 (mixed phase) shows an intermediate behavior. It was also found that when cycled at slow rate (C/50), the LFS400 capacity deteriorates progressively. However, this can be stabilized by firstly cycling at a faster rate (C/20) for a few cycles. The authors also claimed solely from the changes of electrochemical profile (galvanostatic charging/discharging curves and cyclic voltammograms) that the monoclinic phase transforms into an orthorhombic phase. However, no post-mortem analysis was reported in this preliminary study.

2.5.4 Non-electrochemically induced changes of LFS

Due to the complex nature of LFS, in addition to the phase transformation induced by electrochemical cycling as mentioned above [88], other non-electrochemically induced structural changes have also been observed and reported.

2.5.4.1 Electrolyte-induced changes

The LFS has been found using *in situ* Fe-K edge XANES measurements to undergo a spontaneous interphasial reaction upon contact with the $LiPF_6$ in EC/DMC (1:1) electrolyte.[90] From the Fe pre-edge feature of the XANES spectra (Fig. 2.25), it was observed that there is a change from Fe^{2+} to Fe^{3+}, without any electrochemically charging condition being applied.

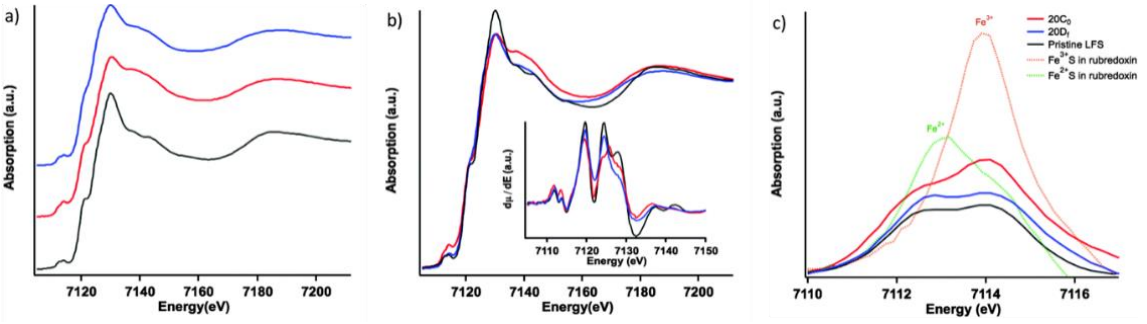

Figure 2.25 The Fe K-edge XANES spectra of pristine LFS (black), uncharged LFS electrode (red) and discharged electrode at C/20 (blue) [90]

2.5.4.2 Aging under ambient temperature

Analogous to the electrolyte induced partial oxidation of Fe^{2+} to Fe^{3+} in LFS, Kojima *et al.* found that Li_2FeSiO_4 becomes trivalent LFS after aging at ambient condition for a year.[91] In other words, all divalent iron becomes trivalent iron, as observed from ^{57}Fe Mossbauer spectroscopy analysis. Using XRD and Rietveld refinement, it is found that the aged material is isostructural to their previously reported cycled LFS, with the monoclinic space group remaining intact. The authors tested its electrochemical behavior in a full cell using graphite as the anode and observed unusually high initial charging capacity. However, the authors claimed that the capacity is not associated with the redox reaction of Fe and it is only from the Li ion migration, which is possibly related to the oxidation of oxygen ion (i.e. O^{2-} becomes O^{-}). The Mossbauer spectrum and the XRD pattern of the aged LFS are shown in Fig. 2.26.

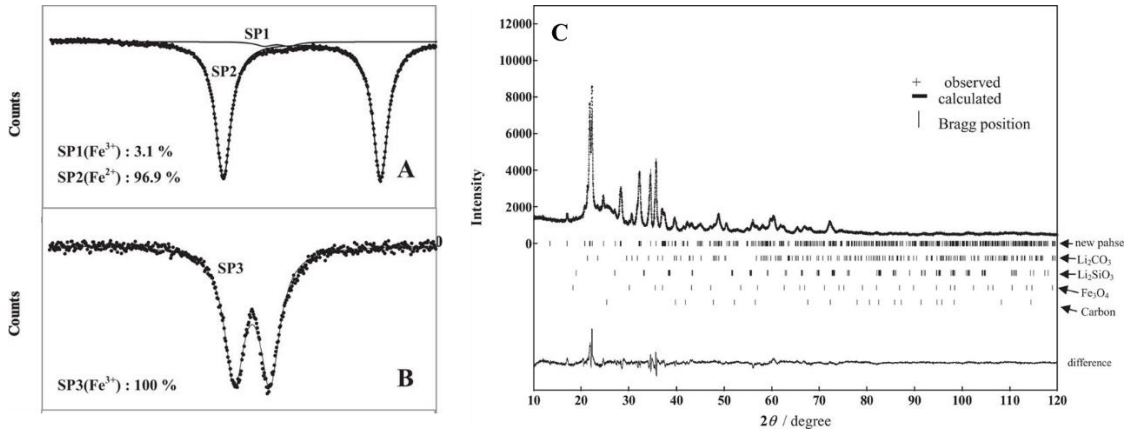

Figure 2.26. The Mossbauer spectra of freshly prepared LFS (A) and aged LFS-C composite (B). The XRD and Rietveld refinement of the aged LFS is shown in (C). Note that it is isostructural to the cycled LFS previously reported by the same group (shown in Fig 2.15b above) [91]

2.5 Summary and gaps of understanding to be further studied

LFS has been studied as a potential cathode candidate since it was firstly proposed and synthesized some 15 years ago. It exists in different polymorphs, monoclinic and orthorhombic, which can be obtained at different synthesis conditions. Various synthesis methods have been reported, including solid state method, hydrothermal synthesis and sol-gel method using complex morphology controlling agents. Most of those existing synthesis methods use ferrous salt precursor, which requires an inert atmosphere for handling, which greatly complicates the production process. Solution-based method with morphology control produces high quality LFS crystals, however, it can

only be accomplished in small quantities and on a lab-scale. An easy, scalable, and sustainable method to produce LFS crystals is yet to be developed. The electrochemistry of these polymorphs has been studied and approximately one Li ion exaction can be reached for the monoclinic phase, although the theoretical capacity is based on two Li ion per formula unit. The questions related to the second Li ion extraction are still not fully addressed by the community. The monoclinic LFS, known to have relatively better electrochemical property among these polymorphs, has been observed to undergo phase transformation upon charging and discharging. Such phase transformation behavior has been studied using various techniques, including XRD and Rietveld refinement, Neutron Diffraction, XANES and Mossbauer spectroscopy and *in situ* techniques to elucidate the underlying mechanism. These studies report contradictory results and different interpretations are suggested. Some groups believe that the monoclinic phase transforms into the orthorhombic phase while some believe that the monoclinic space group symmetry remains; some others believe it is associated with Fe^{4+}, when more than one Li extraction occurs. Most of the studies focus on initial cycle only, with some studies extending to the first ten cycles. The rate-dependent study over longer cycling time is limited and the phase transformation related to long-term electrochemical behavior is absent. In this context, a sustainable and scalable hydrothermal synthesis method is proposed to produce high quality LFS nanoparticles (Chapter 4) to subject to short-term (Chapter 5) and long-term cycling to assess the underlying structural transformations at different cycling rates and cycling times using post-mortem techniques (Chapter 6), which contributes to the further advancement of this important cathode material family.

Finally, Mn-substituted LFS (LFMS) has been proposed previously as interesting alternative to the two pure analogues, LFS and LMS. This suggestion is based in the hope of achieving higher Li-ion reversible capacity (beyond one Li) in the case of LFS due to easier access of the Mn^{IV} state vs. Fe^{IV} state on one hand and on the other in the case of LMS have Fe acting as stabilizer against structure deterioration/capacity fade during cycling. However, there exists significant knowledge gaps and contradictory results in literature. In this context with the aim of obtaining a deeper insight as to how lithiation/delithiation is accommodated when two transition metals participate (LFMS), an *in situ* combined XRD/XANES study is described (Chapter 7) setting the stage for further development efforts.

Chapter 3. Experimental Procedures

In this chapter, details on the different experimental procedures employed during this research project are covered. The chapter consists of two parts. The first part covers the materials and chemicals used, the synthesis method, and the characterization techniques employed (such as X-ray diffraction (XRD), scanning electron microscopy (SEM), transmission electron microscopy (TEM), X-ray photoelectron spectroscopy (XPS), Fourier-transform infrared spectroscopy (FTIR), Raman spectroscopy, thermogravimetric analysis (TGA), Brunauer–Emmett–Teller (BET) gas adsorption analysis, inductively coupled plasma optical emission spectroscopy (ICP-OES), acid digestion and titration analysis to characterize the LFS product). The second part covers the planetary ball-milling of the as-prepared LFS product, the electrode fabrication and coin cell assembly protocol, the electrochemical methods such as galvanostatic charging/discharging and cyclic voltammetry (CV), and the characterization of the post-mortem electrode samples using high-energy synchrotron XRD and X-ray absorption near-edge spectroscopy (XANES). In the end, the overall procedure for materials synthesis and electrochemical testing is schematically summarized with a flowchart.

3.1. Synthesis and characterization of lithium metal silicates

3.1.1 Materials and Chemicals

The raw materials used to synthesize Li_2FeSiO_4 (LFS) were: fumed silica (SiO_2, molecular weight 60.08 g/mol, average particle size 0.2-0.3 μm, CAS number:112945-52-5), ferric nitrate nonahydrate ($Fe(NO_3)_3{\cdot}9H_2O$, molecular weight 404 g/mol, ≥99.95% trace metals basis, CAS number: 7782-61-8), lithium acetate ($LiCOOCH_3$, molecular weight 65.99 g/mol, ≥99.95% trace metals basis, CAS number 546-89-4), ethylene glycol (EG, linear formula $HOCH_2CH_2OH$, molecular weight 62.07 g/mol, 99.8% anhydrous, CAS number: 107-21-1) and ethylenediamine (EN, linear formula $NH_2CH_2CH_2NH_2$, molecular weight 60.10 g/mol, 99.5%, CAS number: 107-15-3), which are available for purchase from Sigma-Aldrich Canada. For synthesis of Mn-substituted LFS, manganese nitrate tetrahydrate ($Mn(NO_3)_2{\cdot}4H_2O$, molecular weight 251 g/mol, ≥98.5% assay complexometric, CAS number: 20694-39-7, Sigma-Aldrich) was used.

3.1.2. Synthesis

The Li_2FeSiO_4 was synthesized using a two-step method: hydrothermal treatment of the precursor mixture to produce a poorly crystalline intermediate followed by thermal transformation/annealing of the latter under reducing atmosphere to induce the crystallization of LFS product. This method was adapted from a previously reported method to produce lithium iron phosphate (LFP).[92] The synthesis sequence involves hydrothermal precipitation of a colloidal precipitate that is subjected to drying before it is further annealed under reducing atmosphere to acquire LFS crystals.

3.1.2.1 Preparation of the precursor solution

The fumed SiO_2 was added (0.03 mol)) to deionized water (140 ml) followed by one hour of ultrasonication. Lithium acetate was then added (0.063 mol) to the suspension with 5% stoichiometric excess followed by half-hour of magnetic stirring. Note that the time of ultrasonication should not exceed 1.5 hours, as Li_2SiO_3 tends to form and interferes with the subsequent synthesis sequence. $Fe(NO_3)_3{\cdot}9H_2O$ was then added (0.03 mol) with the result that the solution changed to a dark red color with a pH of 2. Note that the same procedure is followed for the preparation of Mn-doped lithium metal silicate, simply by replacing $Fe(NO_3)_3{\cdot}9H_2O$ with $Mn(NO_3)_2{\cdot}4H_2O$ proportionally. After another half hour of stirring, 10.4 mL (0.1865 mol) of ethylene glycol (EG) and 10.4 mL (0.1557 mol) of ethylenediamine (EN) were added resulting in the mixture becoming a heavy brownish suspension with a pH of 8 - 9. After another half hour of thorough mixing in ultrasonic bath, the suspension was transferred to a Teflon-lined stainless-steel autoclave (Parr 4567) equipped with stirring (300 rpm) and digital temperature control (Parr 4848). An illustration of the dissembled autoclave is presented in Figure A.1 in the Appendix along some additional technical description information. Typically, hydrothermal reaction was carried out at 180°C for 12 hours followed by natural cooling to room temperature. The resultant slurry was dried in air (i.e. water gets evaporated) on an 80°C stirring hotplate to obtain an amorphous/poorly crystalline intermediate product that was subsequently used in the annealing experiments. It is informative to mention here that adding lithium salt to the initial solution and have the water evaporated after the hydrothermal step is necessary for LFS to be obtained by the subsequent reductive annealing of the complex Li-Fe(III)-SiO_4-EN complex. Thus when LiAc was not added in the initial solution but only after the hydrothermal step directly to the iron silicate precipitate, annealing at 400°C yielded no LFS. In this case the resultant product was a mixture of Fe-Si oxides.

3.1.2.2 Reductive Annealing

Typically, 6 grams of the intermediate precipitate obtained after the drying step was placed in a graphite crucible and subjected to annealing/calcination. Alternatively, ceramic crucibles can be used when the annealing temperature is lower than 700°C. The annealing step was carried out in a tube furnace (Carbolite GHA) under a constant flow (0.5 l/min) of reducing Ar/H_2 gas mixture (95:5 vol:vol, UHP grade 99.999%). An illustration of the furnace is shown in Figure A.2 in the Appendix along some additional info. The initial step of annealing involved purging with the reducing gas for one hour at room temperature. The temperature was then raised to 200°C at a rate of 3°C/min, where it was kept for 3 hours before the temperature was increased again at 3°C/min to a target temperature of 400°C or 700°C to produce two LFS crystalline products: LFS400 and LFS700. This was achieved by holding the LFS crystalline products at the target temperature for a set amount of time (typically 6 hours) followed by natural cooling. Because the annealed LFS product is prone to air oxidation, it is important to open the furnace only after the cooling is complete. After complete cooling to room temperature, the materials were manually ground using a mortar and pestle and transferred inside a glovebox with water and oxygen level less than 1ppm for future use. The air exposure of LFS samples should be minimized during handling and storage due to the air sensitivity of the material.

3.1.3. Characterization

3.1.3.1 Characterization of the reaction intermediate after hydrothermal treatment

After the hydrothermal treatment, the red-brown slurry was analyzed to understand the reaction mechanism throughout the synthesis sequence. After 30 min of centrifuging (Thermo scientific Sorvall ST16 centrifuge, at 3000 rpm) the slurry settled into a red-brown residue precipitate layer (about 15 ml) and a clear supernatant liquid layer (about 35 ml). To understand the ion speciation during the hydrothermal step, the supernatant was collected for ICP analysis to determine the percentage of Li, Fe, and Si distributed in the solution compared to the precipitate. After the slurry drying step (typically 72 hours), the solid residue was collected for XRD and TEM analysis to determine whether the intermediate was amorphous or crystalline by nature. In addition, FTIR spectroscopy was used to study the residual organic molecules from the organic additives. To study the degree of iron reduction (Fe^{3+} vs. Fe^{2+}) after the hydrothermal treatment, the slurry was sampled and digested using hydrochloric acid (HCl) for titration analysis. In the titration experiments, a pre-weighted amount (typically 0.02-0.03g) of powder was firstly digested in 6M hydrochloric

acid (typical 40 ml) at room temperature. Sodium diphenylamine sulfonate was used as redox indicator and 0.01N potassium dichromate was used as titrant. The precision of the titration technique was verified by testing commercially available ferrous chloride ($FeCl_2.4H_2O$, Sigma-Aldrich, 99%) and lithium iron silicate (Li_2FeSiO_4, Sigma-Aldrich 99.7%). Due to the air sensitivity of ferrous iron, the digestion and titration analysis were carefully carried out inside a N_2-filled glovebox equipped with an O_2 sensor, to ensure no oxidation from air. To remove the insoluble carbon residue after digestion, a nylon filter was used over a syringe (0.2 µm pore size) to filter out the carbon.

3.1.3.2 Characterization of the crystalline materials after annealing

As mentioned earlier, due to the air sensitive nature of the LFS materials, all the samples were stored inside glovebox with controlled oxygen or moisture levels and transferred in sealed vials and bags until the time when the characterizations on the samples can be performed. For characterizations that require degassing prior to the analyses, the samples were left in a vacuum oven for at least 24 hours. The characterization analyses included the following:

1. X-Ray Diffraction analysis

X-ray diffraction (Bruker D8 Discover) with Co K_α source of radiation ($\lambda \sim 1.78901$ Å) was used for most of the crystalline LFS powder products after annealing. In the early stages of the research, a Philips diffractometer with Cu source was used to collect the structural information of the reaction intermediate after hydrothermal-drying step and after the 200°C primary annealing step. However, due to the Fe presence, XRD identification of LFS phases using a Cu source was interfered due to the emitted energy of Fe in LFS samples is close to the Cu Kα energy which causes fluorescence and background increase, hence the adoption of Co as radiation source when using a wide-angle 2D XRD detector[93]. In general, around 20 min per frame of exposure time was used to collect an XRD spectrum with good signal to noise ratio. Powder LFS samples were pressed into pellet form prior to XRD analysis. In addition to powder sample XRD, synchrotron hard X-rays at Canadian Light Source Ltd. ($\lambda \sim 0.68989$ Å) were used for the characterization of LFS electrode samples (before and after cycling). In this case the electrode samples were sealed in Kapton tape. The XRD spectra were analyzed using Rietveld refinement by TOPAS Total Pattern Analysis for determination of the phase composition (i.e.

the weight fraction of monoclinic vs. orthorhombic phase). Details on Rietveld refinement are given at the end of the chapter (Section 3.3).

2. Microscopic imaging and analysis

Cold-field emission scanning electron microscopy (SEM, Hitachi SU-8230) was used to obtain the microscopic images. The powder sample was placed on a conductive carbon tape on the sample holder to minimize the charging effect. SEM coupled with Energy dispersive X-ray spectroscopy (EDS) was used to get the chemical information by elemental mapping.

High resolution transmission electron microscopy (FEI F20) was used for microscopic imaging. By coupling with selected area electron diffraction (SAED), the phase information (i.e. monoclinic vs. orthorhombic phase) can be obtained. For powder sample, the sample holder (Cu grid) was dipped in the powder LFS to load the sample. For electrode sample, the electrode was first dissolved in NMP and then the Cu grid was dipped in the solution and air-dried to load the sample.

During the course of this research it was discovered that the crystal structure of the silicate materials was damaged due to high energy electron beam exposure during TEM examination.[85] It was observed that amorphization occurred when a flux of electron beam at the dose of 2×10^4 e/Å^2 s is hitting the LFS sample for 10 ~ 20 seconds.[94] Therefore, lower energy electron beam (less than 20 KeV) was typically applied to the sample to avoid any electron beam induced structural changes during TEM analysis.

3. X-ray photoelectron spectroscopy

XPS (K-Alpha XPS, Thermal Fisher Scientific Inc) was used to obtain the information of the chemical composition especially for the surface of the sample. The XPS was equipped with Al Kα source (1486.6 eV, 0.843 nm), with a spot size of 400 μm in diameter. Because the Li is not detectable by XPS, it is of more interest to analyze the state of Fe (Fe^{2+} vs. Fe^{3+}) and the state of carbon from the decomposition of organic additives (in the form of functional groups). The XPS spectra were fitted with Thermo Avantage.

4. Fourier-Transformed Infrared Spectroscopy (FTIR)

FTIR spectroscopy was used (Bruker Alpha II infrared spectrometer) to obtain the surface bonding information by collecting the infrared spectrum of the sample, especially after the hydrothermal synthesis step to understand the role of the organic additives and how it interacts with the solid precipitate.

5. Raman spectroscopy

Raman spectroscopy was used (Bruker Senterra dispersive Raman microscope) for surface characterizations, especially carbon species. The setup includes a Bruker Senterra confocal Raman microscope and a Bruker MultiRAM FT-Raman spectrometer.

6. X-ray absorption near-edge spectroscopy

XANES employing synchrotron radiation source (Canadian Light Source, HXMA Hard X-ray Micro-Analysis beamline) was used to obtain the X-ray absorption spectra to analyze the chemical bonding nature of the bulk material. The incoming and transmitted X-rays were monitored with He gas-filled ionization chambers and the fluorescence yield was monitored with a N_2 gas-filled Lytle detector. Standard Fe, Mn and Yt samples were used for energy calibration for both XANES and XRD at the HXMA beamline. The Fe and Mn K-edge XANES spectroscopic data were normalized and reduced using Athena software.

7. Thermogravimetric analysis

TGA was used for determining the carbon weight content (TA500 thermogravimetric analyzer) in a mixture of N_2/O_2 (60:40) atmosphere, up to 900°C.

8. BET surface area analysis

BET analysis was done using a Micromeritics TriStar 3000 under nitrogen gas. The typical degassing procedure prior to BET analysis could not be applied to the LFS material samples because LFS (its Fe) is prone to air oxidation especially at higher temperature. Instead of heating up the sample to 200°C in an open tube with minimal N_2 gas flow, the sample was firstly placed in a vacuum oven for 24 hours at 80°C and then transferred to the BET tube with N_2 purging.

9. Inductively coupled plasma optical emission spectroscopy (ICP-OES)

ICP-OES was acquired using a Thermo Scientific iCAP 6500 ICP Spectrometer for solution analysis of the acid-digested powders. The Li, Fe, Mn and Si concentrations were obtained using a three-point linear fit at three concentrations, 0.5 ppm, 5 ppm and 50 ppm, where 1 ppm equals to 1 mg/L. The ICP standard of Li was purchased from SCP and the Fe standard was purchased from PlasmaCal. The Li and Fe standards were used as a multi-standard in 2-5% HNO_3 background. The 4% HNO_3 solution was run as a blank solution. Each calibration test was repeated two to three times at different wavelengths and the wavelength with best correlation coefficient was chosen. The ICP correlation plots are shown in Figures A.3-A.9 in Appendix 1 along details about the different dilution factors.

3.2. Electrochemical testing

3.2.1 Planetary ball milling of pristine material

The as-prepared LFS700 material was subjected to ball milling to reduce the particle size. The LFS400 material was not ball milled because after manual grinding the particle size was already small and comparable to the ball-milled LFS700 sample. The micron-sized particles were firstly ball milled for three hours at 250 RPM in a high energy planetary ball milling machine (Fritsch, Pulverisette 7) in the presence of 10 wt.% of carbon black, using ZrO_2 beads as grinding media and isopropanol as a solvent. Typically, 15 mL of isopropanol was added in the jar. Although the jar size is 80 mL, the actual holding volume is much smaller. The ZrO_2 beads have a diameter of 1mm and typically 25g of beads are placed in each jar. During the 3-hour milling time, a 10-min pause was taken after each hour to avoid excess heat generation within the milling machine. To avoid any air oxidation during milling, all the LFS product and grinding media were pre-transferred to a nitrogen-filled glovebox before the milling jar was closed and tightly sealed inside the glovebox. After milling, the ball milled LFS700 material was recovered and subjected to repeated washing and filtration with isopropanol before drying in the vacuum oven.

3.2.2 Electrode preparation and cell testing

The as-prepared LFS400 material and the ball-milled LFS700 material were subjected to electrochemical testing. The electrode paste was prepared by mixing the active material (LFS), carbon black (Sigma Aldrich, CAS number 1333-86-4) and binder polyvinylidene fluoride (PVDF powder, Sigma Aldrich, CAS number 24937-79-9) in a typical ratio of 8:1:1, using N-Methyl-2-

pyrrolidone (NMP, Sigma Aldrich, CAS number 872-50-4) as a solvent. After mixing the LFS with carbon black and PVDF, the slurry paste was then casted by a doctor blade to deposit a 20µm thick electrode film on aluminum foil and dried in a vacuum oven at 100°C overnight before being punched for further drying at 80°C and coin cell assembly. In the half cells, lithium metal was used as the anode, $LiPF_6$ in a 1:1 ethylene carbonate/dimethyl carbonate (EC anhydrous, Sigma Aldrich, CAS number 96-49-1; DMC anhydrous, Sigma Aldrich, CAS number 616-38-6) solvent mixture was used as the electrolyte, and polypropylene film (Celgard2200) was used as the separator between two electrodes. A schematic illustration and photos of the cell parts used are presented in Figure 3.1.

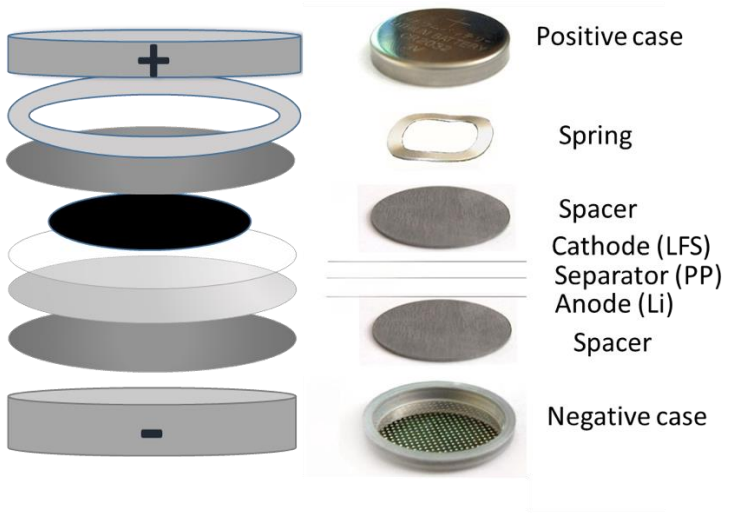

Figure 3.1. Schematic illustration and photos of the coin cell parts used for battery assembly

There are critical steps for successful electrode fabrication and coin cell assembly. Firstly, a thorough grinding and mixing of the active material, carbon and PVDF is necessary. Typically, at least one hour of manual grinding of the three dry ingredients is required before adding the NMP solvent to ensure good paste homogeneity. Secondly, it is essential to deposit enough active material on the current collector to calculate the specific capacity accurately. Typically for a 6 mm electrode with an area of 1.13 cm^2, the total weight including the current collector (Al foil with a thickness of 15 µm), carbon (10 wt.%), and PVDF (10 wt.%) is around 7 mg, and the net weight of the active material is around 5-6 mg, which is equivalent to approximately 5 mg of active material per cm^2. Thirdly, it is necessary to ensure good adhesion between the electrode paste and the current collector. This can be achieved by pressing the electrode sheet with a desktop presser (MTI Co. YLJ-247) after the vacuum drying step and before the punching step. The electrode sheet can be placed under a

piece of aluminum mesh and between two sheets of weighing papers during pressing to prevent the electrode material been peeled off the current collector after pressing.

During the coin cell assembly, it is essential to avoid any possible cross contamination of the two electrodes. Specifically, after handling the lithium metal, the tweezers and gloves should be changed, and the working area should be wiped clean before handling the cathode. It is also important to make sure the edge of lithium disk is smooth after cutting, to avoid any penetration through the separator which may cause the cell to short. Finally, all the components of the cell must be aligned through the centre before crimping (MTI Hydraulic Crimping Machine, MSK-110).

The coin cells were electrochemically tested using the Arbin multi-channel cycler (BT2043-10V-100mA-40) for galvanostatic charging/discharging and the Bio-Logic potentiostat/galvanostatic/EIS system (VSP series) for cyclic voltammetry (CV). CV was carried out at a scan rate of 0.04 mV/s over the first three cycles between 1.50 to 4.67 V. Preliminary charging/discharging studies were carried out for the first three cycles at a rate of C/10 (1C=166 mAh/g) in a 55°C oven (Yamato DVS402C) over a voltage range of 1.50 to 4.67 V. An elevated temperature was used to improve the conductivity of the LFS electrodes. In the later study of the long-term electrochemical cycling study, galvanostatic charging/discharging was performed at various C rates: C/20, C/10, C/5, C/2 (1C=166 mAh/g). The cells were kept in a 45°C oven during cycling, over a voltage range of 1.50 to 4.67 V. The temperature in this series was lowered to 45°C to minimize electrolyte degradation. Typically, 24 hours of aging time at OCV condition was allowed after battery assembly and prior to cycling. The cells were made into two groups and cycled for 7 days and for 30 days under each abovementioned C rate. After the pre-selected cycling time, the cells were discharged to 1.5V and disassembled to retrieve samples of the cycled LFS electrodes. After rinsing with EC/DMC, the cycled electrode samples were sealed in Kapton tape for post-mortem XRD spectra collection and structural analysis. The entire cell disassembling process was carried out in an Ar-filled glovebox (M. Braun Co., with controlled H_2O and O_2 level under 1 ppm) to avoid any parasitic oxidation or hydrolytic reactions. All the cell testing experiments were repeated at least over three cells under each condition to ensure consistent cell reproducibility.

3.2.3 Post-mortem and *in situ* electrode characterization

Long-term cycled LFS electrodes were characterized using synchrotron hard X-ray diffraction at Canadian Light Source (CLS) (λ ~ 0.68989Å). The XRD spectra were analyzed using Rietveld refinement with TOPAS Total Pattern Analysis.

An interesting *in situ* analysis was also performed at CLS to monitor chemical and structural changes during the first cycle of the Mn-doped LFS. For this purpose, the standard coin cell was modified by opening two Kapton windows on the top and bottom cell case to allow X-rays to transmit through and Al mesh was used in place of Al foil as the current collector. The solid disc-shaped spacers were replaced by ring-shaped spacers to allow transmissive X-rays to pass through. A schematic illustration of the *in-situ* coin cell design is shown in Figure 3.2.

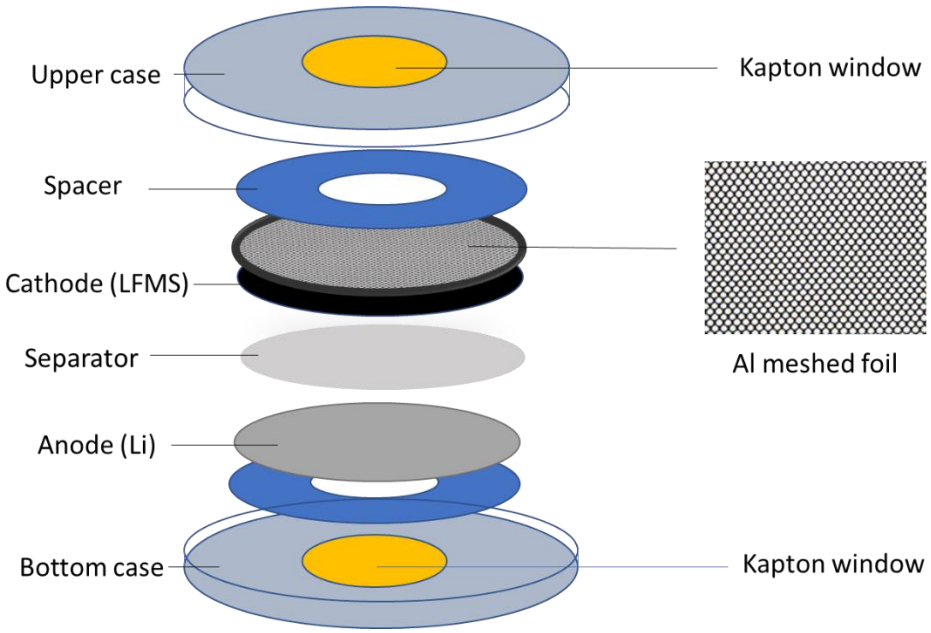

Figure 3.2. Schematic illustration of coin cell design used for *in situ* XRD and XANES analysis

3.3 Structural identification and analysis

The crystal structure and phase identification of the synthesized materials is based on the XRD patterns of the obtained samples. A qualitative analysis is firstly performed by a quick peak search and match to the existing XRD structures in the ICDD database using X´pert HighScore software after baseline correction to subtract the amorphous background, typically with a small bending factor of 5 or less and granularity between 15-30, where the bending factor adjusts the curvature of the background and the granularity changes the numbers of intervals used for

background determination. The background is adjusted until the baseline is smooth without eliminating any of the signature peak features except for the noise peaks. After background determination, the Kα2 line can be stripped from the spectrum. The peak search and match can then proceed either using single-phase or multi-phase analysis scheme, by specifying the known existing chemical elements in the sample mixture, under certain criteria of inclusion and exclusion. In the case of lithium iron silicate, Li, Fe, Si, O are selected and a list of possible candidates with various chemical compositions and crystal structures from the ICDD database are generated. According to the X'pert HighScore scoring scheme and manual peak comparison, the LFS phase with the highest likelihood is identified along with any possible impurities from the remaining unmatchable small peaks. By using the quantitative analysis function, the software also yields an estimated phase ratio of the chosen phases. However, this quantification is only an estimate and for more reliable phase quantification the TOPAS Total Pattern Analysis program was used.

The TOPAS Total Pattern Analysis software allows structure determination, analysis and refinement, as well as quantitative Rietveld analysis. The structure determination is based on the observed structure factors, F^2(obs) using a two-stage method and observed step intensity data, y_i(obs) using Rietveld method.[95] The software performs searching and indexing of diffraction peaks through intensity extraction using Le Bail or Pawley fitting method following the instructions described in Bruker TOPAS manual with an example of the actual fitting curve screenshot provided in Appendix Figure A10. The algorithm used in TOPAS involves iterative use of least squares, or singular value decomposition (SVD) method [96] to solve the reciprocal-lattice equation:

$$X_{hh}\, h^2 + X_{kk}\, k^2 + X_{ll}\, l^2 + X_{hk}\, hk + X_{hl}\, hl + X_{kl}\, kl = 1/\, d^2_{hkl} \qquad (3.1)$$

The Miller indices *hkl* are assigned [97]using randomized lattice parameters with Monte-Carlo approach and the iterative process is executed until convergence. In a typical structure analysis using TOPAS, the following steps are performed in sequence. Firstly, the raw XRD diffraction data is imported after preliminary data treatment using X'pert HighScore, including background subtraction and Kα stripping, and qualitative peak match with the existing structures in the ICDD data base. Alternatively, the background can be determined using TOPAS by setting the Chebychev polynomial, typically at an order of 5. The Goniometer radii, detector information, wavelength and scan range are entered under the instrument information. The Lorenz-Polarization (LP) Factor is set at 0 for synchrotron X-ray data. Then the diffraction data of the reference structures are imported

after converting the reference files into *cif* or *str* format. The obtained XRD pattern is fitted typically using two phases. The weighted scale factor can be adjusted for the two-phase fitting. In general, the lattice parameters, atom coordinates, site occupancy, and thermal factor can be defined iteratively by refining one variable at a time while fixing the rest variables in order to achieve a decent mathematical convergence with reasonable physical properties that describe the crystal structures of the sample. For example, the site occupancy typically should reach a charge balance of all the chemical species, with the anti-site of Li and Fe ions adding up to a total of 1. Other refinement techniques also include firstly fixing the atomic sites of the heavier atoms, such as Fe and Si for the cases of LFS, while refining the position of the lighter atoms such as Li.

3.4 Summary

In this chapter, the experimental methods for the synthesis of lithium iron silicate materials were discussed in detail. The materials characterization techniques, electrochemical testing methods were also described. To summarize, the overall sequence of the material synthesis, characterization, and cell preparation is presented in the flowchart below (Table 3.1).

Table 3.1 Flowchart of the synthesis and battery testing sequence

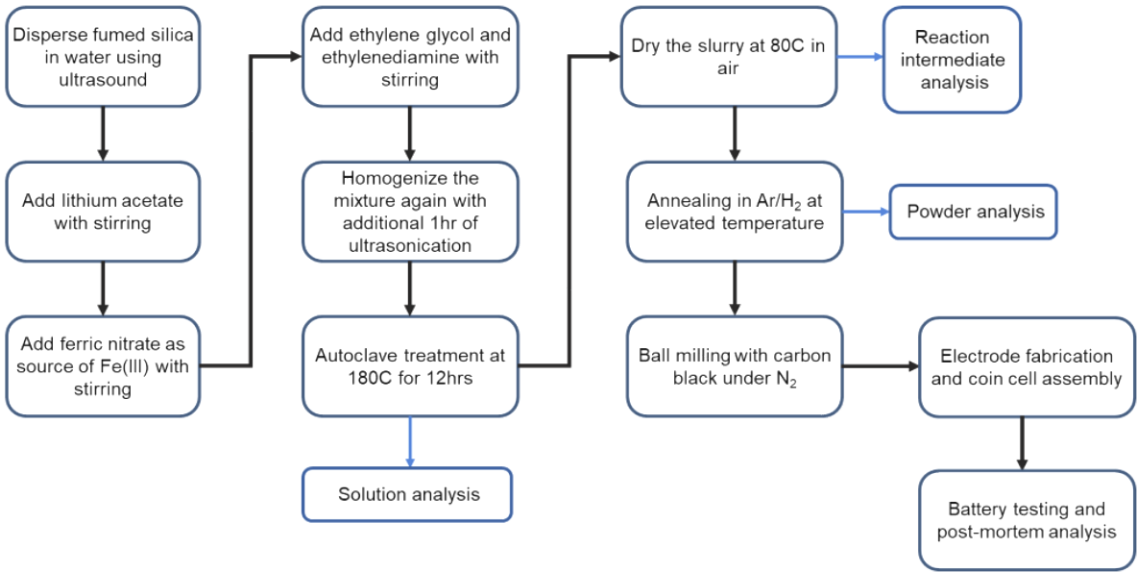

Chapter 4 Synthesis of Mesoporous Nanostructured Li_2FeSiO_4 Materials

This chapter covers the synthesis of the mesoporous nanostructured LFS materials using an ethylenediamine-enabled hydrothermal method from Fe(III) aqueous solution followed by reductive annealing. The chapter is divided into four sections, the crystallization of Li_2FeSiO_4 through the hydrothermal and annealing treatment, the crystal properties of obtained Li_2FeSiO_4 after annealing, the reaction mechanism through the synthesis sequence, and a brief summary at the end.

4.1 Crystallization of Li_2FeSiO_4

The LFS product was prepared using a new dual-step hydrothermal and annealing synthesis method, as described in the previous chapter. The method was an adaptation from a previous work dealing with the synthesis $LiFePO_4$ [92] however, different crystallization paths were observed and described below. In this section, the two-step reaction process, namely, hydrothermal precipitation and reductive annealing is described, and the results are discussed in detail to elucidate the crystallization chemistry leading to LFS formation.

4.1.1 Hydrothermal precipitation

The hydrothermal precipitation step to produce the intermediate for subsequent thermal conversion (annealing) to LFS was performed using an aqueous solution in which CH_3COOLi, $Fe(NO_3)_3$ and SiO_2 were added in addition to two organic chemicals (ethyl glycol and ethylenediamine) used as crystallization modifying agents. To investigate the reactions occurring during the hydrothermal step, the precipitate and the solution obtained after the autoclave treatment were analyzed. From the ICP-OES results, it was found that essentially all of Si (> 99.3%) and Fe (100%) precipitated during hydrothermal reaction step (comparatively, only about 25% of the Li precipitated). The remaining 75% of the Li staying in solution (Table 4.1 below) crystallized out as salt during subsequent solution evaporation/drying treatment.

Table 4.1. Solution analysis of metal ion concentrations after hydrothermal step*

Element/wavelength	Average concentration	Standard deviation	% relative standard deviation
Li/610.3 nm	2027 mg/L	30	1.44
Fe/259.9 nm	Below D.L*	0.01	3.61
Si/251.6 nm	35 mg/L	0.5	1.64

* Note that the concentrations reported in the table are the ICP-OES-determined values multiplied by the dilution factor (100 for Li, 10 for Fe and Si), as described in Chapter 3 (section 3.1.2.3) and Appendix A1. D.L stands for detection limit at 0.1 mg/L

The solution pH remained essentially the same (pH 8-9) before and after the hydrothermal treatment. Titration analysis of the acid-digested precipitate showed negligible signs of reduction from Fe^{3+} to Fe^{2+} (< 0.2%). This finding differs from earlier studies[92] involving the lithium iron phosphate system, where it was reported that Fe^{3+} was reduced to Fe^{2+} during hydrothermal treatment. The authors attributed such reduction of Fe^{3+} to the effect of ethylene glycol (EG) but no direct analysis was provided. It is likely that the difference between the two systems reflects stronger Fe-O bond strength in silicate than in the phosphate. After the evaporative drying step at 80°C, the solids were subjected to XRD analysis. The XRD pattern (Figure 4.1a below) shows a rather amorphous phase with no sharp diffraction peaks, instead, two broad peaks at ~ 30° and ~ 63°, respectively. These broad peaks seem to overlap with the ferric oxy-hydroxide, known as 2-line ferrihydrite ($FeOOH \cdot H_2O$).[98] However, in this case they likely correspond to the amorphous hydrated iron (III) silicate, $Fe_2^{III}(Si_2O_5)(OH)_4 \cdot 2H_2O$ -known as hisingerite, which also exhibits two similar broad peaks.[99] As for the 25% of Li that co-precipitated with the amorphous iron(III)-silica precipitate, it is likely to be in an adsorbed form due to the moderately alkaline pH environment. Following the evaporation of the solution (drying at 80°C), the remaining soluble fraction (75%) of Li crystallized out as lithium acetate into the hydrous ferric silicate matrix (hisingerite) that serves as LFS precursor during subsequent thermal reductive annealing. In other words, no direct crystallization of Li_2FeSiO_4 occurred during the hydrothermal processing step when ferric iron was used as the source of iron, which differs from the cases of hydrothermal synthesis of LFS from ferrous iron precursors.[45, 58, 79, 100] It was also observed from FTIR analysis (Figure 4.2 below) that characteristic C-O, C-H, N-H and O-H bending/stretching modes are present, indicating the organic additives ethylenediamine and ethylene glycol are integral building components of the LFS

intermediate via their known action as bidentate complexing ligand [101] and surface-active agent [102] respectively.

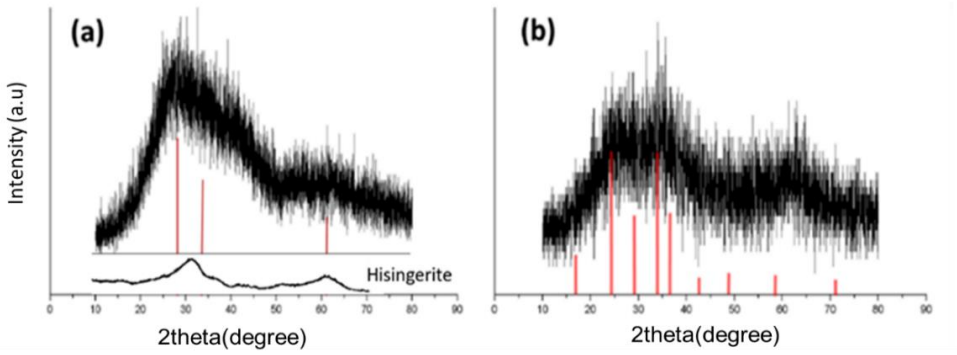

Figure 4.1. (a) The XRD (Cu source) pattern of the reaction intermediate after hydrothermal precipitation (180°C) and drying/evaporation (80°C) (red lines indicate the major 2-line ferrihydrite peak positions and black trace curve indicates the hisingerite $Fe_2^{III}(Si_2O_5)(OH)_4 \cdot 2H_2O$ as reference).[98] (b) The XRD pattern of LFS precursor material after initial annealing of the intermediate at 200°C for 3 hours (red lines indicate the major Li_2FeSiO_4 peak positions as reference ICDD 01-076-8751, which also overlap with the major peaks of $FeSiO_4$, fayalite, PDF# 71-1667).

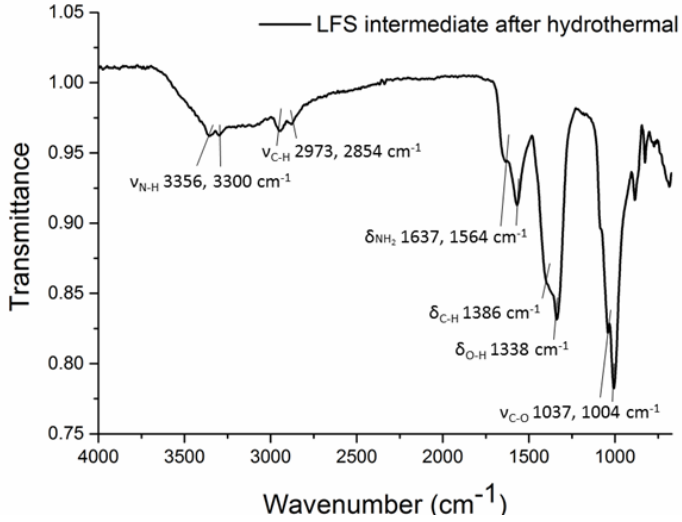

Figure 4.2. FTIR of LFS intermediate after hydrothermal precipitation and drying at 80°C. Various stretching and vibrating modes of organic groups in ethylene glycol and ethylenediamine were observed and labelled. The broad band around 2800-3600 cm^{-1} was due to residual water.

4.1.2 Reductive annealing-nucleation and transformation

After water evaporation, the organic additive-assembled hydrous ferric silicate intermediate was subjected to annealing in a 5% H_2 reducing atmosphere at increasing temperature and time to determine its crystallization pathway. The first XRD spectrum was collected after 3 hours holding time at 200°C (Fig. 4.1b above). According to the XRD pattern, the material remained predominantly amorphous, but weak peaks started emerging at the region of 24° to 37°, where key peaks of crystalline LFS reside. This can be interpreted as evidence of the early stage organization of Li-Fe^{II}-SiO_4 constituents into nuclei of LFS by the reducing action ($Fe^{III} \rightarrow Fe^{II}$) of H_2. The TEM image in Figure 4.3 presents the material morphology and the selected area electron diffraction (SAED) pattern of the hydrous ferric silicate intermediate after hydrothermal treatment, water evaporation and early stage of annealing at 200°C, which confirms the presence of semi-crystalline/semi-amorphous nuclei surrounded by organic layers.

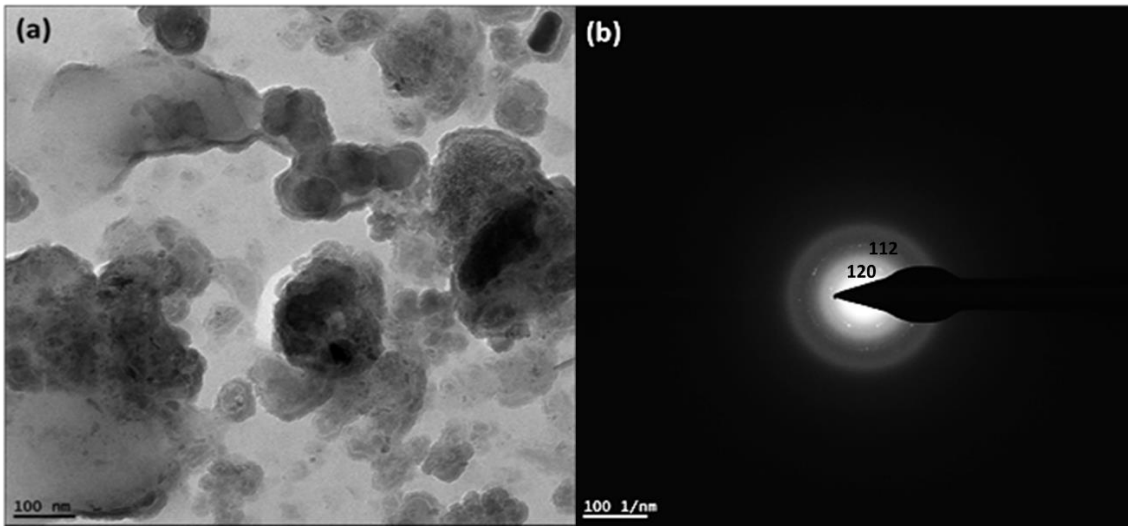

Figure 4.3. (a) The TEM image of LFS intermediate after initial annealing at 200 °C for 3 hours under reductive H_2 atmosphere. Dark regions are LFS nucleation sites due to atomic number contrast (Z contrast); light-gray regions are the organic matrix. (b) SAED pattern of the LFS intermediate after annealing at 200 °C. No obvious signs of crystalline formation were evident yet except for some broken rings at the centre, indicating a semi-crystalline/quasi-amorphous cluster arising from the diffraction of the initially formed nuclei. The rings were indexed as belonging to the (120) and (112) plane family of the ferric silicate (fayalite), which partially agrees with the XRD pattern in Fig. 4.1.

Following this early annealing step at 200°C, the temperature was further increased to 400°C where it was held for different times: 1 min, 1 hr, 3 hrs and 10 hrs. The XRD patterns of Li_2FeSiO_4 annealed at different times at 400°C are shown in Figure 4.4 below. From the XRD pattern of the

material annealed at 400°C for 1 minute, it is observed that crystalline Li_2FeSiO_4 has already formed out of the nucleation cluster observed at 200°C (Fig. 4.1 b above). Comparing the XRD patterns at different annealing times, it is noticed that the full width half maximum (FWHM) decreases as the annealing time increases (Fig 4.4 b), this being indicative of improved crystallinity due to the diffusion-dependent crystal growth and refinement (crystal ordering). It is also noticed that the main crystal phase did not change with increasing annealing time. The monoclinic (112) peak was observed for all samples, as labelled in Figure 4.4, although due to its nanocrystalline nature, some small peak features were not fully resolved.

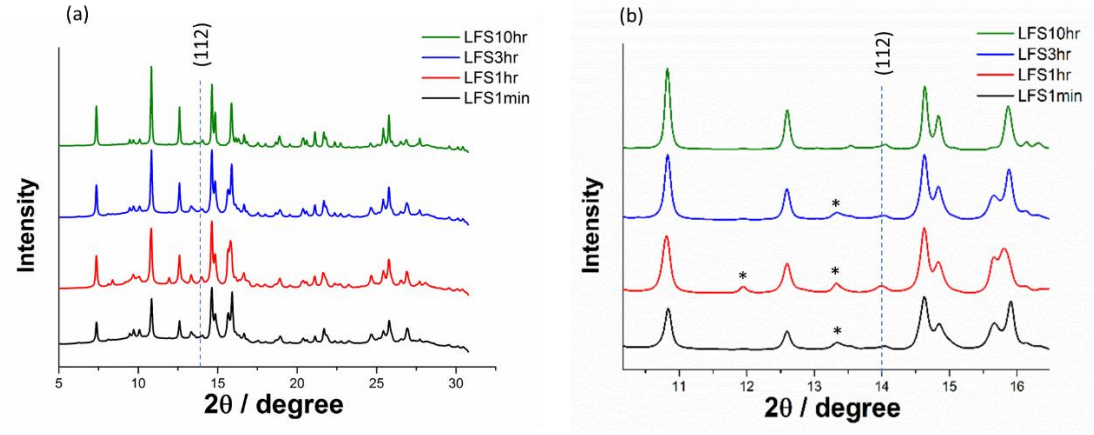

Figure 4.4. (a) XRD patterns (synchrotron source, λ=0.6886 Å) for Li_2FeSiO_4 samples annealed at 400°C for 1 min, 1 hour, 3 hours and 10 hours. (b) A zoomed in view of the XRD patterns in (a) focusing on the range from 10-16°. * indicates presence of minor impurities.

From the TEM images and SAED patterns (Figure 4.5-4.8 below), the predominant presence of monoclinic crystalline LFS phase was observed in all samples annealed from 1 minute up to 10 hours at 400°C. As annealing time increases the small nuclei grow and bond to each other to form polycrystalline particles. A thin amorphous layer with less than 3-5 nanometer thickness was observed in all samples (Figure 4.5-4.8), which most likely represents the *in situ* formed carbon layer from the decomposition of the organics as further discussed in the next section. From this first XRD analysis the co-presence of the LFS orthorhombic phase cannot be ruled out. It is also worth noticing that small impurity peaks (possibly Fe_3O_4 and Li_2SiO_3, labelled with stars) were present at shorter annealing times, which then disappeared as the annealing times increased to 10 hours, indicating the formation of impurity-free LFS nanocrystals.

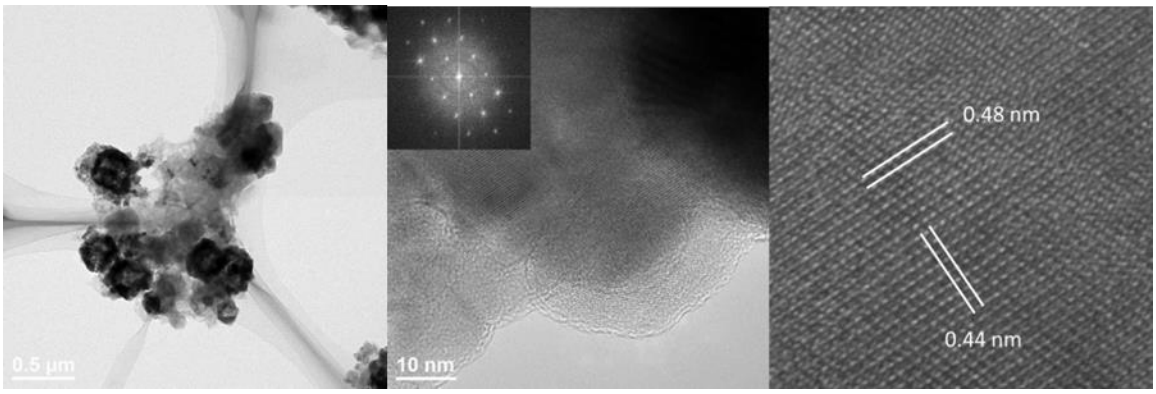

Figure 4.5. TEM images of LFS400-1min sample (after 1 minute of holding time at 400°C and natural cooling).

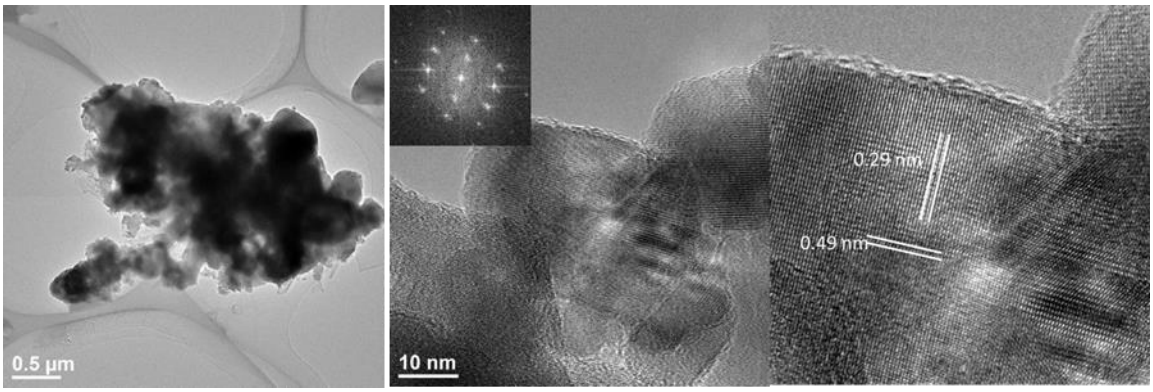

Figure 4.6. TEM images of LFS400-1hr sample (after 1 hour of holding time at 400°C and natural cooling).

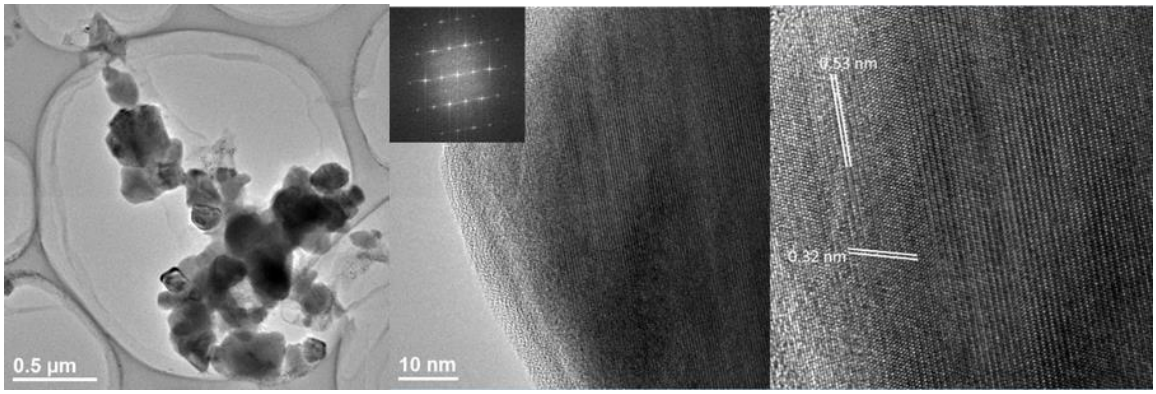

Figure 4.7. TEM images of LFS400-3 hr sample (after 3 hours of holding time at 400°C and natural cooling).

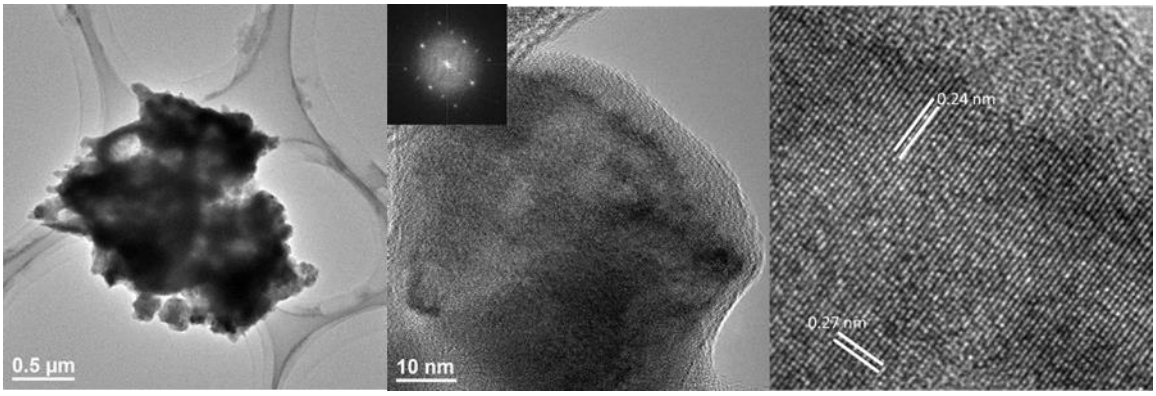

Figure 4.8. TEM images of LFS400-10 hr sample (after 10 hours of holding time at 400°C and natural cooling).

It must be underlined that during annealing, not only a physical transformation of the amorphous precipitate into LFS crystals occurs, but also co-current chemical reduction of ferric iron to ferrous iron by hydrogen. To monitor this reaction, LFS samples at different annealing times were digested and analyzed by titration to determine the percentage content of ferric to ferrous reduction. It was found that after the 1 min annealing point at 400°C, only 60.2% of Fe was reduced to ferrous state; after 3 hrs, the degree of reduction was 69%; after 6 hrs, 97%; no apparent further increase was noted after 10 hrs. Accordingly, 6 hours was selected as the standard annealing time.

4.2. Crystal properties of LFS400 and LFS700 particles

4.2.1. Phase composition

As mentioned in Chapter 2, LFS has been reported to exhibit different crystal phase polymorphs depending on the temperature of synthesis such as low-temperature orthorhombic (*pmn21* or β_{II}) obtained at 200°C, high-temperature monoclinic (*p21n* or γ_s) obtained at 600-800°C, and high-temperature orthorhombic (*pmnb* or γ_{II}) obtained at 900°C.[34, 45] Previous studies have mostly focused on the electrochemistry of the monoclinic (*p21n*) LFS synthesized by annealing of ferrous-derived precursor phases at around 700°C.[40-41, 88, 103] Here, we prepared LFS samples at both 400°C and 700°C to evaluate the impact of the ferric-derived precursor and annealing temperature on crystal phase properties and ultimately their electrochemical responses.

The XRD spectra (Figure 4.9) of both 400°C and 700°C (LFS400 and LFS700) samples (annealed for 6 hours) were fitted using Rietveld refinement to quantify the LFS phases present. The lattice parameters are listed in Table 4.2. The predominant phase in both annealed samples was determined to be the high temperature monoclinic (*p21n*) phase, but to co-exist with a small fraction

of orthorhombic LFS of different space group. The LFS400 material comprised 10% low temperature orthorhombic (*pmn21*), while the LFS700 comprised 25% high temperature orthorhombic (*pmnb*) with the major phase in both cases being the monoclinic (*p21n*) phase. These results show a gradual phase transition with increasing annealing temperature from *pmn21* → *p21n* → *pmnb*. Most of the previously reported studies on the high temperature monoclinic LFS did not mention the presence of the secondary orthorhombic phase except the work by Bini *et al*. [38], despite theoretical predictions of phase co-existence.[47, 104] Interestingly, in an annealing study of the hydrothermally precipitated LFS from Fe(II)-containing solution as the starting material, the LFS phase obtained at 400 °C was identified as *pmn21* instead of *p21n*. [37] Therefore, it becomes evident that the ethylenediamine-Fe(III)-silicate intermediate of the present work facilitates the formation of *p21n* monoclinic LFS phase at a lower annealing temperature by opening a crystallization pathway at lower activation energy.

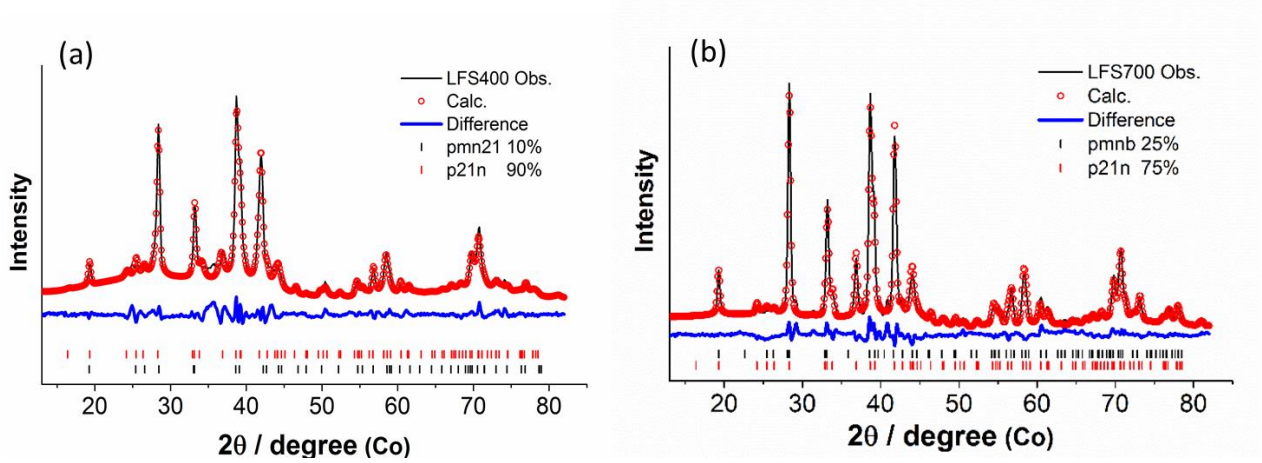

Figure 4.9. The XRD spectra (Co K_α, $\lambda \sim 1.78901$ Å) and Rietveld refinement of LFS400 (a) and LFS700 (b) product. The black lines indicate the experimentally collected XRD spectra, the red bubbles indicate the calculated patterns assuming the coexistence of LFS monoclinic and orthorhombic phases, the blue lines indicate the discrepancies between the experimental and calculated results. The XRD pattern of the LFS400 sample was fitted as a 10:90 mixture of *pmn21* and *p21n* phases and the LFS700 sample as a 25:75 mixture of *pmnb* and *p21n* phases (fitting error within 7%).

Table 4.2 The lattice parameters extracted from the refinement results for the phases present in LFS400 and LFS700

Sample Name	Space Group	a, b, c, (Å)	β (deg)	R_{wp}
LFS400	*pmn21*	6.262, 5.337, 4.985	90.0	4.86
	p21n	8.253, 5.037, 8.238	98.9	
LFS700	*p21n*	8.249, 5.192, 8.225	99.1	3.92
	pmnb	6.282, 10.693, 5.149	90.0	

4.2.2 Morphology

TEM coupled with SAED analysis confirmed the co-existence of phases, consistent with the phase identifications from the XRD results of the LFS400 and LFS700 samples. The TEM and SAED results are shown in Fig. 4.10 below. Both monoclinic and orthorhombic regions were visualized distinctly in LFS400 and LFS700 nano/submicron particles. In the LFS400 sample, (102) and $(31\bar{1})$ planes were detected with interplanar d-spacing of 0.35 nm and 0.24 nm, which correspond to a monoclinic region of the sample; (001) and $(2\bar{1}0)$ planes were detected with interplanar d-spacing of 0.52 nm and 0.26 nm, which correspond to an orthorhombic region of the sample. Similarly, in the LFS700 sample, the (010) and (102) planes were detected with interplanar d-spacing of 0.52 nm and 0.38 nm, corresponding to a monoclinic region of the sample; the (100) and (010) planes were detected with interplanar d-spacing of 0.31 nm and 0.52 nm, corresponding to an orthorhombic region of the sample. From the TEM images, the crystallite size in LFS400 sample was deduced to be around 50 nm while for the LFS700 sample it was close to 200 nm due to grain coarsening effect. It is also noticed that the crystallite clusters were covered with carbon and had some degree of porosity (Figure 4.11, 4.12 below), which are desirable features for a cathode material as they allow for electrolyte infiltration and enhanced conductivity.[105]

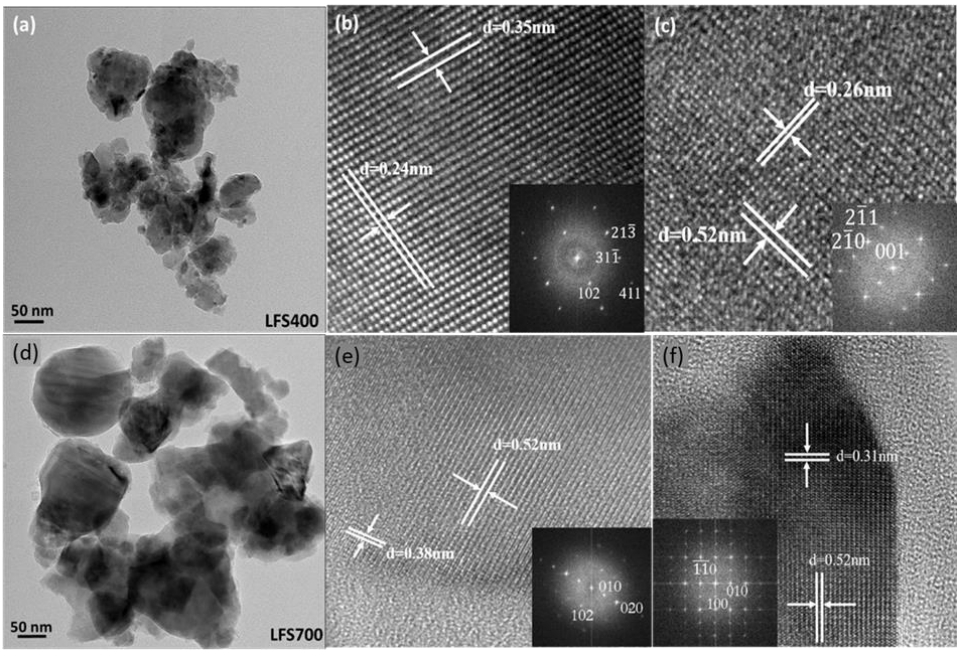

Figure 4.10. TEM characterization of LFS400 (a, b, c) and LFS700 (d, e, f) samples. (a, d) Typical crystal morphology and size. (b) A monoclinic region of the LFS400 sample, where the diffraction spots of the (102) and (31$\bar{1}$) planes are observed with interplanar d-spacing of 0.35 nm and 0.24 nm and (c) an orthorhombic region, where the diffraction spots of the (001) and (2$\bar{1}$0) planes are seen with interplanar d-spacing of 0.52 nm and 0.26 nm. The incident electron beam was parallel to the [120] zone axis. (e) A monoclinic region of the LFS700 sample, where the diffraction spots of the (010) and (102) planes are observed with interplanar d-spacing of 0.52 nm and 0.38 nm, indexed to the zone axis [$\bar{2}$01] and (f) an orthorhombic region of the same sample, where the diffraction spots of the (100) and (010) planes are seen with interplanar d-spacing of 0.31 nm and 0.52 nm. The incident electron beam was parallel to the [001] zone axis.

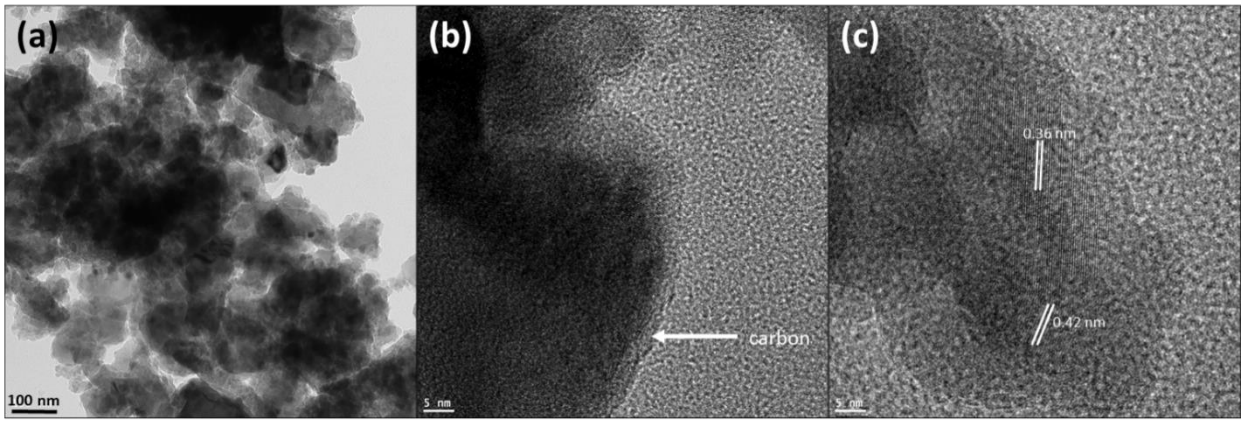

Figure 4.11. TEM images of LFS400-6 hr sample (after 6 hours of holding time at 400°C and natural cooling).

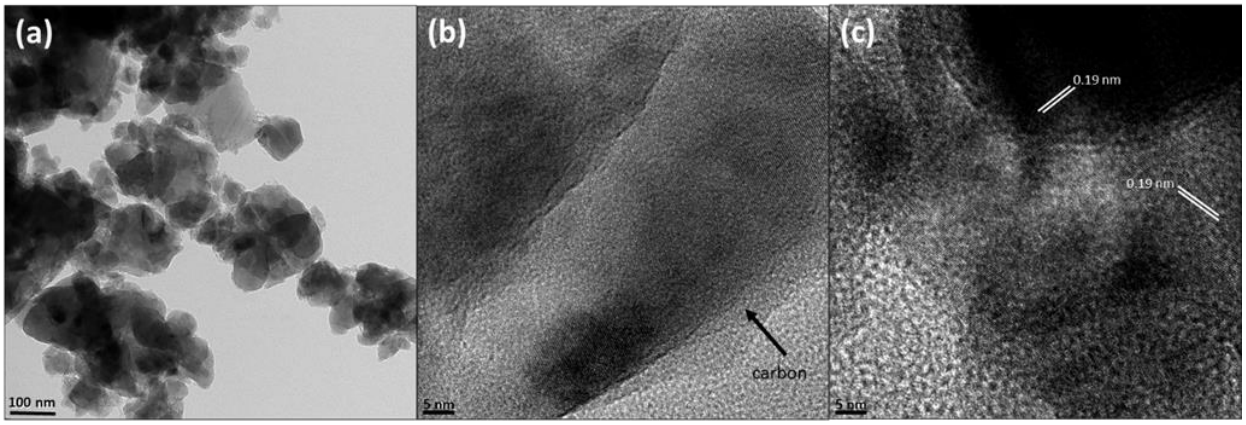

Figure 4.12. TEM images of LFS700-6 hr sample (after 6 hours of holding time at 700°C and natural cooling).

The size and morphology of LFS400 and LFS700 nanostructured particles were also examined using scanning electron microscopy (SEM) (Fig. 4.13). The LFS400 image (Fig 4.13a) shows that the material was in the form of secondary submicron sized porous agglomerates of unitary primary nanoparticles (typically around 40-60 nm). The LFS700 image (Fig. 4.13b) shows that the agglomerates hierarchically organized into a 3D framework of rings of unitary crystallites. The primary crystallites have grown to bigger size (around 100-200 nm) due to the coarsening effect of the elevated annealing temperature (700°C). The rings form open connected porous cages of submicron size. Such porous structure can be advantageous for the LFS cathode as it would allow unhindered electrolyte infiltration and enhanced lithium ion transport.[105] Additional EDS analysis coupled with SEM imaging (Figure 4.14 and 4.15) revealed the key constituent elements (C, Si, Fe, O) to be uniformly dispersed in the selected region with obvious signs of impurities (*i.e.* SiO_2 where Fe was deficient or iron oxides where Si was deficient) in both LFS400 and LFS700 samples. Furthermore, the Barrett-Joyner-Halenda (BJH) pore size distribution derived from the BET adsorption measurement showed that the LFS400 material had an average pore width around 50 nm, which corresponds to mesoporous material (Fig. 4.16a). For the LFS700 pristine sample, the BJH pore size distribution was rather flat (Fig 4.16b) extending over the macroporous range, after ball milling however, it shows comparable pore size as LFS400 sample. The corresponding BET isotherms and associated specific surface areas shown in the Appendix, Fig. A11-A13. This confirmed their microscopically observed porous structure.

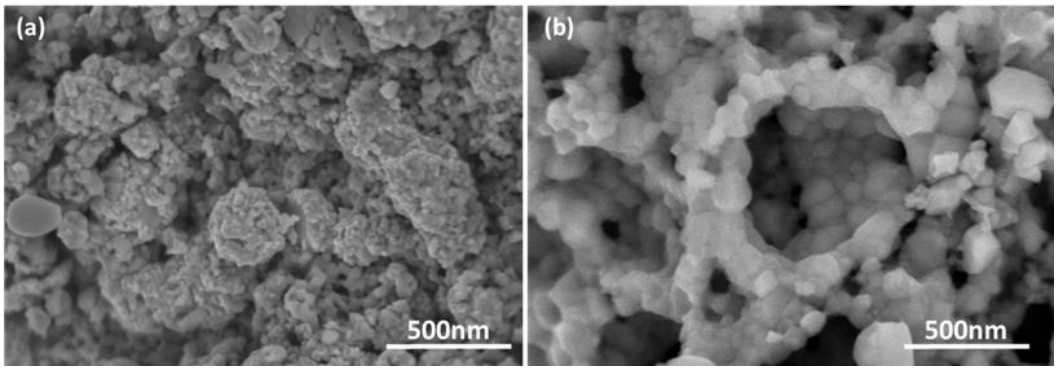

Figure 4.13. SEM secondary electron images of LFS400 (a) and LFS700 (b) samples.

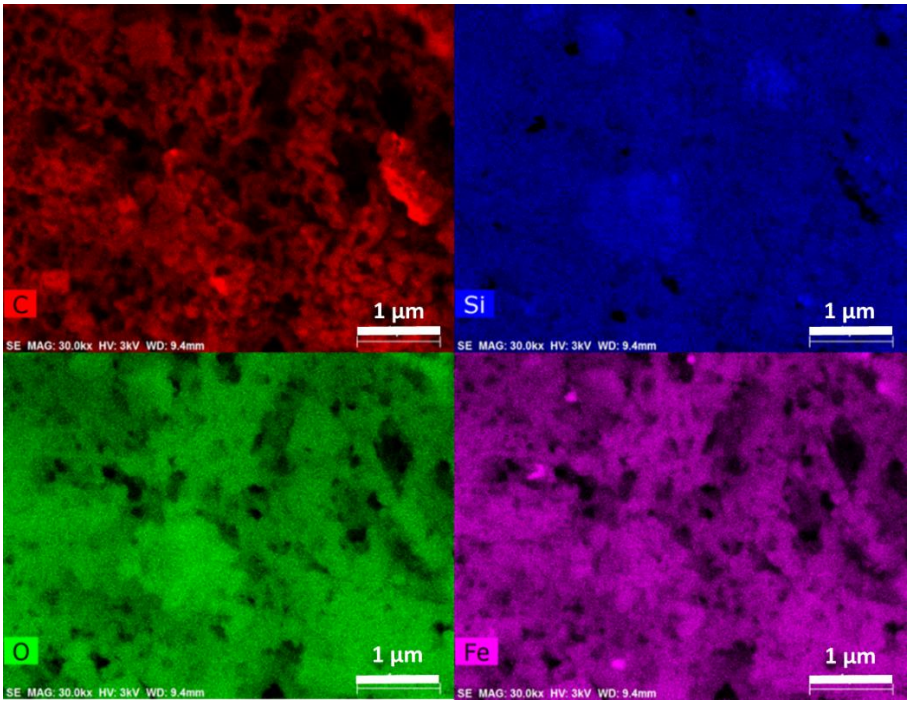

Figure 4.14. EDS mapping (C, Si, O, Fe) of LFS400-6hr sample.

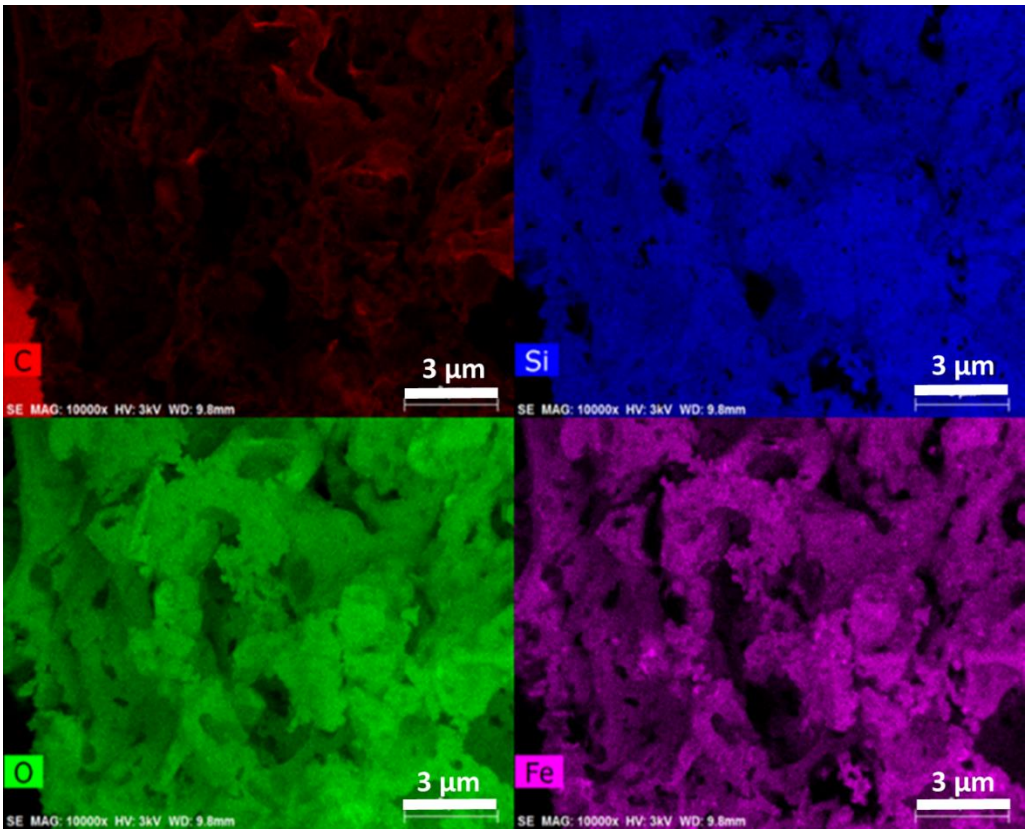

Figure 4.15. EDS mapping (C, Si, O, Fe) of LFS700-6hr sample.

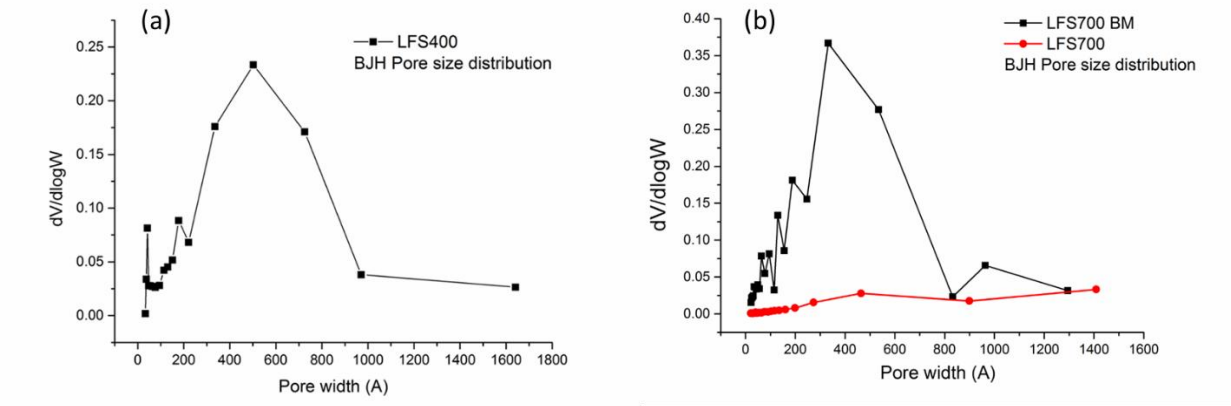

Figure 4.16. (a) BJH pore size distribution of LFS400 sample (after 6 hrs annealing) (b) BJH pore size distribution of LFS700 samples before (red) and after ball milling (black).

4.2.3 Carbon coating and iron speciation

In addition to the above-mentioned phase and morphology characteristics of the two annealed LFS samples, the *in situ* coated carbon layer (evident in the TEM images given in Figure 4.11, 4.12 above) and the chemical states of the surface Fe species, are also important material attributes for LFS in Li-ion battery cathode application. The LFS particles were coated with carbon as a result of the decomposition of the surface-anchored organic additives (ethylenediamine and ethylene glycol) during annealing. The carbon content was quantified using TGA (in the atmosphere of N_2: O_2 at 60:40) to be 8% for LFS400 (Figure 4.17a) and 2% for LFS700 (Figure 4.17b). At 200°C, residual water and minor volatile organic components start to escape from the sample contributing to about 0.8% of initial weight loss. Over the temperature range between 350°C and 500°C, the removal of elemental carbon coating takes place via oxidation initially (see weight gain at ~300°C) and volatilization of degradation products resulting in a weight loss of 7.6%. The decomposition of LFS via oxidation, above 800°C, leads to the formation of oxides, namely iron oxide (Fe_3O_4) and silicon oxide (SiO_2). [107] In addition, the Raman spectra of LFS400 and LFS700 sample both show the carbon D and G band (Figure 4.18) as well the SiO_4 stretching peaks and the presence of Fe_2O_3 as impurity. Furthermore, XPS spectra confirmed the presence of carbon on the surface of LFS particles as shown in Figure 4.19 (a, c). Various carbon bonds were detected, including C-C, C-O, and C=O, located at 284.8 eV, 286.6 eV, and 289.9 eV respectively[108-109] in both LFS400 and LFS700 samples. Besides carbon, nitrogen signals were also detected (as -C-N- (quaternary), -C=C-NH (pyrrolic) and -C-N=C- (pyridinic) bonds- as shown in Figure 4.20, strongly suggesting the decomposition of ethylenediamine rendering the carbon layer N-doped. The presence of *sp2*-typed unsaturated carbon bonds together with the N bonding made the carbon layer potentially more conductive due to the additional electrons donated to the conduction band, [110-111] an important aspect in enhancing the functionality of LFS that has very poor electronic conductivity (10^{-12} – 10^{-16} S • cm^{-1} at room temperature, as measured by compressing the sample into a pore-free pallet and using the four-probe method). [63]

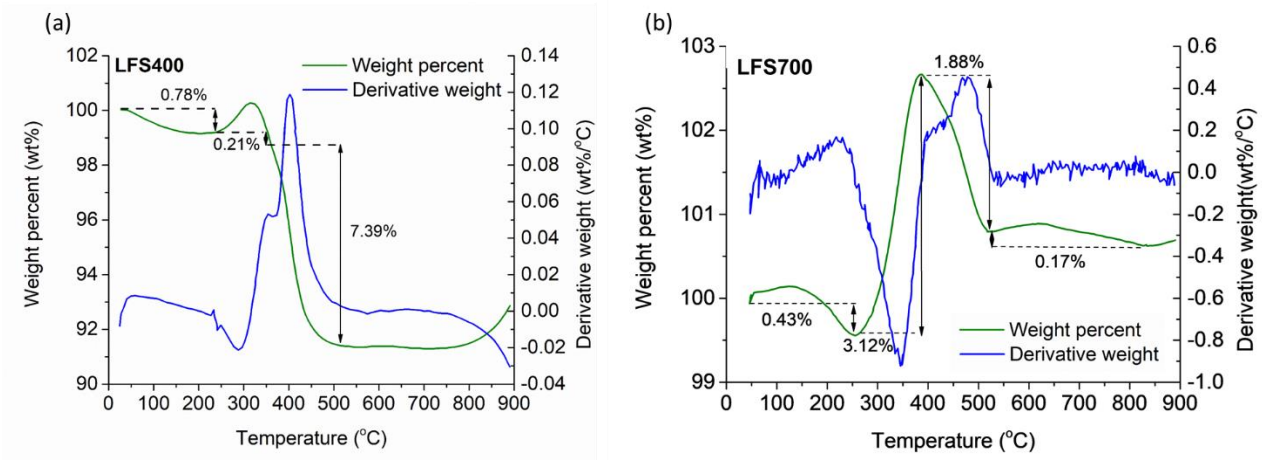

Figure 4.17. TGA traces of (a) LFS400 sample and (b) LFS700 sample (N_2: O_2 at 60:40, scan rate 20 °C/min). It is seen the weight loss from 350 °C to 800 °C to be representing the amount of carbon coating due to the thermal decomposition of organic compound. Below 300 °C the weight loss is resulted from the residual water. Above 800 °C the material is seen to start gaining weight, which is attributed to the oxidation and decomposition of LFS by oxygen at such high temperature. The possible reaction is shown here: $4\ Li_2FeSiO_4 + O_2 \rightarrow 4\ Li_2O + 2\ Fe_2O_3 + 4\ SiO_2$

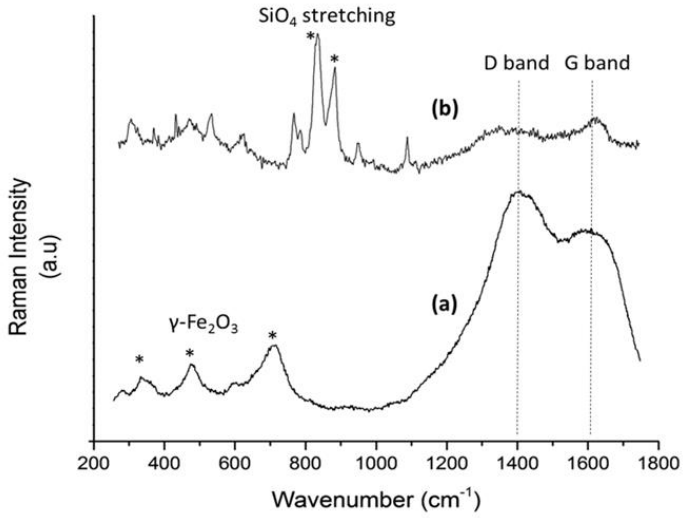

Figure 4.18. The Raman spectra of LFS400 (a) and LFS700 (b) samples. The LFS400 spectrum shows three signature peaks at 200-700 cm^{-1}, corresponding to the γ-Fe_2O_3 [112] impurity appearing due to air oxidation at the surface of the nanocrystals. The two broad bands around 1400 and 1600 cm^{-1} correspond to carbon D and G band, respectively.[113] For LFS700, the carbon bands become less dominant and the silicate SiO_4 stretching is clearly observed around 836 and 880 cm^{-1}.[114]

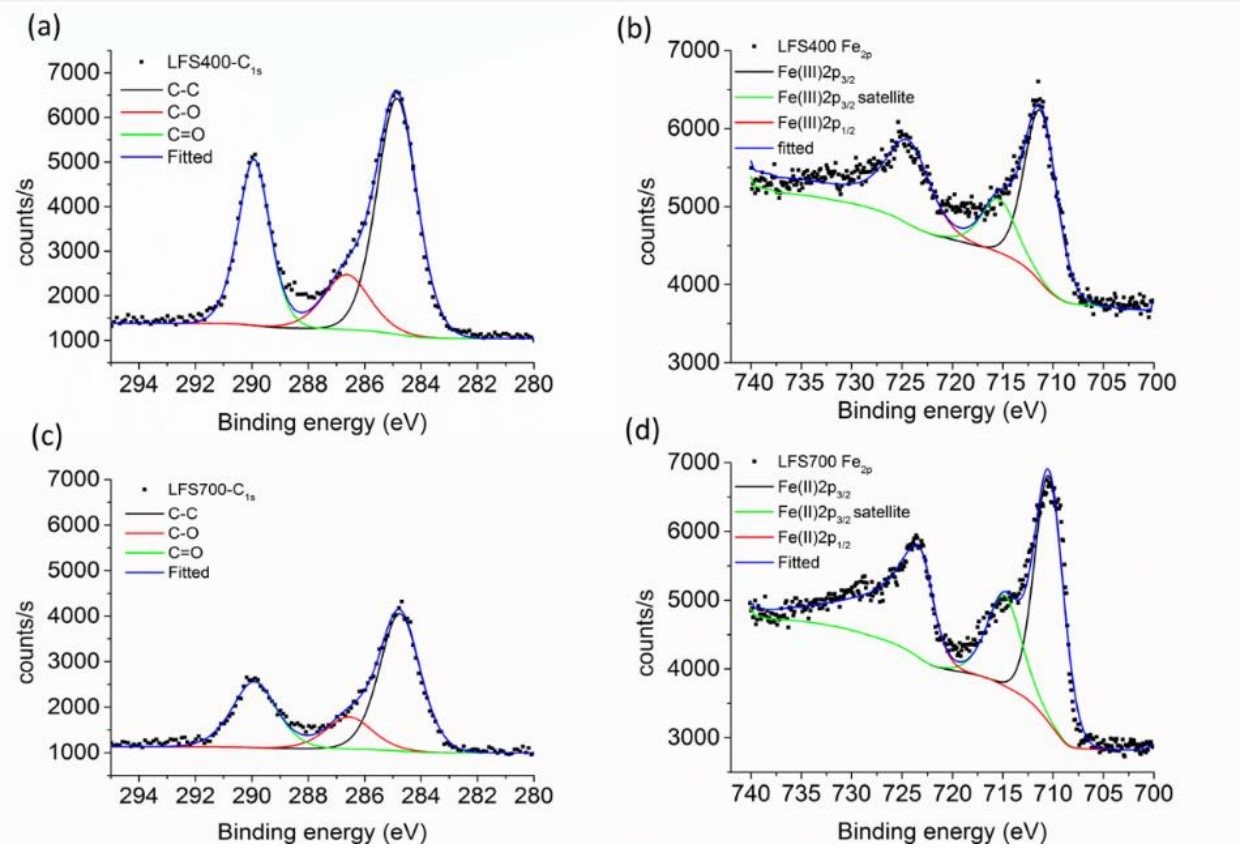

Figure 4.19. XPS spectra of LFS400 (a, b) and LFS700 (c, d) samples. The carbon spectra (a, c) were fitted to various C-C and C-O bonds. The Fe spectrum for LFS400 sample (b) shows a shift of binding energy towards 711.4 eV suggesting the presence of minor ferric impurity at the surface. The Fe spectrum of LFS700 sample (d) however shows a peak binding energy at 710.4 eV corresponding solely to ferrous signal.

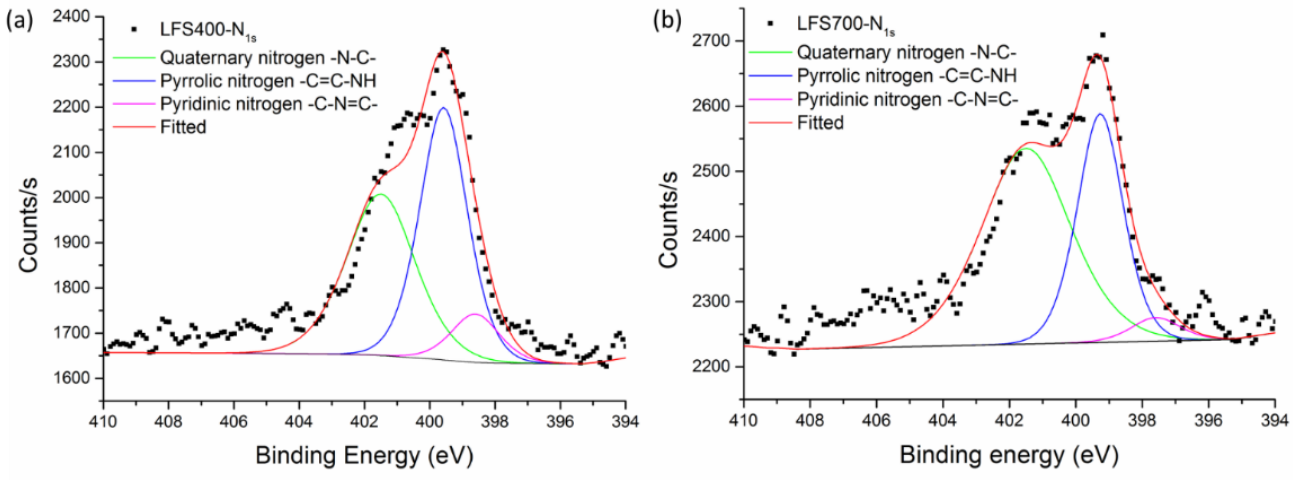

Figure 4.20. The nitrogen XPS spectra of the LFS400 and LFS700 products.

XPS Fe spectra analysis revealed the LFS400 nanoparticles to have some Fe^{3+} species at the outmost surface but not the LFS700 particles (Figure 4.19 b, d). The Fe $2p_{3/2}$ bonding at 711.4 eV of the LFS400 spectrum corresponds to the ferric oxidation state while the Fe $2p_{3/2}$ binding at 710.4 eV of the LFS700 spectrum to the Fe^{2+} oxidation state. [92] The presence of the ferric species in LFS400 was ascribed in part to the inevitable air oxidation of the nanoparticles (smaller size than that of LFS700). The presence of ferric species in the bulk of the samples was quantified by chemical titration following digestion. The corresponding quantities in LFS400 and LFS700 was 4% and 1% ferric respectively. In addition to surface oxidation, incomplete reduction of ferric to ferrous during reductive annealing is responsible for the higher ferric fraction in LFS400 in agreement with the analysis presented in the previous section. Other than quantifying the ferric amount, the chemical analysis of the digested solids revealed certain deficiency in Li content (i.e. less than 2 Li per formula unit), with the Li: Fe ratio been 1.69 and 1.72 in LFS400 and LFS700 respectively (Table 4.3 below). Such ratio corresponds to 15% of the iron as ferric in pure LFS. Because very little ferric (<4%) is present, this may imply from a charge balance point of view the possible presence of about 10% of fayalite (Fe_2SiO_4) as an impurity, which as an isostructural olivine type mineral with the LFS[115] is not XRD distinguishable.

Table 4.3. ICP analysis of LFS700, LFS400 and commercial LFS (Sigma-Aldrich 790974) after acid digestion. *

Sample	Fe/239.5 nm	Li/460.2 nm	Fe concentration	Li concentration	Li : Fe ratio
LFS700	5.96 mg/L	1.27 mg/L	0.11 mmol/L	0.18 mmol/L	1.72
LFS400	8.78 mg/L	1.84 mg/L	0.16 mmol/L	0.26 mmol/L	1.69
Commercial LFS	6.34 mg/L	1.26 mg/L	0.11 mmol/L	0.18 mmol/L	1.60

*Note that each sample was tested three times and the reported value in the Table represents the average of the three repeats. The statistical errors are presented as following. For Fe2395, standard deviation is 0.05-0.06, %RSD is 0.92-1.03 for the three samples. For Li4602, the standard deviation is 0.02-0.05, %RSD is 0.57-1.03 for the three samples.

4.3 Particle formation mechanism

As mentioned earlier, in addition to the three constituent components of LFS introduced as CH_3COOLi, $Fe(NO_3)_3$ and SiO_2, ethylenediamine (EN) and ethylene glycol (EG) were also employed as organic additives. By performing parallel tests without the two organic additives or

using one (EN or EG) organic additive, it was determined that only when EN is present, the ferric iron silicate co-precipitate gel formed during the hydrothermal step could lead to the crystallization of LFS upon reductive annealing. The XRD patterns of the respective annealed products in the parallel tests are shown in Figure 4.21 below.

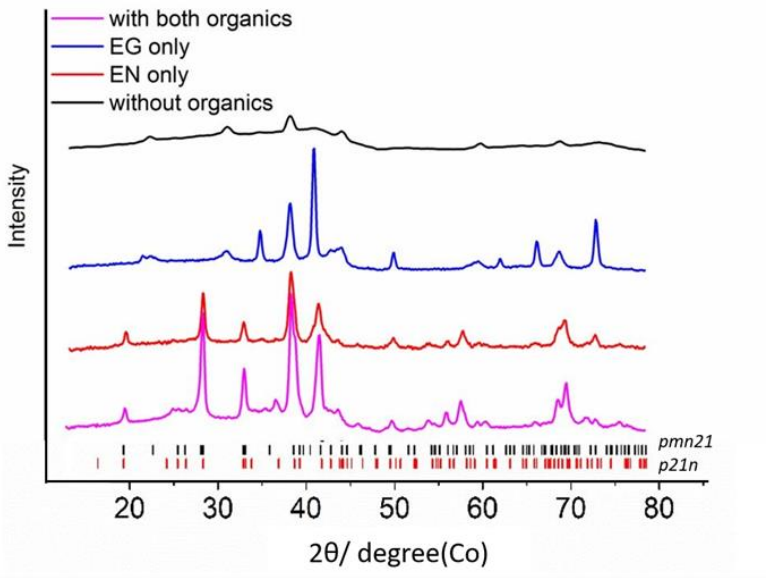

Figure 4.21. XRD patterns of the annealed products obtained from the tests with different organic additives: both organics (EN and EG) used (pink); only one of the organics EN (red) or EG (blue) used; neither of the two organics used (black). Only in the presence of EN (red and pink), LFS was produced. The detailed synthesis conditions are as following. When both EN and EG were used, the standard synthesis protocol (annealed at 400°C for 6 hours) was followed, with a precursor solution at pH 8-9. In the cases where only one organic was used, the standard amount of the selected organic additive was used and the pH of the solution –which was acidic at pH~2- was then adjusted by adding aqueous ammonia so it became similar (pH of 8-9) with that when EN was present.

The enabling role of ethylenediamine (EN) may be linked to its dual function as a bidentate ligand (NH_2-CH_2-CH_2-NH_2) [116] and alkaline reagent that permits via complexation ($Fe^{3+} + zEN \rightarrow Fe(EN)_z^{3+}$), the controlled reaction of ferric ions [101] with silicate anions *(Reaction 1* in Scheme 4.1) generated *in situ* by dissolution of silica as consequence of the released alkalinity (pH ~9). Without EN the spontaneous hydrolysis of free (uncomplexed) ferric ions [117] leads to intermediates that are not amenable to transformation upon annealing to LFS. Meanwhile ethylene glycol (EG) that is known for its surface-active properties [102] plays a supporting role to EN by stabilizing the hydrothermally formed precursor particles into a gel-like assembly that upon subsequent annealing leads to mesoporous LFS crystal formation. It is interesting that EG alone is not effective in

rendering the Fe(III)-derived precipitate amenable to transformation by reductive annealing to LFS even if the solution pH was the same (8-9) as when EN was used (see XRD patterns in Figure 4.20 above). By contrast, when hydrothermal precipitation was done from Fe(II) solution, EG as per previous work [118] was effective as crystallization additive to obtain LFS. Therefore, the key in controlling the formation of the Li-Fe^{III}-SiO_4 precursor is the bidentate complexing effect of ethylenediamine on ferric ions, which has provided favorable crystallization pathway to obtain LFS by reductive annealing (*Reaction 2* in Scheme 4.1).

The present LFS hydrothermal synthesis system that features ferric as the source of iron differs from the hydrothermal system reported by Sirisopanaporn *et al.*[45] where the LFS crystals formed directly by hydrothermal precipitation. In their system, similar temperature/time conditions were used except for the substitution of ferrous chloride for ferric nitrate. It appears therefore that with the initial presence of Fe^{3+} ions, the direct formation of crystalline $Li_2Fe^{II}SiO_4$ or the delithiated $Li_1Fe^{III}SiO_4$ crystalline structure is blocked. Instead, an amorphous precipitate of Li-Fe^{III}-SiO_4 (resembling hisingerite: $Fe^{III}_2(Si_2O_5)(OH)_4 \cdot 2H_2O$) was formed via the mediation action of EN.[101, 119] The EN and EG organics of the resultant hydrothermal intermediate acted as a source of carbonization during annealing forming an *in situ* carbon coating increasing the material's conductivity – an essential property in Li-ion electrode materials. The two-step (hydrothermal precipitation and reductive annealing) reaction is graphically summarized in Scheme 4.1.

$$2Fe^{3+} + 2SiO_2 + 4OH^- + H_2O + Li^+ \rightarrow Li - Fe_2^{III}(Si_2O_5)(OH)_x \quad \textit{(reaction 1; hydrothermal reaction)}$$

$$Li - Fe_2^{III}Si_2O_5(OH)_x + H_2 + 3Li^+ \rightarrow 2Li_xFe_{1-x}^{III}Fe_x^{II}SiO_4$$

$$\xrightarrow[\textit{and Li incorporation}]{\textit{Further reduction}} Li_2Fe^{II}SiO_4 \ (reaction\ 2; reductive\ transformation)$$

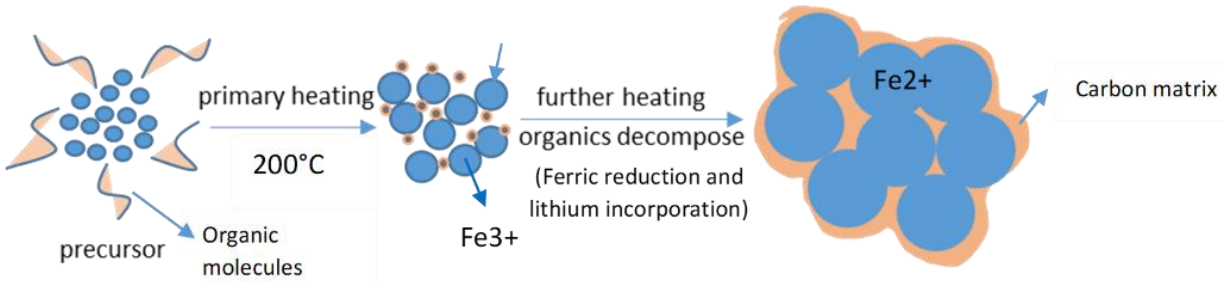

Scheme 4.1. Reactions and schematic depicting the organic-stabilized amorphous precursor and its reactive transformation during annealing under hydrogen into carbon-coated mesoporous LFS crystals.

4.4 Summary

In this Chapter, we demonstrate that nanostructured Li_2FeSiO_4 mesoporous particles have been successfully synthesized using a novel sustainable two-step process that show highly promising characteristics for fabricating Li-ion battery cathodes. The first step involves ethylenediamine-regulated hydrothermal precipitation from an aqueous solution at 180°C containing iron as ferric salt rather than ferrous salt that previous studies have employed, plus colloidal silica and lithium acetate. This step leads to the formation of a hydrous ferric silicate gel that is further stabilized by the co-presence of ethylene glycol. Upon drying, the hydrothermal intermediate is subjected to annealing in the presence of diluted H_2 gas within its safety range (≤5vol% H_2/Ar) that triggers reduction of Fe^{III} to Fe^{II} and simultaneous formation of crystalline Li_2FeSiO_4. We also demonstrate that unless ethylenediamine is used as complexing agent during hydrothermal precipitation no LFS production is possible. Ethylenediamine is shown to assist in the formation of the hydrated iron (III) silicate complex that provides a favorable crystallization pathway for LFS. After reductive annealing at 200°C for 3 hours, a nucleation cluster was found to form that subsequently grows into mainly monoclinic phase (*p21n*) crystallites that assemble into porous cage-like aggregates as temperature is raised to 400°C and 700°C. The effect of annealing time was investigated up to 10 hours at 400°C and, it was found to promote crystallinity and modest growth of nanocrystallites to ~40-50 nm size with 97% reduction of Fe(III) to Fe(II) after 6 hours. The LFS400 material is mesoporous with nanograin structure. By contrast the LFS700 material is made of coarser grains (150-250 nm) that upon mechanical milling become mesoporous as well. In both cases, the particles are found to be coated with a N-doped carbon layer as result of *in situ* decomposition of the organic additives.

Chapter 5 Comparative Electrochemical Assessment of LFS400 and LFS700

This chapter evaluates the electrochemical responses of the two LFS materials annealed at different temperature as described in the previous chapter, LFS400 and LFS700 in order to assess the impact of their nanostructural characteristics on Li-ion storage properties and mechanism. The current chapter includes three parts, the first part deals with the nanosizing of the LF700 material via high-energy milling, the second part describes the electrochemical behavior of the initial cycles for the LFS400 and ball-milled LFS700 sample and a comparison of their electrochemical behaviors. The last part is a brief summary of the chapter.

5.1 Nanosizing of LFS700

LFS400 and LFS700 samples were subjected to a head-to-head electrochemical comparison by measuring their initial galvanostatic charging/discharging behavior at a rate of C/10 at 55°C. This comparative study was motivated as in the past the majority of LFS studies have dealt with the high temperature (~700°C) monoclinic LFS phase (LFS700) and not with the lower temperature monoclinic LFS synthesized in this work at 400°C (LFS400). It was of interest to evaluate if differences in nanostructured characteristics and phase composition as described in Chapter 4 had an impact on Li-ion storage properties. The 700°C monoclinic LFS phase (*p21n* or γ_s) is well established in literature to undergo a phase transition to low temperature orthorhombic one (*pmn21* or β_{II}).[40, 88-89, 105, 120] However, due to the favorable energetic phase-coexisting behavior[47, 104] and the characterization findings of this work (refer to section 4.2.1), the presence and type of the secondary orthorhombic phase (*pmn21* in LFS400 vs. Pmnb in LFS700) should not be ignored, as it may play an important role in triggering the monoclinic to orthorhombic phase transformation during electrochemical cycling.[89] In other words, the secondary phase (*pmn21*) nanograins may alter the phase transformation reaction (*p21n* → *pmn21*) by acting as nucleation (seed) sites and in doing so affecting the cycling performance of LFS cathodes. In order to link any electrochemical differences between the two materials, LFS400 and LFS700, to their nanofeatures and phase composition it was necessary for both materials to have similar nanocrystal size. As described in the previous chapter the LFS400 material had a nanoparticle size ~50 nm while the LFS700 material was coarser about 150-250 nm size. LFS700 was thus subjected to high-energy milling to nanosize it down to similar

size (~50 nm) as the LFS400. The TEM picture of the ball milled LFS700 material is given in Fig. 5.1.

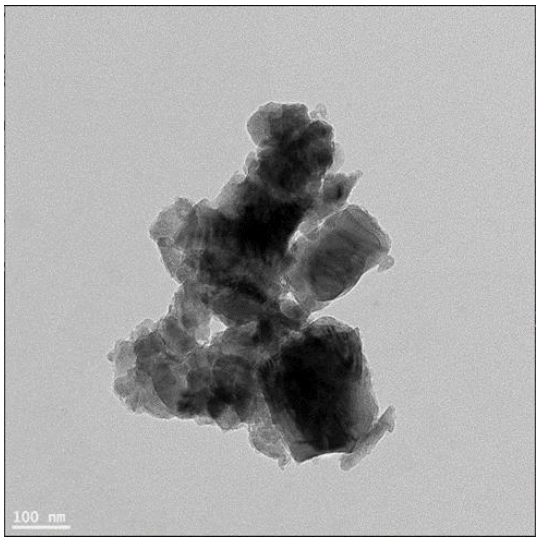

Figure 5.1. TEM image of LFS700 material after ball milling (LFS700BM) with an average crystallite size of ~50nm.

5.2 Electrochemical response of LFS400 and LFS700

The LFS400 and LFS700BM materials were subjected to parallel galvanostatic charging and discharging tests. The first three charge/discharge cycles for the two LFS materials are shown in Figure 5.2. Considering the charging profiles, in both samples, significant polarization has occurred during the first charge despite their nanosizing as originally reported by Nyten et al.[41] This first-charge severe polarization has been attributed to structure rearrangement[80,75] linked to the occurrence of anti-site (Li/Fe intermixing) defects hampering Li-ion diffusion in the pristine material. Thereafter, (cycles 2 and 3) the intrinsic LFS polarization was significantly removed possibly due to the reduction of anti-site defects[75] and the charging profiles were stabilized with practically equivalent corresponding charging capacities: 180 and 170 mAh/g for LFS400 and LFS700, respectively. These capacities correspond to slightly over 1 Li extraction as per charging reaction (5.1):

$$Li_2Fe^{II}SiO_4 \rightarrow LiFe^{III}SiO_4 + Li^+ + e^- \qquad (5.1)$$

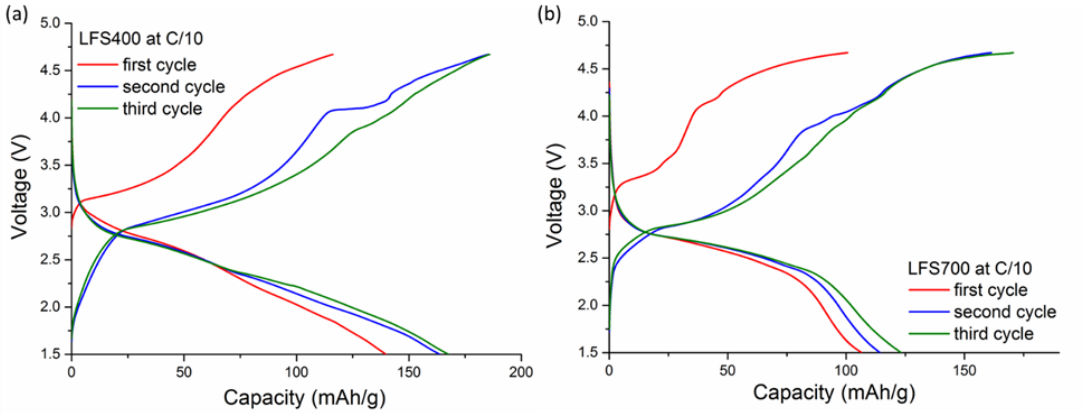

Figure 5.2. The first three galvanostatic charging/discharging cycles of the LFS400 and LFS700 (ball milled) samples at charging rate of C/10 (1C=166 mAh/g) at 55°C. Note that the upper cutoff voltage is at 4.67V, which is supposed to be within the stability window of the electrolyte,[88, 120] considering only the initial three cycles were tested.

In the discharging profiles, the two LFS materials exhibited significant differences despite both being predominantly monoclinic and having similar nanoparticle size. Thus, while LFS400 exhibited almost full reversibility after the third cycle (170 mAh/g discharge capacity vs. 180 mAh/g charge capacity) the LFS700 exhibited only 125 mAh/g discharge capacity vs. 170 mAh/g charge capacity. The Coulombic efficiency of the initial three cycles of both LFS400 and LFS700 were calculated and the results are shown in Table 5.1. The formation cycles of both samples exhibit a Coulombic efficiency temporarily exceeding 100%, which is possibly owing to a side surface reaction with the electrolyte (associated with SEI formation), where similar scenarios have been also reported for other types of lithium ion batteries.[121] In the subsequent cycles, the Coulombic efficiency drops to around 89% and 73% for the LFS400 and LFS700 respectively.

Table 5.1 The Coulombic efficiency (C.E) of the initial three cycles of LFS400 and LFS700

Sample name	1st cycle C.E	2nd cycle C.E	3rd cycle C.E
LFS400	118.9%	87.2%	89.3%
LFS700	106.7%	70.0%	72.9%

The relatively low discharge capacity and Coulombic efficiency in the 2nd and 3rd cycle of the LFS700 sample indicate that the re-lithiation of the charged LFS700 (reversal of reaction (5.1)) was severely hampered by some material defects. This could have been for example, the presence of the high-temperature orthorhombic phase (*pmnb*), as commented next, or persistence of anti-site

defects (intermixing of Li/Fe sites). This capacity differential (charge vs. discharge capacity that amounts to 26%) for the LFS700 material seems to correspond to the presence of 25% high-temperature orthorhombic phase (*pmnb*), which was found in an earlier study to suffer from severe polarization.[89] CV analysis (curves presented in Figure 5.3b) seems to support this postulation as evident by the extra oxidation peaks present in the initial charging cycle which are not reversible in the subsequent cycles. Thus, in the formation cycle of the LFS700 cathode, three anodic peaks were evident, namely at 2.86V, 3.15V, and 3.40V. As per Sirisopanaporn *et al*., [45] *pmnb* has the lowest anodic potential (~2.9V vs. Li^+/Li) among the different LFS polymorphs reflecting a more covalent crystal structure (shorter Fe-O bond) than the monoclinic *p21n*, hence its irreversible behavior resulting in lower discharge capacity. Alternatively, the higher charge capacity differential vis-à-vis the discharge capacity for LFS700 might indicate a contribution from a side reaction [41] between the pristine LFS electrode and the electrolyte.[90]

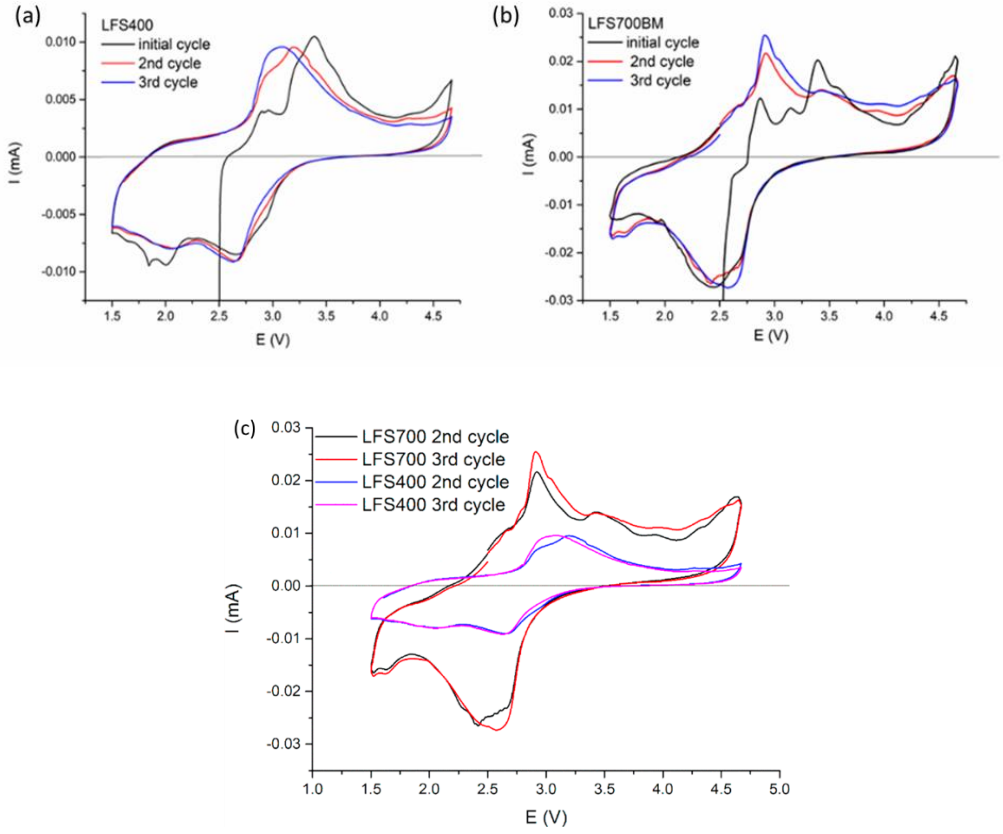

Figure 5.3. Cyclic voltammograms of LFS400 (a) and LFS700 (ball milled) (b) over the first three cycles and (c) direct comparison of their second and third cycles at 0.04 mV/s (corresponding to C/20) over the voltage range from 1.5 V to 4.67 V and 45°C.

Meanwhile from the shape of the discharging curves in Figure 5.2, the differences in the Li-ion storage mechanism between the two LFS materials can be deduced. Thus, the LFS700 (ball milled) sample that exhibited a quasi-plateau in the 2.8-2.5V discharge range has the characteristics of two-phase reaction storage mechanism as also proposed in earlier studies involving monoclinic LFS synthesized at 600-800°C.[41, 88] In contrast, the discharge curves of LFS400 were sloped indicative of continuous solid solution mechanism: $Li_{2-x}Fe_{1-x}^{II}Fe_x^{III}SiO_4$. These observations were further corroborated by the shape of the CV curves for the second and third cycles presented in Figure 5.3. Thus, in the case of LFS700 the oxidation/reduction peaks (2.9 and 2.6 V) were relatively narrow and more defined than the corresponding ones (3.1 and 2.6 V) of LFS400, indicating the Li extraction/reinsertion reaction in LFS700 is characteristic of a two-phase reaction mechanism [41] and LFS400 is more of solid-solution type. This distinct Li-ion storage behavior of LFS400 is owed to its nanograined structure (abundance of nanoscale grain boundaries).[122] It is the combined effects of ethylenediamine/ ethylene glycol and medium range annealing temperature (400°C) as presented earlier in this work that endowed the LFS with mesoporosity and nanograined structure. Post-synthesis high energy ball milling of the coarser LFS700 particles, although successful in rendering the material mesoporous and nanosized, did not have the same effect on Li-ion storage properties as the LFS400. This clearly exemplifies the importance of achieving nanostructure control during the actual crystallization process rather than through mechanical means.

Finally, it is of interest to compare these preliminary electrochemical measurements obtained with the Fe(III)-derived LFS700 material of the present work to the performance of the most common Fe(II)-derived LFS materials. For comparison, the monoclinic LFS (*p21n*) reported by Xu et al. [118] was chosen as it had similar porous structure obtained also via a combination of hydrothermal precipitation (assisted with ethylene glycol) and annealing/carbonization (for carbon coating) at 650ºC. Thus, in the latter case the initial discharge capacity at C/10 (the same rate as applied here) was 72 mAh/g, increasing and stabilizing at 110 mAh/g after 30 cycles. This increase in capacity was attributed to time required for the electrolyte to completely contact the cathode porous material during cycling. By contrast our LFS700 exhibited initially 105 mAh/g discharge capacity that increased to 125 mAh/g after only the third cycle (Figure 5.2). This higher and faster capacity attainment other than being due to the higher cycling temperature must at least in part reflect a superior porous cathode structure. Other than superior cathode material characteristics, the new synthesis route developed in this work provides attractive sustainability features when compared to

the typical synthesis approach as exemplified by the method of Xu et al.[118] The advantages include shorter hydrothermal processing time (12 hours vs. 72 hours), near stoichiometric use of lithium (10% excess vs. 100%), higher yield with the use of concentrated solutions (1 mol/L Fe vs. 0.16 mol/L Fe), lower cost abundant precursor chemicals (Fe(III) vs. Fe(II) salts and SiO_2 vs. $Si(OC_2H_5)_4$ (TEOS)), and ease of handling (use of Fe(III) vs. air-sensitive Fe(II) precursors). In addition, the H_2/Ar (3-5vol% H_2) gas mixture used is within safety range and is widely employed in the metal treatment and semiconductor manufacturing industries for annealing purposes.

5.3 Summary

In this chapter the effect of annealing temperature (LFS400 vs. LFS700) on the microstructure/phase composition of LFS is examined in terms of electrochemical response as graphically illustrated in Figure 5.4. More specifically, head-to-head electrochemical comparison of the two LFS materials revealed significant differences in terms of mode of Li-ion storage that correlates to their nanostructure features and type of co-existing orthorhombic phase (*Pmn2* vs. *Pmnb*). The LFS400 material enriched with abundant nanoscale grain boundaries exhibits near one-Li discharge capacity and solid solution storage mechanism while the LFS700 material exhibits two-phase storage mechanism and somewhat lower capacity. Overall, the mesoporous C-coated nanostructured LFS materials derived from Fe(III) salt compare favorably to those obtained more commonly from Fe(II) salt and, as such, are viable cathode candidates. Although from the initial cycles, the LFS400 materials exhibits better capacity than the LFS700, it is questionable from a long-term perspective that the nanostructured LFS400 will still outperform the LFS700. Previous researchers have noticed that while some nanomaterials are promising cathode candidates due to their high porosity and surface area, it can also be potentially disadvantageous for the long-term stability of the cell and cause faster deterioration for various reasons such as the over-consuming of the electrolyte, the higher concentration of defects inside the structure, and the lack of thermodynamic stability (being rather metastable) [123] regardless of better electrochemical behavior at the initial cycles. For these reasons, in the following Chapter, the LFS700 is chosen to study the long-term behavior and structural transformations at elevated cycling temperature after extended cycling period.

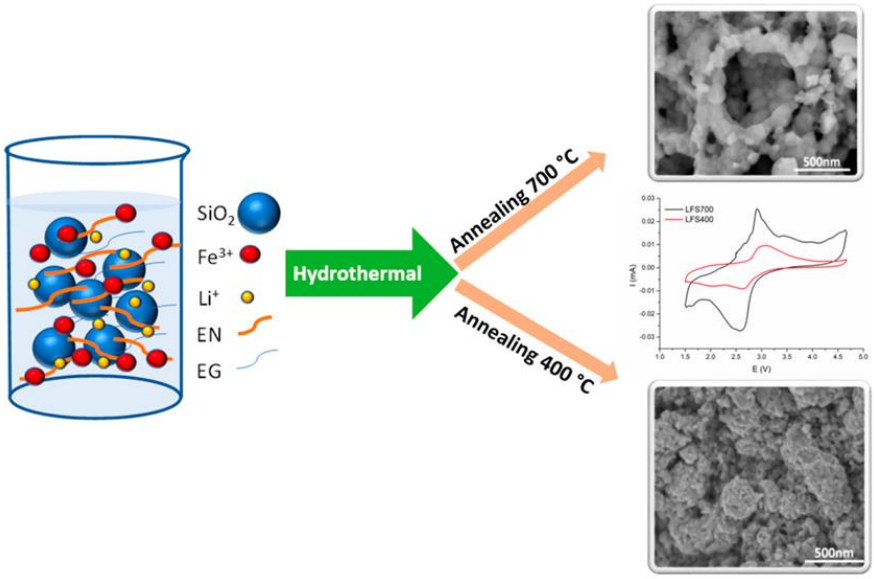

Figure 5.4. Schematic representation of the effect of annealing temperature on microstructure of LFS particles derived from hydrothermal synthesis and corresponding CV response.

Chapter 6 Structural Changes During Long-Term Electrochemical Cycling of LFS700 Cathode

After discussing the synthesis of LFS (Chapter 4) and the preliminary electrochemical tests of LFS400 and LFS700 (Chapter 5), the long-term electrochemical behavior of LFS will be discussed here in Chapter 6. The LFS700 monoclinic material was chosen as it is the one that previous researchers have commonly concentrated on, and it is expected based on the results of Chapter 5 to have higher long-term stability over the LFS400 counterpart. To probe the structural transformations during cycling, the structure of the LFS700 was monitored starting from the battery assembly step, up to 30 days of cycling at different rates. Variable rates were tested as previous studies [88-89] have provided evidence of different phase transition response over the first few cycles. Here, the focus is to extend this investigation over a much longer time and correlate underlying structural changes monitored by post-mortem analysis to electrochemical dynamics.

In Chapter 6, all cycling tests were carried out at 45 ºC. The earlier short-term investigation reported by our group [89] involved cycling at room temperature. As LFS is characterized by low conductivity [57] and the objective here was to study the long-term cycling behavior of this material at an elevated temperature (45ºC). However, when a higher temperature was attempted (55ºC), a high occurrence of cell failure was observed. The relevant data is summarized in Appendix A.2 at the end of the thesis.

6.1 As-prepared LFS before cycling

The XRD pattern and the TEM images of the as-prepared LFS700 sample are shown in Figure 4.9 (b) and 4.10 (d-f) in the previous chapter. Rietveld refinement showed the pristine sample to be predominantly monoclinic, consisting of 75% monoclinic (*p21n*) and 25% orthorhombic (*pnma*) phase. The co-existence of both phases was further confirmed by SAED analysis using TEM. Such co-existence is justified because the two phases are very close thermodynamically with only a 0.04 eV difference in energy of formation. [47] Previous researchers have claimed the LFS they synthesized by annealing at 700°C (same temperature as in present work) to be “phase pure” monoclinic [43, 45-46, 124] contrasting the present thesis findings of mixed phase composition that are more alligned with thermodynamic predictions. The phase composition has been found not to change upon ball milling or after electrode fabrication, i.e. the 75% monoclinic (*p21n*) and 25% orthorhombic (*pnma*) phase ratio remains.

The first sign of LFS change has been observed after the pristine electrode was soaked in the electrolyte but before any electrochemical current passing through the cell (sample labelled as C0 before cycling). The contact with electrolyte before cycling caused a slight increase in the XRD background, in particular at the 2θ range 9-12° and 14-17° (Fig. 6.1), indicating some potential disordering have taken place. Such disordering manifested as an increase in the XRD backgound became progressively more significant after cycling starts as will be discussed in Section 6.3.2.

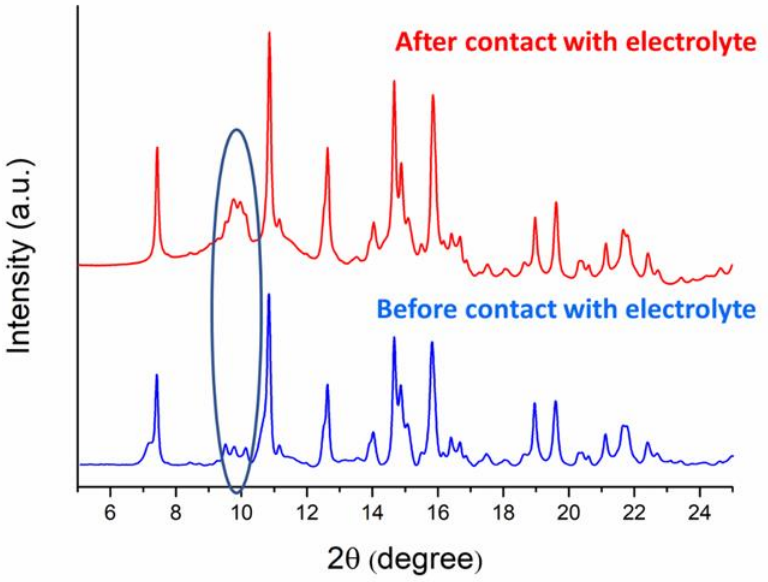

Figure 6.1. XRD patterns showing the initial structural changes (located within the oval scheme) of the LFS electrode sample before (blue) and after (red) contact with the electrolyte. Note that the new doublet peaks in the red graph is at the same 2θ position as the triplet peaks in the blue graph.

In addition to the increase in XRD background intensity, a new pair of doublet peaks appeared at the 2θ angle around 10° where it was previously a triplet in the pristine sample of monoclic LFS. (Fig. 6.1) These doublet peaks grew significantly in intensity after the start of electrochemical cycling. This change is attributed to the partial oxidation of Fe^{2+} to Fe^{3+} in LFS once in contact with electrolyte, as confirmed by XANES measurement from previous work.[90] Such spontaneous reaction with the electrolyte has led to partial delithiation before any current is being applied, which transforms a fraction of the original Li_2FeSiO_4 phase into a partially delithiated phase, $Li_{2-x}Fe^{II}_{1-x}Fe^{III}_{x}\ SiO_4$.

The new doublet peak at 10° is also present in the monoclinic $LiFeSiO_4$ (Figure 6.2), therefore, the partial delithiation leads to a fraction of the original monoclinic $Li_2Fe^{II}SiO_4$ phase transforming into monoclinic $LiFe^{III}SiO_4$. Rietveld refinement of the C0 electrode shows that 12% of the monoclinic Li_2FeSiO_4 fraction (75% of total LFS) has become monoclinic $LiFeSiO_4$ (Fig. 6.3 with associated lattice parameters presented in Table 6.1). This phase transformation starts at open circuit voltage (OCV) condition, after cell assembly and before the application of any current. This pre-cycling initiation of phase transformation acts effectively as nucleation stage, continuing as growth stage during the subsequent electrochemical cycling, as it is discussed in the following sections.

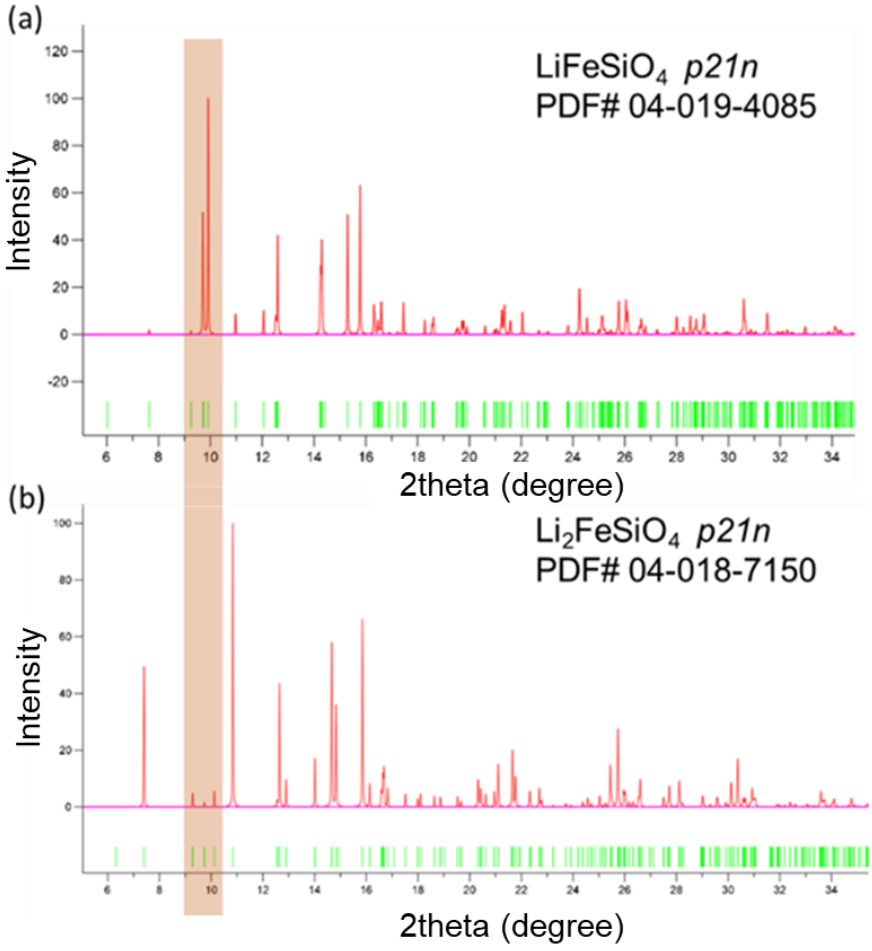

Figure 6.2. Simulated XRD patterns (at the wavelength of 0.68989 Å) of the monoclinic $LiFeSiO_4$ (PDF# 04-019-4085; top) and the monoclinic Li_2FeSiO_4 (PDF# 04-018-7150; bottom). The orange shadow indicates a significant change from the flat triplet peaks to a new pair of sharp doublet peaks as the original monoclinic Li_2FeSiO_4 transforms into the delithiated monoclinic $LiFeSiO_4$.

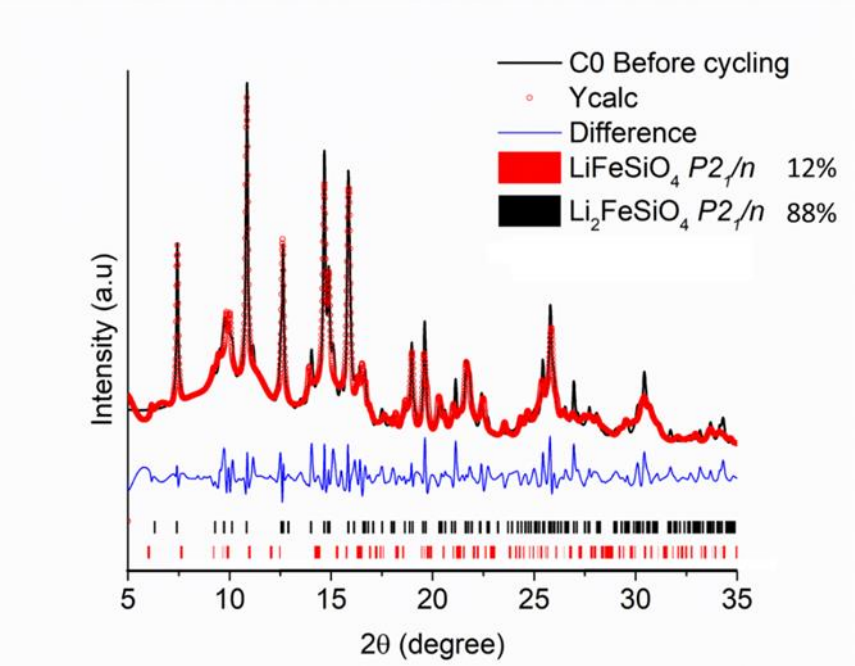

Figure 6.3. Rietveld refinement of the electrode sample (C0) after contact with the electrolyte but before electrochemical cycling. 12% of the original monoclinic Li_2FeSiO_4 has transformed into $LiFeSiO_4$.

Table 6.1. The lattice parameter of the refined C0 electrode sample after contact with the electrolyte and before cycling

Sample Name	Phase	a, b, c, (Å)	β (deg)	R_{wp}
C0 electrode before cycling	Li_2FeSiO_4 *p21n*	8.263, 5.217, 8.250	98.1	5.93
	$LiFeSiO_4$ *p21n*	8.270, 5.211, 8.258	102.8	

6.2 Electrochemical cycling

The electrochemical testing was carried out at 45°C at four different C rates, C/2, C/5, C/10 and C/20, for up to 30 days, where 1C=166 mA/g. The galvanostatic charging/discharging curves and capacity retention at the rate of C/2 and C/20 are given in Figure 6.4; the C/5, C/10 data are given in Figure 6.5. At slow rate (i.e. C/20), the first charging curve is exceptionally long (Figure 6.6) with the first charging capacity over 240 mAh/g, which is not reversible as the first dicharging capacity is only 140 mAh/g. The second charging cycle has a more defined quasi dual-pleateau feature representing the Li-ion extraction at voltage around 3.3 and 4.1 V, resembling a two-phase reaction mechanism. In the following cycles, the dual-pleateau feature gradully becomes a slope feature. At fast rate (i.e. C/2), a slope feature is observed instead of the dual-plateau feature from the

formation cycle, resembling a solid solution type reaction, and the capacity is fully reversible from the initial cycle to 800 cycles. This behavior can be explained by the different reaction kinetics at different C rates. The solid solution type reaction was also seen in our preliminary electrochemical studies of the LFS400 nanomaterial reported in section 4.2 and here.[89] The LFS700 material resembles the LFS400 material in terms of mode of storage at fast C rate. At fast C rate, Li ion diffusion can only happen near the surface of the grains. Thus the limited intra-particle diffusion at high C rate of LFS700 is manifested as solid solution storage similar to the LFS400 material characterized by nanograined structure. On the contrary, at slower C rate there is enough time for Li ions to migrate deeper inside the grains, and being extracted from the inner region of the grains.

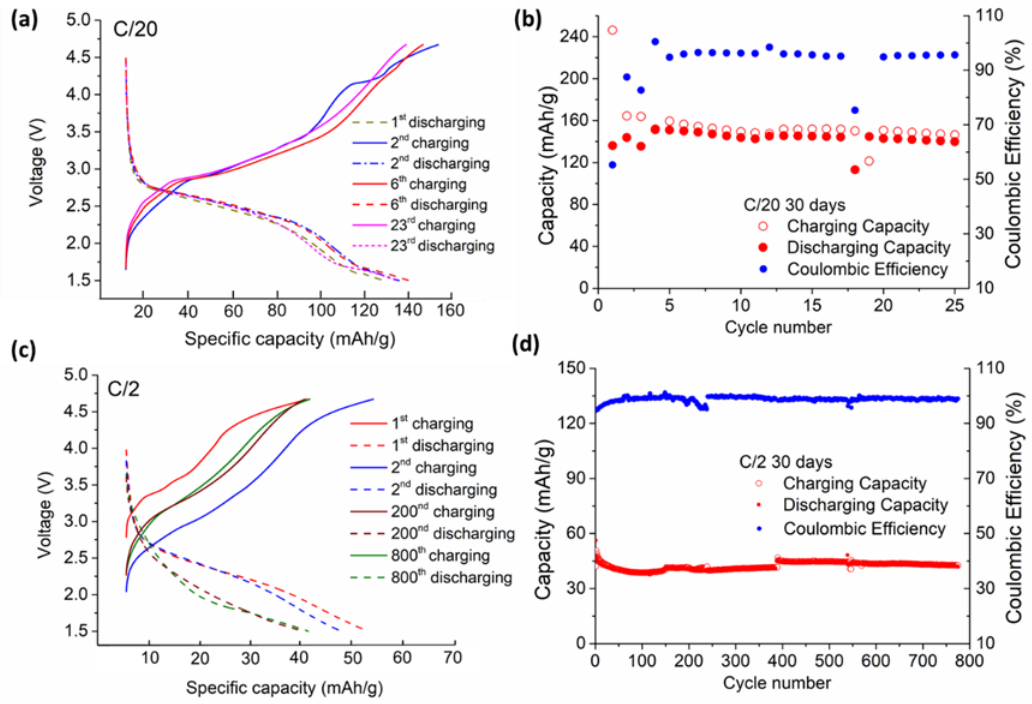

Figure 6.4. The galvanostatic charging and discharging curves and capacity retention over 30 days at C rate of C/20 (a, b) and C/2 (c, d). The Coulombic efficiency (blue dots) at C/2 stablizes at 99% and for C/20 it stabilizes at 95%. Note that the capacity is normalized to the percentage (75%) of monoclinic LFS phase in the sample.

According to the capacity retention graphs (Figure 6.4 (b, d), no significant capacity fading was observed up to 30 days at both C rates. For C/2 the charging capacity stabilizes at 42 mAh/g and the C/20 capacity stabilizes at 147 mAh/g, which correspond to 0.25 and 0.89 Li per formula unit, respectively. It is also noticed that the Coulombic efficiency (defined as discharge

capacity/charge capacity) differs significantly for the two rates (98.9% for C/2 vs. 95.4% for C/20, after 30 days), indicating different Li storage mechanisms.

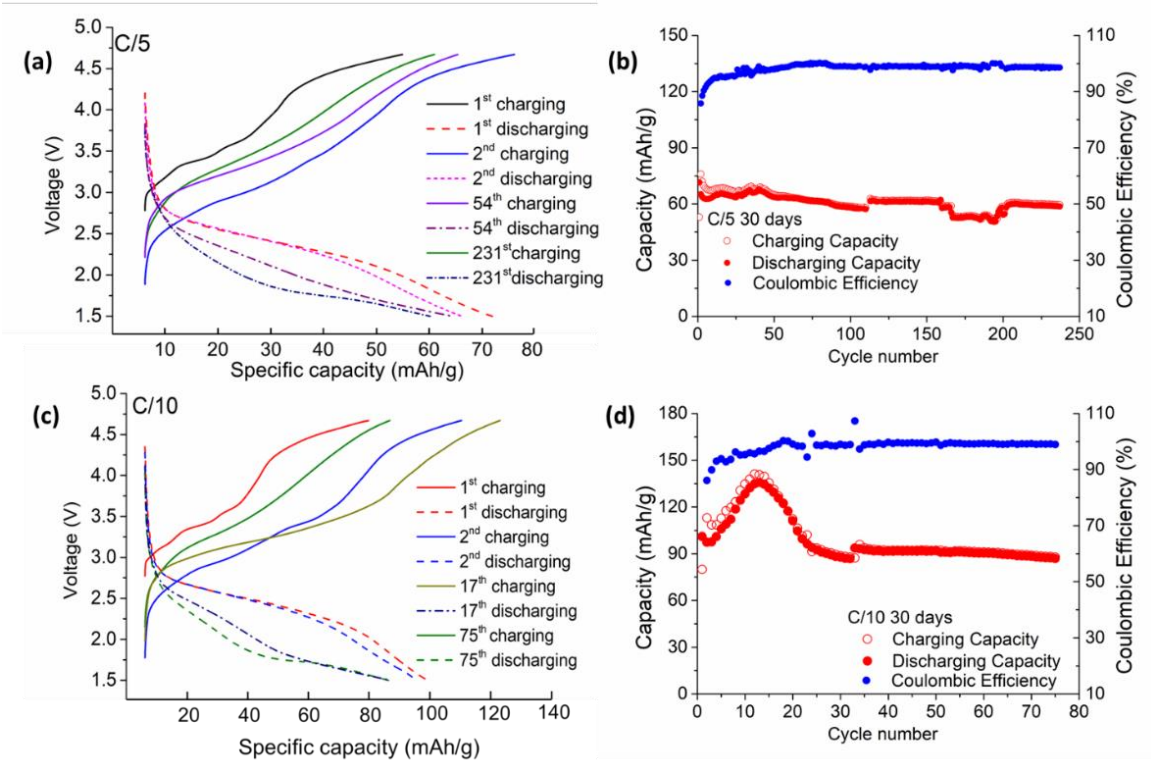

Figure 6.5. The galvanostatic charging and discharging curves and capacity retention over 30 days at C rate of C/5 (a, b) and C/10 (c, d). The Coulombic efficiency (blue dots) at both rates stabilizes at 99%.

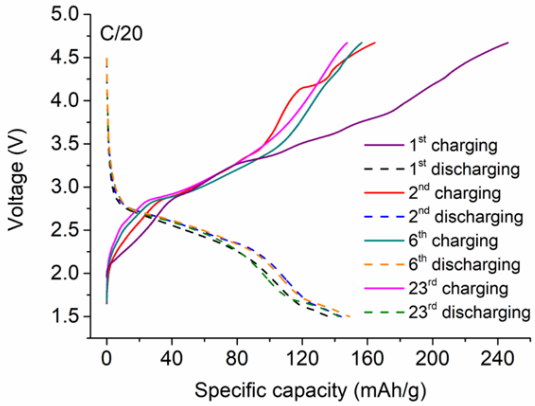

Figure 6.6. The galvanostatic charging/discharging curves of LFS700 at C/20. The 6th and 23rd cycles correspond to the end of 7 days and 30 days of cycling. The unusual shape of the first charging curve with exceptionally high initial charging capacity indicate irreversible reaction during the formation cycle. The dual-quasi plateau feature starts appearing in the second cycle of charging.

When the sample consists of a mixed phase of monoclinic and orthorhombic LFS, it is assumed that (de)lithiation happens only inside the monoclinic portion, with the orthorhombic portion remaining inactive contributing little or no storage to the overall capacity. This assumption is made on the basis that the high-temperature *pnma* phase (typically obtained at 900 °C [45-46]) is reported to have very poor reversible capacity as low as 20 mAh/g.[58, 89] Reversible Li extraction and insertion of the *pnma* LFS phase is hindered by the fewer possible Li transportation pathways than the monoclinic LFS, as suggested by theoretical calculation results.[47 35] In our case, we assume that essentially only the 75% monoclinic fraction of the LFS sample is active, while the 25% orthorhombic fraction remains inert upon cycling, *i.e.* it is assumed that no changes occur within the 25% orthorhombic phase (due to no intercalation activity) and any phase transformation involves only the 75% monoclinic phase. This assumption is important in our subsequent post-mortem structural analysis.

6.3 Post-mortem analysis and structural change mechanism

6.3.1 Identification of the cycled phase

As mentioned in Chapter 2, post-mortem XRD patterns previously reported by other groups are similar, with all showing a new doublet peak at the 2θ position where it was previously a flat triplet peak.[43 86-88] Similar XRD patterns were observed in this case as in previous studies however, with higher resolution over a much longer cycling period at different C rates. There are some conflicting results, however, with respect to the identification of the cycled phase (obtained through transformation of the *p21n* monoclinic phase). Kojima *et. al.* claim the new cycled phase to be monoclinic $LiFeSiO_4$ phase (i.e. the charged phase with one lithium ion extracted), which belongs to the same space group as the starting monoclinic Li_2FeSiO_4 phase.[86] Armstrong *et. al.* reported Li_2FeSiO_4 with *p21n* initial structure to have converted to *pmn21* space group symmetry at the end of discharging after 10 cycles.[43] Although the two groups reported different post-cycling structures, their post-mortem XRD patterns are quite similar when comparing them at the end of discharging state (Figure 5d in Kojima's paper compared to Figure 3b in Armstrong's paper, reproduced as new composite Figure 6.7 (a, b)). Both patterns show the signature new doublet peak at the position of the original triplet peak position in the monoclinic Li_2FeSiO_4; (2θ position ~10 degree in Kojima's case, ~28-29 degree in Armstrong's case) and similarly the next two major peaks with slight difference in intensity overlap with the third and fourth major peak in the monoclinic Li_2FeSiO_4 (2

theta position ~15-16 degree in Kojima's case, ~41-43 degree in Armstrong's case).

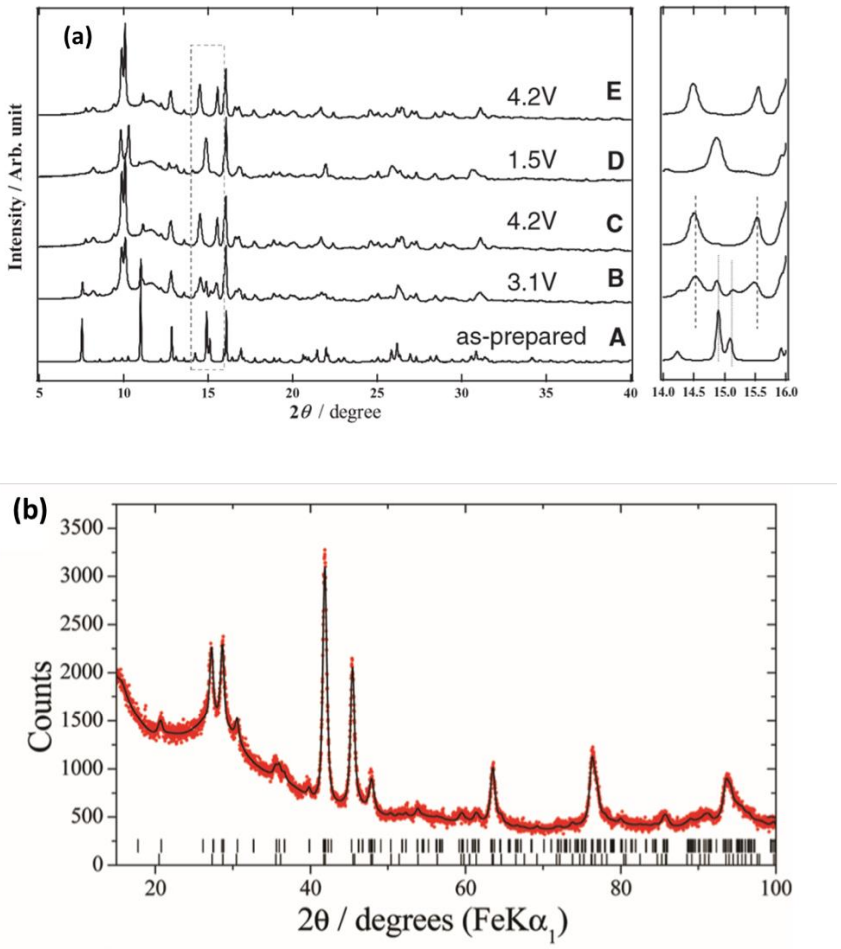

Figure 6.7. Post-mortem XRD patterns of the discharged monoclinic Li_2FeSiO_4, reported in literature: (a) Li_2FeSiO_4 upon the first discharging (circled in the red box) at the rate of 0.07C, 60°C, in the voltage range from 1.5 to 4.2V.[86] The authors fitted it as a *p21n* monoclinic LFS phase. (b) Li_2FeSiO_4 after the 10th cycle of discharging, at the rate of C/16 (10mA/g), 50°C, in the voltage range from 2.0 to 3.7 V.[43] The author fitted it as a *pmn21* phase.

In another case, similar post-mortem XRD pattern was observed by Masese *et al*., where the end of discharging phase at C/50 was identified as a *pmn2₁* phase, reported in their Figure S6 in the supporting information, reproduced below in Fig. 6.8(a).[88] Masese *et al.* reported the phase transition behavior at two different cycling rates however only the initial 1.5 cycle was studied, where they claimed the end of first discharging phase to be *pmn21* at C/50, and *p21n* at C/10. In the *in situ* studies reported by Lv *et al*., again similar end of discharging XRD pattern was observed (Figure 7c-I in Lv *et al.*'s paper, reproduced in Figure 6.8 (b)) and it was labelled as a new phase associated

with Fe^{4+}.[87] Only the first cycle was reported, and it is not discussed whether the excess capacity corresponding to over one Li ion extraction is reversible or not in the subsequent cycles.

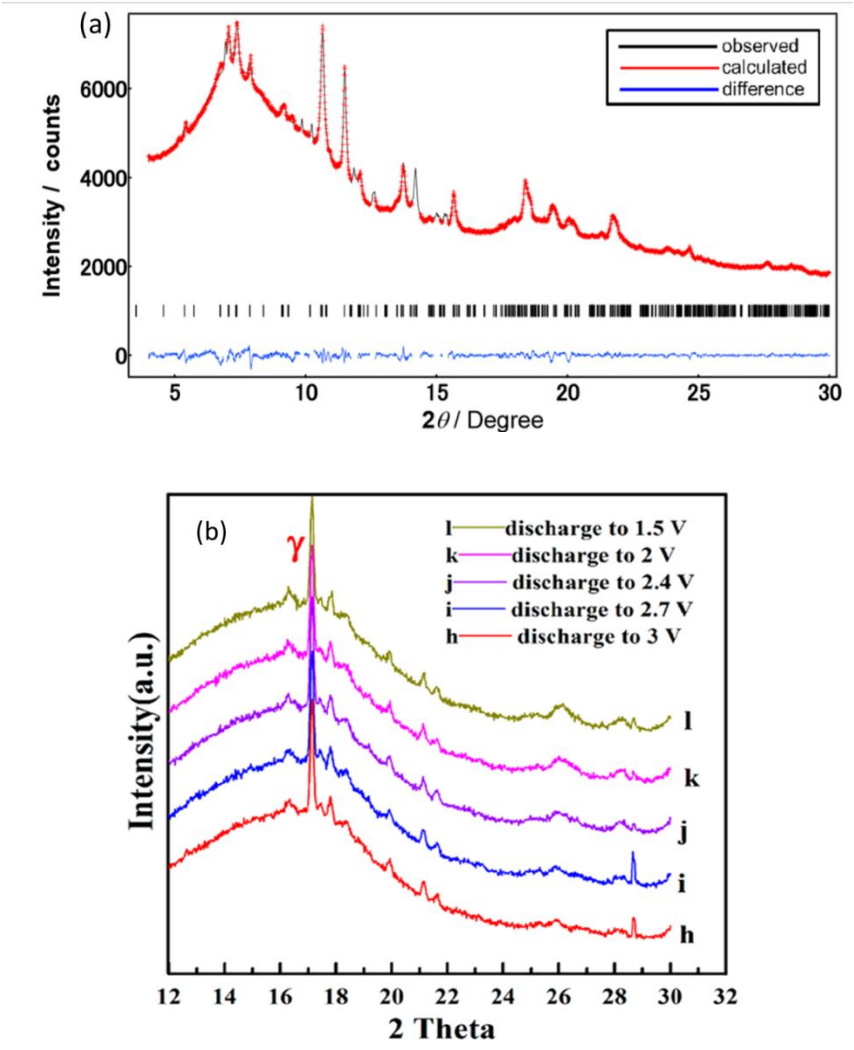

Figure 6.8. Post-mortem XRD patterns of the discharged monoclinic Li_2FeSiO_4, reported in literature: (a) Discharged Li_2FeSiO_4 obtained upon the first discharging at C/50 rate, room temperature, assigned as a *pmn21* phase. The authors also claimed that when cycling at C/10, the monoclinic phase remains unchanged (XRD data not given) at the end of discharging.[88] (b) Discharged Li_2FeSiO_4 after the first cycle, at the current density of 10 and 20 mA/g, for charging and discharging respectively, at room temperature from 1.5 to 4.8 V. The new phase (the authors labelled as γ) was claimed to be a $Li_{0.5}FeSiO_4$ phase associated with a mixed Fe $^{(III)}$ and Fe $^{(IV)}$ phase.[87]

To achieve better identification of the new phase, a detailed search into the database was made and it was found only the monoclinic $LiFeSiO_4$ phase (PDF reference: 04-019-4085) proposed by Kojima can well fit the new doublet peaks, 2θ at 9.7 and 9.9 degree at the wavelength of 0.68989

Å, corresponding to [002] and [-111] plane family. The simulated XRD pattern was shown in Figure 6.2 at the beginning of this Chapter. Rietveld refinement attempts showed the monoclinic $LiFeSiO_4$ phase to give the best overall fitting to the new doublet peaks, in good agreement in other words with Kojima's phase identification results. Based on our observation of the spontaneous reaction with the electrolyte that causes some of the Fe^{2+} to be oxidized before any electrochemical cycling is applied, it is proposed that some fraction (12% based on Figure 6.3 above) of the original monoclinic *p21n* becoming partially delithiated and transforming into the $LiFeSiO_4$ phase. The latter phase also belongs to the monoclinic *p21n* space group, isostructural to the original monoclinic *p21n* phase; while the 25% orthorhombic phase remains inert. In addition, a slight increase in the background is observed, indicating some degree of disordering happening upon contact with the elctrolyte (Figure 6.3 above).

6.3.2 Crystal disordering

Upon close examination of the XRD patterns of the post-mortem electrode samples cycled at different C rates, it becomes evident that there are two structural changes occuring simutaneously: the reduction of crystallinity as indicated by the increase of XRD background and the phase change in the crystalline portion as indicated by a characteristic XRD peak shift. These changes can be seen in the post-mortem XRD patterns corresponding to the two extreme C rates C/2 and C/20, after 7 and 30 days in Figure 6.9. The detailed XRD spectra with Rietveld refinement at all four different C rates for samples cycled for 7 and 30 days are given later to explain the phase changes. To quantify these two changes, namely, the crystal disordering and phase transformation, the reduction of degree of crystallinity was calculated as compared to C0 for all the 8 post-mortem cycled electrode samples and Rietveld refinemnt was performed to quantify the different phase ratios in the crystalline portion.

The degree of crystallinity was calculated according to the following equation [125],

$$\text{degree of crystallinity} = \frac{integrated\ under\ peak\ area}{integrated\ total\ area} \times 100\% \quad (6.1)$$

Where the total area is the sum of under the peak area and under the background area of the raw XRD pattern. The background baseline determination was based on adjacent point averaging method with a total of 30 marking points over the entire 2θ range. The degree of crystallinity of each post-mortem sample was then compared with the C0 electrode sample (before cycling) to get the relative difference in the degree of crystallinity (an indicator of structure disorder). The structural disordering

behavior has been seen in many of the cathode materials such as in $Li_{1.2}Ni_{0.175}Mn_{0.525}Co_{0.1}O_2$ (LNMCO) [126], in $LiCoO_2$ [127], and in $LiMnPO_4$ [128].

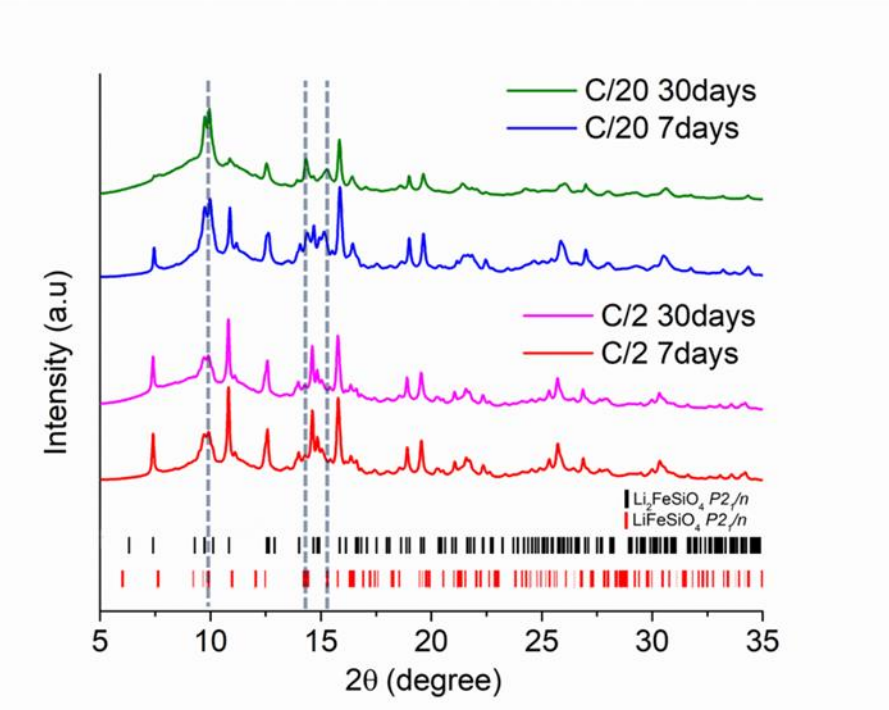

Figure 6.9. The post-mortem XRD patterns of C/2 vs. C/20 after 7 and 30 days cycling. Dashed lines indicate the new peaks which are only present in the $LiFeSiO_4$ phase. The reference patterns are shown as the stick patterns at the bottom. (Black: Li_2FeSiO_4; red: $LiFeSiO_4$)

The reduction of crystallinity relative to C0 is plotted in Fig. 6.10 with the detailed quantification results given in Table 6.2. The C/20 sample after 30 days shows a 60% reduction of crystallinity as compared to C0 while the C/2 after 30 days shows only 13% reduction. The loss of crystallinity is possibly due to a nanograining/ amorphization process, and it is more pronouced at slower rate (e.g. C/20) than at faster rate (e.g. C/2), indicating that at slower rate, there is a higher tendency for the crystalline LFS with longer-range order to convert into shorter-range order.

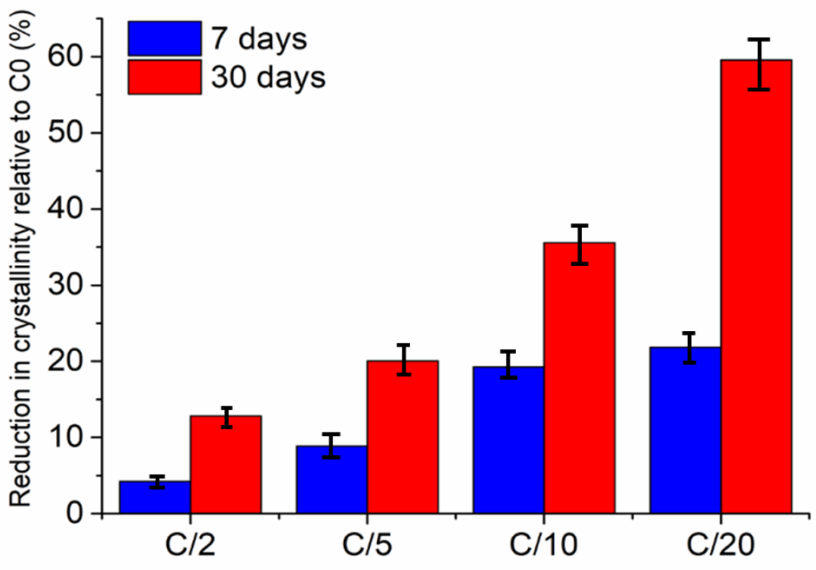

Figure 6.10. The reduction in crystallinity relative to C0 of the post-mortem samples at the rate of C/2, C/5, C/10 and C/20, after 7 and 30 days cycling.

Table 6.2. Summary of percentage of reduction of crystallinity compared to C0 at different rates, after 7 days and 30 days cycling (note that the error is within 7% confidence interval of each reported value based on three repeated calculations)

	Reduction of crystallinity relative to C0	
Rate	7 days	30 days
C/2	4%	13%
C/5	9%	20%
C/10	19%	36%
C/20	22%	60%

6.3.3 Quantification of crystal phase change

In addition to the observed reduction of crytallinity, there are crystalline phase changes as already mentioned above. These changes indicated by the shift in XRD peaks were studied using TOPAS whole pattern fitting.[129] Rietveld refinement was performed to identify and quantify the phase transformations occuring in the remaining crystalline portion (made of Li_2FeSiO_4 and $LiFeSiO_4$ as determined previously) of the cycled LFS cathode. The structural analysis was carried out based on the abovementioned assumption, *i.e.* the orthorhombic portion remains unchanged upon cycling due to the fact that it is electrochemically inactive by fixing the scale factor of the orthorhombic portion so only the changes within the monoclinic portion are discussed. In addition,

several fitting criteria are applied including the possible cation disordering of Li and Fe at the 4e1 and 4e2 sites in discharged Li_2FeSiO_4 phase with their occupancy (g) added up to 1, as the cationic mixing of Li and Fe upon cycling is commonly observed and reported by other groups[48, 75]. Based on Kojima's observation, the Li-Fe mixing is not possible at the 4e3 site due to the yield of negative g values during Rietveld refinement.[86] Therefore the chemical formula used in the fitting model can be described as $[Li_aFe_{1-a}]_{4e1}[Li_bFe_{1-b}]_{4e2}Fe_{4e3}SiO_4$ after considering the cation mixing of Li and Fe at 4e1 and 4e2 sites based on the initial formula $Li_{4e1}Li_{4e2}Fe_{4e3}SiO_4$ without Li/Fe mixing, both with the space group of *p21n*, which agrees with Kojima's fitting model.[86] For the partially delithiated monoclinic $LiFeSiO_4$ phase, the cations only exist at the 4e1 and 4e2 sites, resulting in a chemical formula as $[Li_aFe_{1-a}]_{4e1}[Li_bFe_{1-b}]_{4e2}SiO_4$ considering the Li/Fe cation disordering. The phase ratios of the monoclinic Li_2FeSiO_4 and $LiFeSiO_4$ are quantified for each cycled electrode sample. Depending on the cycling rate and cycling time, the rate of phase transformation of the monoclinic Li_2FeSiO_4 to monoclinic $LiFeSiO_4$ varies. Detailed refinement results are given in Figures 6.11-6.14. The lattice parameters (*a, b, c, β*), reliable factors (R_{wp}), site occupancy (*g*), atomic positions (*x, y, z*) and isotropic atomic displacement factors (*B*) are extracted from TOPAS and listed in the associated Tables 6.3-6.6.

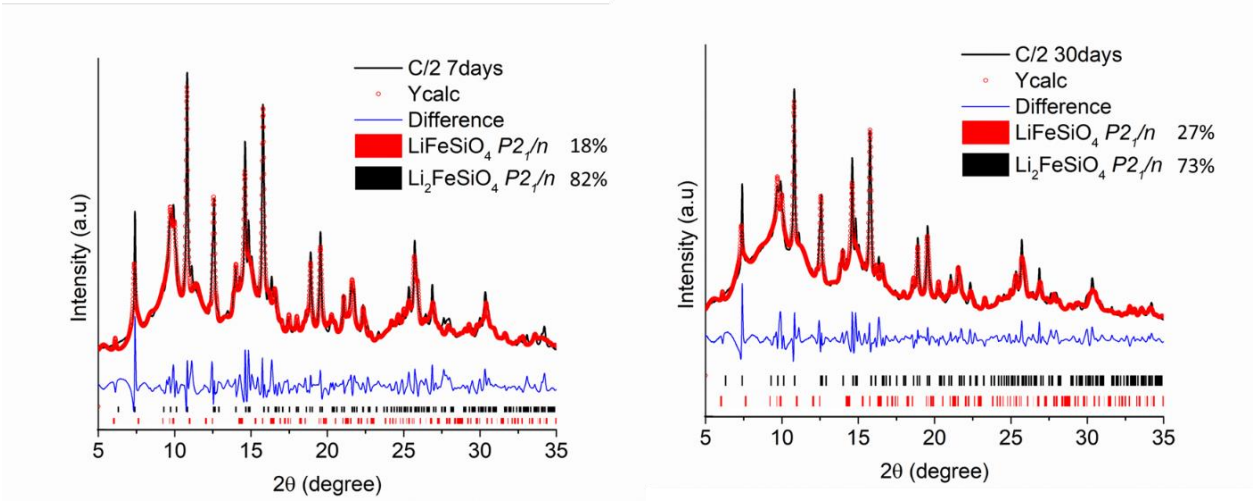

Figure 6.11. Rietveld refinement of the post-mortem samples at C/2 after 7 days (left) and 30 days (right) of cycling. 18% of the original monoclinic Li_2FeSiO_4 has been found transformed into $LiFeSiO_4$ after 7 days and 27% of the original monoclinic Li_2FeSiO_4 has been found transformed into $LiFeSiO_4$ after 30 days.

Table 6.3. The refined lattice parameters (*a, b, c, β*), reliable factors (R_{wp}), site occupancy (*g*), atomic positions (*x, y, z*) and isotropic atomic displacement factors (*B*) of the materials cycled at C/2 for 7 days (7D) and 30 days (30D) respectively

Sample Name	Phase	a, b, c, (Å)	β (deg)	Cell Volume (Å^3)	R_{wp}
C/2 7D	Li_2FeSiO_4 *p21n*	8.268, 5.223, 8.259	98.1	353.097	4.73
	$LiFeSiO_4$ *p21n*	8.273, 5.219, 8.262	102.9	347.723	
C/2 30D	Li_2FeSiO_4 *p21n*	8.272, 5.229, 8.263	98.0	353.931	4.81
	$LiFeSiO_4$ *p21n*	8.282, 5.217, 8.269	103.1	347.982	

C/2 7D	Li_2FeSiO_4 *p21n*					
Atoms	Sites	x	y	z	g	B
Li1/Fe1	4e1	0.65194	0.83125	0.68788	0.48/0.52	0.291
Li2/Fe2	4e2	0.63864	0.18572	0.10755	0.52/0.48	0.396
Li3	4e3	0.31095	0.86649	0.54767	1	0.695
Si	4e	0.03754	0.81303	0.79122	1	0.562
O1	4e	0.80557	0.75095	0.82664	1	0.406
O2	4e	0.45187	0.20114	0.76608	1	0.462
O3	4e	0.69104	0.84197	0.45715	1	0.424
O4	4e	0.96485	0.82450	0.22773	1	0.289
C/2 7D	$LiFeSiO_4$ *p21n*					
Atoms	Sites	x	y	z	g	B
Li1/Fe1	4e1	0.67854	0.83353	0.62912	0.51/0.49	0.657
Li2/Fe2	4e2	0.59928	0.19003	0.07846	0.49/0.51	0.543
Si	4e	0.03106	0.78857	0.78011	1	0.540
O1	4e	0.08517	0.69548	0.84018	1	0.683
O2	4e	0.43904	0.28964	0.89219	1	0.568
O3	4e	0.70173	0.76060	0.41124	1	0.482
O4	4e	0.95103	0.89262	0.21650	1	0.271

C/2 30D	Li_2FeSiO_4 *p21n*					
Atoms	Sites	x	y	z	g	B
Li1/Fe1	4e1	0.67347	0.75119	0.67594	0.44/0.56	0.588
Li2/Fe2	4e2	0.60148	0.16458	0.09019	0.56/0.44	0.813
Li3	4e3	0.28937	0.79374	0.54388	1	0.585

Si	4e	0.03544	0.81072	0.79692	1	0.228
O1	4e	0.86672	0.69134	0.89050	1	0.121
O2	4e	0.43139	0.22465	0.88479	1	0.139
O3	4e	0.66527	0.76541	0.43616	1	0.269
O4	4e	0.96751	0.83310	0.20333	1	0.543
C/2 30D	$LiFeSiO_4$ *p21n*					
Atoms	Sites	x	y	z	g	B
Li1/Fe1	4e1	0.64282	0.84090	0.63619	0.54/0.46	0.491
Li2/Fe2	4e2	0.58323	0.18299	0.06207	0.46/0.54	0.744
Si	4e	0.02505	0.80025	0.76308	1	0.475
O1	4e	0.86229	0.69257	0.82730	1	0.693
O2	4e	0.43274	0.23408	0.88425	1	0.475
O3	4e	0.69453	0.75855	0.40363	1	0.469
O4	4e	0.98393	0.89474	0.23954	1	0.317

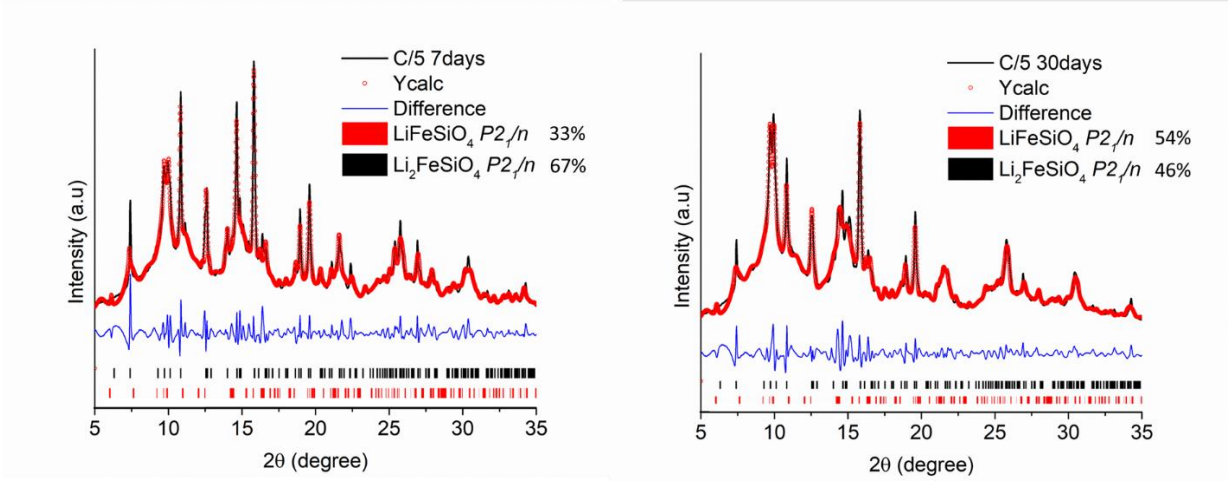

Figure 6.12. Rietveld refinement of the post-mortem samples at C/5 after 7 days (left) and 30 days (right) of cycling. 33% of the original monoclinic Li_2FeSiO_4 has been found transformed into $LiFeSiO_4$ after 7 days and 54% of the original monoclinic Li_2FeSiO_4 has been found transformed into $LiFeSiO_4$ after 30 days.

Table 6.4. The refined lattice parameters (*a, b, c, β*), reliable factors (R_{wp}), site occupancy (*g*), atomic positions (*x, y, z*) and isotropic atomic displacement factors (*B*) of the materials cycled at C/5 for 7 days and 30 days respectively

Sample Name	Phase	a, b, c, (Å)	β (deg)	Cell Volume (Å^3)	R_{wp}
C/5 7D	Li_2FeSiO_4 *p21n*	8.271, 5.228, 8.263	98.2	353.645	4.35
	$LiFeSiO_4$ *p21n*	8.276, 5.220, 8.265	102.9	348.042	

C/5 30D	Li_2FeSiO_4 *p21n*	8.275, 5.226, 8.268	98.0	354.071	3.94
	$LiFeSiO_4$ *p21n*	8.285, 5.219, 8.274	103.3	348.167	

C/5 7D	Li_2FeSiO_4 *p21n*					
atoms	sites	x	y	z	g	B
Li1/Fe1	4e1	0.65947	0.76285	0.66732	0.44/0.56	0.339
Li2/Fe2	4e2	0.58772	0.16574	0.10681	0.56/0.44	0.170
Li3	4e3	0.29857	0.79609	0.55427	1	0.874
Si	4e	0.03360	0.81198	0.78685	1	0.586
O1	4e	0.85936	0.69816	0.83270	1	0.327
O2	4e	0.42075	0.21869	0.87826	1	0.321
O3	4e	0.67306	0.79868	0.43154	1	0.570
O4	4e	0.95884	0.85382	0.22194	1	0.274
C/5 7D	$LiFeSiO_4$ *p21n*					
atoms	sites	x	y	z	g	B
Li1/Fe1	4e1	0.63085	0.82204	0.63068	0.54/0.46	0.624
Li2/Fe2	4e2	0.59079	0.18690	0.06377	0.46/0.54	0.885
Si	4e	0.02425	0.78975	0.79140	1	0.181
O1	4e	0.85705	0.68454	0.82775	1	0.537
O2	4e	0.43515	0.24150	0.88473	1	0.236
O3	4e	0.68863	0.75434	0.41345	1	0.206
O4	4e	0.96669	0.88732	0.22737	1	0.053

C/5 30D	Li_2FeSiO_4 *p21n*					
atoms	sites	x	y	z	g	B
Li1/Fe1	4e1	0.65887	0.76803	0.67169	0.41/0.59	0.911
Li2/Fe2	4e2	0.60821	0.16672	0.11096	0.59/0.41	0.845
Li3	4e3	0.29103	0.79937	0.54239	1	0.583
Si	4e	0.03469	0.81175	0.79745	1	0.158
O1	4e	0.87470	0.69460	0.82092	1	0.433
O2	4e	0.43609	0.22254	0.88003	1	0.412
O3	4e	0.67329	0.80500	0.42530	1	0.202
O4	4e	0.94463	0.87164	0.21885	1	0.575
C/5 30D	$LiFeSiO_4$ *p21n*					

atoms	sites	x	y	z	g	B
Li1/Fe1	4e1	0.64235	0.82715	0.63047	0.57/0.43	0.592
Li2/Fe2	4e2	0.57368	0.19104	0.06984	0.43/0.57	0.600
Si	4e	0.02783	0.80482	0.79441	1	0.290
O1	4e	0.86310	0.69890	0.82436	1	0.334
O2	4e	0.43439	0.23324	0.88932	1	0.789
O3	4e	0.70273	0.75527	0.40690	1	0.172
O4	4e	0.97582	0.88630	0.22026	1	0.171

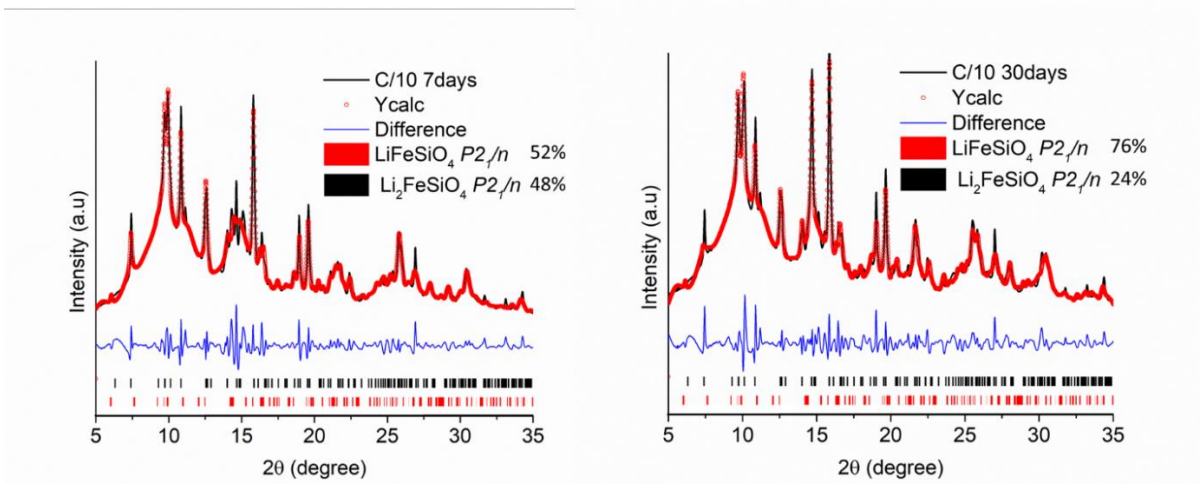

Figure 6.13. Rietveld refinement of the post-mortem samples at C/10 after 7 days (left) and 30 days (right) of cycling. 52% of the original monoclinic Li_2FeSiO_4 has been found transformed into $LiFeSiO_4$ after 7 days and 76% of the original monoclinic Li_2FeSiO_4 has been found transformed into $LiFeSiO_4$ after 30 days.

Table 6.5. The refined lattice parameters (*a, b, c, β*), reliable factors (R_{wp}), site occupancy (*g*), atomic positions (*x, y, z*) and isotropic atomic displacement factors (*B*) of the materials cycled at C/10 for 7 days and 30 days respectively

Sample name	phase	a, b, c, (Å)	β (deg)	Cell volume (Å^3)	R_{wp}
C/10 7D	Li_2FeSiO_4 *p21n*	8.276, 5.231, 8.267	98.2	354.234	4.72
	$LiFeSiO_4$ *p21n*	8.282, 5.223, 8.270	103.0	348.566	
C/10 30D	Li_2FeSiO_4 *p21n*	8.282, 5.229, 8.271	98.1	354.615	4.84
	$LiFeSiO_4$ *p21n*	8.289, 5.225, 8.276	103.4	348.676	

C/10 7D	Li_2FeSiO_4 *p21n*					
atoms	sites	x	y	z	g	B
Li1/Fe1	4e1	0.65992	0.78302	0.67331	0.38/0.62	0.342

Li2/Fe2	4e2	0.60384	0.16624	0.10675	0.62/0.38	0.829
Li3	4e3	0.28749	0.80473	0.54932	1	0.371
Si	4e	0.03392	0.80492	0.79566	1	0.593
O1	4e	0.86223	0.70490	0.82171	1	0.241
O2	4e	0.43533	0.21981	0.86031	1	0.332
O3	4e	0.67736	0.79839	0.42977	1	0.425
O4	4e	0.95414	0.87197	0.22032	1	0.249
C/10 7D	$LiFeSiO_4$ *p21n*					
atoms	sites	x	y	z	g	B
Li1/Fe1	4e1	0.64089	0.82841	0.62834	0.55/0.45	0.729
Li2/Fe2	4e2	0.58511	0.18928	0.06469	0.45/0.55	0.692
Si	4e	0.02498	0.78839	0.79413	1	0.343
O1	4e	0.86388	0.69254	0.82059	1	0.273
O2	4e	0.43381	0.23022	0.87601	1	0.293
O3	4e	0.70063	0.75682	0.41401	1	0.261
O4	4e	0.96917	0.87381	0.22699	1	0.303

C/10 30D	Li_2FeSiO_4 *p21n*					
atoms	sites	x	y	z	g	B
Li1/Fe1	4e1	0.66218	0.78723	0.67721	0.34/0.66	0.732
Li2/Fe2	4e2	0.58212	0.16936	0.10592	0.66/0.34	0.805
Li3	4e3	0.28093	0.80191	0.54837	1	0.740
Si	4e	0.03391	0.81754	0.79955	1	0.139
O1	4e	0.85909	0.69961	0.81983	1	0.253
O2	4e	0.42701	0.21923	0.87803	1	0.212
O3	4e	0.67428	0.80192	0.43349	1	0.205
O4	4e	0.95021	0.87006	0.22034	1	0.254
C/10 30D	$LiFeSiO_4$ *p21n*					
atoms	sites	x	y	z	g	B
Li1/Fe1	4e1	0.65022	0.82964	0.63174	0.60/0.40	0.782
Li2/Fe2	4e2	0.59961	0.19042	0.06984	0.40/0.60	0.746
Si	4e	0.02783	0.81488	0.80482	1	0.145
O1	4e	0.86203	0.70324	0.82369	1	0.562
O2	4e	0.43699	0.23242	0.88432	1	0.245
O3	4e	0.70273	0.78598	0.41657	1	0.276

O4	4e	0.98409	0.89962	0.21926	1	0.382

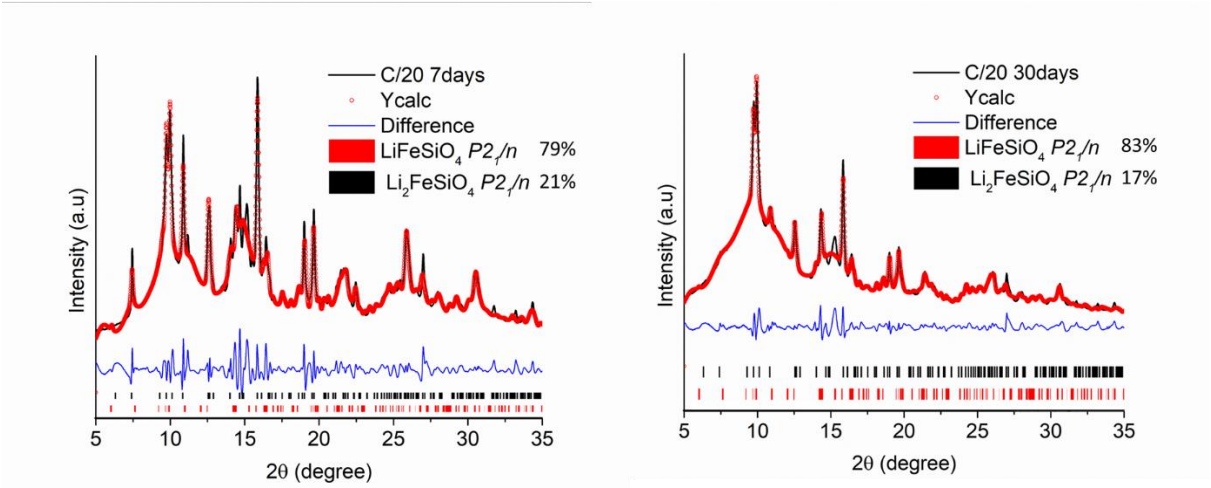

Figure 6.14. Rietveld refinement of the post-mortem samples at C/20 after 7 days (left) and 30 days (right) of cycling. 79% of the original monoclinic Li_2FeSiO_4 has been found transformed into $LiFeSiO_4$ after 7 days and 83% of the original monoclinic Li_2FeSiO_4 has been found transformed into $LiFeSiO_4$ after 30 days.

Table 6.6. The refined lattice parameters (*a, b, c, β*), reliable factors (R_{wp}), site occupancy (*g*), atomic positions (*x, y, z*) and isotropic atomic displacement factors (*B*) of the materials cycled at C/20 for 7 days and 30 days respectively

Sample name	phase	a, b, c, (Å)	β (deg)	Cell volume (Å^3)	R_{wp}
C/20 7D	Li_2FeSiO_4 *p21n*	8.280, 5.232, 8.270	98.2	354.602	5.01
	$LiFeSiO_4$ *p21n*	8.286, 5.226, 8.274	103.3	348.676	
C/20 30D	Li_2FeSiO_4 *p21n*	8.291, 5.231, 8.274	98.3	355.087	3.43
	$LiFeSiO_4$ *p21n*	8.298, 5.224, 8.282	103.7	348.801	

C/20 7D	Li_2FeSiO_4 *p21n*					
atoms	sites	x	y	z	g	B
Li1/Fe1	4e1	0.68478	0.74211	0.66729	0.32/0.68	0.762
Li2/Fe2	4e2	0.60127	0.16483	0.09612	0.68/0.32	0.645
Li3	4e3	0.28567	0.80096	0.56422	1	0.878
Si	4e	0.03631	0.80898	0.79629	1	0.145
O1	4e	0.86068	0.70911	0.82081	1	0.227
O2	4e	0.42705	0.22261	0.88206	1	0.221
O3	4e	0.67806	0.80168	0.43454	1	0.243
O4	4e	0.95841	0.87038	0.22112	1	0.254

C/20 7D	$LiFeSiO_4$ *p21n*					
atoms	sites	x	y	z	g	B
Li1/Fe1	4e1	0.63185	0.82904	0.63243	0.65/0.35	0.734
Li2/Fe2	4e2	0.58899	0.19083	0.06341	0.35/0.65	0.880
Si	4e	0.02491	0.80020	0.80122	1	0.381
O1	4e	0.87192	0.70452	0.83391	1	0.245
O2	4e	0.43581	0.23421	0.89380	1	0.221
O3	4e	0.70025	0.77494	0.42905	1	0.206
O4	4e	0.98685	0.89691	0.22984	1	0.250

C/20 30D	Li_2FeSiO_4 *p21n*					
atoms	sites	x	y	z	g	B
Li1/Fe1	4e1	0.67931	0.78036	0.68396	0.29/0.71	0.762
Li2/Fe2	4e2	0.60892	0.16878	0.10962	0.71/0.29	0.607
Li3	4e3	0.28504	0.79991	0.54393	1	0.508
Si	4e	0.03512	0.81358	0.79797	1	0.288
O1	4e	0.86479	0.71406	0.82819	1	0.333
O2	4e	0.42731	0.21851	0.88239	1	0.412
O3	4e	0.68329	0.78533	0.42391	1	0.398
O4	4e	0.94636	0.87148	0.22283	1	0.576
C/20 30D	$LiFeSiO_4$ *p21n*					
atoms	sites	x	y	z	g	B
Li1/Fe1	4e1	0.65246	0.83815	0.63437	0.70/0.30	0.607
Li2/Fe2	4e2	0.57367	0.18907	0.06303	0.30/0.70	0.643
Si	4e	0.02691	0.80528	0.78992	1	0.207
O1	4e	0.86268	0.69642	0.82682	1	0.287
O2	4e	0.43622	0.23570	0.89221	1	0.234
O3	4e	0.71117	0.77291	0.40921	1	0.272
O4	4e	0.97210	0.89212	0.22941	1	0.230

The Rietveld refinement results of the cycled samples showing the different ratios of monoclinic Li_2FeSiO_4 vs. $LiFeSiO_4$ are summarized in Figure 6.15. By comparing the fractions of Li_2FeSiO_4 and $LiFeSiO_4$ phases at different C rates, it is noticed that at slower rate such transformation towards $LiFeSiO_4$ is more significant than at faster rate. At C/20, the conversion of

monoclinic Li_2FeSiO_4 to $LiFeSiO_4$ after 7 days reached 21% Li_2FeSiO_4 : 79% $LiFeSiO_4$ compared to the starting 88% Li_2FeSiO_4 :12% $LiFeSiO_4$. After 30 days of cycling at C/20 the ratio becomes 17% Li_2FeSiO_4 : 83% $LiFeSiO_4$, indicating the transformation from the monoclinic Li_2FeSiO_4 towards $LiFeSiO_4$ is almost complete with the space group symmetry remaining the same. By comparing the XRD patterns of the C/20-7 days sample and C/20-30 days sample, it is deduced that the cycled $LiFeSiO_4$ phase represented by the new doublet peak at around 10° keeps growing in intensity and gradually becomes more predominant while the original Li_2FeSiO_4 phase peaks diminish gradually (see Figure 6.14 above).

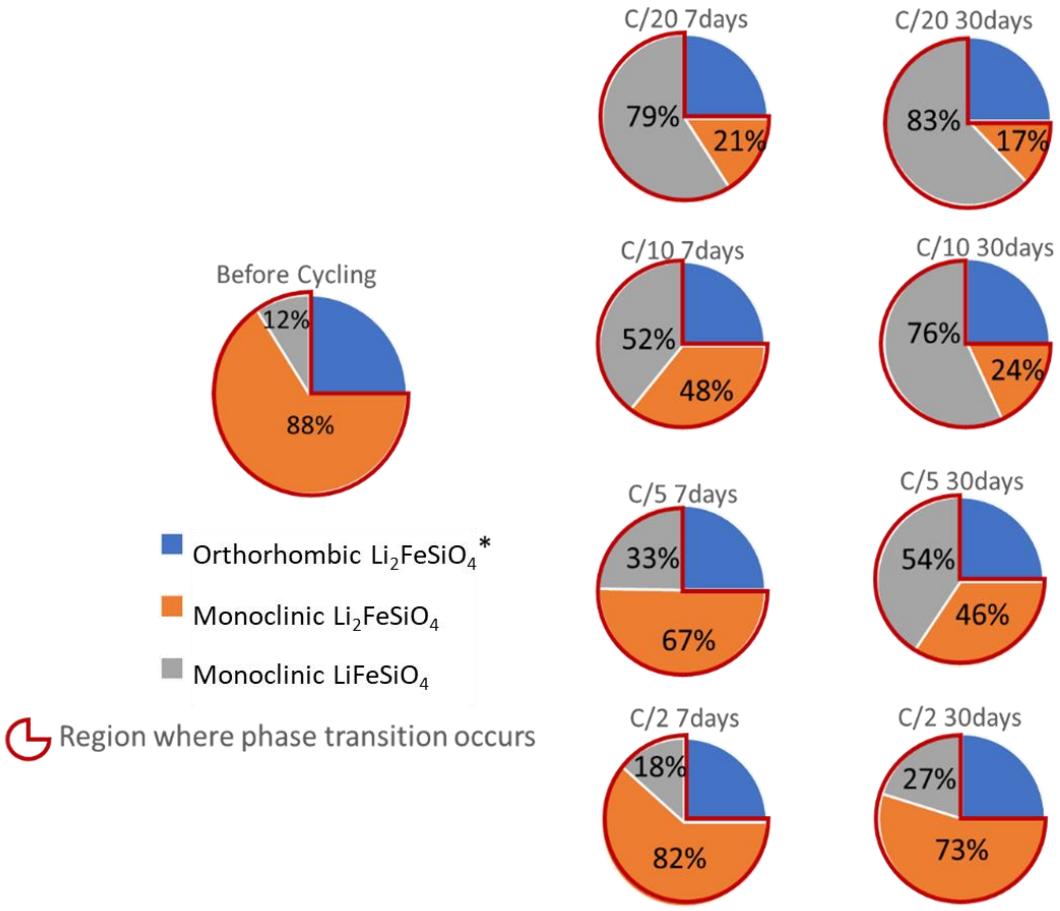

Figure 6.15. Schematic summarizing the approximate quantification of phase conversion of monoclinic Li_2FeSiO_4 towards $LiFeSiO_4$ after cycling at four different C rates for 7 days and 30 days. *Note that the initial 25% orthorhombic Li_2FeSiO_4 is assumed to remain unchanged and therefore it is left out from the total percentage for simplicity. (weighted profile R-factor, or *Rwp* [130] typically around 4-5 for the phase quantification) Also note that the schematic only

summarizes the changes in the crystalline portion of the LFS samples. The reduction of crystallinity/partial disordering of the structure is presented in Fig. 6.10 above.

In addition to the overall phase ratio changes of monoclinic Li_2FeSiO_4 and $LiFeSiO_4$ phases at different C rates, there are several other interesting observations from the changes of lattice parameters and cationic mixing, as revealed from the data listed in the Tables 6.3-6.6 above. Firstly, it is observed by comparing the lattice parameters that the lattice unit cell expands along the a and c axes upon cycling but not as significnt along the b axis, and the angle β between a and c axes also increases, resulting in a slighted distorted unit cell with certain volume expansion. 3-D schematics indicating the structure changes within a given unit cell are presented in Figures 6.16 and 6.17. Depending on the cycling rates, it is observed that the volume expansion increases with longer cycling time associated with slower C rates. (Cell volumes are calculated and presented in the Tables 6.3-6.6 above.) In additon, more cationic disordering at Li-Fe sites is observed with longer cycling time and slower C rates.

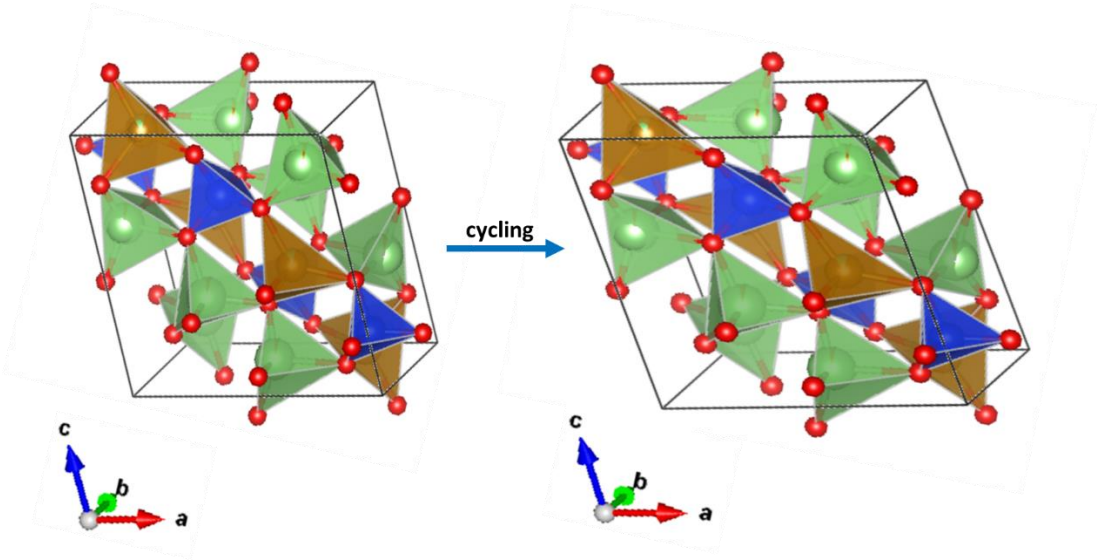

Figure 6.16 Cycling-induced lattice distortion in the monoclinic Li_2FeSiO_4 phase.

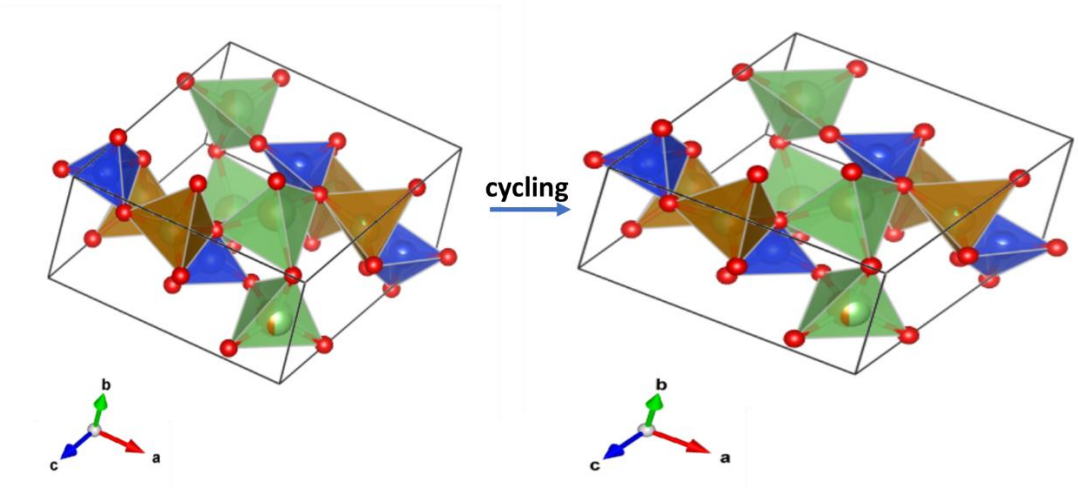

Figure 6.17 Cycling-induced lattice distortion in the monoclinic $LiFeSiO_4$ phase.

It must be noted here that according to the different rate cycling data collected, the rate C/20 at 45°C cycling temperature applied was found to represent a threshold condition for the cathode in undergoing the above described complex structrural changes without failure of the cell. Thus, when the cycling rate was reduced to C/50 (at 45°C cycling always) the cell failed within the first week of cycling. It is hypothesized at this point that the failure at low rate may be linked to full irreversible conversion of crystalline Li_2FeSiO_4 to $LiFeSiO_4$, although the root cause for this behavior is unclear. Based on the data of Figure 6.15, failure is triggered when the crystalline fraction of Li_2FeSiO_4 is less than 17% or conversely the relative crystalline fraction of $LiFeSiO_4$ is more than 83%. By contrast, when the cycling rate was faster than C/20, less conversion towards $LiFeSiO_4$ was observed with time and this was associated with longer cycle life (refer to Figures 6.4 b,d and 6.5 b,d). Considering the case where the cycling rate is C/2, only 18% of $LiFeSiO_4$ is seen to have formed after 7 days and 27% after 30 days (Fig. 6.11 above). The major peaks of the original Li_2FeSiO_4 phase remain even after 30 days of cycling, with the relative peak intensity of the new doublet peak at 10° representing the cycled $LiFeSiO_4$ phase remaining lower than the intensity of the original Li_2FeSiO_4 peaks. Under this condition, a much longer cycle life is observed albeit at a lower accessible capacity of ~ 40 mAh/g. For the case of C/5, 33% of $LiFeSiO_4$ is observed after 7 days and 54% after 30 days; for the case of C/10, 52% of $LiFeSiO_4$ is observed after 7 days and 76% after 30 days.

6.3.4 Mechanism discussion

By comparing the different phase ratios at different cycling rates, a higher tendency of the orginal monoclinic Li_2FeSiO_4 phase converting to $LiFeSiO_4$ at slower cycling rate is observed. One possible explanation is that at faster cycling rate the material is at metastable state and there is no sufficient time for the conversion from Li_2FeSiO_4 to $LiFeSiO_4$ to take place[88]; while at slower cycling rate the transformation from Li_2FeSiO_4 to $LiFeSiO_4$ reaches essentially equilibrium upon the first few cycles. Secondly, since the post-mortem samples were obtained at the end of discharging and theoretically the major phase is expected to be Li_2FeSiO_4, the fact that a signicant amount of $LiFeSiO_4$ was found to be present instead, can be taken as indication that the transformation from Li_2FeSiO_4 to $LiFeSiO_4$ is rather irreversible, *i.e.* re-lithiation of $LiFeSiO_4$ is not favorable. Kojima et al. who also reported the presence of $LiFeSiO_4$ at the end of discharging did not run but only the first two cycles not providing information on the structural changes upon longer cycling or for that matter at different rates as done here.[86] Since the formed $LiFeSiO_4$ phase seems not to reversibly convert back to Li_2FeSiO_4 and it represents 83% of the crystalline fraction of discharged LFS after 30 days cycling at C/20, the question arises as to how the charging/discharging capacity stabilizes at 147 mAh/g (per gram of original amount of monoclinic LFS or 89% of 1 Li storage) without any noticeable loss of capacity. This apparent paradox can be understood on the basis of the observed loss of crystallinity (introduction of disordering).

To recap from the post-mortem sample analysis, it becomes evident that the LFS cathode undergoes two structural transformation reactions, *i.e.* the irreversible crystal transformation of monoclinic Li_2FeSiO_4 to monoclinic $LiFeSiO_4$ plus the parallel disordering of Li_2FeSiO_4 (manifested as gradual loss of crystallinity) upon cycling. The kinetics of the first type of transformation are dependent on the applied current (C rate) during cycling being more pronouced at slower rate (C/20). Since this type of transformation seems to be irreversible, it then must be the other type of transformation that of long-range order Li_2FeSiO_4 converting to the disordered (short-range ordered) Li_2FeSiO_4 contributing to the reversible capacity (~140 mAh/g at C/20) by accommodating Li and providing short Li-ion diffusion pathways. In fact, such short range order or crystal disordering has been recently demonstrated to accommodate high Na-ion intercalation storage in another polyanionic cathode material, $NaFePO_4$ [131-132] and spinel $LiNi_{0.5}Mn_{0.5}O_4$ material. [133] In both cases however, such disordering was induced either by mechanical milling or by applying different

synthesis conditions while in the present case, it is thought to result from intra-particle strain induced during the cycling-triggered phase change events.

The schematic in Figure 6.18 is an attempt to visualize this complex sequence of events. It is suggested the disordering/re-nucleation reversible reaction of Li_2FeSiO_4 upon each charging/discharging cycle competes with the irreversible heterogeneneous nucleation and crystal growth of the new (inert) $LiFeSiO_4$ phase. At slower rate, the $LiFeSiO_4$ is more likely to form because there is sufficient time to allow crystal nucleation and growth of the $LiFeSiO_4$ phase as more Li ions are extracted from the cell. At faster rate, the LFS particle capacity is not fully reached (*i.e.* less Li ions being extracted/inserted which reduces the capacity but without sacrificing the Coulombic efficiency) while there is insufficient time for nucleation and growth of the $LiFeSiO_4$ phase. It is also important to note that at a fast rate, the inner core region of a crystal grain is unlikely to be intercalated with the reactions happening near the surface only, while at slow rate the core region is intercalated because Li has sufficient time to migrate deeper into the crystal.

Evidence for the strain-induced disordering suggested above as a collateral event of the formation of the $LiFeSiO_4$ phase is provided with the TEM data in Figure 6.19. TEM images of the partially delithiated LFS C0 post mortem sample show significant amount of stacking faults even before the cycling starts (Figure 6.19 (b, c)). The stacking faults can be seen as partial dislocation of certain planes due to high inner grain stress from the new $LiFeSiO_4$ phase. In addition, such stacking fault formation may introduce nanograin boundaries on the original Li_2FeSiO_4 crystals and divide them into smaller crystals giving rise to more extended disordering in Li_2FeSiO_4.

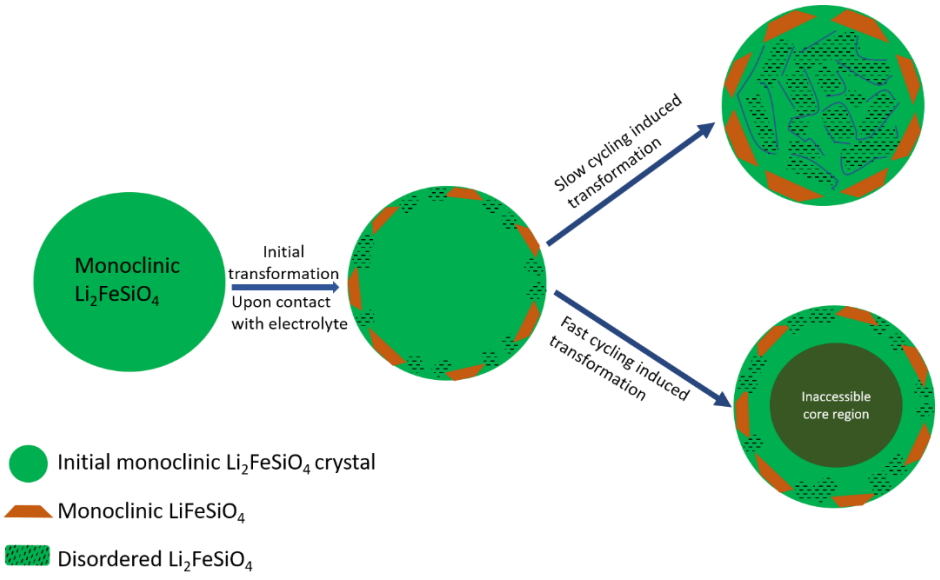

Figure 6.18. Schematic depicting LFS700 transformation events in terms of crystal disordering (dotted region) and structural transformation of monoclinic Li_2FeSiO_4 to $LiFeSiO_4$ (brown region). Initial formation of $LiFeSiO_4$ is observed upon contact with electrolyte, accompanied by some degree of crystal disordering before cycling starts and such reaction is expected to occur near surface. Upon cycling at slow rate, siginicant loss of crystallinity and a high tendency for $LiFeSiO_4$ formation is observed. The $LiFeSiO_4$ phase is allowed sufficient time to grow bigger and reach the inner region of the grain, dividing the original Li_2FeSiO_4 crystal into smaller regions that can further break the long range order of the structure. At fast rate, less loss of crystallinity is observed and the $LiFeSiO_4$ phase does not have sufficent time to grow. In the latter case the inner core region remains inaccessible in terms of Li-ion diffusion but stable the overall particle-crystal in terms of cyclability.

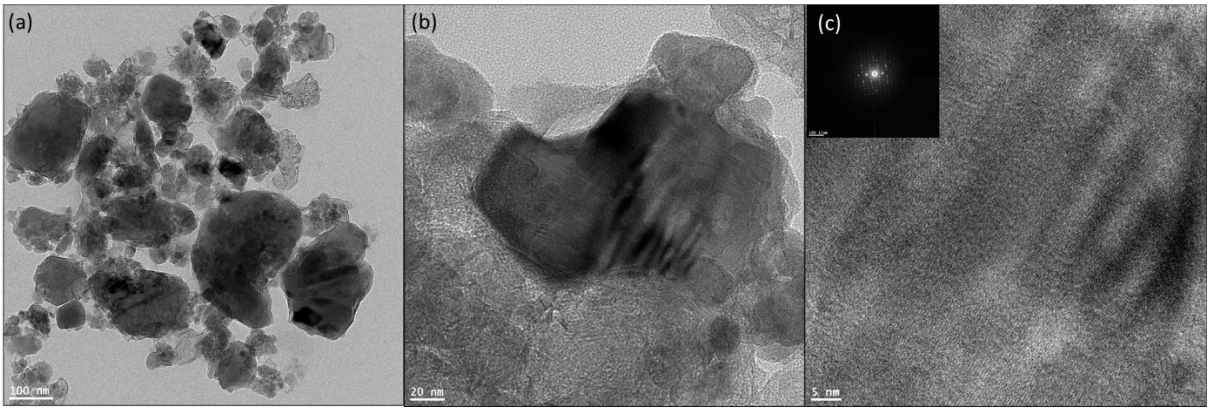

Figure 6.19. (a) TEM image of recovered particles from C0 electrode after treatment in NMP solvent to remove the PVDF binder. (b) Contrasting dark striped regions attributed to high lattice strain. (c) Vertical lines in the SAED pattern (inset) indicate the presence of stacking faults in the crystal structure.

6.3.5 Summary

In this Chapter the long-term electrochemical behaviour of the LFS700 was studied and discussed in detail. From the synchrotron XRD analysis of post-mortem samples collected at different times and rates, a complex structural evolution picture was revealed manifested as a combination of irreversible crystal transformation of monoclinic $Li_2Fe^{II}SiO_4$ to monoclinic $LiFe^{III}SiO_4$ (inert) and simultaneous introduction of crystal disordering. Judging from the long-term capacity retention behavior, the introduced crystal disordering is considered to have a beneficial effect to cycling stability counter balancing at least partially the irreversible transformation from $Li_2Fe^{II}SiO_4$ to inert (in terms of intercalation) monoclinic $LiFe^{III}SiO_4$. Such behaviour starts at the pre-cycling stage and becomes more pronounced as the cycling continues. The kinetics of these structural transformations are dependent on the applied cycling rates, with slower rates promoting more the irreversible formation of $LiFe^{III}SiO_4$ than faster cycling rates. The results of this study provide significant new insight in understanding the complex dynamic material chemistry of Li_2FeSiO_4 cathodes.

Chapter 7 Study of Manganese-substituted Lithium Iron Silicate

In the previous chapters, the lithium iron silicate compound has been studied in terms of its crystallization and structural properties, electrochemical behavior and cycling-induced changes. The aim of the present chapter is to examine the effect of Mn substitution on $Li_2Fe_{1-x}Mn_xSiO_4$ (LFMS) redox intercalation reactions.

As discussed in Chapter 2, the Mn-Fe mixed lithium metal silicates have attracted interest[34, 48, 52] due to the thermodynamically easier accessibility of Mn^{IV} than Fe^{IV} that is required to have > 1 Li exchange and storage.[134] This is reflected in the potential required for the second Li extraction (Equation 7.2 below), namely 4.5V for Mn^{III}/Mn^{IV} vs. 4.8V for Fe^{III}/Fe^{IV}. The respective intercalation reaction steps and theoretically calculated potentials are presented in the following equations:[33,134]

$$Li_2M^{II}SiO_4 \rightarrow LiM^{III}SiO_4 + Li^+ + e^-,\ E\ (vs.\ Li/Li^+) = 3.15V\ (Fe)\ or\ 4.1V\ (Mn) \quad (7.1)$$

$$LiM^{III}SiO_4 \rightarrow M^{IV}SiO_4 + Li^+ + e^-,\ E\ (vs.\ Li/Li^+) = 4.8V\ (Fe)\ or\ 4.5V\ (Mn) \quad (7.2)$$

However, the published experimental studies report contradictory results as is for example the works of R. Chen *et al.*[33], who found LFMS to suffer from serious amorphization and capacity fade while Zhang *et al.*[82] reported stable cycling and good capacity retention. The explanation provided by the latter group for the better performance was the nanoplatelet crystal morphology. However, while such morphological feature can influence the kinetics there is still lack of clear understanding of the underlying redox chemistry and associated phase transitions in the mixed metal (Fe, Mn) silicate structure. This is important to elucidate for progress to be made with the further development of these potentially high energy density cathode materials.

In this context, mixed lithium iron manganese silicates were synthesized by employing the newly developed process described in Chapter 4, which after characterization to confirm they are solid solutions and not mere mixtures of the single metal silicates, were galvanostatically tested while simultaneously monitoring *in situ* or post mortem their first cycle structural and chemical transformations.

7.1 Synthesis and characterization of $Li_2Fe_xMn_{1-x}SiO_4$ compounds

The lithium iron manganese silicate samples were synthesized using the method described previously in Chapters 3 & 4. The synthesis protocol of producing mixed lithum iron manganese silicate is analogous to the synthesis of pure lithium iron silicate by stoichiometrically substituting manganese salt for part of iron salt when preparing the precursor solution. Following the initial hydrothermal step and removal of water the obtained intermediate precipitate was subjected to annealing at various temperatures and at different Fe to Mn ratios followed by structural and morphological characterization.

7.1.1 The Effect of Mn/Fe Ratio on Crystal Phase Composition

The first series of synthesized LFMS materials were annealed at 700°C at different Fe to Mn molar ratios had the following nominal composition: $Li_2Fe_{0.75}Mn_{0.25}SiO_4$, $Li_2Fe_{0.5}Mn_{0.5}SiO_4$, $Li_2Fe_{0.25}Mn_{0.75}SiO_4$, and Li_2MnSiO_4. This annealing temperature, 700 °C , was selected to be the same as that of LFS700, whose structural changes during cycling were investigated in the previous Chapter 6 so to provide a direct head-to-head comparison with the Mn-substituted counterparts. Moreover, 700°C has been the commonly studied annealing temperature[36, 54, 56] allowing for broader comparison and discussion of the results of this investigation. An important question this series of tests sought to answer is to what extent structurally these mixed metal silicates are characterized by homogeneous cationic mixing of Fe and Mn in a solid solution form versus formation of Li_2FeSiO_4 and Li_2MnSiO_4 in separate domains of the crystalline product. This was verified by examining their XRD patterns using synchrotron X-ray source (λ=0.6886Å), which are presented in Figure 7.1. All peaks can be seen to correspond to LMS crystalline phase peaks (with major peaks in low angle region labelled with blue four-pointed stars) with no apparent evidence of impurties validating the effectiveness of the newly developed synthesis method. On the same Figure, zoomed-in views of selected lower-angle regions of major diffraction peaks are provided as well, where a slight shift in 2-theta peak position is observed. This peak shift indicates a change in lattice parameter as the Fe:Mn ratio changes, due to the larger ionic radius of Mn^{2+} than Fe^{2+} (2.42Å vs. 2.26Å)[135] as a result of stronger electrostatic interaction between the nucleus and the outer electron cloud in Fe^{2+} than Mn^{2+}. The lattice parameter increase as the Mn fraction increases, resulting in a decrease in 2-theta is in agreement with Bragg's law, i.e. $n\lambda=2d\sin\theta$, where the interplanar spacing d increases as the Mn^{2+}

fraction increases, Therefore this angle shift in XRD peaks can be regarded as an evidence of interstitial cationic mixing inside the lattice, i.e. solid solution formation. This finding agrees with previously reported results where similar XRD peak shifts with varying Fe: Mn ratio in the mixed lithium Fe-Mn silicate were also observed.[54, 56]

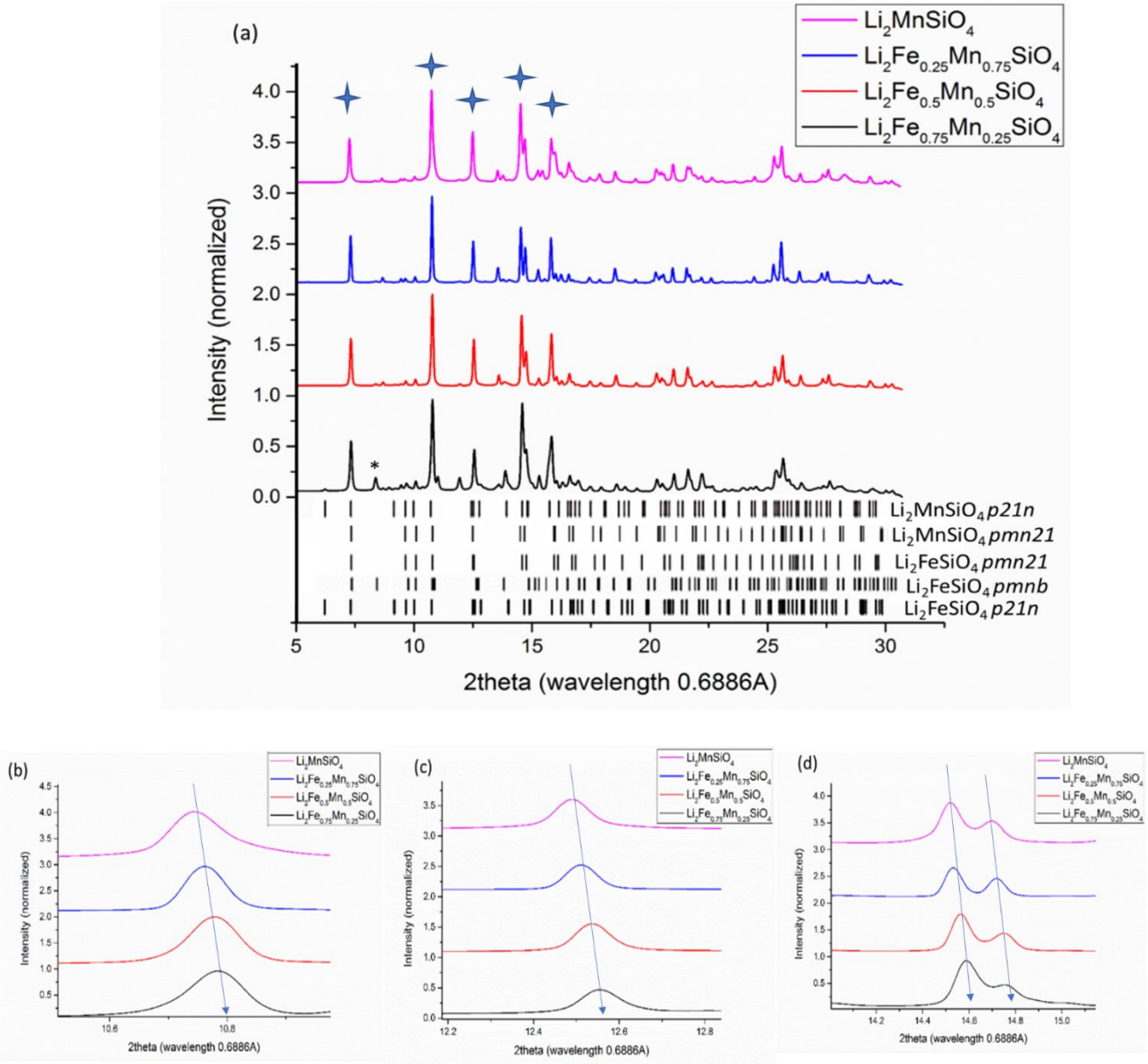

Figure 7.1 (a) The full XRD patterns and (b,c,d) the zoomed-in 2 theta regions of $Li_2Fe_{1-x}Mn_xSiO_4$ materials with composition varying from x=0, 0.25, 0.5, and 0.75, to 1.

As previously mentioned in Chapter 2, LFMS forms different polymorphs as in the case of LFS, the formation of which is temperature-dependent starting from the low-T orthorhombic phase, *pmn21,* to high-T monoclinc phase, *p21n* and finally to high-T orthorhombic phase, *pmnb*.[36] Moreover it has been reported that as the Mn content in LFMS increases, the phase transition temperature increases as well due to the fact that Li_2MnSiO_4 has higher phase transition temperature than Li_2FeSiO_4.[36] Similar trend was observed in the present work. Thus according to the Rietveld refinement results presented in Chapter 4, the synthesized at 700°C Li_2FeSiO_4 (LFS700) is made of approximately 75% *p21n* and 25% *pmnb*. However, when the XRD patterns of LFMS are examined in Figure 7.1(a), the *pmnb* signature peak (marked with *) dimishes as the Mn fraction increases. To quantify the phase ratio in LFMS, the equimolar $Li_2Fe_{0.5}Mn_{0.5}SiO_4$ compound (sample named LFMS700, tested at λ=0.6886Å) was chosen for Rietveld refinement analysis. Based on the refined XRD pattern presented in Figure 7.2, it is found that the LFMS700 compound consists of approximately 59% *p21n* and 41% *pmn21* phase (fitting error within 3%). The lattice parameters of the *p21n* phase and *pmn21* phase are listed in Table 7.1 below and are compared to previously reported results by Longo *et al*.[136] and Chen *et al*.[33] It is noticed that the lattice parameters of the *pmn21* phase are fairly consistent between our results and the results reported by the other two groups while the *p21n* phase shows somehow discrepancies among all three results. Interestingly R. Chen *et al.*[33] also reported their $Li_2Fe_{0.5}Mn_{0.5}SiO_4$ annealed at 700°C to be made of the same mixed polymorphs (*p21n* and *pmn21*) but without quantifying their relative ratios. In other words it is verfied that at 700°C the (high-T orthorhombic) *pmnb* phase gradually decreases as Fe concentration decreases and replaced by the (low-T orthorhombic) *pmn21* phase that is thermodynamically favored in Li_2MnSiO_4.[38] This trend of phase transition agrees with the results reported by Sirisopanaporn *et al.*[36]

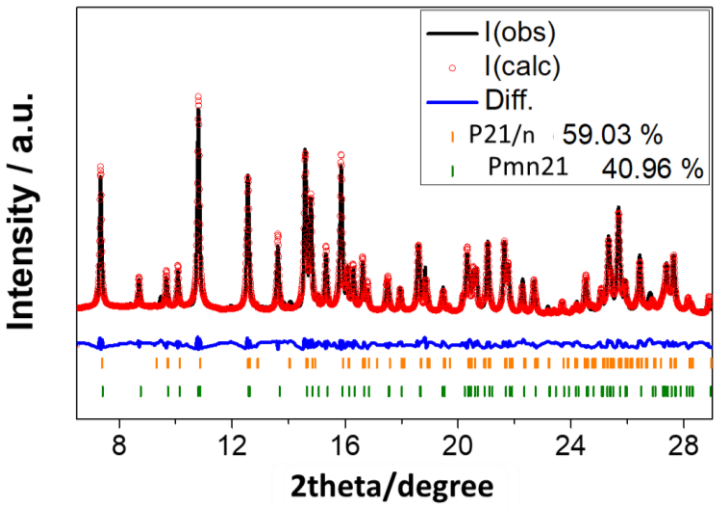

Figure 7.2. The Rietveld refinement of $Li_2Fe_{0.5}Mn_{0.5}SiO_4$ compound. The black line represents the experimental XRD pattern and the red bubble curve represents the fitted pattern. The blue line represents the difference. The peak positions of the reference patterns are shown in the yellow and green stick patterns.

Table 7.1 Lattice parameters of $Li_2Fe_{0.5}Mn_{0.5}SiO_4$ and comparison with previously reported results by Longo *et al.*[136] (DFT calculated results) and Chen *et al.*[33] (experimentally prepared sample), note that unit is in Å for all values.

	a	b	c	β	V	R_{wp}
p21n	8.242	5.017	8.244	99.19	84.13	2.18
pmn21	6.280	5.347	4.970	90.00	83.46	
p21n (Longo)	4.139	4.868	8.283	101.15	81.89	-
pmn21 (Longo)	6.339	5.274	4.864	89.99	81.31	
p21n(Chen)	6.986	8.030	5.990	95.19	83.68	0.74
pmn21(Chen)	6.284	5.391	5.015	-	84.96	

7.1.2 The Effect of Annealing Temperature on Crystal Phase Composition

Having confirmed that the newly synthesized LFMS compounds at 700°C are in solid solution form, next the effect of annealing temperature on crystal phase composition of the equimolar $Li_2Fe_{0.5}Mn_{0.5}SiO_4$ compound was investigated. The annealing temperature was varied from 400°C to 1000°C at intervals of 150°C with 6 hours holding time and the corresponding produced silicates are labeled LFMS400, LFMS550, LFMS700, LFMS850 and LFMS1000. The

XRD patterns (tested at λ=0.6886Å) of the mixed metal silicates produced at different annealing temperatures are presented in Figure 7.3. An increase of crystallinity is observed as annealing temperature increases, as judged from the sharpening and better resolution of the diffraction peaks. Although even at 400°C crystalline structure has apparently formed the lack of peak intensity and the presence of background suggests the LFMS400 and LFMS550 to be nanocrystalline. Fully developed crystal structure can be observed with the LFMS700 material implying the crystallization process is complete after 6 hours of annealing at 700°C. Other than evolution of crystallinity with increasing temperature there can be seen phase transitions to occur as revealed from the change in XRD peaks in the 10° to 15° region (Figure 7.3(a) blue region, or zoomed-in view in 7.3(b)). The monoclinic signature peak at 13° (marked with * in the orange shaded region) corresponding to the (112) plane was absent in LFMS400 and LFMS550 products, indicating the absence of *p21n* phase at low temperature. Instead at the lower temperature range the *pmn21* phase dominates. The monoclinic signature peak at 13° becomes clearly pronounced at 700 °C and 850°C, however diminises again at 1000 °C. At the latter temperature the *pmnb* phase is seen to dominate. This change in crystal phase composition is in agreement with previous findings as discussed in Chapter 2 (refer to Figure 2.7).[44]

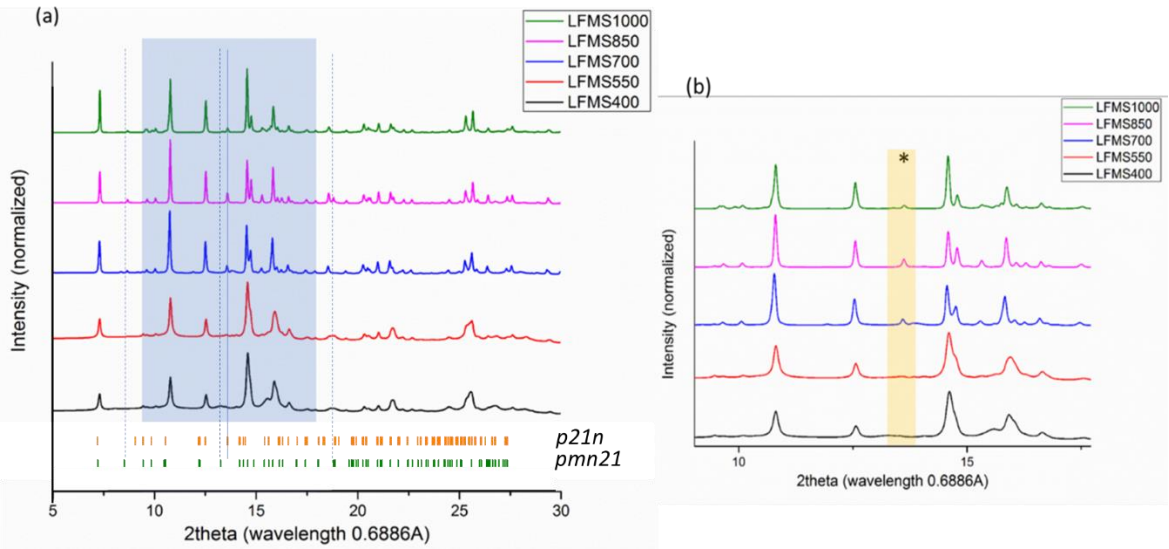

Figure 7.3 (a) The full powder XRD patterns and (b) the zoomed-in region of the LFMS obtained at different annealing temperatures. The blue shaded region in (a) indicates the zoomed-in region and the orange shaded region in (b) signifies the signature monoclinic peak corresponding to characteristic plane (112) (marked with *). Additional peaks that differentiate the monoclinic (*p21n*) and orthorhombic (*pmn21*) phases are labelled with thin blue lines in (a).

7.1.3 LFMS Crystal Morphology

The pristine $Li_2Fe_{0.5}Mn_{0.5}SiO_4$ (LFMS700) material was characterized in terms of particle morphology and elemental compsition SEM images of the pristine material are shown in Figure 7.4 (a,b). The material is in largely aggregated state with primary particle size ranging around 100 nm-200 nm. TEM combined with EELS performed at Hydro-Quebec's IREQ Institute by fellow student F. Voisard yielded the data presented in Figure 7.4 (c). As it can be deduced from the elemental maps on a single nanoparticle there is full intermixing of Mn and Fe with no evidence of segragation confirming the XRD conclusion that LFMS is in solid solution. Would be interesting in future work to seek elucidate the different nanodomains of the two polymorphs, *p21n* and *pmn21*, of which LFMS is made as seen in the previous section.

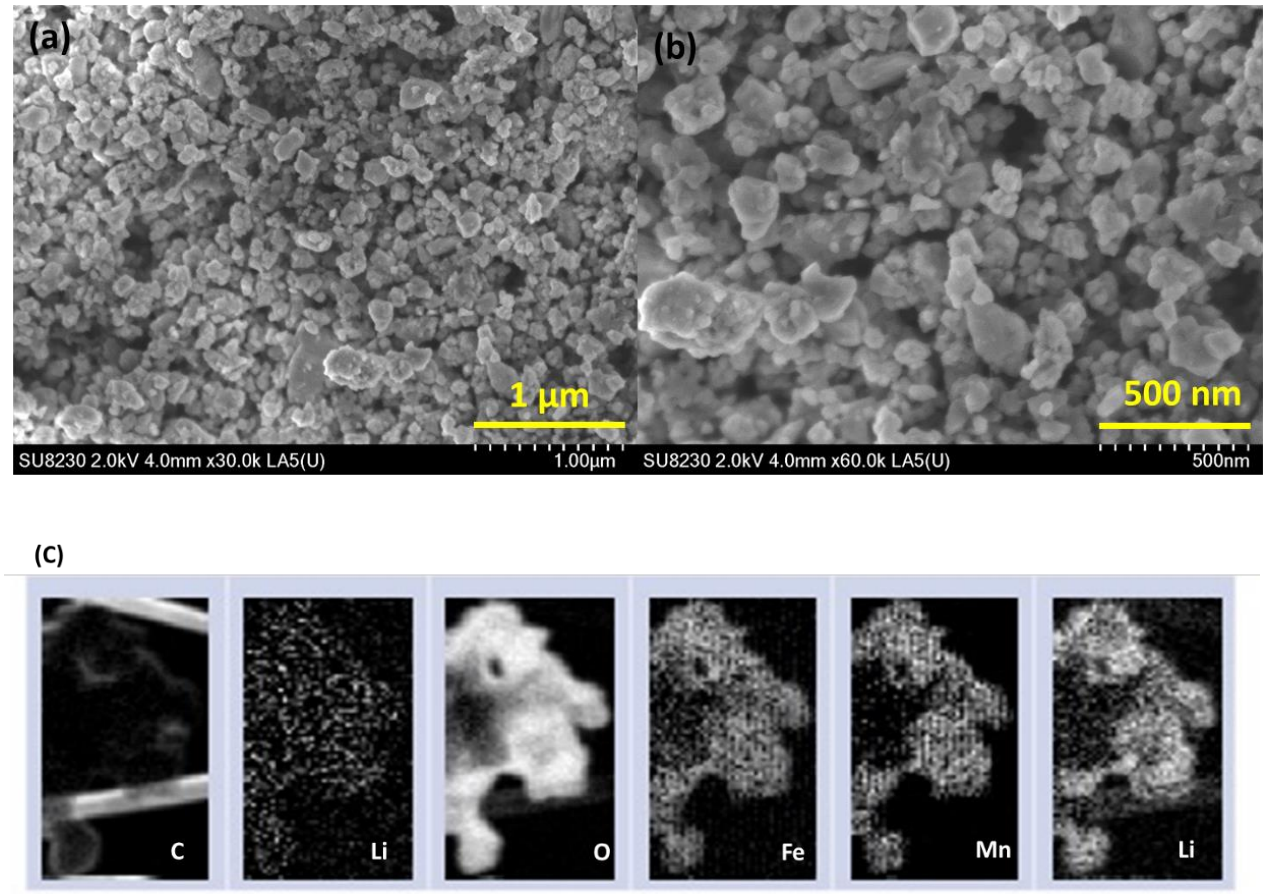

Figure 7.4. (a,b) Secondary electron microscopic images of $Li_2Fe_{0.5}Mn_{0.5}SiO_4$ (LFMS700) material. (c) TEM image and elemental maps of single LFMS particle (F. Voisard).

7.2 Structural and redox evolution during initial charging/discharging

7.2.1 Charge vs. discharge behavior

The pristine equimolar $Li_2Fe_{0.5}Mn_{0.5}SiO_4$ (LFMS700) material was subjected to one and a half cycle galvanostatic charging-discharging-charging while monitoring *in-situ or post mortem* its chemical and structural changes in order to probe the redox reaction sequence of Fe and Mn in connection to the extent of Li-ion extraction and insertion. The *in-situ* analysis was performed at Canadian Light Source (CLS) using a modified coin cell as described in Chapter 3 (Figure 3.2). The LFMS material was fabricated into electrode in the same manner as the LFS material (details in Chapter 3) however without ball-milling it in this case. The paste mixture had the standard composition of LFMS/carbon/PVDF of 8:1:1. The cell was tested at C/40 and 55°C over the voltage range 1.5 V to 4.6 V. After the formation (first) cycle and the second charging cycle, the test was stopped during the second discharging cycle at 2.75 V, as the current study focused on the formation cycle out of necessity due to limited access to beamline (one cycle and a half taking a full week, ~100 hours). The galvanostatic charging/discharging curves are presented in Figure 7.5. On the same graph are marked different states of charging (C0 to C5) and discharging (D1 to D4) where *in situ* and *post-mortem* X-ray characterization was performed and described in the following section.

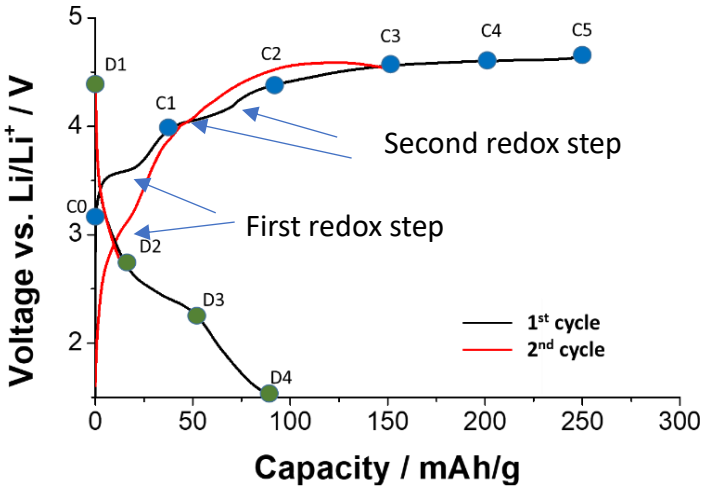

Figure 7.5. The galvanostatic charging and discharging curves of the $Li_2Fe_{0.5}Mn_{0.5}SiO_4$ (LFMS700) electrode at C/40 and 55°C. Black curve represents the first (formation) cycle and the red curve represents the second cycle (unfinished). The colored dots represent different charging/discharging states during the initial cycle where *post-mortem* and *in situ* analysis was performed.

Upon examining the initial charging curve, two quasi-plateaus (indicated with arrows) may be noticed at ~3.6 V and ~4.2 V (vs. Li/Li^+) that can be attributed respectively to the Fe^{II}/Fe^{III} and Mn^{II}/Mn^{III} couples associated with first Li-ion extraction (equation (7.1)). The corresponding theoretical potentials (refer to equation (7.1)) are 3.15 V and 4.1 V.[33, 134] The much higher potential registered for the Fe^{II}/Fe^{III} indicates large polarization. In contrast negligible polarization is linked to the Mn^{II}/Mn^{III} couple. A significant amount of the Fe^{II}/Fe^{III} polarization though was removed during the second charge: ~3.05 V vs. 3.6 V, an observation that is common in the case of LFS and attributed to phase transition from *p21n* to inverse *pmn21*.[76] Meanwhile upon examining the first discharge curve (D1 to D4) only one quasi-plateau can be discerned at ~2.7 V (D2 point) that should be attributed to Fe^{III}/Fe^{II} as it occurs in LFS.[89]

Another interesting observation that can be made examining the data in Figure 7.5 is that during the formation cycle, an exceptionally high charging capacity around 250 mAh/g (1.5 Li) was achieved corresponding to the following charged LFMS formula $Li_{0.5}Fe_{0.5}Mn_{0.5}SiO_4$ (1 Li corresponds to 166 mAh/g). However, the first discharging capacity was only 90 mAh/g (or 0.54 Li), followed by a charging capacity of 150 mAh/g (or 0.9 Li) during the second charge. This indicates extensive degree of irreversibility. It is interesting that similar assymetric behaviour in terms of large charge capacity vs. much lower discharge capacity in the first cycle has been reported previously as well [81-82] but in that case the huge discrepancy was attributed to decomposition of the electrolyte. However, the authors did not present any evidence to this effect, nor provided the redox reactions involved in charging and discharging. For the present work, a possible reaction sequence to account for the first cycle charging/discarging behaviour observed (Figure 7.5) may be the following:

<u>First Charge:</u>

$Li_2Fe_{0.5}^{II}Mn_{0.5}^{II}SiO_4 \rightarrow Li_1Fe_{0.5}^{III}Mn_{0.5}^{III}SiO_4 + \mathbf{Li}^+ + e^-$ (7.3a)

$Li_1Fe_{0.5}^{III}Mn_{0.5}^{III}SiO_4 \rightarrow Li_{0.5}Fe_{0.5}^{III}Mn_{0.5}^{IV}SiO_4 + \mathbf{0.5Li}^+ + 0.5e^-$ (7.3b)

Total amount of Li extracted: $\mathbf{1.5Li}^+$

<u>First Discharge:</u>

$Li_{0.5}Fe_{0.5}^{III}Mn_{0.5}^{IV}SiO_4 + \mathbf{0.5Li}^+$ (90 mAh/g) $+ 0.5e^- \rightarrow Li_1Fe_{0.5}^{III}Mn_{0.5}^{III}SiO_4$ (7.4a)

or $\rightarrow Li_1Fe_{0.5}^{II}Mn_{0.5}^{IV}SiO_4$ (7.4b)

Total amount of Li re-inserted: **$0.5Li^+$**

The proposed redox reactions for first charge (Equations 7.3a,b) are supported by computational predictions made by T. Yi *et al.*[137] who deduced that delithiation of $Li_xFe_{0.5}Mn_{0.5}SiO_4$ is associated with the following redox couples: Fe^{II}/Fe^{III} for $2 \geq Li \geq 1.5$, Mn^{II}/Mn^{III} for Li=1.0, and Mn^{III}/Mn^{IV} for Li=0.5, although no evidence of plateau corresponding to the latter couple (expected at ~ 4.5 V[33]) was detected (Figure 7.5). In terms of discharge, based on the single quasi-plateau at ~2.7 V, the re-insertion of 0.5Li (Eq. 7.4) seems to point to $Li_1Fe_{0.5}^{II}Mn_{0.5}^{IV}SiO_4$ (Eq. 7.4b) as most likely product. By comparison R. Chen *et al.*[33] in their respective study of $Li_2Fe_{0.5}Mn_{0.5}SiO_4$ reported 1Li extraction (corresponding to Eq. 7.3a) and re-insertion with the latter starting at 4.2 V ($Mn^{III} \rightarrow Mn^{II}$) and continuing with reduction of $Fe^{III} \rightarrow Fe^{II}$ at 3.4 V.

With the view of sheding light as to the origin of the high initial (>1 Li) charge capacity, the observed irreversible behaviour during the first charging/discharging cycle and the associated Mn/Fe redox reactions involved, post-mortem and *in situ* XANES and XRD techniques were used to characterize the structural and oxidation state changes of the $Li_2Fe_{0.5}Mn_{0.5}SiO_4$ cathode at different states of charge (SOC). Five points at different SOC were chosen along the first charging curve, where C0 represents the electrode right before charging starts and C5 represents the end of charging. C1 to C4 lie along the charging curve between C0 and C5 based on a 50 mAh/g increment of charging capacity. Similarly, four points were chosen along the discharging curve, where D1 represents the start of discharging and D4 represents the end of discharging. D2 and D3 lie along the discharging curve based on a 30 mAh/g increment of discharging capacity. The post-mortem samples were collected by interrupting the test after the cell had reached the pre-selected SOC, whereas the *in situ* samples were tested in modified coin cells (refer to Chapter 3), by holding temporarily the cell voltage at selected stages.

7.2.2 Structural evolution during first cycle

The XRD patterns of the post-mortem samples obtained at different states of charge (SOC; Figure 7.5) are shown in Figure 7.6; in Figure 7.6(a) are the patterns corresponding to first charging and in Figure 7.6(b) the patterns corresponding to first discharging. Upon examination of the XRD

patterns, it is noticed that the overall shape and positions of the diffraction peaks did not change significantly during the first charging and discharging.

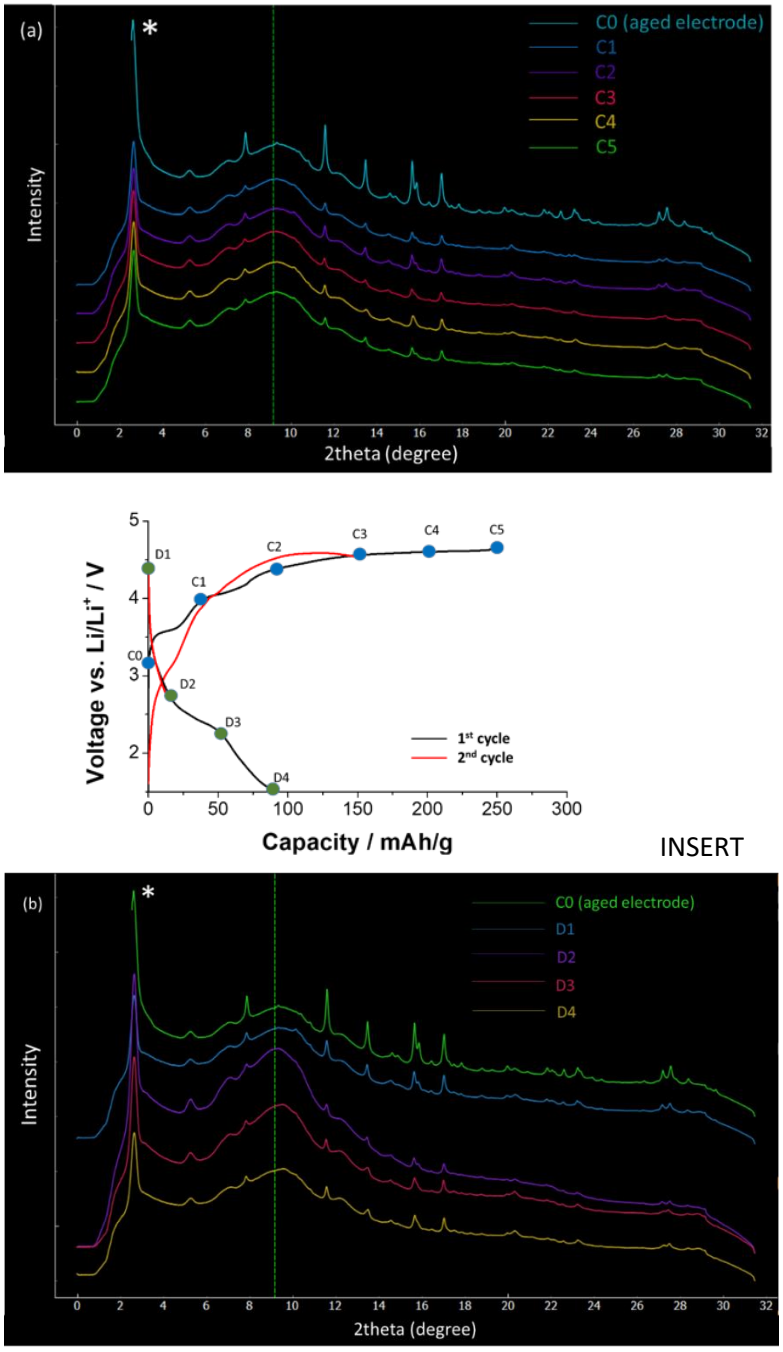

Figure 7.6. The post-mortem XRD patterns obtained at different SOC (see insert) during charging (a) and discharging (b). The asterisk indicates a peak due to instrument artifact. The green dash line indicates the amorphous backgound induced upon electrode/electrolyte contact ("aging"-refer to Figure 6.1 in Chapter 6) and first cycle charging/discharging. Note that the pattern for C0 is included in both Figures for comparison and the background is not removed in order to preserve the low intensity XRD peaks.

The overall structure, independent of charging or discharging state, is deduced (by comparing the respective patterns to that of C0 aged electrode) to be made of a mixture of *p21n* and *pmn21* phases. Note that due to the low signal quality the XRD patterns could not be analyzed by Rietveld refinement. However, an increase in background (indicated by the vertical green dask line) and simultaneous decrease in peak intensity and increase of peak width of the major diffraction peaks are observed. These XRD pattern changes suggest a certain degree of crystallinity loss and structural disordering induced during the first cycle beyond what is attributed to pristine electrode contact with the electrolyte ("aging") as discussed in Section 6.1 and reported in another study of our group.[91]

This increased extent of amorphization behavior in Mn-containing lithium iron orthosilicates vis-à-vis Mn-free LFS has also been reported by Kokalj *et al.*[138] Similar conclusions were also reported by Chen *et al.*[33] Unlike the post-mortem Li_2FeSiO_4 samples disscused in Chapter 6 where new XRD peak formation was observed upon battery cycling, no obvious appearance of new peaks was observed for the LFMS sample, suggesting different structural evolution mechanism between the pure Fe and the Fe-Mn mixed orthosilicate. Although the underlying mechanism may remain unclear one thing is certain, as also Chen *et al.* [33] found, the mixed Fe-Mn metal composition, $Li_2Fe_{0.5}Mn_{0.5}SiO_4$, leads to an increased structural disorder this apparently relating to Mn presence.

7.2.3 Redox chemical state changes during first cycle

Other than structural changes, the change of the oxidation states of Fe and Mn during the first charging/discharging cycle were monitored by both post-mortem and *in situ* X-ray absorption near edge spectroscopy (XANES) technique, in order to probe the redox reactions associated with delithiation and re-lithiation. The collected Fe and Mn K-edge XANES spectra of the uncycled electrode are shown in Figure 7.7 and those of the cycled electrode in Figure 7.8 (post-mortem) and 7.9 (*in situ*). As per Figure 7.7 the dominant Fe and Mn oxidation state in the uncycled LFMS is their divalent cations as expected from the theoretical formula: $Li_2Fe_{0.5}^{II}Mn_{0.5}^{II}SiO_4$. However, a small amount of Fe^{3+} being present cannot be ignored given the spontaneous reaction with the electrolyte as discussed in Section 6.1,[91] which is confirmed by the Fe K pre-edge feature[91,123] as presented in Figure 7.7(c). The collected XANES spectra were normalized to the size of the edge jump by firstly substracting a linear fit to the pre-edge background. In addition, the Fe-O bond in the FeO_4 tetrahedra can experience distorion during Li ion removal and the pre-edge feature is particularly sensitive during charge transfer[90, 139]. In the C0 LFMS electrode the Fe pre-edge features

show an overlap of Fe^{2+} and Fe^{3+}, which indicate the mixed ferric and ferrous content before the cycling starts due to the spontaneous reaction with electrolyte as also comfirmed by Arthur *et al.* previouly[90].

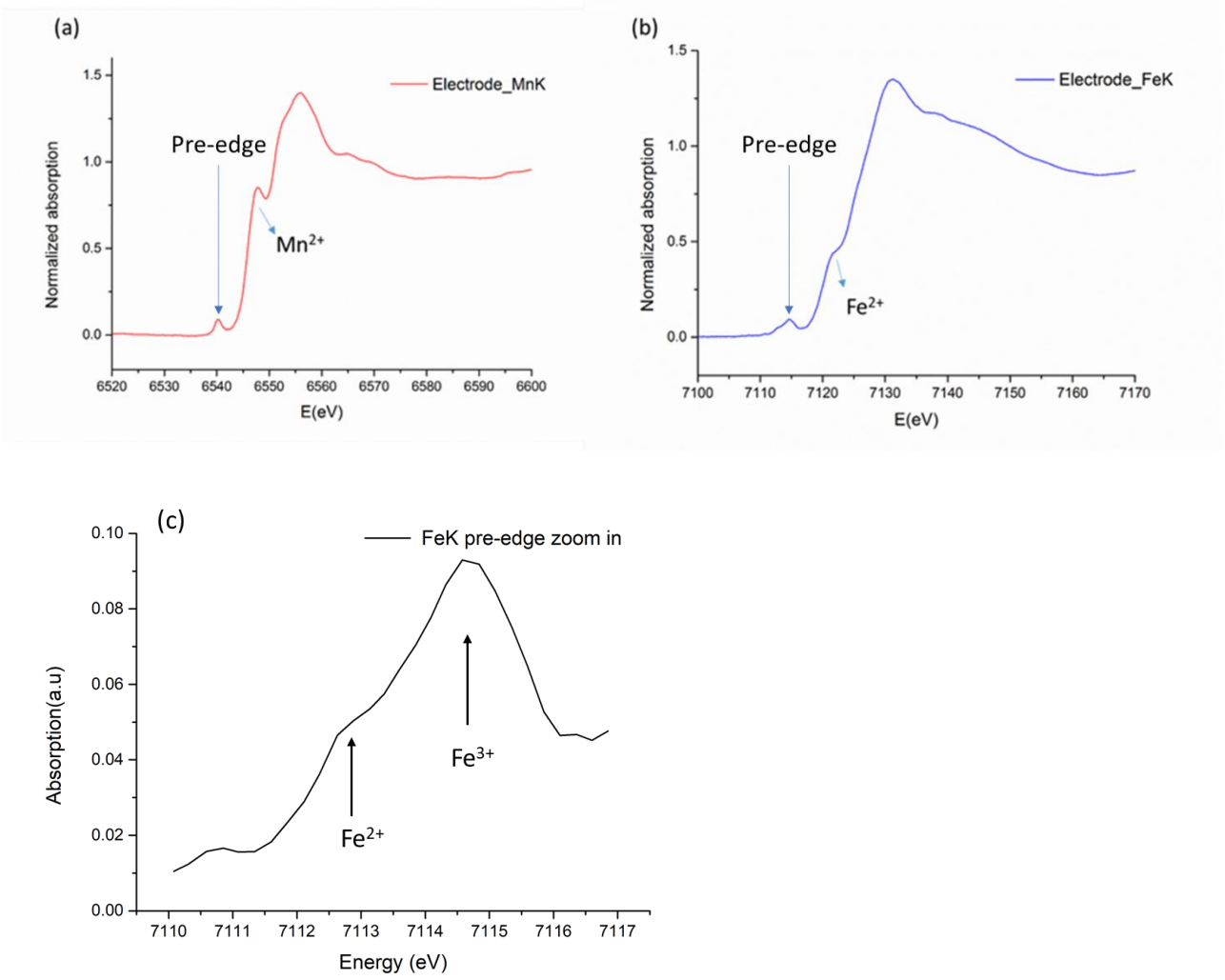

Figure 7.7. The Fe (a) and Mn (b) K-edge XANES spectra of the $Li_2Fe_{0.5}Mn_{0.5}SiO_4$ electrode sample C0 before cycling. The pre-absorption shoulder peaks (blue arrow) indicate the presence of Mn^{2+} and Fe^{2+}. A zoomed-in view of the detailed Fe K pre-edge feature is presented in (c).

Turning our attention to Figure 7.8(a,b), even if the changes associated with Fe^{2+} signal are rather subtle, there a reduction in intensity may be discerned moving from C0 to C5 (Figure 7.8(a)) due to apparent oxidation to Fe^{3+}, i.e. $Li_{0.5}Fe_{0.5}{}^{III}Mn_{0.5}{}^{Y}SiO_4$, as per Equation 7.3(b) (the oxidation state of Mn is discussed in next paragraph). However, during discharging, the Fe^{3+} is not seemingly reversible to Fe^{2+} (Figure 7.8(b)). Chen *et al.* also found in their XANES analysis "…*only part of*

the Fe^{3+} was reduced to Fe^{2+} during the first discharge of $Li_2Fe_{0.5}Mn_{0.5}SiO_4$".[33] Nevertheless, unless further analysis of the pre-edge feature is done[91,123], it remains tentative to what extent reduction of Fe^{3+}has happened.

In contrary, the Mn^{2+} shoulder peak seems to remain unchanged during charging (Figure 7.8(c)) and it agrees with the previous result reported by Dominko *et al*.[39, 56]; this behaviour may be interpreted as Mn not participating in charge compensation via its oxidation from Mn^{2+} to Mn^{3+} (or even to Mn^{4+} as per Equation 7.3b) and thereby to the charging capacity like Fe^{2+} does. However, this is highly unlikely as iron alone (representing only 50% of the transition metal content) cannot be seen to be able to accommodate more than 0.5 Li charge capacity (Equation 7.3a). According to Chen *et al*., [33] Mn^{3+} trivalent state is not stable having a tendency towards reduction to Mn^{2+}, which may explain the difficulty in observing Mn^{3+} in the post mortem XANES analysis. Interestingly, the Mn-K-edge spectra during discharging (Figure 7.8(d)) show that the Mn^{2+} signal remains stable until close to the end of discharging (D3 and D4) when its shoulder peak is seen to diminish and deform due to apparent change in the chemical environment and valence state similar to obserbations made by Dominko *et al*..[74] In other words, from the post-mortem XANES analysis the Mn^{2+} to Mn^{3+} transition was not clear until the end of discharging (D3/D4). These XANES results for the discharged LFMS (presence of Fe^{3+} and Mn^{3+}) as first conclusion seem therefore to support the formula, $Li_1Fe_{0.5}^{\mathbf{III}}Mn_{0.5}^{\mathbf{III}}SiO_4$ that was proposed earlier (refer to Equation 7.4b).

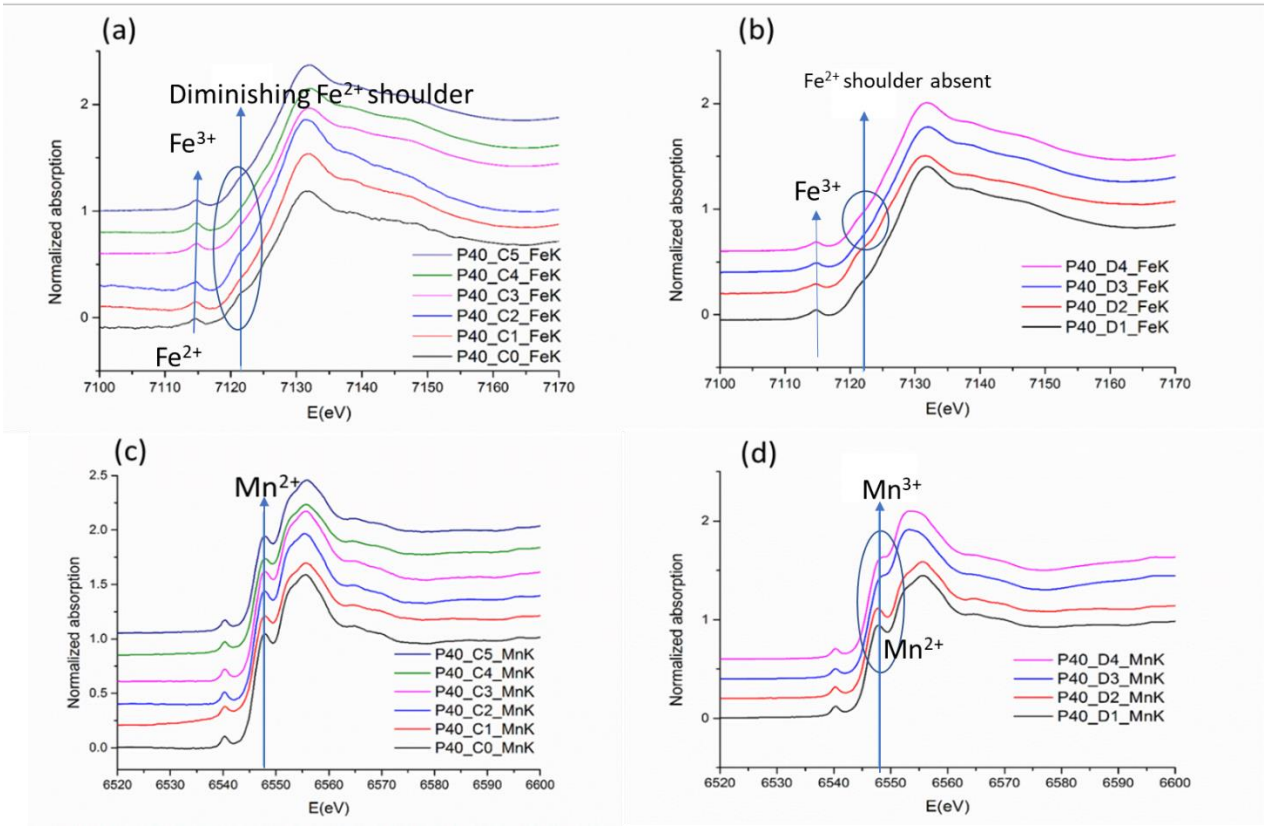

Figure 7.8. The post mortem Fe and Mn K-edge XANES spectra of the $Li_2Fe_{0.5}Mn_{0.5}SiO_4$ electrode samples obtained at differenct SOC during the first charging (a, b) and discharging (c, d) at C/40. The blue lines indicate the Mn^{2+} and Fe^{2+} peak positions[39, 56].

It is not clear whether the observations from the post-mortem XANES analysis accurately reflect the actual real-time changes in chemical states or are altered because of relaxation prior to analysis. To verify this, ***in situ*** XANES experiments were carried out to obtain *in operando* XANES spectra at selected SOC during charging (C0 to C5, see Figure 7.5) by holding the voltage constant when the spectra were collected. The obtained *in situ* spectra are presented in Fig. 7.9. For Fe K-edge, the post-mortem and *in situ* XANES spectra are quite similar although this time the reduction of intensity of the Fe^{2+} shoulder peak (due to conversion to Fe^{3+}) is better resolved (Fig. 7.9(a) vs. Fig. 7.8(a)). However the Mn K-edge spectra this time clearly reveal the oxidation of Mn^{2+} to Mn^{3+} during charging as evident by the diminishing/deformation of the Mn^{2+} shoulder peak towards the end of *in situ* charging (C4 and C5 in Fig. 7.9(b)) as opposed to the *ex situ* (post mortem) spectra (Fig. 7.8(c)) that did not detect Mn^{3+} due to its apparent reversing back to its thermodynamically stable Mn^{2+} state as postulated earlier. This is an important observation pointing to limitations of the

post mortem analysis method in favour of the dynamic *in situ* technique for truthful representation of the actual changes taking place during charging and discharging.

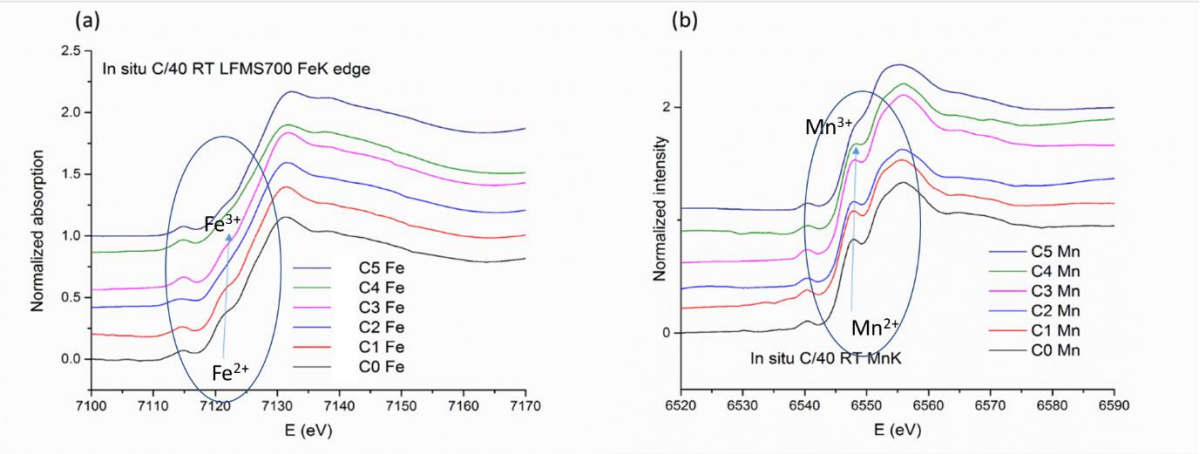

Figure 7.9. The *in situ* Fe and Mn K-edge XANES spectra of the LFMS sample obtained at different SOC during the first charging at C/40. Blue arrows indicate the Mn^{2+} and Fe^{2+} peak positions.[39, 56]

Furthermore, by closely examining the respective Fe (Figure 7.9(a)) and Mn (Figure 7.9(b)) K-edge spectra, it becomes evident that Fe^{2+} appears to oxidize (see C2 Fe spectrum) before Mn^{2+} (see C4 Mn spectrum) does during the *in situ* charging reaction, which is consistent with the two quasi-plateaus identified on Figure 7.5 (Section 7.1.1) as also determined by Chen *et al*..[33] Finally, it is worthy pointing that no evidene for Fe^{4+} or Mn^{4+} was detected. Although the absence of Fe^{4+} is not surprising as computational studies predict a higher potential (4.8 V) for its formation (in the present study the upper cut-off voltage was 4.6 V) but more importantly if indeed this state is attained remains highly questionable.[106, 120, 140] The possible formation of Mn^{4+} on the other hand may not be ignored or rejected as computationally it should be attainable at 4.5 V.[137, 140] Indeed the oxidation of Mn^{3+} to Mn^{4+} as proposed in Equation 7.3b can provide charge compensation for the excess beyond one Li attained capacity (see Equation 7.3b). However, direct experimental evidence could not be ascertained in this work or in previous works.[33]

7.2.4 LFMS particle morphology evolution during first cycle

The size and morphology of LFMS particles were also examined post mortem using scanning electron microscopy (SEM) at different states of charge (Fig. 7.10). The material after contact with the electrolyte and prior to cycling (C0, refer to Figure 7.5) exhibited the same morphology as the pristine LFMS (see Figure 7.3) material. The material is in largely aggregated state with primary

particle size ranging around 100 nm-200 nm. Upon charging (C5, Figure 7.10(b)) and eventual discharging (D4, Figure 7.10(c)) there appears some particle changes to have happened as evident (in particular in Figure 7.10(c)) by the increased occurrence of smaller particles (< 100 nm) but also appearance of a few elongated ones. The smaller particles may have formed as result of mechanical breakdown of the aggregates due to stesses from associated volume changes induced by the delithiation/re-lithiation process. These stresses may have also contributed to the partial loss of crystallinity as evident by the larger background and weaker intensity of the XRD pattern registered in Figure 7.6. Alternatively stresses may have developed as result of induced structural changes (phase transition) during cycling as it is known to occur with Li_2FeSiO_4 that converts from *p21n* to *pmn21*.[123] [88]Unfortunately the diffraction intensities for the $Li_2Fe_{0.5}Mn_{0.5}SiO_4$ were too weak to allow for quantitative estimation of the phase composition as also discovered by Chen *et al.* in their respective study.[33]

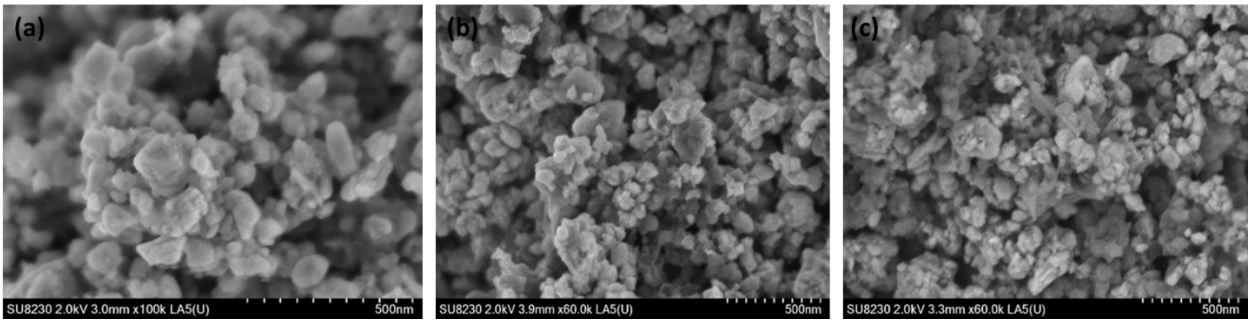

Figure 7.10. SEM images of $Li_2Fe_{0.5}Mn_{0.5}SiO_4$ at different SOC: (a) before cycling (C0; left), (b) charged (C5) and (c) discharged (D4).

7.2.5 Discussion

The results presented confirm previous works[33] that during initial charging of $Li_2Fe_{0.5}^{II}Mn_{0.5}^{II}SiO_4$, Fe^{2+} oxidizes first to Fe^{3+} at ~3.1-3.6V followed by oxidation of Mn^{2+} to Mn^{3+}at ~ 4.2V, accounting for 1 exchangeable Li or capacity ~ 165mAh/g as indicated by Equation 7.3a:

$$Li_2Fe_{0.5}^{II}Mn_{0.5}^{II}SiO_4 \rightarrow Li_1Fe_{0.5}^{III}Mn_{0.5}^{III}SiO_4 + \mathbf{Li}^+ + e^- \qquad (7.3a)$$

It was not possible to confirm experimentally the subsequent oxidation of Mn^{3+} to Mn^{4+} (Equation 7.3b) that should occur at ~4.5V according to computational calculations[137] but this does not mean that Mn^{4+} is not involved at least partly. This raises the question as to what is the origin of the beyond one lithium -irreversible- recorded capacity (~250 mAh/g) if not relating to Mn^{4+}. One

possibility as also suggested previously by others[81] is to have oxidation of some of the electrolyte components due to high upper cut-off voltage. However additionally, there is recently growing computational (mostly) evidence of oxygen redox activity involving oxidation of oxygen anions (O^{2-}) during charging and as such participating potentially in the charge compensation mechanism.[106] In particular the redox activity of oxygen has been suggested by Masese *et al.*[121] as responsible for achieving the second Li extraction from the L_2FeSiO_4 electrode that enables more than 165 mAh/g (>1 Li exchange) capacity to be attained. The authors presented evidence that during the second lithium extraction process ligand holes formed in the O 2p band rather than oxidation of Fe^{3+} to Fe^{4+} states. Recently P. Zhang and S-H Wei [140]considered not only LFS but also L_2MnSiO_4 in their computational calculations and concluded the charge compensation in L_2MSiO_4 (*M*= Fe or Mn) upon delithiation (i.e. charging) is achieved by a combined transition metal and oxygen redox process that is followed by the irreversible formation of O vacancies (V_O).The latter were deemed to cause destabilization of the host structure and loss of reversibility as observed in this work (compare first charge and discharge in Figure 7.5 and XRD recorded loss of crystallinity (increased degree of distortion) (refer to Figure 7.6). Attributing thus the excess capacity of the first charge to electrolyte oxidation and at least partially to oxygen redox activity, the discharge reaction (Equation 7.4a,b) can be re-written as follows (Equation 7.4c):

$$Li_1Fe_{0.5}^{III}Mn_{0.5}^{III}SiO_4 + \mathbf{0.5Li^+}\ (90\ mAh/g) + 0.5e^- \rightarrow Li_{1.5}Fe_{0.5}^{II}Mn_{0.5}^{III}SiO_4 \quad (7.4c)$$

As for the second charge that registered 150 mAh/g capacity (almost equivalent to 1 Li) the following redox reaction is proposed (Equation 7.5) involving charge compensation via the two transition metals although partial involvement of oxygen redox may still be involved:

$$Li_{1.5}Fe_{0.5}^{II}Mn_{0.5}^{III}SiO_4 \rightarrow Li_{0.5}Fe_{0.5}^{III}Mn_{0.5}^{IV}SiO_4 + \mathbf{Li^+} + e^- \quad (7.5)$$

The interest in LFMS as stated earllier is stemming from the expectation of reaching a higher capacity (beyond 1 Li) thanks to more favourable thermodynamic potential for Mn^{3+}/Mn^{4+} than Fe^{3+}/Fe^{4+}. This seems to occur though only in the initial charge (oxidation direction) as observed in this work (Figure 7.5) with the discharge process (reduction) to suffer from highly irreversible capacity loss. As with the Li_2MnSiO_4 itself that has been found to suffer from severe capacity fade due to so-called Jahn Teller distortion phenomenon,[141] it seems the mixed Fe-Mn counterpart is equally prone to loss of capacity even after one cycle. This raises the question as to why Mn (despite its favorable thermodynamic potential) cause destabilization of the lithium iron silicate host structure.

The observed changes in XANES absorption spectra (Figures 7.8 and 7.9) are signs of the changes in the local chemical bonding environment of Fe and Mn cations.[33] Since Fe and Mn reside in the transition metal oxide tetrahedra, the local bonding of Fe-O and Mn-O could be altered upon cycling not only because of their valence change but also the alluded oxygen anion redox involvement. In fact Dominko *et al.* [56] reported the changes in Fe-O bonding distance upon cycling to vary from 1.94Å to 2.03Å based on an off-centered FeO_4 tetrahedron prediction. Meanwhile for Mn-O the neighbouring atomic distance they found to vary from 1.86Å to 2.23Å,[56] indicating a more severe distortion in MnO_4 tetrahedra. Such lattice distortion may deterioate the overall structural stability, especially for the long range order of Mn-O and can lead to capacity fading and structure collapse. Recent first principles computational modeling predictions by T. Yi *et al.*[137], provide further insight as to the induced structure destabilization by Mn. According to these authors when $Li_xFe_{0.5}Mn_{0.5}SiO_4$ is delithiated to $x < 1.0$, the average valence of Mn ions (between Mn^{3+} and Mn^{4+}) is greater than that of Fe^{3+} ions causing lattice changes that eventually lead (at $x=0.5$) to a collapsed structure. Their energy calculations showed that under the action of the even larger attraction force from Mn^{4+} ions, the nearest FeO_4 tetrahedron to a Mn ion is pulled closer to the Mn ion creating a large distortion in shape and a big shrinkage in volume of crystal structure.

7.2.6 Summary

In this Chapter mixed metal (Fe-Mn) orthosilicates ($Li_2Fe_{1-x}Mn_xSiO_4$) were successfully synthesized using the earlier described novel synthesis method in Chapters 3 & 4. The synthesized materials were confirmed to be solid solutions with mixed phase composition: *p21n* and *pmn21*. The relative amount of *pmn21* increased with an increasing amount of Mn. The equimolar composition LFMS, $Li_2Fe_{0.5}Mn_{0.5}SiO_4$ was further evaluated in terms of its first cycle electrochemical and structural behavior to probe the underlying metal redox changes involved in charge compensation and Li-ion storage. The material registered a 1.5 Li exchange during the first charge which however was found to be followed by severe irreversible loss during discharge. Post mortem and *in situ* XRD and XANES analysis carried out at Canadian Light Source revealed the most likely metal redox sequence but further research is needed to substantiate the suspected oxygen redox activity as well as probe structural evolution beyond one cycle.

Chapter 8 Synopsis

8.1. Global Conclusions

In this work, a systematic study of lithium iron silicate, Li_2FeSiO_4 (LFS), and manganese-substituted $Li_2Fe_{1-x}Mn_xSiO_4$ in terms of synthesis and electrochemistry was undertaken with the objective of understanding and correlating their performance as Li-ion battery cathode materials to crystal formation and cycling-induced structural transformations. In a departure from previous studies, two new nanostructured LFS powder materials were successfully produced using a novel two-step synthesis method, one at 400°C and the other at 700°C. The first step of the new synthesis process is hydrothermal precipitation from a ferric nitrate-lithium acetate-colloidal silica system that leads to the formation of a ferric-silicate reaction intermediate under the regulation of two organic additives (ethylene glycol and ethylenediamine), and with lithium incorporation upon the subsequent drying. The second step is a reductive annealing step that promotes crystallization of the reaction intermediate towards porous nanostructured LFS particles with the organic additives decomposed as a carbon coating. Ethylenediamine proved critical as organic additive in regulating the crystallization process towards formation of LFS. The two LFS products obtained at different annealing conditions, 400°C and 700°C, were characterized using various methods and they were found to be predominantly monoclinic (*p21n*) but both containing a small fraction of either low temperature orthorhombic (*pmn21*, 10% in LFS400) or high-temperature orthorhombic (*pmnb*, 25% in LFS700). The mesoporous LFS400 material is endowed with nanograined structure (nanocrystallites of ~40-50 nm size). By contrast, the LFS700 material is made of coarser grains (150-250 nm) that upon mechanical milling become mesoporous as well.

The different nano-structural characteristics of LFS400 and LFS700 materials were found to greatly impact their Li-ion storage properties when they were compared for the first 3 charging and discharging cycles. The LFS400 material enriched with abundant nanoscale grain boundaries exhibits near one-Li discharge capacity and solid solution storage mechanism while the LFS700 material exhibits two-phase storage mechanism and somewhat lower capacity. Despite the initial higher capacity of the LFS400 material, it was concluded to have poor capacity retention thus it was the LFS700 material retained for long-term cycling investigation.

The LFS700 material was cycled under different cycling rates (C/20 to C/2) for extended periods of time at 45°C. Lower rate (C/50) or elevation of cycling temperature to 55°C was found to lead to cell failure. Using synchrotron XRD for post-mortem structural analysis, it was found that the predominantly monoclinic (75% *p21*n) LFS700 material to undergo partial oxidation after the initial contact with electrolyte that led to an irreversible formation of partially delithiated monoclinic LFS phase ($LiFe^{III}SiO_4$), accompanied by a certain degree of crystal disordering. With the progression of cycling these structural changes continue with the irreversible formation of the (inert to intercalation) delithiated monoclinic $LiFe^{III}SiO_4$ phase favored at slower cycling rates. In contrast the observed crystal disordering is deemed to have a beneficial effect to the overall Li-ion storage as no obvious capacity fading was observed at least for 30 days at different rates from C/20 to C/2. As a result, it appears opting for cycling conditions favoring crystal disorder of $Li_2Fe^{II}SiO_4$ and avoidance of formation of the irreversible $LiFe^{III}SiO_4$ phase should be considered in future work to improve the performance of the LFS cathode.

In the end, manganese-substituted $Li_2Fe_{1-x}Mn_xSiO_4$ (LFMS) compounds were synthesized successfully and confirmed to be solid solutions with mixed phase composition: *p21n and pmn21* with the latter phase increasing with increasing Mn content. The equimolar composition LFMS, $Li_2Fe_{0.5}Mn_{0.5}SiO_4$ was further evaluated in terms of its first cycle electrochemical and structural behavior to probe the underlying metal redox changes involved in charge compensation and Li-ion storage using post-mortem and *in situ* XRD and XANES techniques. Although Mn substitution enabled an initial charging capacity of over one Li (250 mAh/g), there was significant irreversible loss during discharge and simultaneous appearance of structure disordering. In terms of charge compensation, it was confirmed this to proceed first the Fe^{2+}/Fe^{3+} couple at ~ 3.1-3.6 V and followed by the Mn^{2+}/Mn^{3+} couple at ~4.2 V. Further oxidation to Mn^{4+} state could not be experimentally confirmed as predicted by previous computational studies to occur at ~4.5 V calling for further studies.

8.2. Original contributions to knowledge

This work provides new methods and insight into the synthesis of LFS and LFMS, the structural evolution of LFS during long term cycling, and the Mn influence on the first cycle redox chemistry of $Li_2Fe_{0.5}Mn_{0.5}SiO_4$. As such it contributes to the continuing efforts of further understanding and development of the orthosilicates as cathode materials. More specifically, this

thesis has made the following original contributions to the development of lithium metal silicates as cathode materials:

1. A novel synthesis method was developed and studied for the first time based on the use of concentrated ferric salt aqueous solution as a precursor and reductive annealing allowing for the formation of nanostructured Li_2FeSiO_4 particles, with the possibility to substitute Mn for Fe at different stoichiometric ratios. The new method provides a facile alternative to previous works which make use of ferrous salts as precursor and require handling in inert atmosphere throughout the synthesis process, while other methods use complex procedures like sol-gel that involve multiple steps and expensive organic solvents hardly amenable to scale up.
2. The work has demonstrated that unless ethylenediamine is used as complexing agent during hydrothermal precipitation, no LFS production from ferric salt precursors is possible. Ethylenediamine is shown to assist in the formation of the hydrated iron (III) silicate complex that provides a favorable crystallization pathway for LFS upon annealing. The crystallization mechanism was revealed to proceed via formation of a nucleation cluster – as annealing temperature is raised and Fe^{3+} is reduced to Fe^{2+} (by the action of H_2) – that gradually grows into mainly monoclinic phase (*p21n*) crystallites which assemble into porous cage-like aggregates.
3. A head-to-head electrochemical comparison of two predominantly monoclinic (*p21n*) Li_2FeSiO_4 materials obtained at different annealing temperature (LFS400 vs. LFS700) was made for the first time revealing significant differences in terms of mode of Li-ion storage reflecting differences in their nanostructure features and type of co-existing orthorhombic phase (*pmn21 vs. pmnb*).
4. The structural evolution of the monoclinic Li_2FeSiO_4 (LFS700) cathode during long-term electrochemical cycling was studied for the first time at different rates (C/2 to C/20). Previous works on the structural transformations of LFS mostly have focused on the initial cycle or the first 1.5 cycles having as consequence a knowledge gap to exist as to the correlation between long term electrochemical cycling and structural behavior. In this work, using synchrotron XRD and quantitative structural analysis, the cycled structure was identified as a delithiated monoclinic (and not orthorhombic) phase of LFS, $LiFe^{III}SiO_4$. Furthermore, it was determined that this cycled LFS phase to be rather inert without contributing to the exchangeable Li-ion storage, hence its extensive formation should be

avoided. Finally, clear evidence was presented that crystal disordering during cycling is beneficial to reversible Li-ion storage, another finding not described or discussed previously.

5. During the study of the first cycle behavior of $Li_2Fe_{0.5}Mn_{0.5}SiO_4$ by post-mortem and in-situ XANES analysis at different states of charge, it was only the in-situ method that detected the Mn^{2+} to Mn^{3+} oxidation during charging. This apparently happens because of Mn^{3+}' tendency towards the reduction to Mn^{2+}. This is an important observation pointing to the limitations of the commonly employed post mortem analysis method in favour of the dynamic *in situ* technique for truthful representation of the actual changes taking place during cycling studies of cathode materials.

8.3. Perspective, challenges, and limitations

Lithium metal orthosilicate (Li_2MSiO_4) is a promising sustainable cathode material as it is made of abundant elements and it has high theoretical capacity equivalent to two Li. However, the actual capacity is much lower and its reversibility and structural stability upon cycling remain formidable challenges. In the lithium metal silicate community, efforts have been made to synthesize, characterize and electrochemically test and explain the structure evolutions during cycling and charge compensation mechanism. However, there remain knowledge gaps and material development challenges with the L*M*S that call for further studies if the full potential for this promising cathode material is to be materialized.

1. In this work, using synchrotron XRD and quantitative structural analysis, the cycled structure was identified as a delithiated monoclinic phase of LFS, $LiFe^{III}SiO_4$ that proved inert in terms of exchangeable Li-ion storage hence its formation should be avoided. Since its formation was initiated by the LFS/electrolyte reaction prior to starting of cycling, it will be of interest to study if a change in electrolyte or using a protective coating on LFS would avoid this problem.
2. Although the theoretical capacity of LFS is based on two lithium ions per formula unit, only one lithium is reversibly accessible in the actual battery testing. Moreover, when during charging at high voltage, over one lithium extraction is observed (as in the case of the Mn-substituted LFMS), it is unclear what exactly is the charge compensation mechanism. The oxidation of Mn^{3+} to Mn^{4+} can provide at least partial charge compensation for the excess

beyond one Li attained capacity (as computational studies predict) but direct experimental evidence could not be ascertained in this work or in previous works and this should be further studied. As a further extension to the work presented in Chapter 7, the Mn-substituted LFMS compound can be further studied in terms its long-term cycling behavior. Other spectroscopic techniques including Mossbauer spectroscopy, ^{6}Li NMR spectroscopy and XAFS and can be used to understand the Mn and Fe changes of local bonding environment and quantify the degree of oxidation/reduction upon (de)lithiation.

3. There is recently growing computational (mostly) evidence of oxygen redox activity involving oxidation of oxygen anions (O^{2-}) during charging and as such participating potentially in the charge compensation mechanism when more than one Li is extracted. Hence future work on L*M*S should include experimental validation of this possibility and its consequences.
4. The LFS material is sensitive and the structure is known to alter under certain circumstances, including air oxidation, electron beam damage, and reaction with electrolyte (as mentioned in earlier chapters). This makes it tricky to handle and used as a commercial cathode material. In this regard core-shell strategies may be explored to control this type of undesirable LFS surface reactivity while still the selected shell coating permitting electron and ion conduction.
5. Due to the low intrinsic conductivity of L*M*S materials, more effective carbon coating methods can be applied to enhance their conductivity. In this project although organic additives used during the synthesis led to formation of carbon coating upon annealing this may need to be further improved by additional conductive carbon coating strategies involving for example lactose decomposition, graphene or carbon nanotubes.
6. So far most of the works with LFS have focused on the high-temperature monoclinic phase (*p21n*) synthesized at 600-800°C (LFS700 in this work) and to lesser extent the low temperature orthorhombic phase *pmn21*. No systematic electrochemical study on the other major LFS phase forming at temperatures above 800°C, the so called high-temperature orthorhombic with space group *pmnb* has been undertaken. A such study could shed further light on the dependency of electrochemistry of different orthosilicate structures that upon comparison to similar studies involving *p21n* and *pmn21* may lead to identifying a stable in terms of cycling-induced phase transition phase. This study may be extended equally to Mn- or other transition metal- substituted LFS having the *pmnb* structure.

References

1. Li, M., World Energy 2018-2050: World Energy Annual Report (Part 1). *Peak Oil Barrel* 2018.
2. Lu, L.; Han, X.; Li, J.; Hua, J.; Ouyang, M., A review on the key issues for lithium-ion battery management in electric vehicles. *Journal of Power Sources* **2013,** *226*, 272-288.
3. Etacheri, V.; Marom, R.; Elazari, R.; Salitra, G.; Aurbach, D., Challenges in the development of advanced Li-ion batteries: a review. *Energy & Environmental Science* **2011,** *4* (9), 3243-3262.
4. Bard, A. J.; Faulkner, L. R.; Leddy, J.; Zoski, C. G., *Electrochemical methods: fundamentals and applications*. wiley New York: 1980; Vol. 2.
5. Goodenough, J. B.; Park, K.-S., The Li-Ion Rechargeable Battery: A Perspective. *Journal of the American Chemical Society* **2013,** *135* (4), 1167-1176.
6. Moo, C.; Ng, K.; Chen, Y.; Hsieh, Y. In *State-of-charge estimation with open-circuit-voltage for lead-acid batteries*, 2007 Power Conversion Conference-Nagoya, IEEE: 2007; pp 758-762.
7. Blomgren, G. E., The development and future of lithium ion batteries. *Journal of The Electrochemical Society* **2017,** *164* (1), A5019-A5025.
8. Huggins, R., *Advanced batteries: materials science aspects*. Springer Science & Business Media: 2008.
9. Julien, C. M.; Mauger, A.; Zaghib, K.; Groult, H., Comparative issues of cathode materials for Li-ion batteries. *Inorganics* **2014,** *2* (1), 132-154.
10. Whittingham, M. S., Ultimate limits to intercalation reactions for lithium batteries. *Chemical reviews* **2014,** *114* (23), 11414-11443.
11. Shi, J. L.; Xiao, D. D.; Ge, M.; Yu, X.; Chu, Y.; Huang, X.; Zhang, X. D.; Yin, Y. X.; Yang, X. Q.; Guo, Y. G., High-capacity cathode material with high voltage for Li-ion batteries. *Advanced Materials* **2018,** *30* (9), 1705575.
12. Armand, M.; Michot, C.; Ravet, N.; Simoneau, M.; Hovington, P., Lithium insertion electrode materials based on orthosilicate derivatives. Google Patents: 2000.
13. Alper, J., The Battery: Not Yet a Terminal Case. *Science* **2002,** *296* (5571), 1224-1226.
14. Whittingham, M. S., Lithium Batteries and Cathode Materials. *Chemical Reviews* **2004,** *104* (10), 4271-4302.
15. Mizushima, K.; Jones, P. C.; Wiseman, P. J.; Goodenough, J. B., LixCoO2 (0<x<-1): A new cathode material for batteries of high energy density. *Materials Research Bulletin* **1980,** *15* (6), 783-789.
16. Yazami, R.; Ozawa, Y.; Gabrisch, H.; Fultz, B., Mechanism of electrochemical performance decay in LiCoO2 aged at high voltage. *Electrochimica Acta* **2004,** *50* (2), 385-390.
17. Doughty, D. H. *Vehicle battery safety roadmap guidance*; National Renewable Energy Lab.(NREL), Golden, CO (United States): 2012.
18. Cho, J.; Kim, G., Enhancement of Thermal Stability of LiCoO2 by LiMn2 O 4 Coating. *Electrochemical and solid-state letters* **1999,** *2* (6), 253-255.
19. Chen, Z.; Dahn, J. R., Methods to obtain excellent capacity retention in LiCoO2 cycled to 4.5 V. *Electrochimica Acta* **2004,** *49* (7), 1079-1090.
20. Islam, M. S.; Fisher, C. A., Lithium and sodium battery cathode materials: computational insights into voltage, diffusion and nanostructural properties. *Chemical Society Reviews* **2014,** *43* (1), 185-204.
21. Thackeray, M. M.; David, W. I. F.; Bruce, P. G.; Goodenough, J. B., Lithium insertion into manganese spinels. *Materials Research Bulletin* **1983,** *18* (4), 461-472.
22. Ferg, E.; Gummow, R.; De Kock, A.; Thackeray, M., Spinel anodes for lithium-ion batteries. *Journal of the Electrochemical Society* **1994,** *141* (11), L147-L150.
23. Gummow, R. J.; de Kock, A.; Thackeray, M. M., Improved capacity retention in rechargeable 4 V lithium/lithium-manganese oxide (spinel) cells. *Solid State Ionics* **1994,** *69* (1), 59-67.

24. Jang, D. H.; Shin, Y. J.; Oh, S. M., Dissolution of spinel oxides and capacity losses in 4 V li/li x Mn2 O 4 cells. *Journal of The Electrochemical Society* **1996,** *143* (7), 2204-2211.
25. Thackeray, M. M., Spinel electrodes for lithium batteries. *Journal of the American Ceramic Society* **1999,** *82* (12), 3347-3354.
26. Padhi, A. K.; Nanjundaswamy, K. S.; Goodenough, J. B., Phospho‐olivines as positive‐electrode materials for rechargeable lithium batteries. *Journal of the electrochemical society* **1997,** *144* (4), 1188-1194.
27. Nishijima, M.; Ootani, T.; Kamimura, Y.; Sueki, T.; Esaki, S.; Murai, S.; Fujita, K.; Tanaka, K.; Ohira, K.; Koyama, Y.; Tanaka, I., Accelerated discovery of cathode materials with prolonged cycle life for lithium-ion battery. *Nature Communications* **2014,** *5*, 4553.
28. Satyavani, T. V. S. L.; Srinivas Kumar, A.; Subba Rao, P. S. V., Methods of synthesis and performance improvement of lithium iron phosphate for high rate Li-ion batteries: A review. *Engineering Science and Technology, an International Journal* **2016,** *19* (1), 178-188.
29. Tarascon, J.-M.; Armand, M., Issues and challenges facing rechargeable lithium batteries. In *Materials for Sustainable Energy: A Collection of Peer-Reviewed Research and Review Articles from Nature Publishing Group*, World Scientific: 2011; pp 171-179.
30. Andersson, A. S.; Thomas, J. O.; Kalska, B.; Häggström, L., Thermal Stability of LiFePO4‐Based Cathodes. *Electrochemical and Solid-State Letters* **2000,** *3* (2), 66-68.
31. Wang, J.; Sun, X., Understanding and recent development of carbon coating on LiFePO 4 cathode materials for lithium-ion batteries. *Energy & Environmental Science* **2012,** *5* (1), 5163-5185.
32. Chung, S.-Y.; Bloking, J. T.; Chiang, Y.-M., Electronically conductive phospho-olivines as lithium storage electrodes. *Nature Materials* **2002,** *1* (2), 123-128.
33. Chen, R.; Heinzmann, R.; Mangold, S.; Chakravadhanula, V. K.; Hahn, H.; Indris, S., Structural Evolution of Li2Fe1-y Mn y SiO4 (y= 0, 0.2, 0.5, 1) Cathode Materials for Li-Ion Batteries upon Electrochemical Cycling. *The Journal of Physical Chemistry C* **2013,** *117* (2), 884-893.
34. Islam, M. S.; Dominko, R.; Masquelier, C.; Sirisopanaporn, C.; Armstrong, A. R.; Bruce, P. G., Silicate cathodes for lithium batteries: alternatives to phosphates? *Journal of Materials Chemistry* **2011,** *21* (27), 9811-9818.
35. Eames, C.; Armstrong, A.; Bruce, P.; Islam, M., Insights into changes in voltage and structure of Li2FeSiO4 polymorphs for lithium-ion batteries. *Chemistry of Materials* **2012,** *24* (11), 2155-2161.
36. Sirisopanaporn, C.; Dominko, R.; Masquelier, C.; Armstrong, A. R.; Mali, G.; Bruce, P. G., Polymorphism in Li2(Fe,Mn)SiO4: A combined diffraction and NMR study. *Journal of Materials Chemistry* **2011,** *21* (44), 17823-17831.
37. Armstrong, A. R.; Sirisopanaporn, C.; Adamson, P.; Billaud, J.; Dominko, R.; Masquelier, C.; Bruce, P. G., Polymorphism in Li2MSiO4 (M = Fe, Mn): A Variable Temperature Diffraction Study. *Zeitschrift für anorganische und allgemeine Chemie* **2014,** *640* (6), 1043-1049.
38. Bini, M.; Ferrari, S.; Ferrara, C.; Mozzati, M. C.; Capsoni, D.; Pell, A. J.; Pintacuda, G.; Canton, P.; Mustarelli, P., Polymorphism and magnetic properties of Li2MSiO4 (M = Fe, Mn) cathode materials. *Scientific Reports* **2013,** *3*, 3452.
39. Dominko, R.; Arčon, I.; Kodre, A.; Hanžel, D.; Gaberšček, M., In-situ XAS study on Li2MnSiO4 and Li2FeSiO4 cathode materials. *Journal of Power Sources* **2009,** *189* (1), 51-58.
40. Brownrigg, A. W.; Mountjoy, G.; Chadwick, A. V.; Alfredsson, M.; Bras, W.; Billaud, J.; Armstrong, A. R.; Bruce, P. G.; Dominko, R.; Kelder, E. M., In situ Fe K-edge X-ray absorption spectroscopy study during cycling of Li 2 FeSiO 4 and Li 2.2 Fe 0.9 SiO 4 Li ion battery materials. *Journal of Materials Chemistry A* **2015,** *3* (14), 7314-7322.
41. Nytén, A.; Abouimrane, A.; Armand, M.; Gustafsson, T.; Thomas, J. O., Electrochemical performance of Li2FeSiO4 as a new Li-battery cathode material. *Electrochemistry Communications* **2005,** *7* (2), 156-160.
42. Nishimura, S.-i.; Hayase, S.; Kanno, R.; Yashima, M.; Nakayama, N.; Yamada, A., Structure of Li2FeSiO4. *Journal of the American Chemical Society* **2008,** *130* (40), 13212-13213.

43. Armstrong, A. R.; Kuganathan, N.; Islam, M. S.; Bruce, P. G., Structure and lithium transport pathways in Li2FeSiO4 cathodes for lithium batteries. *Journal of the American Chemical Society* **2011,** *133* (33), 13031-13035.
44. Qu, L.; Li, M.; Liu, P.; Tian, X.; Yi, Y.; Yang, B., A High-Performance Li2FeSiO4/C Cathode Enhanced by a Novel Liquid-State Carbon Source. *INTERNATIONAL JOURNAL OF ELECTROCHEMICAL SCIENCE* **2018,** *13* (12), 12311-12319.
45. Sirisopanaporn, C.; Masquelier, C.; Bruce, P. G.; Armstrong, A. R.; Dominko, R., Dependence of Li2FeSiO4 Electrochemistry on Structure. *Journal of the American Chemical Society* **2011,** *133* (5), 1263-1265.
46. Boulineau, A.; Sirisopanaporn, C.; Dominko, R.; Armstrong, A. R.; Bruce, P. G.; Masquelier, C., Polymorphism and structural defects in Li2FeSiO4. *Dalton Transactions* **2010,** *39* (27), 6310-6316.
47. Lu, X.; Chiu, H.-C.; Bevan, K. H.; Jiang, D.-T.; Zaghib, K.; Demopoulos, G. P., Density functional theory insights into the structural stability and Li diffusion properties of monoclinic and orthorhombic Li 2 FeSiO 4 cathodes. *Journal of Power Sources* **2016,** *318*, 136-145.
48. Dominko, R.; Bele, M.; Gaberšček, M.; Meden, A.; Remškar, M.; Jamnik, J., Structure and electrochemical performance of Li2MnSiO4 and Li2FeSiO4 as potential Li-battery cathode materials. *Electrochemistry Communications* **2006,** *8* (2), 217-222.
49. Lee, H.; Park, S.-D.; Moon, J.; Lee, H.; Cho, K.; Cho, M.; Kim, S. Y., Origin of poor cyclability in Li2MnSiO4 from first-principles calculations: Layer exfoliation and unstable cycled structure. *Chemistry of Materials* **2014,** *26* (13), 3896-3899.
50. Zhu, J.; Tang, H.; Tang, Z.; Ma, C., Improved electrochemical performance of zinc oxide coated lithium manganese silicate electrode for lithium-ion batteries. *Journal of Alloys and Compounds* **2015,** *633*, 194-200.
51. Liu, W.; Xu, Y.; Yang, R., Synthesis and electrochemical properties of Li 2 MnSiO 4/C nanoparticles via polyol process. *Rare metals* **2010,** *29* (5), 511-514.
52. Dominko, R.; Bele, M.; Kokalj, A.; Gaberscek, M.; Jamnik, J., Li2MnSiO4 as a potential Li-battery cathode material. *Journal of Power Sources* **2007,** *174* (2), 457-461.
53. Devaraju, M. K.; Tomai, T.; Unemoto, A.; Honma, I., Novel processing of lithium manganese silicate nanomaterials for Li-ion battery applications. *RSC advances* **2013,** *3* (2), 608-615.
54. Shao, B.; Abe, Y.; Taniguchi, I., Synthesis and electrochemical characterization of Li2FexMn1−xSiO4/C ($0 \leqq x \leqq 0.8$) nanocomposite cathode for lithium-ion batteries. *Powder Technology* **2013,** *235*, 1-8.
55. Gao, K., Effect of Mn doping on electrochemical properties of Li 2 FeSiO 4/C cathode materials based on a vacuum solid-state method. *Ionics* **2014,** *20* (6), 809-815.
56. Dominko, R.; Sirisopanaporn, C.; Masquelier, C.; Hanzel, D.; Arcon, I.; Gaberscek, M., On the origin of the electrochemical capacity of Li2Fe0. 8Mn0. 2SiO4. *Journal of the Electrochemical Society* **2010,** *157* (12), A1309.
57. Yi, L.; Wang, G.; Bai, Y.; Liu, M.; Wang, X.; Liu, M.; Wang, X., The effects of morphology and size on performances of Li2FeSiO4/C cathode materials. *Journal of Alloys and Compounds* **2017,** *721*, 683-690.
58. Dominko, R.; Conte, D.; Hanzel, D.; Gaberscek, M.; Jamnik, J., Impact of synthesis conditions on the structure and performance of Li 2 FeSiO 4. *Journal of Power Sources* **2008,** *178* (2), 842-847.
59. Chen, J., A review of nanostructured lithium ion battery materials via low temperature synthesis. *Recent patents on nanotechnology* **2013,** *7* (1), 2-12.
60. Bai, J.; Gong, Z.; Lv, D.; Li, Y.; Zou, H.; Yang, Y., Nanostructured 0.8 Li 2 FeSiO 4/0.4 Li 2 SiO 3/C composite cathode material with enhanced electrochemical performance for lithium-ion batteries. *Journal of Materials Chemistry* **2012,** *22* (24), 12128-12132.
61. Zaghib, K.; Shim, J.; Guerfi, A.; Charest, P.; Striebel, K., Effect of carbon source as additives in LiFePO4 as positive electrode for lithium-ion batteries. *Electrochemical and Solid-State Letters* **2005,** *8* (4), A207-A210.

62. Zaghib, K.; Dubé, J.; Dallaire, A.; Galoustov, K.; Guerfi, A.; Ramanathan, M.; Benmayza, A.; Prakash, J.; Mauger, A.; Julien, C. M., Enhanced thermal safety and high power performance of carbon-coated LiFePO4 olivine cathode for Li-ion batteries. *Journal of Power Sources* **2012,** *219*, 36-44.
63. Ni, J.; Zhang, L.; Fu, S.; Savilov, S.; Aldoshin, S.; Lu, L., A review on integrating nano-carbons into polyanion phosphates and silicates for rechargeable lithium batteries. *Carbon* **2015,** *92*, 15-25.
64. Oghbaei, M.; Baniasadi, F.; Asgari, S., Lithium iron silicate sol–gel synthesis and electrochemical investigation. *Journal of Alloys and Compounds* **2016,** *672*, 93-97.
65. Qu, L.; Fang, S.; Yang, L.; Hirano, S.-i., Li2FeSiO4/C cathode material synthesized by template-assisted sol–gel process with Fe2O3 microsphere. *Journal of power sources* **2012,** *217*, 243-247.
66. Devaraju, M.; Tomai, T.; Honma, I., Supercritical hydrothermal synthesis of rod like Li2FeSiO4 particles for cathode application in lithium ion batteries. *Electrochimica Acta* **2013,** *109*, 75-81.
67. Muraliganth, T.; Stroukoff, K. R.; Manthiram, A., Microwave-Solvothermal Synthesis of Nanostructured Li2MSiO4/C (M = Mn and Fe) Cathodes for Lithium-Ion Batteries. *Chemistry of Materials* **2010,** *22* (20), 5754-5761.
68. Rangappa, D.; Murukanahally, K. D.; Tomai, T.; Unemoto, A.; Honma, I., Ultrathin Nanosheets of Li2MSiO4 (M = Fe, Mn) as High-Capacity Li-Ion Battery Electrode. *Nano Letters* **2012,** *12* (3), 1146-1151.
69. Gao, H.; Hu, Z.; Zhang, K.; Cheng, F.; Chen, J., Intergrown Li2FeSiO4·LiFePO4–C nanocomposites as high-capacity cathode materials for lithium-ion batteries. *Chemical Communications* **2013,** *49* (29), 3040-3042.
70. Xie, M.; Luo, R.; Chen, R.; Wu, F.; Zhao, T.; Wang, Q.; Li, L., Template-assisted hydrothermal synthesis of Li2MnSiO4 as a cathode material for lithium ion batteries. *ACS applied materials & interfaces* **2015,** *7* (20), 10779-10784.
71. Yang, X.-F.; Yang, J.-H.; Zaghib, K.; Trudeau, M. L.; Ying, J. Y., Synthesis of phase-pure Li2MnSiO4@ C porous nanoboxes for high-capacity Li-ion battery cathodes. *Nano energy* **2015,** *12*, 305-313.
72. Zhang, F.; An, Y.; Zhai, W.; Gao, X.; Feng, J.; Ci, L.; Xiong, S., Nanotubes within transition metal silicate hollow spheres: Facile preparation and superior lithium storage performances. *Materials Research Bulletin* **2015,** *70*, 573-578.
73. Ma, Y.; Ulissi, U.; Bresser, D.; Ma, Y.; Ji, Y.; Passerini, S., Manganese silicate hollow spheres enclosed in reduced graphene oxide as anode for lithium-ion batteries. *Electrochimica Acta* **2017,** *258*, 535-543.
74. Gong, Z.; Yang, Y., Recent advances in the research of polyanion-type cathode materials for Li-ion batteries. *Energy & Environmental Science* **2011,** *4* (9), 3223-3242.
75. Nytén, A.; Kamali, S.; Häggström, L.; Gustafsson, T.; Thomas, J. O., The lithium extraction/insertion mechanism in Li2FeSiO4. *Journal of Materials Chemistry* **2006,** *16* (23), 2266-2272.
76. Chen, W.; Lan, M.; Zhu, D.; Ji, C.; Feng, X.; Yang, C.; Zhang, J.; Mi, L., Synthesis of Li2FeSiO4/C and its excellent performance in aqueous lithium-ion batteries. *Journal of Materials Chemistry A* **2013,** *1* (36), 10912-10917.
77. Chen, Z.; Qiu, S.; Cao, Y.; Qian, J.; Ai, X.; Xie, K.; Hong, X.; Yang, H., Hierarchical porous Li 2 FeSiO 4/C composite with 2 Li storage capacity and long cycle stability for advanced Li-ion batteries. *Journal of Materials Chemistry A* **2013,** *1* (16), 4988-4992.
78. Zhang, L.; Ni, J.; Wang, W.; Guo, J.; Li, L., 3D porous hierarchical Li2FeSiO4/C for rechargeable lithium batteries. *Journal of Materials Chemistry A* **2015,** *3* (22), 11782-11786.
79. Kageyama, H.; Hashimoto, Y.; Oaki, Y.; Imai, H., Six-armed twin crystals composed of lithium iron silicate nanoplates and their electrochemical properties. *CrystEngComm* **2015,** *17* (44), 8486-8491.
80. Yang, J.; Kang, X.; He, D.; Peng, T.; Hu, L.; Mu, S., Hierarchical shuttle-like Li2FeSiO4 as a highly efficient cathode material for lithium-ion batteries. *Journal of Power Sources* **2013,** *242*, 171-178.
81. Jiang, X.; Xu, H.; Liu, J.; Yang, J.; Mao, H.; Qian, Y., Hierarchical mesoporous Li2Mn0. 5Fe0. 5SiO4 and Li2Mn0. 5Fe0. 5SiO4/C assembled by nanoparticles or nanoplates as a cathode material for lithium-ion batteries. *Nano Energy* **2014,** *7*, 1-9.

82. Zhang, S.; Li, Y.; Xu, G.; Li, S.; Lu, Y.; Toprakci, O.; Zhang, X., High-capacity Li2Mn0. 8Fe0. 2SiO4/carbon composite nanofiber cathodes for lithium-ion batteries. *Journal of Power Sources* **2012,** *213*, 10-15.
83. Guo, H.; Cao, X.; Li, X.; Li, L.; Li, X.; Wang, Z.; Peng, W.; Li, Q., Optimum synthesis of Li2Fe1− xMnxSiO4/C cathode for lithium ion batteries. *Electrochimica Acta* **2010,** *55* (27), 8036-8042.
84. Deng, C.; Zhang, S.; Yang, S., Effect of Mn substitution on the structural, morphological and electrochemical behaviors of Li2Fe1− xMnxSiO4 synthesized via citric acid assisted sol–gel method. *Journal of Alloys and Compounds* **2009,** *487* (1-2), L18-L23.
85. Zhang, D.; Ding, Z.; Zhao, S.; Yang, Y.; Feng, Y.; Xiao, L.; Ji, R.; Chen, L.; Wei, W., Morphological evolution and kinetic enhancement of Li2FexMn1-xSiO4/C cathodes for Li-ion battery. *Progress in Natural Science: Materials International* **2018,** *28* (5), 535-541.
86. Kojima, A.; Kojima, T.; Sakai, T., Structural analysis during charge-discharge process of Li2FeSiO4 synthesized by molten carbonate flux method. *Journal of The Electrochemical Society* **2012,** *159* (5), A525-A531.
87. Lv, D.; Bai, J.; Zhang, P.; Wu, S.; Li, Y.; Wen, W.; Jiang, Z.; Mi, J.; Zhu, Z.; Yang, Y., Understanding the High Capacity of Li2FeSiO4: In Situ XRD/XANES Study Combined with First-Principles Calculations. *Chemistry of Materials* **2013,** *25* (10), 2014-2020.
88. Masese, T.; Orikasa, Y.; Tassel, C.; Kim, J.; Minato, T.; Arai, H.; Mori, T.; Yamamoto, K.; Kobayashi, Y.; Kageyama, H.; Ogumi, Z.; Uchimoto, Y., Relationship between Phase Transition Involving Cationic Exchange and Charge–Discharge Rate in Li2FeSiO4. *Chemistry of Materials* **2014,** *26* (3), 1380-1384.
89. Lu, X.; Wei, H.; Chiu, H.-C.; Gauvin, R.; Hovington, P.; Guerfi, A.; Zaghib, K.; Demopoulos, G. P., Rate-dependent phase transitions in Li2FeSiO4 cathode nanocrystals. *Scientific Reports* **2015,** *5*, 8599.
90. Arthur, Z.; Chiu, H.-C.; Lu, X.; Chen, N.; Emond, V.; Zaghib, K.; Jiang, D.-T.; Demopoulos, G. P., Spontaneous reaction between an uncharged lithium iron silicate cathode and a LiPF 6-based electrolyte. *Chemical Communications* **2016,** *52* (1), 190-193.
91. Kojima, A.; Kojima, T.; Mitsuharu, T.; Sakai, T., Crystal structure and electrochemical performance of a new lithium trivalent iron silicate. *Journal of the Electrochemical Society* **2012,** *159* (6), A725-A729.
92. Sun, C.; Rajasekhara, S.; Goodenough, J. B.; Zhou, F., Monodisperse Porous LiFePO4 Microspheres for a High Power Li-Ion Battery Cathode. *Journal of the American Chemical Society* **2011,** *133* (7), 2132-2135.
93. Fransen, M. In *1-and 2D Detectors and Sample Fluorescence in XRD*, ACTA CRYSTALLOGRAPHICA A-FOUNDATION AND ADVANCES, INT UNION CRYSTALLOGRAPHY 2 ABBEY SQ, CHESTER, CH1 2HU, ENGLAND: 2005; pp C146-C146.
94. Wei, B.; Lu, X.; Voisard, F. d. r.; Wei, H.; Chiu, H.-c.; Ji, Y.; Han, X.; Trudeau, M. L.; Zaghib, K.; Demopoulos, G. P., In Situ TEM Investigation of Electron Irradiation Induced Metastable States in Lithium-Ion Battery Cathodes: Li2FeSiO4 versus LiFePO4. *ACS Applied Energy Materials* **2018,** *1* (7), 3180-3189.
95. Young, R. A., *The rietveld method*. Oxford university press Oxford: 1993; Vol. 6.
96. Nash, J., The singular-value decomposition and its use to solve least-squares problems. *Compact Numerical Methods for Computers: Linear Algebra and Function Minimisation* **1990**, 30-48.
97. Altomare, A.; Burla, M. C.; Giacovazzo, C.; Guagliardi, A.; Moliterni, A. G.; Polidori, G.; Rizzi, R., Quanto: a Rietveld program for quantitative phase analysis of polycrystalline mixtures. *Journal of Applied Crystallography* **2001,** *34* (3), 392-397.
98. Jia, Y.; Xu, L.; Fang, Z.; Demopoulos, G. P., Observation of Surface Precipitation of Arsenate on Ferrihydrite. *Environmental Science & Technology* **2006,** *40* (10), 3248-3253.
99. Manceau, A.; Ildefonse, P.; Hazemann, J. L.; Flank, A. M.; Gallup, D., Crystal chemistry of hydrous iron silicate scale deposits at the Salton Sea geothermal field. *Clays and Clay Minerals* **1995,** *43* (3), 304-317.
100. Zeng, Y.; Chiu, H.-C.; Rasool, M.; Brodusch, N.; Gauvin, R.; Jiang, D.-T.; Ryan, D. H.; Zaghib, K.; Demopoulos, G. P., Hydrothermal crystallization of Pmn21 Li2FeSiO4 hollow mesocrystals for Li-ion cathode application. *Chemical Engineering Journal* **2019,** *359*, 1592-1602.

101. Zhang, M.; Chen, K.; Chen, X.; Peng, X.; Sun, X.; Xue, D., Ethylenediamine-assisted crystallization of Fe 2 O 3 microspindles with controllable size and their pseudocapacitance performance. *CrystEngComm* **2015,** *17* (7), 1521-1525.
102. Kim, D.-H.; Kim, J., Synthesis of LiFePO4 nanoparticles in polyol medium and their electrochemical properties. *Electrochemical and Solid-State Letters* **2006,** *9* (9), A439-A442.
103. Ferrari, S.; Capsoni, D.; Casino, S.; Destro, M.; Gerbaldi, C.; Bini, M., Electrochemistry of orthosilicate-based lithium battery cathodes: a perspective. *Physical Chemistry Chemical Physics* **2014,** *16* (22), 10353-10366.
104. Saracibar, A.; Van der Ven, A.; Arroyo-de Dompablo, M., Crystal structure, energetics, and electrochemistry of Li2FeSiO4 polymorphs from first principles calculations. *Chemistry of Materials* **2012,** *24* (3), 495-503.
105. Ni, J.; Jiang, Y.; Bi, X.; Li, L.; Lu, J., Lithium Iron Orthosilicate Cathode: Progress and Perspectives. *ACS Energy Letters* **2017,** *2* (8), 1771-1781.
106. Schneider, P., Adsorption isotherms of microporous-mesoporous solids revisited. *Applied Catalysis A: General* **1995,** *129* (2), 157-165.
107. Wang, Z.; Peng, B.; Zhang, L.; Zhao, Z.; Liu, D.; Peng, N.; Wang, D.; He, Y.; Liang, Y.; Liu, H., Study on formation mechanism of fayalite (Fe 2 SiO 4) by solid state reaction in sintering process. *JOM* **2018,** *70* (4), 539-546.
108. Gelius, U.; Heden, P.; Hedman, J.; Lindberg, B.; Manne, R.; Nordberg, R.; Nordling, C.; Siegbahn, K., Molecular spectroscopy by means of ESCA III. Carbon compounds. *Physica Scripta* **1970,** *2* (1-2), 70.
109. Pertsin, A.; Gorelova, M.; Levin, V. Y.; Makarova, L., An XPS study of the surface–bulk compositional differences in siloxane-containing block copolymers and polymer blends. *Journal of applied polymer science* **1992,** *45* (7), 1195-1202.
110. Liu, H.; Zhang, Y.; Li, R.; Sun, X.; Désilets, S.; Abou-Rachid, H.; Jaidann, M.; Lussier, L.-S., Structural and morphological control of aligned nitrogen-doped carbon nanotubes. *Carbon* **2010,** *48* (5), 1498-1507.
111. Wang, H. g.; Wu, Z.; Meng, F. l.; Ma, D. l.; Huang, X. l.; Wang, L. m.; Zhang, X. b., Nitrogen-Doped Porous Carbon Nanosheets as Low-Cost, High-Performance Anode Material for Sodium-Ion Batteries. *ChemSusChem* **2013,** *6* (1), 56-60.
112. De Faria, D.; Venâncio Silva, S.; De Oliveira, M., Raman microspectroscopy of some iron oxides and oxyhydroxides. *Journal of Raman spectroscopy* **1997,** *28* (11), 873-878.
113. Ferrari, A. C.; Robertson, J., Interpretation of Raman spectra of disordered and amorphous carbon. *Physical review B* **2000,** *61* (20), 14095.
114. Zaghib, K.; Salah, A. A.; Ravet, N.; Mauger, A.; Gendron, F.; Julien, C., Structural, magnetic and electrochemical properties of lithium iron orthosilicate. *Journal of power sources* **2006,** *160* (2), 1381-1386.
115. Zhang, Q.; Ge, S.; Xue, H.; Wang, X.; Sun, H.; Li, A., Fabrication of a fayalite@C nanocomposite with superior lithium storage for lithium ion battery anodes. *RSC Advances* **2014,** *4* (102), 58260-58264.
116. Paoletti, P., Formation of metal complexes with ethylenediamine: a critical survey of equilibrium constants, enthalpy and entropy values. *Pure and Applied Chemistry* **1984,** *56* (4), 491-522.
117. Cheng, T. C.; Demopoulos, G. P., Hydrolysis of Ferric Sulfate in the Presence of Zinc Sulfate at 200 °C: Precipitation Kinetics and Product Characterization. *Industrial & Engineering Chemistry Research* **2004,** *43* (20), 6299-6308.
118. Xu, Y.; Shen, W.; Zhang, A.; Liu, H.; Ma, Z., Template-free hydrothermal synthesis of Li2FeSiO4 hollow spheres as cathode materials for lithium-ion batteries. *Journal of Materials Chemistry A* **2014,** *2* (32), 12982-12990.
119. Acharya, S.; Maheshwari, N.; Tatikondewar, L.; Kshirsagar, A.; Kulkarni, S., Ethylenediamine-mediated wurtzite phase formation in ZnS. *Crystal Growth & Design* **2013,** *13* (4), 1369-1376.

120. Masese, T.; Tassel, C. d.; Orikasa, Y.; Koyama, Y.; Arai, H.; Hayashi, N.; Kim, J.; Mori, T.; Yamamoto, K.; Kobayashi, Y., Crystal Structural Changes and Charge Compensation Mechanism during Two Lithium Extraction/Insertion between Li2FeSiO4 and FeSiO4. *The Journal of Physical Chemistry C* **2015,** *119* (19), 10206-10211.
121. Gyenes, B.; Stevens, D.; Chevrier, V.; Dahn, J., Understanding anomalous behavior in coulombic efficiency measurements on Li-ion batteries. *Journal of The Electrochemical Society* **2014,** *162* (3), A278.
122. Lu, X.; Chiu, H.-C.; Arthur, Z.; Zhou, J.; Wang, J.; Chen, N.; Jiang, D.-T.; Zaghib, K.; Demopoulos, G. P., Li-ion storage dynamics in metastable nanostructured Li2FeSiO4 cathode: Antisite-induced phase transition and lattice oxygen participation. *Journal of Power Sources* **2016,** *329* (Supplement C), 355-363.
123. Palacín, M. R.; Simon, P.; Tarascon, J.-M., Nanomaterials for electrochemical energy storage: the good and the bad. *Acta Chimica Slovenica* **2016,** *63*, 417-423.
124. Politaev, V. V.; Petrenko, A. A.; Nalbandyan, V. B.; Medvedev, B. S.; Shvetsova, E. S., Crystal structure, phase relations and electrochemical properties of monoclinic Li2MnSiO4. *Journal of Solid State Chemistry* **2007,** *180* (3), 1045-1050.
125. Rabiej, S., A comparison of two X-ray diffraction procedures for crystallinity determination. *European Polymer Journal* **1991,** *27* (9), 947-954.
126. Dixit, H.; Zhou, W.; Idrobo, J.-C.; Nanda, J.; Cooper, V. R., Facet-dependent disorder in pristine high-voltage lithium–manganese-rich cathode material. *ACS nano* **2014,** *8* (12), 12710-12716.
127. Wang, H.; Jang, Y. I.; Huang, B.; Sadoway, D. R.; Chiang, Y. M., TEM study of electrochemical cycling-induced damage and disorder in LiCoO2 cathodes for rechargeable lithium batteries. *Journal of The Electrochemical Society* **1999,** *146* (2), 473-480.
128. Fang, H.; Pan, Z.; Li, L.; Yang, Y.; Yan, G.; Li, G.; Wei, S., The possibility of manganese disorder in LiMnPO4 and its effect on the electrochemical activity. *Electrochemistry Communications* **2008,** *10* (7), 1071-1073.
129. Coelho, A. A., TOPAS and TOPAS-Academic: an optimization program integrating computer algebra and crystallographic objects written in C++. *Journal of Applied Crystallography* **2018,** *51* (1), 210-218.
130. Toby, B. H., R factors in Rietveld analysis: how good is good enough? *Powder diffraction* **2006,** *21* (1), 67-70.
131. Xiong, F.; An, Q.; Xia, L.; Zhao, Y.; Mai, L.; Tao, H.; Yue, Y., Revealing the atomistic origin of the disorder-enhanced Na-storage performance in NaFePO4 battery cathode. *Nano Energy* **2019,** *57*, 608-615.
132. Kim, J.; Seo, D.-H.; Kim, H.; Park, I.; Yoo, J.-K.; Jung, S.-K.; Park, Y.-U.; Goddard Iii, W. A.; Kang, K., Unexpected discovery of low-cost maricite NaFePO4 as a high-performance electrode for Na-ion batteries. *Energy & Environmental Science* **2015,** *8* (2), 540-545.
133. Yang, J.; Han, X.; Zhang, X.; Cheng, F.; Chen, J., Spinel LiNi0.5Mn1.5O4 cathode for rechargeable lithiumion batteries: Nano vs micro, ordered phase (P4332) vs disordered phase (Fd$\bar 3$m). *Nano Research* **2013,** *6* (9), 679-687.
134. Arroyo-de Dompablo, M.; Armand, M.; Tarascon, J.; Amador, U., On-demand design of polyoxianionic cathode materials based on electronegativity correlations: An exploration of the Li2MSiO4 system (M= Fe, Mn, Co, Ni). *Electrochemistry Communications* **2006,** *8* (8), 1292-1298.
135. Rahm, M.; Hoffmann, R.; Ashcroft, N., Atomic and ionic radii of elements 1–96. *Chemistry–A European Journal* **2016,** *22* (41), 14625-14632.
136. Longo, R. C.; Xiong, K.; Kc, S.; Cho, K., Crystal structure and multicomponent effects in Tetrahedral Silicate Cathode Materials for Rechargeable Li-ion Batteries. *Electrochimica Acta* **2014,** *121*, 434-442.
137. Yi, T.; Li, Y.; Cheng, X.; Zhang, Y., Local structure evolution of Li2Fe0.5Mn0.5SiO4 during delithiation/lithiation processes: A first-principles investigation. *Computational Materials Science* **2015,** *99*, 96-104.

138. Kokalj, A.; Dominko, R.; Mali, G.; Meden, A.; Gaberscek, M.; Jamnik, J., Beyond One-Electron Reaction in Li Cathode Materials: Designing Li2Mn x Fe1-x SiO4. *Chemistry of Materials* **2007,** *19* (15), 3633-3640.
139. Westre, T. E.; Kennepohl, P.; DeWitt, J. G.; Hedman, B.; Hodgson, K. O.; Solomon, E. I., A multiplet analysis of Fe K-edge 1s→ 3d pre-edge features of iron complexes. *Journal of the American Chemical Society* **1997,** *119* (27), 6297-6314.
140. Zhang, P.; Wei, S.-H., Origin of charge compensation and its effect on the stability of oxide cathodes for Li-ion batteries: The case of orthosilicates. *Electrochimica Acta* **2018,** *270*, 409-416.
141. He, G.; Manthiram, A., Nanostructured Li2MnSiO4/C Cathodes with Hierarchical Macro‐/Mesoporosity for Lithium‐Ion Batteries. *Advanced Functional Materials* **2014,** *24* (33), 5277-5283.

APPENDIXES

Appendix 1-Supplementary Information on Synthesis and Chemical Analysis

Hydrothermal Reactor: An illustration of the dissembled autoclave used for hydrothermal sysnthesis is presented in Figure A.1

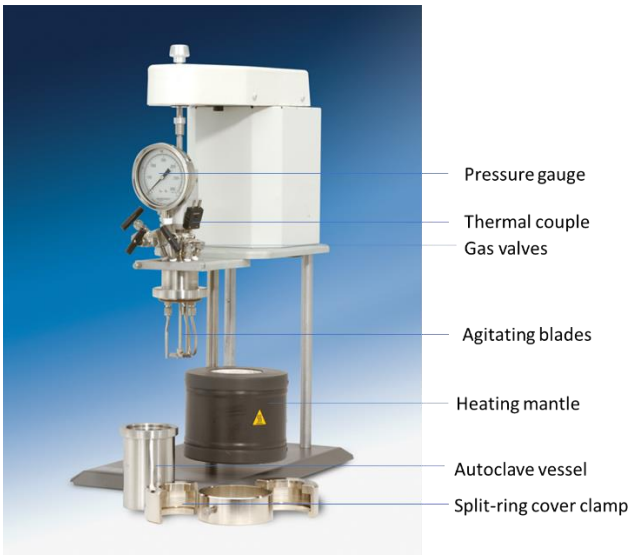

Figure A.1. A photo illustration of a Parr 4567 autoclave with agitation (dissembled)

Because the autoclave is a pressurized reactor operating at elevated pressure and temperature, it is important to take into consideration the pressure limit of the reactor and calculate the maximum volume of the liquid inside the vessel and the corresponding vapor pressure at certain temperature before conducting an experiment. In the case of water as a solvent, the vapor pressure at 180°C the experiments were carried out is approximately 1 MPa, or 10.5 bar. The stainless steel made autoclave was rated for 350°C and 2000 psi (138 bar), quite high upper limits to be of concern. It is important, however from a safety point of view to never overfill the autoclave vessel as in this case, as dictated by the ideal gas law (PV=nRT), confinement of vapor in a tiny volume would lead to large pressure increase potentially reaching the limit of the safety disc of the reactor leading to violent steam escape. Thus as a safety precaution in this work the autoclave vessel (450 mL capacity) was no more than 2/3 full. In addition to avoid any corrosion problems a Teflon liner as opposed to a Pyrex liner that could introduce excess Si into the alkaline reaction system was used. The use of Teflon liner set

another limit as to the upper temperature because this material starts softening significantly at 220 °C. For cleaning the autoclave (from some iron oxide type scale) after each experiment, diluted HCl solution was used to soak the liner and the internal agitator parts overnight, and then mild soap and water was used with a soft brush to gently brush away any remaining brown deposit of iron. The rest part of the autoclave was wiped clean with a damp paper towel and air-dried after each use for proper maintenance.

Annealing Furnace: An illustration of the furnace is shown in Figure A.2 The side lids were drilled to open a pair of holes with 3 cm in diameter and hoses were connected as gas inlet and outlet. The gas outlet was passed through a water-filled flask before released into the fume hood. The speed of gas flow was controlled together by the regulator on the gas cylinder and the gas flow meter equipped on the furnace (0.5 L/min). The major challenge of this furnace is that the large volume of the chamber may result in uneven heating temperatures (especially in high temperature annealing experiments above 800°C where deposition of SiO_2 on the ceramic crucible was observed, that is why graphite crucibles are preferred especially for high temperature annealing experiments) and extremely slow cooling rate (typically 16 hours of cooling time from 700°C to room temperature).

Figure A.2. A photo illustration of Carbolite GHA tube furnace

ICP Analysis: The ICP correlation plots are shown in Figures A.3-A.9 in Appendix 1 along details about the different dilution factors. The ICP samples were diluted multiple times so that the actual concentration of each element falls within the linear range of the calibration plots. For Fe and Si, the dilution factor was 10. i.e. the sample solution was diluted with 4% HNO_3 in a ratio of 1:10. For Li, the dilution factor was 100. i.e. the sample was diluted with 4% HNO_3 in a ratio of 1:10 and then diluted once again in a ratio of 1:10, for a total of 1:100.

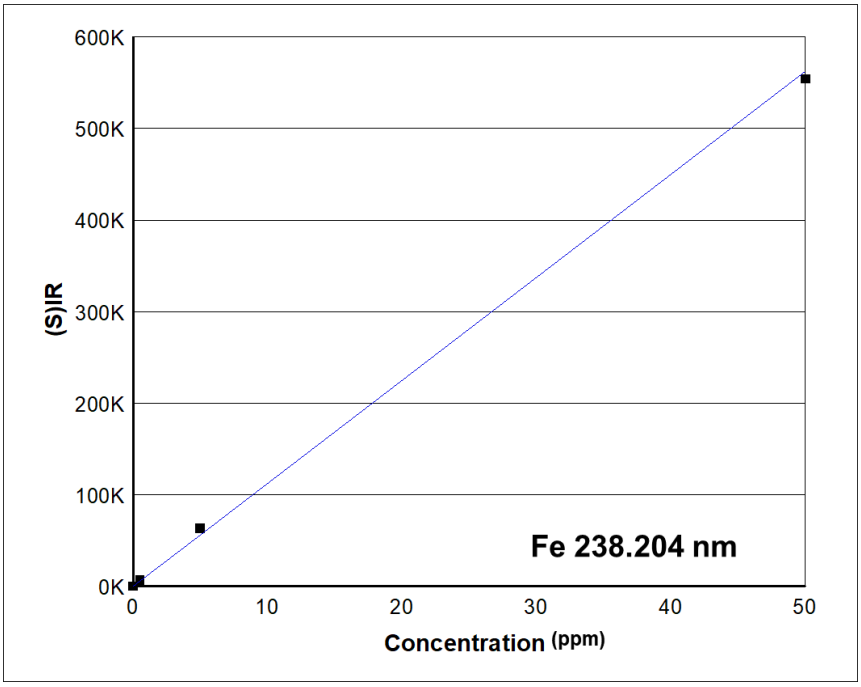

Figure A.3. ICP calibration curve of the Fe at the wavelength of 238.204 nm, correlation 0.998985.

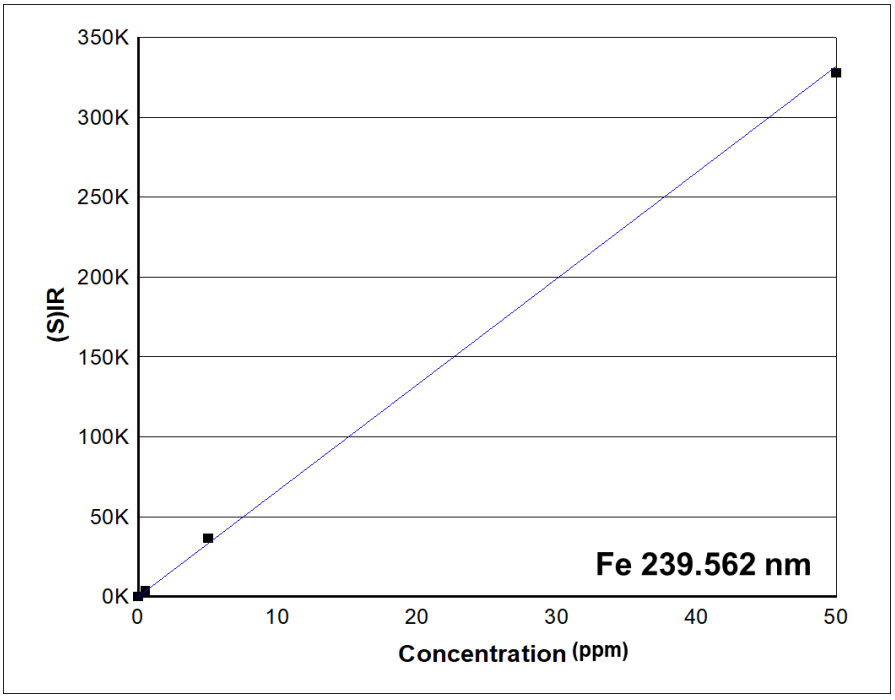

Figure A.4. ICP calibration curve of the Fe at the wavelength of 239.562 nm, correlation 0.999235.

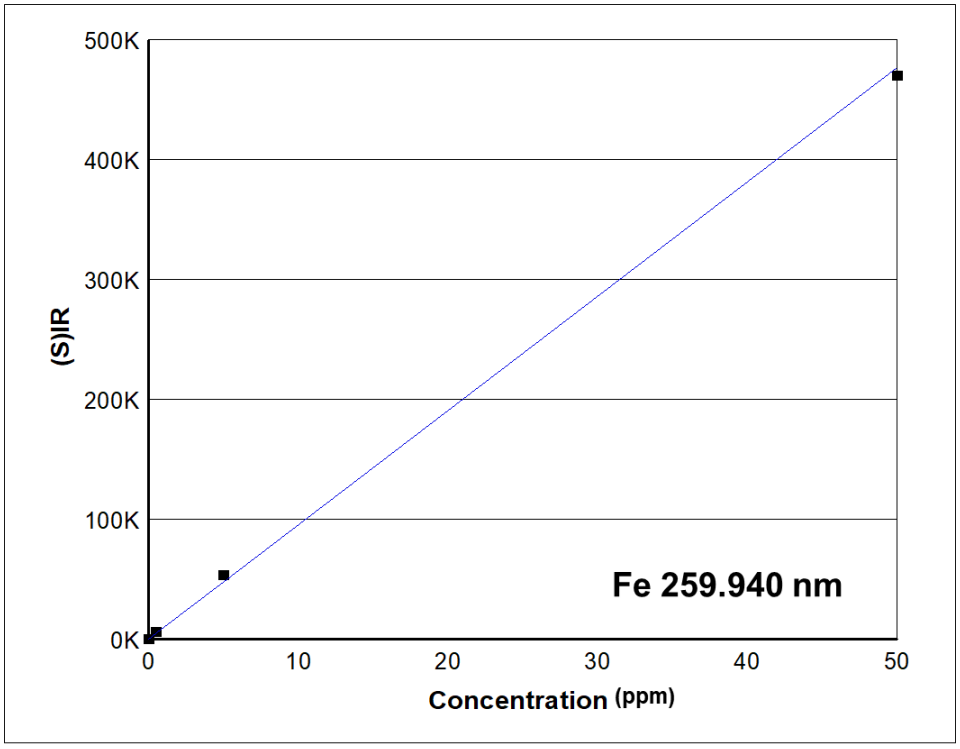

Figure A.5. ICP calibration curve of the Fe at the wavelength of 259.940 nm, correlation 0.999081

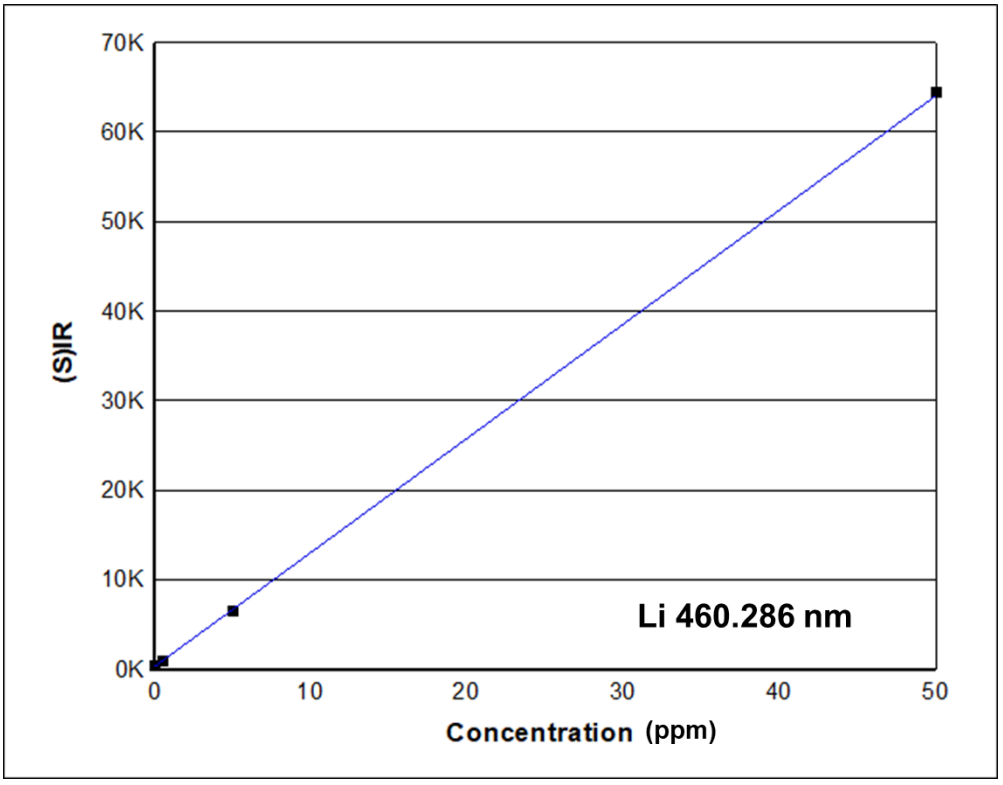

Figure A.6. ICP calibration curve of the Li at the wavelength of 460.286 nm, correlation 0.999787

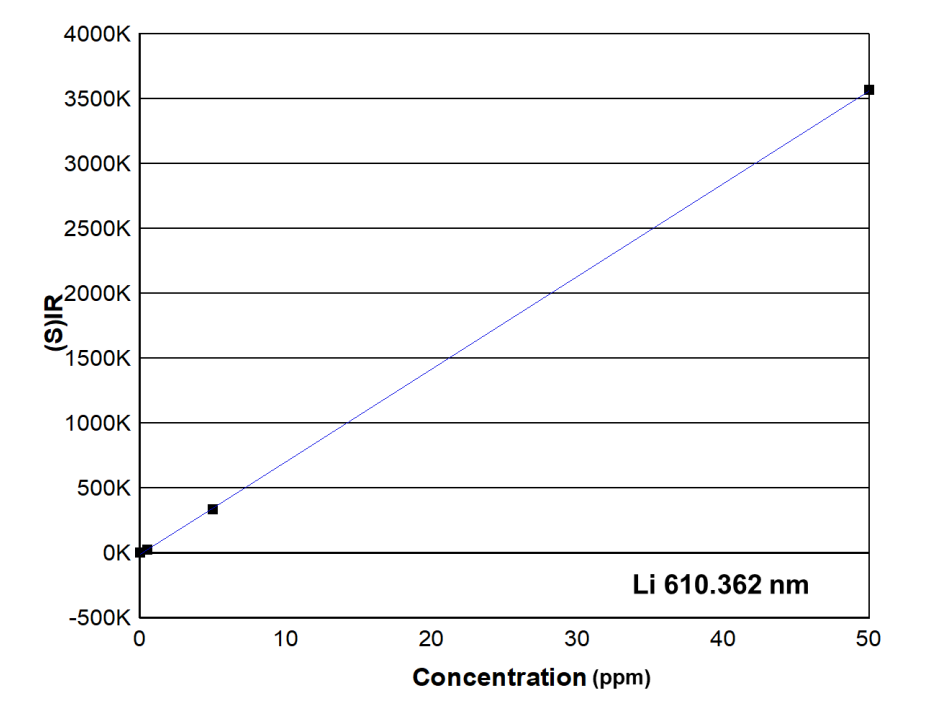

Figure A.7. ICP calibration curve of the Li at the wavelength of 610.362 nm, correlation 0.999970

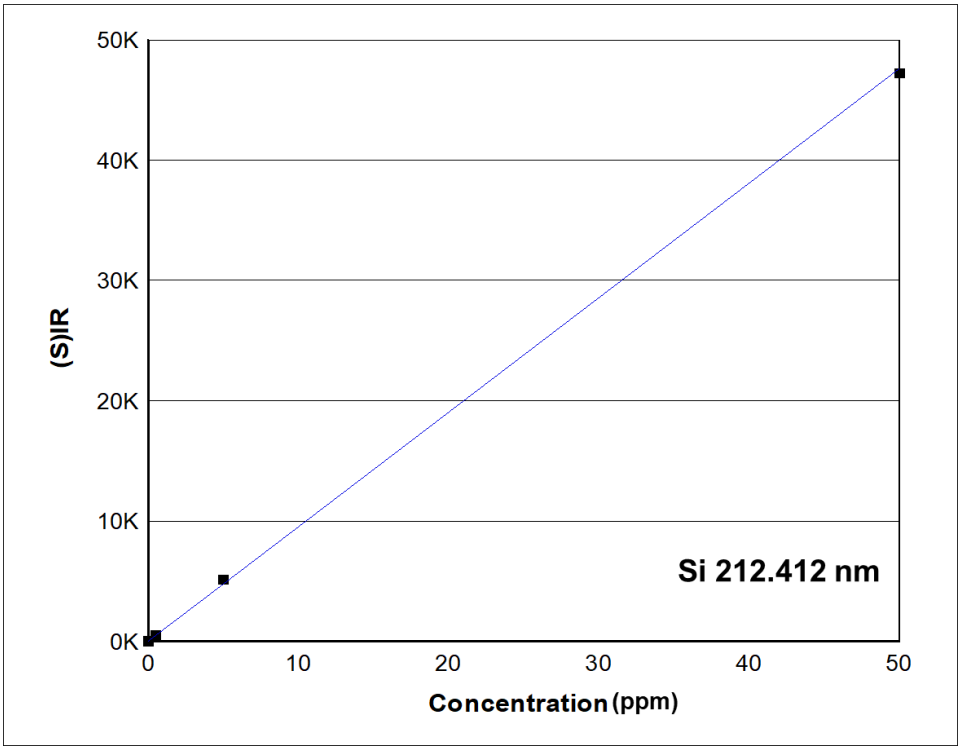

Figure A.8. ICP calibration curve of the Si at the wavelength of 212.412 nm, correlation 0.999653

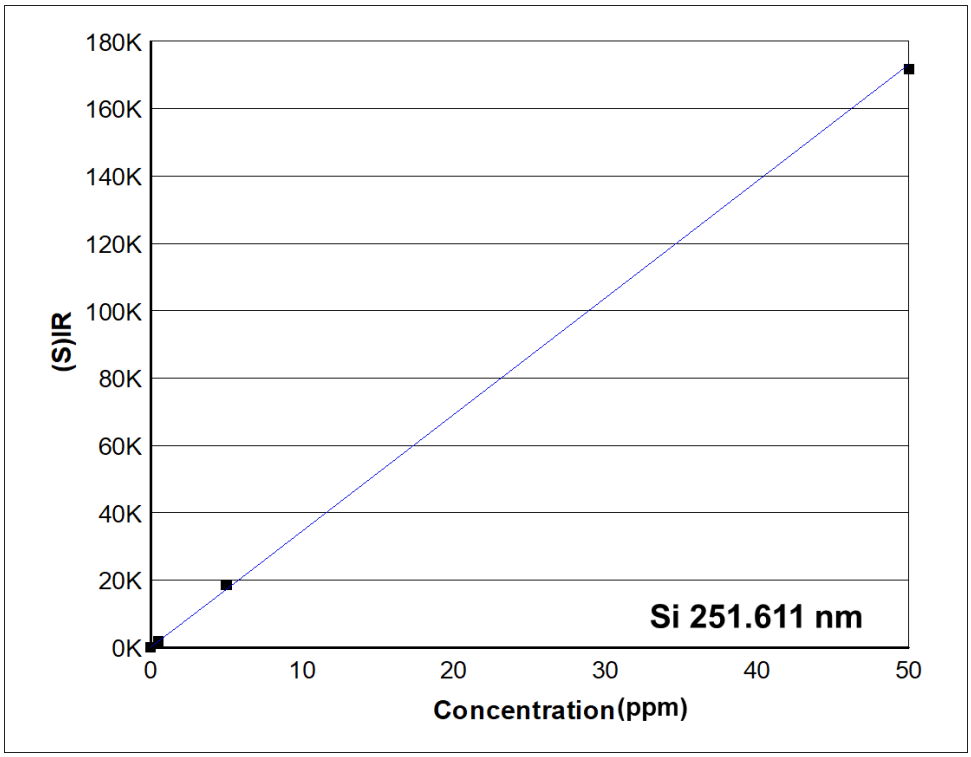

Figure A.9 ICP calibration curve of the Si at the wavelength of 251.611 nm, correlation 0.999710

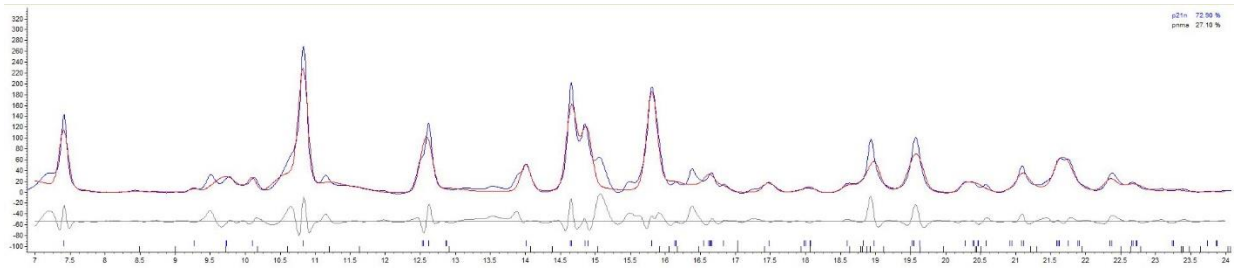

Figure A.10 Screenshot of a quantitative structural fitting using TOPAS on the LFS700 ball milled sample

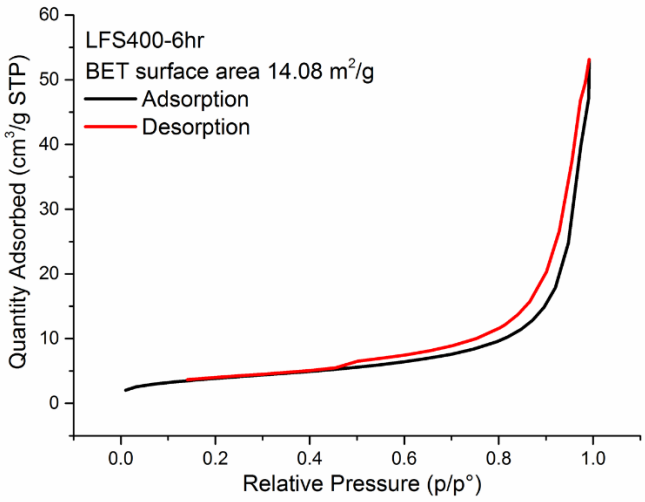

Figure A.11 BET isotherms of LFS400 sample

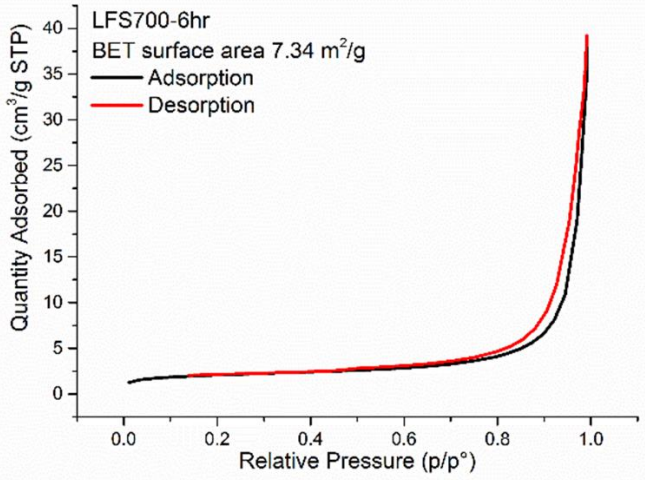

Figure A.12 BET isotherms of LFS700 pristine sample

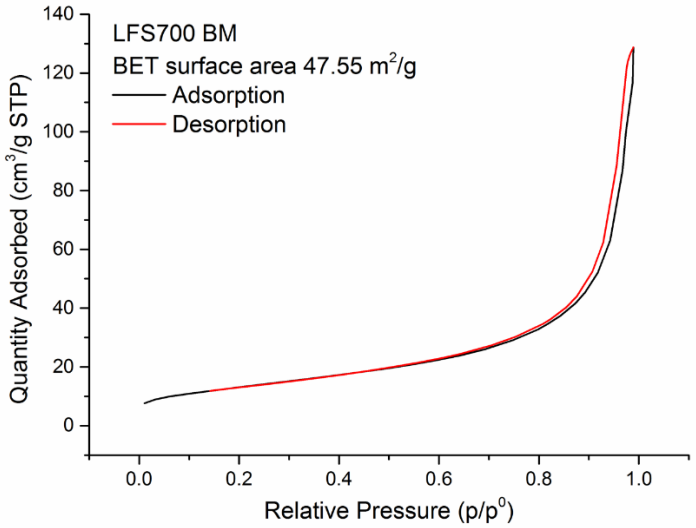

Figure A.13 BET isotherms of LFS700 ball milled sample

Appendix 2- Cycling of LFS700 at 55 ºC and Cell Failures

As it was described in Chapter 6, the structural changes of the monoclinic LFS cathode depended greatly on the applied rate. Further it was mentioned that cycling at C/50 could not reach one week as the cells failed prematurely at 45 ºC. However, according to earlier tests run at C/50 and room temperature no similar failure incidence was observed for LFS700 [89]. In other words the stability of the cells seems to be affected not only by the rate but also the cycling temperature. Thus, tests run at 55 ºC (data reported in Figure A.10) showed the cells to fail after 3 cycles at C/50, or 4 cycles at C/20. The failed third/fourth charging of the correspondine galvanostatic series are labelled with an asteristic mark in Fig. A.10. Notice that the first two chargings exhibit fairly high charging capacity (above 1 Li). On the contrary, the C/20 cell did not undergo cell failure at 45°C for more than 30 days, as mentioned earlier.

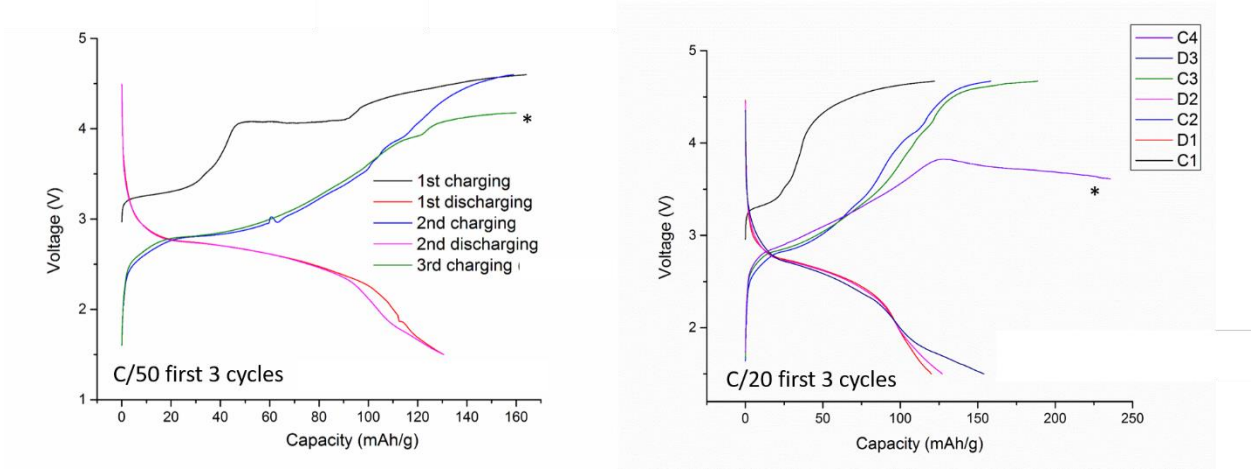

Figure. A.14. The 55°C cell cycling behavior at C/50 and C/20. The cells fail at the third charging at C/50 (left) and the fourth charging at C/20 (right), as labelled with the asterisk marks. Notice that the charging capacity exceeded 160 mAh/g (one Li extraction) before the cell failure.

It was also noticed that if the cells are cycled firstly at a faster rate for a certain amout of time, (in this case, the pristine cell is initially cycled at C/2, for more than 300 cycles at 55°C), and then switched to slower rate (in this case, C/20 at 55°C), the cell life is extended without failure even at 55°C. This behavior can be attributed to the fact that initial fast cycling rate stabilizes the cell behavior. Similar behavior was noticed earlier with the LFS700 material under cycling at room temperature.[89] Fig. A.14 shows the galvanostatic charging/discharging behavior (voltage vs. time) after switching to C/20 from C/2. The initial charging and discharging capacity after switching is around 170 mAh/g and 190 mAh/g, respectively, which is equivalent to over 1 Li. Capacity fading was observed after 40 cycles and stablized at about 35 mAh/g, which is close to the initial capacity obtained at C/2 (Fig. 6.4).

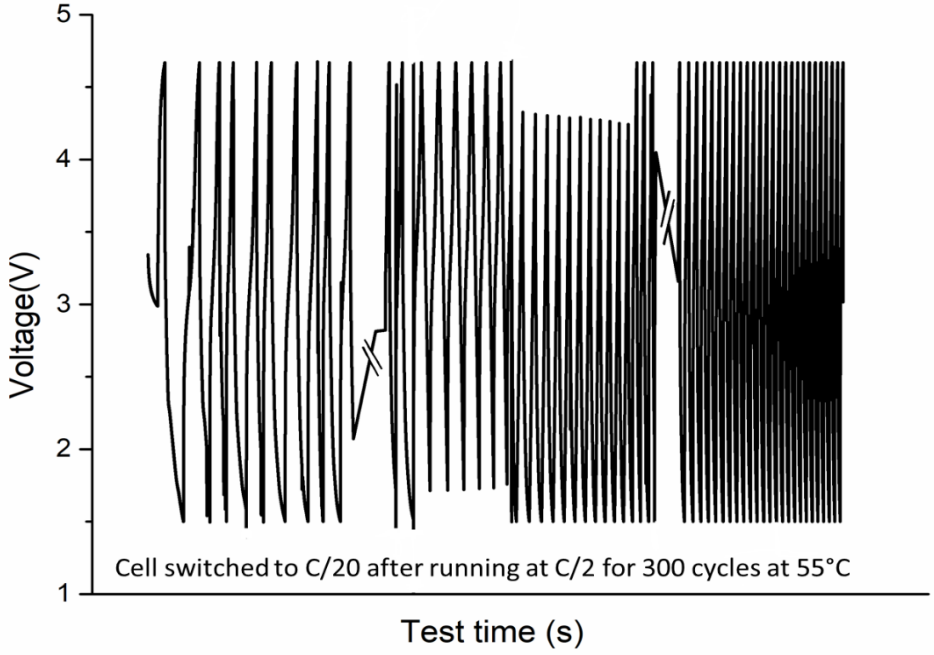

Figure. A.15 The cycle vs. time curve after switching to C/20 at 55°C; the cell had been firstly cycled at C/2, 55°C for over 300 cycles.

For other faster rates, namely C/10, C/5 and C/2, the cells did not fail at 45°C or 55°C. Gradual capacity loss was observed starting after 25 cycles for slow rate (C/10) at 55°C (Fig. A.15), while at 45°C the capacity loss was less noticeable even after 80 cycles at the same cycling rate (Fig. 6.5, c, d). For the C/2, no significant capacity fading was observed for both 45°C (Fig. 6.4) and 55°C (Fig. A.17). Given that fast rate the cells start with fairly low capacity (50 mAh/g at 55°C), no noticeable capacity fading was observed even after 300 cycles.

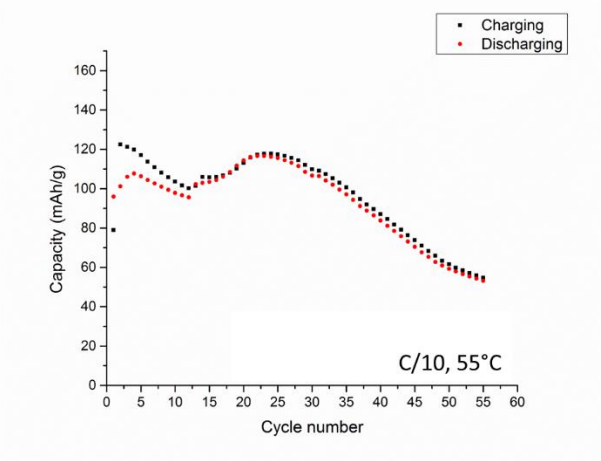

Figure. A.16 The capacity retention behavior at C/10, 55°C over the initial 60 cycles. Notice the gradual loss of capacity starting at around 25th cycle. This capacity fading behavior was not observed when the cell testing temperature was lowered to 45°C at C/10 (compare with Fig. 6.5 c, d).

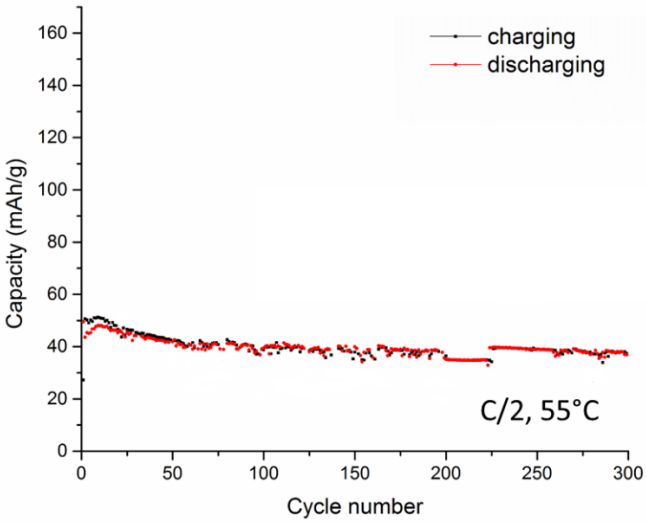

Figure. A.17 The capacity retention behavior at C/2, 55°C over the initial 300 cycles. The capacity is stabilized around 40 mAh/g without significant capacity fading behavior.

Based on these observations, it can be concluded that the threshold condition for the LFS700 material to survive the battery testing condition is a combined effect of both the cycling rate and cycling temperature. The table below summarizes the effect on the cell behavior, where the green checkmark indicates the cell can survive long-term battery testing without failure; while the red checkmark indicates the cell cannot survive for more than 3-4 cycles. The cells fail (*i.e.* fail within

the first three cycles) under extreme conditions when the testing temperaure is too high (55°C) or when the cycling rate is too slow (C/50), or as a combined effect of both factors. This can be either due to the over consumption of electrolyte from parasitic reactions, especially at high temperatures, or due to the irreversible structural transformation especially at slow C rate, or both.

Table A.1 Summary of cell failure/survival (green check mark indicates the cell cycles normally within the battery testing time frame up to 10 weeks, red check mark indicates the cell cannot survive the initial three cycles) under various battery cycling conditions of cycling rate (C/2 to C/50), testing temperature (RT, 45 and 55°C), and number of cycles.

Temperature / Rate	55°C	45°C	Room Temperature
C/50	✗	✗	✓
C/20	✗	✓	✓
C/10	✓	✓	
C/5	✓	✓	
C/2	✓	✓	
C/2 then C/20	✓		